A PHYSICS BASED INVESTIGATION OF GURNEY FLAPS FOR ENHANCEMENT OF ROTORCRAFT FLIGHT CHARACTERISTICS

A Dissertation
Presented to
The Academic Faculty

by

Byung-Young Min

In Partial Fulfillment
of the Requirements for the Degree
Doctor of Philosophy in the
School of Aerospace Engineering

Georgia Institute of Technology
May 2010

A PHYSICS BASED INVESTIGATION OF GURNEY FLAPS FOR ENHANCEMENT OF ROTORCRAFT FLIGHT CHARACTERISTICS

Approved by:

Dr. Lakshmi N. Sankar, Advisor
School of Aerospace Engineering
Georgia Institute of Technology

Dr. Daniel P. Schrage, Co-advisor
School of Aerospace Engineering
Georgia Institute of Technology

Dr. J. V. R. Prasad
School of Aerospace Engineering
Georgia Institute of Technology

Dr. Stephen M. Ruffin
School of Aerospace Engineering
Georgia Institute of Technology

Dr. Mark Costello
School of Aerospace Engineering
Georgia Institute of Technology

Dr. Yung H. Yu
Department of Aerospace Information Engineering
Konkuk University

Date Approved: [March 24, 2010]

[Dedicated to my parents and brothers]

ACKNOWLEDGEMENTS

I would like to express my heartfelt appreciation to my advisor and mentor, Dr. Lakshmi N. Sankar, whose encouragement, guidance and support enabled me to accomplish this research work. His kindness, patience, and great personality have always been a strong backbone during this journey. It was my great pleasure to pursue my Ph. D under his advice.

I would also like to thank Dr. Daniel P. Schrage, my co-advisor, for his support. Without his financial support and encouragement during the early years of my doctoral studies, I certainly could not have accomplished this research work.

I would like to thank my thesis reading committee members, Dr. J.V.R Prasad, Dr. Stephen Ruffin, and Dr. Mark Costello for providing valuable feedback on this research. I would especially like to thank Dr. Yung H. Yu, my external reading committee member, Dr. Jae-Woo Lee, my former advisor for my Master's degree, and Dr. Yung-Hwan Byun in Konkuk University for their continuous encouragement and support. They have provided invaluable support that influences my current and future life.

I would like to acknowledge Korean Science and Engineering Foundation for providing the scholarship under Abroad Master's and Doctoral Degree Scholarship program (M06-2004-000-10668-0) for the first two years of my studies in Georgia Tech.

I would like to thank Dr. Joon W. Lim for providing me with the HART-II rotor data. I would also like to thank Dr. Haiying Liu for her support. She provided the structural model of HART-II for DYMORE and kindly answered all my questions.

I would like to thank all my colleagues in the CFD lab, Dr. Chanin Tongchitpakdee, Dr. Vishwas Iyengar, Dr. Mina Zaki, Goktan Guzel, Nischint Rajmohan, Nandita Yeshala, Jeremy Bain, Lan Wu, Michael Nucci, Rick Deresz, and Ashley Flick for their friendship and support during my years in the lab. Special thanks to Nandita Yeshala for her proofreading of my thesis and Nischint Rajmohan for his valuable discussion on the research work.

I would like to thank all of my Korean friends, both, in the United States and Korea, for their support and friendship. I also thank my friends Dr. Mandy Goltsch, Dr. James Rigsby, Dr. Alex Moodie, and Dr. Irian Ordaz for their friendship.

I owe my deepest gratitude to my parents, brothers, and sisters-in-law. I would not be where I am without their support, encouragement and love. This thesis work is dedicated to them.

TABLE OF CONTENTS

LIST OF TABLES

LIST OF FIGURES

NOMENCLATURE

a	Speed of sound
A	Amplitude, Disk area
A, B, C	Flux Jacobian matrices
b	Wing semi-span
c	Chord
C_c	Chord-wise force coefficient ($F_c/(q_{ref}c_{ref})$)
C_d	Sectional drag force coefficient ($D/(q_{ref}c_{ref})$)
Cfx, Cfy, Cfz	Force coefficient along x, y, z direction ($F/(\rho_\infty AV_{tip}^2)$)
C_l	Sectional lift force coefficient ($L/(q_{ref}c_{ref})$)
C_m	Sectional moment coefficient ($M/(q_{ref}c_{ref}^2)$)
C_M	Moment coefficient ($M/(\rho_\infty AV_{tip}^2 R)$)
C_N, C_n	Normal force coefficient ($N/(q_{ref}c_{ref})$)
C_p	Specific heat at constant pressure, Pressure coefficient ($(p-p_\infty)/q_{ref}$)
C_{PM}	Pitching moment coefficient ($PM/(\rho_\infty AV_{tip}^2 R)$)
C_q	Sectional torque coefficient ($Q/(\rho_\infty AV_{tip}^2 Rs)$)
C_Q	Torque coefficient ($Q/(\rho_\infty AV_{tip}^2 R)$)
C_{RM}	Rolling moment coefficient ($RM/(\rho_\infty AV_{tip}^2 R)$)
C_t	Sectional thrust coefficient ($T/(\rho_\infty AV_{tip}^2 s)$)
C_T	Thrust coefficient ($T/(\rho_\infty AV_{tip}^2)$)
d	Distance from the wall
D	Drag force

D'	Sectional drag force
De	Equivalent drag force
e	Total energy per unit volume, Hinge offset
E, F, G	Inviscid flux matrices
E_v, F_v, G_v	Viscous flux matrices
F/M	Force and moment
F_1	Aerodynamic force
F_c	Chord-wise force
F_z	Force along z-direction
g	Acceleration of gravity
h_0	Specific total enthalpy
I	Identity matrix
J	Jacobian of transformation
k	Thermal conductivity, Reduced frequency
k_β	Hinge spring constant
l	Length
L	Lift force, Reference length, Load, Rotational matrix
L'	Sectional lift force
L, D, U	Lower, diagonal and upper block triangular matrix
m	Mass
M	Million
M	Mach number
max	Maximum
M_z	Yaw moment
n	Number of harmonics

N	Normal force
N_b	Number of blade
n_t	Grid velocity in the surface normal direction
n_x, n_y, n_z	Surface normal vector
p	Pressure
P	Per-revolution
Pr	Prandtl number
Pr_t	Turbulent Prandtl number
Psi	Azimuth angle
q	Primitive variable
q_{ref}	Dynamic pressure ($\frac{1}{2}\rho_\infty V_{tip}^2$ for rotor analysis)
Q	State variable vector, Vorticity and strain rate balance, Torque
r	Radial location
R	Riemann invariant, Rotor radius
Re	Reynolds number
RHS	Shorthand notation for the terms on the right hand side for any equation
s	Sectional span length
S	Vorticity
$\tilde{\vec{S}}$	Estimated surface vector
S_{ij}	Strain rate
t	Time, Thickness
T	Temperature, Thrust
u, v, w	Cartesian components of velocity
U, V, W	Contravarient velocity

V	Velocity
$\forall$	Volume
w	Weight function
x, y, z	Cartesian coordinates
y^+	Viscous sub-layer length scale ($y\sqrt{\rho\tau_w}/\mu$)

Greek Symbols

α	Angle of attack
α_s	Shaft tilt angle
β	Flapping angle
δ	Central difference operator
Δ	Difference, Grid spacing
ε	Turbulent dissipation
ϕ	Limiter function, Phase angle
$\Delta\phi, \Delta\theta, \Delta\psi$	Euler angles
γ	Specific heat ratio
Γ	Vortex strength
κ	Turbulent kinetic energy
λ	Eigenvalue
μ	Viscosity, Advance ratio
μ_l	Molecular viscosity
μ_t	Turbulent viscosity
θ	Pitch angle
ρ	Denisty
σ	Solidity

τ_{ij}	Shear stress tensor component
ω	Turbulent specific dissipation
ξ, η, ζ	Curvilinear coordinates
ψ, Ψ	Azimuth angle
Ω	Rotational speed

Subscripts

0	Amplitude of zero-th harmonic
$1c, 1s$	Amplitude of first harmonic
el	Elastic
i, j, k	Indices in three coordinate directions
LL	Lifting line
LM	Linear aerodynamic model
L, R	Left and right sides of the cell faces
max	Maximum
n	Normal direction
p	Pressure, Pre-cone
t	Derivative with respect to time
tip	Value at the blade tip
tw	Twist
$wall$	Variable on the wall surface
x, y, z	Derivatives with respect to Cartesian coordinates
ξ, η, ζ	Derivatives with respect to curvilinear coordinates
∞, inf, ref	Reference value

Superscripts

-1	Inverse matrix
l, r	Left and right sides of the cell faces
m, m+1	Sub-iteration level
n, n+1	Time level
sgs	Sub-grid scale
*	Non-dimensional variable
^	Dimensional variable
–	Matrix in the computational domain
~	Roe-averaged quantity
+	Positive eigenvalue
-	Negative eigenvalue
'	Fluctuation quantity after average

Acronyms and Abbreviations

2-D	Two Dimensional
3-D	Three Dimensional
ACF	Actively Controlled Flap
ATR	Active Twist Rotor
BC	Boundary Condition
BL	Baseline
BVI	Blade Vortex Interaction
CFD	Computational Fluid Dynamics
CSD	Computational Structural Dynamics
DES	Detached Eddy Simulation

ENO	Essentially Non-Oscillatory
FDS	Flux Difference Splitting
FSI	Fluid Structure Interface
GCL	Geometric Conservation Law
GF	Gurney Flap
HART	Higher harmonic control Aeroacoustics Rotor Test
HHC	Higher Harmonic Control
HRKES	Hybrid RANS-KES
IBC	Individual Blade Control
KES	Kinetic Eddy Simulation
LES	Large Eddy Simulation
LU-SGS	Lower-Upper Symmetric Gauss Seidel
MiTEs	Miniature Trailing-Edge Efffectors
MUSCL	Monotone Upstream-centered Scheme for Conservation Laws
OBC	On-Board Control
PDE	Partial Differential Equation
RANS	Reynolds Averaged Navier-Stokes
RHS	Right Hand Side
rpm	Rotation-per-minute
SA, S-A	Spalart-Allmaras
SST	Shear Stress Transform
T.E	Trailing Edge
UAV	Unmanned Aerial Vehicle
VLES	Very Large Eddy Simulation
WENO	Weighted Essentially Non-Oscillatory

SUMMARY

Helicopters are versatile vehicles that can vertically take off and land, hover, and perform maneuver at very low forward speeds. These characteristics make them unique for a number of civilian and military applications. However, the radial and azimuthal variation of dynamic pressure causes rotors to experience adverse phenomena such as transonic shocks and 3-D dynamic stall. Adverse interactions such as blade vortex interaction and rotor-airframe interaction may also occur. These phenomena contribute to noise and vibrations. Finally, in the event of an engine failure, rotorcraft tends to descend at high vertical velocities causing structural damage and loss of lives.

A variety of techniques have been proposed for reducing the noise and vibrations. These techniques include on-board control (OBC) devices, individual blade control (IBC), and higher harmonic control (HHC). Addition of these devices adds to the weight, cost, and complexity of the rotor system, and reduces the reliability of operations. Simpler OBC concepts will greatly alleviate these drawbacks and enhance the operating envelope of vehicles.

In this study, the use of Gurney flaps is explored as an OBC concept using a physics based approach. A three dimensional Navier-Stokes solver developed by the present investigator is coupled to an existing free wake model of the wake structure. The method is further enhanced for modeling of Blade-Vortex-Interactions (BVI). Loose coupling with an existing comprehensive structural dynamics analysis solver (DYMORE) is implemented for the purpose of rotor trim and modeling of aeroelastic effects.

Results are presented for Gurney flaps as an OBC concept for improvements in autorotation, rotor vibration reduction, and BVI characteristics. As a representative rotor, the HART-II model rotor is used.

It is found that the Gurney flap increases propulsive force in the driving region while the drag force is increased in the driven region. It is concluded that the deployable Gurney flap may improve autorotation characteristics if deployed only over the driving region. Although the net effect of the increased propulsive and drag force results in a faster descent rate when the trim state is maintained for identical thrust, it is found that permanently deployed Gurney flaps with fixed control settings may be useful in flare operations before landing by increasing thrust and lowering the descent rate.

The potential of deployable Gurney flap is demonstrated for rotor vibration reduction. The 4P harmonic of the vertical vibratory load is reduced by 80% or more, while maintaining the trim state. The 4P and 8P harmonic loads are successfully suppressed simultaneously using individually controlled multi-segmented flaps.

Finally, simulations aimed at BVI avoidance using deployable Gurney flaps are also presented.

CHAPTER 1

INTRODUCTION

1.1 Background

Helicopters are versatile vehicles that can vertically take off and land, hover, and perform maneuvers at a very low forward speed. These characteristics make them unique for a number of civilian and military applications. However, the radial and azimuthal variation of dynamic pressure causes rotors to experience adverse phenomena such as transonic shocks and 3-D dynamic stall. Adverse interactions such as blade vortex interaction and rotor-airframe interaction also occur. These phenomena contribute to noise and vibrations [1]. Finally, in the event of an engine failure, rotorcraft tends to descent at high vertical velocities causing structural damage and occasionally a loss of lives.

A variety of techniques have been proposed for reducing the noise and vibrations. These include on-board control (OBC) devices, individual blade control (IBC) [2,3], and higher harmonic control (HHC) [4,5]. Addition of these devices adds to the weight, cost, and complexity of the rotor system and reduces reliability of operations. Simpler OBC concepts will greatly alleviate these drawbacks and enhance the operating envelope of vehicles.

From the very beginning of helicopter development, vibration and noise have been challenging issues requiring the attention of designers and rotorcraft researchers. Reichert [6] and Loewy [7] present various sources of the vibration and approaches that

have been used through the early 1980s for the reduction of vibratory loads. Up to that time, vibration reduction mainly relied on passive approaches such as structural optimization, and on vibration absorbers or isolators. These devices successfully reduced vibration but came with a significant weight and drag penalty.

Friedmann and his coworkers [8,9] provide an excellent review on passive and active control methods for vibration reduction. Active control approaches include higher harmonic control (HHC) [4,5] and individual blade control (IBC) [2,3]. HHC is applied at the fixed frame through a higher harmonic swash plate control, whereas the IBC is applied on the rotating frame. Many wind tunnel and flight tests have been performed demonstrating the potential of higher harmonic control for noise and vibration reduction. However, due to its installment cost, relatively high actuation power requirement, and pitch link fatigue issues, very few of helicopters in production or under development are equipped with HHC despite its technology maturity.

Early IBC concepts used actuators at the blade root that replace or augment the pitch link. This requires a significant control power because of the need to move the entire blade. Subsequently, IBC concepts (or OBC) such as actively controlled flaps (ACF) [10,11], active twist rotor (ATR) [12,13], and miniature trailing-edge effectors (MiTEs) [14] were investigated, while retaining the swash plate for pilot control. These recent IBC methods require less control power compared to HHC and conventional IBC methods. However, ACF still requires a non-negligible actuation power, and has a drag penalty [11]. Both ACF and ATR require extensive modification to the rotor blade to accommodate trailing edge flap (ACF), or smart material (ATR). A more promising concept is the micro trailing edge (MiTE) flap. The MiTE flap (an outgrowth from

Gurney flap) is very small in size (1~5% chord length), and requires low actuation power. Their installment or retrofit is relatively easy, and piezo-electric actuators have also been used for the control of the device [15].

A benefit of active control is that it can be used to overcome other performance limitations besides vibration reduction. Examples include BVI noise reduction, dynamic stall alleviation, and improvement of autorotation characteristics. BVI noise and attendant vibration are closely related to each other, and may be minimized often simultaneously. Dynamic stall may be alleviated by avoiding high pitch angles with the aid of the high lift capability of the ACF [10], MiTEs or Gurney flap. Gurney flap, with its low power requirement, is an attractive device for improving the autorotation characteristics as well [16] for enhancing the safety and improving crashworthiness.

1.2 Gurney Flap

Gurney flap was first introduced by Dan Gurney in the Indy racecar to improve cornering performance by increasing down force [17]. This is a 1 to 5 % of chord length device installed on the trailing edge (Figure 1.1) that can enhance circulation and increase L, with little incremental drag. Thus the L/D ratio is high compared to a conventional airfoil at lift settings that for which the baseline airfoil is not optimized. Figure 1.2 illustrates flow field around Gurney flap equipped trailing edge. The Gurney flap and the recirculation bubbles provide effective camber and turn the flow so that the circulation is enhanced.

Retrofitting an existing surface with a Gurney flap would require only small modification to the overall design compared to other high lift devices which require extensive structural modifications. Because of this benefit, Gurney flaps have been used

in rotorcraft to retrofit horizontal and vertical stabilizers without major structural modification at the later stages of vehicle development [18].

The downside to using Gurney flap instead of a cambered high lift airfoil is in its relative drag increase. Since the flap is installed normal to the ambient flow, the flow separates behind the flap and forms a high pressure stagnation region on the windward surface. The low pressure in the aft region combined with the high pressure on the windward side increases drag. Although the drag increase is small due to the small size of the flap, a conventional cambered clean airfoil would produces lower drag at a lift coefficient it is designed for. Thus, Gurney flap is generally not considered as a high lift device candidate in the early design stage unless the airfoil shape is constrained. The high pressures over the windward side, along with the long moment arm from the center of gravity, produces additional pitching moment, which may lead to structural fatigue and high pitch link loads. Another factor that mitigates the effectiveness of Gurney flaps is the separated flow over the main airfoil. For the Gurney flap to be effective, the flow over the main airfoil upstream of the flap should be attached. Otherwise this separated flow is not deflected and the circulation is not enhanced.

1.2.1 Deployable Gurney Flap

In addition to its use as retrofits to an existing surface, Gurney flaps may be considered as effective active control devices in early stages of design. Because Gurney flap is small and light in weight, a small low-power actuator such as a piezoelectric device may be used for deploying and retracting a Gurney flap if necessary [15]. Figure 1.3 illustrates various deployable Gurney flap concepts studied by researchers. An example of piezoelectric device as an actuator is also shown in Figure 1.3-d). As seen in

Figure 1.3-a) and b), the small flaps may be segmented and distributed along the span, providing comprehensive controllability.

In this study, a Gurney flap is deployed either at the lower or upper surfaces near the trailing edge. Figure 1.4 represents possible deployment mechanisms for the configuration considered in this study. A T-shaped flap in neutral position is hidden inside the airfoil. As the servo is rotated, the flap moves upward or downward through the slot on the airfoil surface (Figure 1.4-a)). Since the flap size is small, even a relatively thin structural element may be enough to withstand the aerodynamic forces. The flap element slides through the surface slot as it is pushed or pulled by a servo (Figure 1.4-b)).

1.2.2 Previous Studies on the Gurney Flap or Micro-Flaps.

Computational and experimental studies have been done to explore the static lift and drag characteristics of Gurney flaps [23-27] and to explore the ability of Gurney flap in mitigating the adverse effects of dynamic stall [28-31]. It has also been studied for use in vertical lift systems such as Micro UAVs [32] for increased thrust production. Researchers at the US Army Aeroflightdynamics Directorate have conducted a series of tests recently to understand the physical mechanisms behind the high lift generation [29]. Static airfoil data as well as dynamic stall data was collected and compared against similar results for a plain airfoil (without Gurney flap) and against an airfoil with a variable droop leading edge shape.

Guzel et al. [31] have recently studied the steady and unsteady load characteristics of a VR-12 airfoil with and without the Gurney flap. It was found that the use of a Gurney flap could improve the static lift characteristics giving rise to a higher $C_{l,max}$ (close to 1.8) compared to the conventional airfoil (close to 1.4). The dynamic stall

characteristics of the Gurney flap equipped sections were not sufficiently different from that of a VR-12 airfoil, however.

Min et al. [16] examined the beneficial effects of Gurney flaps on helicopter rotors in descent. It was found that an existing rotor (similar to that used in BO-105), when retrofitted with a Gurney flap, could dramatically improve the thrust characteristics. It was found that the autorotative characteristics of the rotor (where a portion of the lift is tilted forward, causing an induced thrust rather than induced drag) could be improved with a Gurney flap equipped rotor.

Liu and Friedmann [33] studied deployable Gurney flap for hub vibratory load reduction using a comprehensive analysis that used a table look up of airfoil + flap data from 2-D Navier-Stokes computations. This study showed considerable potential for normal force vibration reduction via deployable Gurney flap. Min et al. [34] have also studied the effect of dynamically deployed Gurney flap on the hub vibratory loads and moments in steady forward flight condition, and showed that the Gurney flap could reduce peak to peak values of the vibratory loads and moments. Bae and Gandhi [35] have also examined deployable Gurney flap using 2-D table look-up approach, and showed potential of power reduction through redistribution of the air load. Roget and Chopra [36] have performed experimental test with an actively controlled 20% chord length of trailing edge flap. Although the size and operating mechanism differ from the Gurney flap, potential vibration reduction using the actively controlled lift control device (trailing edge flap) was successfully demonstrated with closed-loop control.

The potential of Gurney flaps, both as a means of improved power production and airload alleviation, has been recognized by researchers working in the area of wind

energy. Van Dam et al. have explored the 2-D characteristics of wind turbine airfoil sections from this perspective [37-39]. Tongchitpakdee [40] studied whether the power generation capabilities of an existing wind turbine (NREL Phase VI rotor) will benefit from a retrofit of the rotor with Gurney flaps. Three Gurney flap configurations (set at 45, 60 and 90 degrees relative to the chord line) with a 1.5% of chord length at low wind speed were tested. The computational studies showed a 18~43% increase in the torque extracted for a large range of operating conditions - wind speed, yaw angle of the rotor shaft relative to the wind. At high wind speeds, massive separation of the flow from the leading edge occurred and the Gurney flap was ineffective.

The effect of the Gurney flap was also studied from overall rotor performance perspective. Yeo [41] and Kinzel et al. [14] evaluated rotor performance using a comprehensive analysis code with table look-up, and showed that Gurney flap increases maximum blade loading capability and expands flight envelopes. Yee et al. [42] examined Gurney flap equipped airfoils for various freestream conditions corresponds to conventional helicopter flight regime using a two dimensional Navier-Stokes solver, and found that Gurney flaps may improve vehicle performance.

In addition to those benefits addressed above, Gurney flap is also being studied for alleviating the adverse effects of aircraft wake vortices for fixed wing applications [43,44].

1.3 Hybrid Methodology

The flow field around helicopter rotors is very complex. The rotor blades encounter wide variations in dynamic pressure (from incompressible flow to transonic flow), dynamic stall, and interaction with the self-generated wake. These effects

contribute to loss in performance, noise, and vibrations. Because self-induced velocity of the vortex wake plays a dominant role in these phenomena, it is necessary to employ efficient and accurate techniques for capturing the tip vortex strength and the temporal and spatial distribution of the vortex wake.

Full Navier-Stokes simulation of the vortical flow around a rotor requires large amount of grid points, especially for an accurate modeling of BVI phenomena. The number of grid points may be reduced with an adaptive grid or an overset mesh, but the computational cost in terms of time and memory is still prohibitive for engineering calculations. On the other hand, vortex fitting techniques (free wake and prescribed wake methods) that model the wake as vortex sheets, tip vortex filaments, and point vortices do not adequately model close blade-vortex encounters.

An alternative to wake capturing and free wake methods is a hybrid method that combines the best features of vortex capturing and vortex fitting techniques. These are Navier-Stokes/Free wake methods which solve the flow around the rotor using Reynolds Averaged Navier-Stokes equations, while capturing the far wake using discrete free wake models. Sankar et al. [45] has developed hybrid method that combines Navier-Stokes solver (inner region) with full potential solver (outer region) to reduce computational time. The hybrid solver was demonstrated for a fixed wing and hovering rotor, and showed the same level of accuracy with the full Navier-Stokes solver, while requiring almost half the computational time. Berezin and Sankar [46] have extended the hybrid method to unsteady forward flight case through loose coupling between the hybrid and a comprehensive rotor/wake/trim code, RDYNE [47]. The control deflections, blade twist, elastic deformations, and far wake induced velocities were fed to the CFD code in the

form of effective angle of attack. The method has been applied to UH-60A rotor and showed good agreement with full Navier-Stokes solution and measured data. Berkman and Sankar [48] improved the hybrid method with additional Lagrangian treatment of the tip vortices (free-wake model) on top of the Navier-Stokes/Full potential flow solver. The accuracy and efficiency of the method has been proven with Caradonna and Tung [49] and UH-60A rotor for hover cases. Yang and Sankar [50] further extended the work of [46] and [48] for accurate prediction of a rotor in forward flight. In this extension, the rotor was trimmed for a desired thrust and the grid was deformed accordingly. Recently, the full potential part of the hybrid method has been removed and the free-wake model was directly coupled with Navier-Stokes solver through outer surface boundary condition. In addition, the hybrid method has been coupled with CSD (Computational Structural Dynamics) code for accurate modeling of aeroelastic phenomena and rotor trim in loose or tight coupling manner. Such a method has been applied to rotors in forward flight conditions and showed good agreement with measured data [51-53]. In spite of the progress that has been made with hybrid methods, BVI prediction of the hybrid method on coarse grids is unsatisfactory to date [16, 54].

1.4 Research Objectives and Scope

The goal of this research is to explore the possibility of Gurney flaps as an effective control device for improved rotor flight characteristics. Gurney flaps, due to their inherently small size and their location on the blade (near the trailing edge), have lower power requirements compared to other active blade control concepts. Retrofitting existing vehicles with Gurney flaps, without significantly changing the overall dynamic

characteristics or the weight of the rotors, is an attractive concept. The current research is motivated by this possibility.

The primary objective is to study the effects of Gurney flaps on rotor performance in steady flight. Specifically, the effects of the Gurney flap on the autorotation, hub vibratory loads, and blade-vortex-interaction (BVI) phenomena are studied. In autorotative operation, the Gurney flap is permanently deployed and its effect on the required rotor descent rate to sustain autorotation state is examined. The physics of how the Gurney flap impacts the autorotation characteristics is studied as well. The deployable Gurney flap is studied to examine its potential vibration reduction capability. First, two-dimensional studies are carried out to understand the characteristics of the air loads response to the unsteady Gurney flap deployment. Subsequently, a rotor in a descent flight mode is examined with deployable Gurney flap to assess its vibration reduction capability. The deployment schedule is manually adjusted so that the vibratory load is cancelled out by the increase or decrease in airloads due to the Gurney flap. Adverse effects of the Gurney flaps are identified as well. Finally, the rotor in the maximum BVI condition is re-trimmed to an alternate state using a deployable Gurney flap, and the change in the BVI events is examined.

In order to efficiently achieve this primary objective, a high fidelity Navier-Stokes solver, capable of modeling BVI phenomena, has been developed. This solver is an enhanced version of a baseline solver, GENCAS, developed by this author. An existing free wake model from the work of references [48,50-52] is integrated into the Navier-Stokes solver. The new solver is designed for generic multi-block grids required for

complex Gurney flap modeling. The hybrid method is further enhanced to increase its BVI capturing capability as well as its accuracy and computational speed.

The hybrid code is coupled to a CSD code in a loosely coupled manner. The CSD code provides blade deformations including elastic, control inputs, and corresponding flapping deflections while maintaining trimmed state.

Figure 1.1 Gurney flap

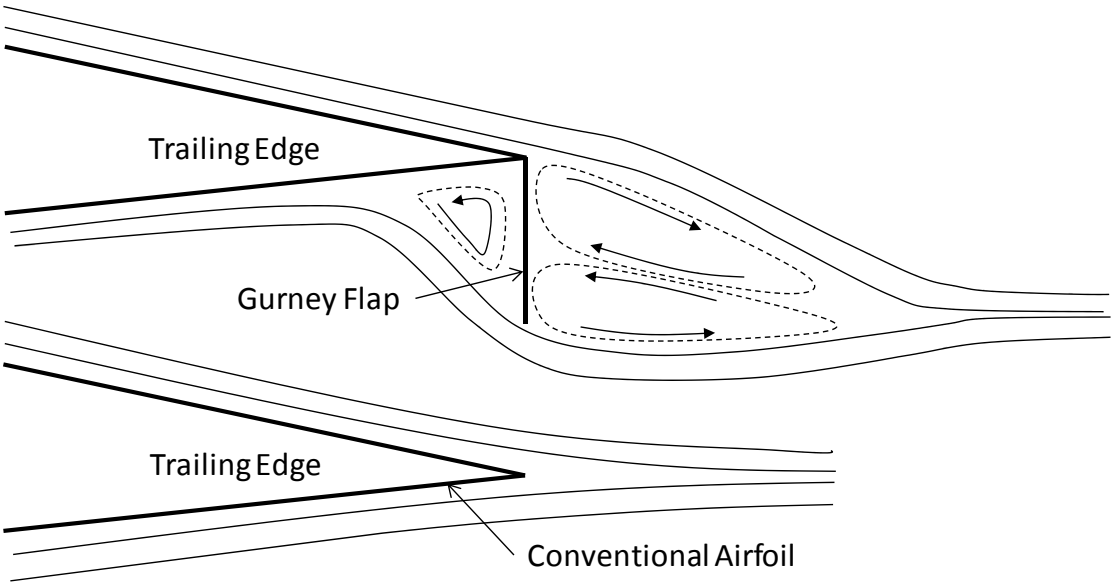

Figure 1.2 Flow around Gurney flap

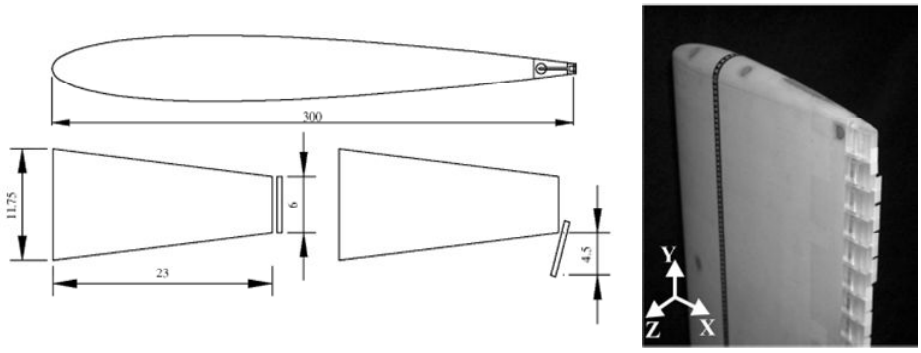

a) Gurney flap installed at blunt trailing edge. (from Ref.[19])

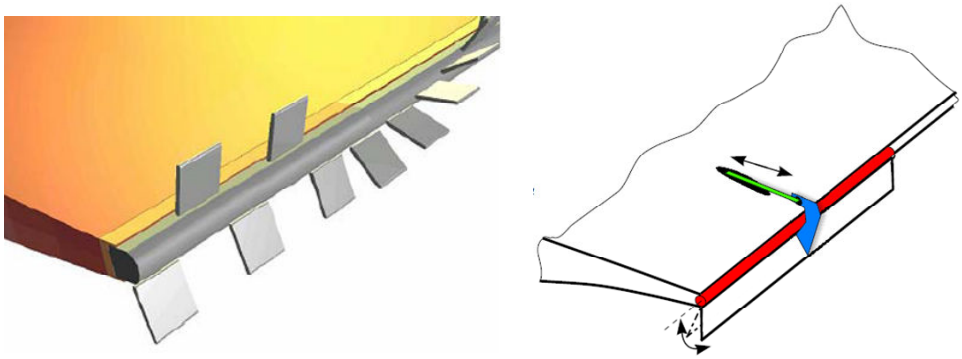

b) Hinged Gurney flap (left: Ref. [20], right: Ref.[21])

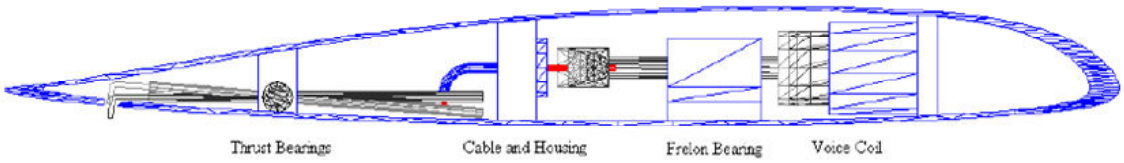

c) Gurney flap deployable on the lower surface (from Ref. [15])

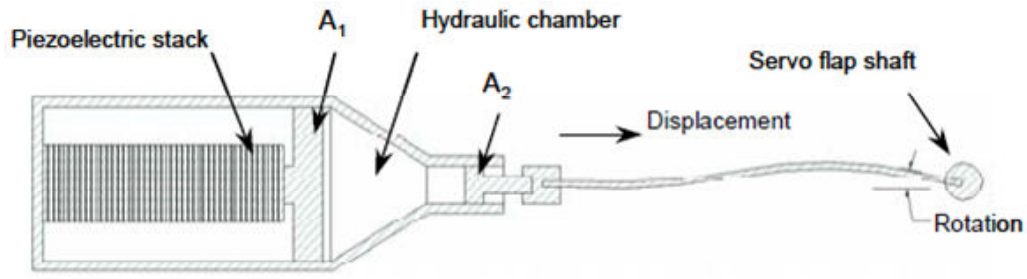

d) An example of flap actuation mechanism using piezoelectric device (Ref. [22])

Figure 1.3 Various deployable Gurney flaps and actuator mechanism

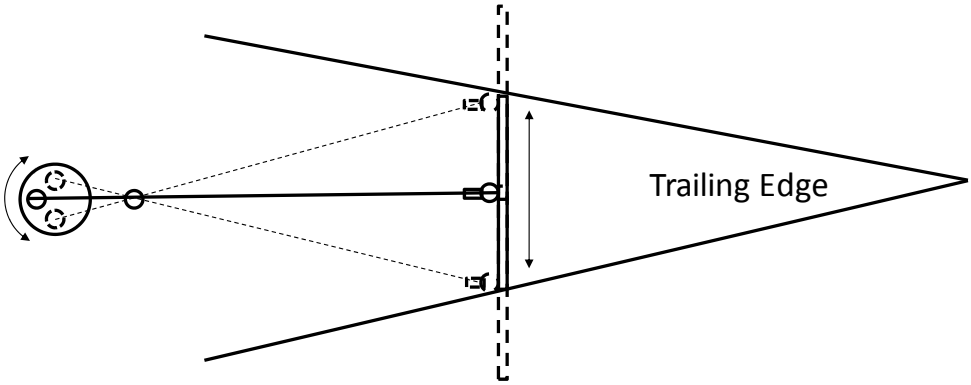

a) T-shaped micro-flap with hinge

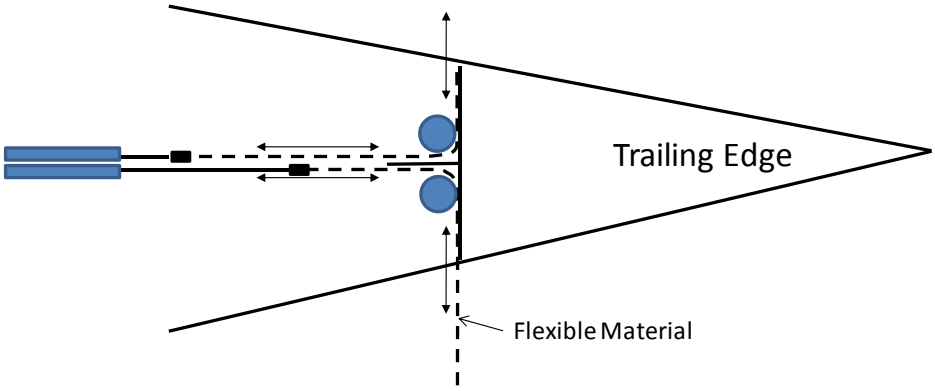

b) Flexible material flap

Figure 1.4 Deployable Gurney flap concepts considered in this study

CHAPTER 2

METHODOLOGY

2.1 Mathematical Formulation

2.1.1 Governing Equations

A general purpose multi-block solver called GENCAS (Generic Numerical Compressible Airflow Solver) has been developed by present investigator [16,34,55-57]. This is a generic Reynolds Averaged Navier-Stokes (RANS) solver that may be used to model a broad class of internal and external flows. A PDE form of the three dimensional Navier-Stokes equations in Cartesian coordinate system may be written as follows:

$$\frac{\partial Q}{\partial t}+\frac{\partial E}{\partial x}+\frac{\partial F}{\partial y}+\frac{\partial G}{\partial z}=\frac{\partial E_v}{\partial x}+\frac{\partial F_v}{\partial y}+\frac{\partial G_v}{\partial z} \tag{2.1}$$

Where Q is the flow vector, E, F and G are the inviscid flux vectors, E_v, F_v and G_v are the viscous flux vectors.

$$Q=\begin{Bmatrix}\rho\\ \rho u\\ \rho v\\ \rho w\\ e\end{Bmatrix} \tag{2.2}$$

$$E=\begin{Bmatrix}\rho\\ \rho u^2+p\\ \rho uv\\ \rho uw\\ u(e+p)\end{Bmatrix}, F=\begin{Bmatrix}\rho\\ \rho uv\\ \rho v^2+p\\ \rho vw\\ v(e+p)\end{Bmatrix}, G=\begin{Bmatrix}\rho\\ \rho uw\\ \rho vw\\ \rho w^2\\ w(e+p)\end{Bmatrix} \tag{2.3}$$

$$E_v = \begin{Bmatrix} 0 \\ \tau_{xx} \\ \tau_{yx} \\ \tau_{zx} \\ E_x \end{Bmatrix}, F_v = \begin{Bmatrix} 0 \\ \tau_{xy} \\ \tau_{yy} \\ \tau_{zy} \\ E_y \end{Bmatrix}, G_v = \begin{Bmatrix} 0 \\ \tau_{xz} \\ \tau_{yz} \\ \tau_{zz} \\ E_z \end{Bmatrix} \tag{2.4}$$

Here, ρ is the density, u, v, w are the Cartesian velocity components, p is the static pressure, and e is the total energy per unit volume. The quantity of e is the summation of internal energy and kinetic energy.

$$e = \frac{p}{\gamma - 1} + \frac{1}{2}\rho(u^2 + v^2 + w^2) \tag{2.5}$$

The stress terms in the viscous fluxes are defined as:

$$\begin{gathered} \tau_{xx} = (\lambda + 2\mu)u_x + \lambda v_y + \lambda w_z \\ \tau_{yy} = \lambda u_x + (\lambda + 2\mu)v_y + \lambda w_z \\ \tau_{zz} = \lambda u_x + \lambda v_y + (\lambda + 2\mu)w_z \\ \tau_{xy} = \tau_{yx} = \mu(u_y + v_x) \\ \tau_{xz} = \tau_{zx} = \mu(u_z + w_x) \\ \tau_{yz} = \tau_{zy} = \mu(v_y + w_y) \\ E_x = u\tau_{xx} + v\tau_{xy} + w\tau_{xz} + k\frac{\partial T}{\partial x} \\ E_y = u\tau_{yx} + v\tau_{yy} + w\tau_{yz} + k\frac{\partial T}{\partial y} \\ E_z = u\tau_{zx} + v\tau_{zy} + w\tau_{zz} + k\frac{\partial T}{\partial z} \end{gathered} \tag{2.6}$$

Using the Stokes hypothesis, the value λ is assumed to be related to molecular viscosity, μ, as:

$$\lambda = -\frac{2}{3}\mu \tag{2.7}$$

In turbulent flows, if an eddy viscosity model is used, the viscosity, μ, is represented as the sum of molecular viscosity (laminar viscosity) and eddy viscosity (turbulent viscosity) as shown below:

$$\mu = \mu_l + \mu_t \tag{2.8}$$

In this study, the laminar viscosity, μ_l, is estimated using Sutherland's law and the turbulent viscosity is estimated using one or two equation models. More details are described in a later section.

Using the estimated viscosity, the thermal conductivity, k, is obtained as:

$$k = \frac{\mu_l C_p}{Pr} + \frac{\mu_t C_p}{Pr_t} \tag{2.9}$$

Where C_p is the specific heat at constant pressure, Pr is the Prandtl number (≈ 0.72), and Pr_t is the turbulent Prandtl number (≈ 0.91).

2.1.2 Non-dimensionalized Governing Equations

The governing equations, Eqn. (2.1), are non-dimensionalized using the following parameters.

L: Reference length

a_∞: Reference speed of sound

ρ_∞: Reference density

p_∞: Reference pressure

μ_∞: Reference viscosity

$$x^* = \frac{\hat{x}}{L} \qquad y^* = \frac{\hat{y}}{L} \qquad z^* = \frac{\hat{z}}{L} \qquad t^* = \frac{\hat{t} a_\infty}{L}$$

$$u^* = \frac{\hat{u}}{a_\infty} \qquad v^* = \frac{\hat{v}}{a_\infty} \qquad w^* = \frac{\hat{w}}{a_\infty} \qquad \rho^* = \frac{\hat{\rho}}{\rho_\infty}$$

$$p^* = \frac{\hat{p}}{\gamma p_\infty} \qquad \mu^* = \frac{\hat{\mu}}{\mu_\infty} \qquad e^* = \frac{\hat{e}}{\rho_\infty a_\infty^2}$$

The superscript asterisk denotes a dimensionless variable and that of the hat denotes a dimensional variable. Generally the reference value is taken from the free stream property, and the reference length is the inverse of the scale factor used in the computational grid generation. Once the governing equations are non-dimensionalized using the reference values, Eqn. (2.1) takes following form.

$$\frac{\partial Q^*}{\partial t^*} + \frac{\partial E}{\partial x^*} + \frac{\partial F}{\partial y^*} + \frac{\partial G}{\partial z^*} = \frac{M_\infty}{Re_\infty}\left(\frac{\partial E_v}{\partial x^*} + \frac{\partial F_v}{\partial y^*} + \frac{\partial G_v}{\partial z^*}\right) \tag{2.10}$$

The only difference between Eqn. (2.1) and Eqn. (2.10) is the appearance of the reference Mach number and Reynolds number on the viscous flux terms. The reference Mach number and Reynolds number is defined as follows:

$$\begin{aligned} M_\infty &= \frac{V_\infty}{a_\infty} \\ Re_\infty &= \frac{\rho_\infty V_\infty L}{\mu_\infty} \end{aligned} \tag{2.11}$$

Here, V_∞ is the free stream velocity, or blade tip velocity if rotor is the application. Hereafter, for brevity, the superscript asterisk denoting a non-dimensionalized variable is dropped.

2.1.3 Governing Equations in Generalized Coordinate System

The governing equations in the Cartesian coordinate system (t, x, y, z) are transformed to a curvilinear coordinate system (t, ξ, η, ζ) using the link between them.

$$\begin{aligned} \xi &= \xi(x, y, z, t) \\ \eta &= \eta(x, y, z, t) \\ \zeta &= \zeta(x, y, z, t) \end{aligned} \tag{2.12}$$

The details of the coordinate transformation are given in Appendix A. After the transformation procedure, the governing equation, Eqn. (2.10), is re-written in the curvilinear coordinate system as Eqn. (2.13).

$$\frac{\partial \bar{Q}}{\partial t}+\frac{\partial \bar{E}}{\partial \xi}+\frac{\partial \bar{F}}{\partial \eta}+\frac{\partial \bar{G}}{\partial \zeta}=\frac{\partial \bar{E}_v}{\partial \xi}+\frac{\partial \bar{F}_v}{\partial \eta}+\frac{\partial \bar{G}_v}{\partial \zeta} \tag{2.13}$$

$$\bar{Q}=\frac{1}{J}\begin{Bmatrix}\rho\\ \rho u\\ \rho v\\ \rho w\\ e\end{Bmatrix} \tag{2.14}$$

$$\bar{E}=\frac{1}{J}\begin{Bmatrix}\rho U\\ \rho uU+\xi_x p\\ \rho vU+\xi_y p\\ \rho wU+\xi_z p\\ (e+p)U-\xi_t p\end{Bmatrix},\bar{F}=\frac{1}{J}\begin{Bmatrix}\rho V\\ \rho uV+\eta_x p\\ \rho vV+\eta_y p\\ \rho wV+\eta_z p\\ (e+p)V-\eta_t p\end{Bmatrix},\bar{G}=\frac{1}{J}\begin{Bmatrix}\rho W\\ \rho uW+\zeta_x p\\ \rho vW+\zeta_y p\\ \rho wW+\zeta_z p\\ (e+p)W-\zeta_t p\end{Bmatrix} \tag{2.15}$$

$$\bar{E}_v=\frac{1}{J}\frac{M_\infty}{Re_\infty}\begin{Bmatrix}0\\ \xi_x\tau_{xx}+\xi_y\tau_{xy}+\xi_z\tau_{xz}\\ \xi_x\tau_{yx}+\xi_y\tau_{yy}+\xi_z\tau_{yz}\\ \xi_x\tau_{zx}+\xi_y\tau_{zy}+\xi_z\tau_{zz}\\ \xi_x E_x+\xi_y E_y+\xi_z E_z\end{Bmatrix},$$

$$\bar{F}_v=\frac{1}{J}\frac{M_\infty}{Re_\infty}\begin{Bmatrix}0\\ \eta_x\tau_{xx}+\eta_y\tau_{xy}+\eta_z\tau_{xz}\\ \eta_x\tau_{yx}+\eta_y\tau_{yy}+\eta_z\tau_{yz}\\ \eta_x\tau_{zx}+\eta_y\tau_{zy}+\eta_z\tau_{zz}\\ \eta_x E_x+\eta_y E_y+\eta_z E_z\end{Bmatrix}, \tag{2.16}$$

$$\bar{G}_v=\frac{1}{J}\frac{M_\infty}{Re_\infty}\begin{Bmatrix}0\\ \zeta_x\tau_{xx}+\zeta_y\tau_{xy}+\zeta_z\tau_{xz}\\ \zeta_x\tau_{yx}+\zeta_y\tau_{yy}+\zeta_z\tau_{yz}\\ \zeta_x\tau_{zx}+\zeta_y\tau_{zy}+\zeta_z\tau_{zz}\\ \zeta_x E_x+\zeta_y E_y+\zeta_z E_z\end{Bmatrix}$$

Where J is the Jacobian of the transformation, and U, V, W are the contravariant velocity components along the ξ, η, and ζ coordinate direction.

$$U = \xi_t + \xi_x u + \xi_y v + \xi_z w$$

$$V = \eta_t + \eta_x u + \eta_y v + \eta_z w \tag{2.17}$$

$$W = \zeta_t + \zeta_x u + \zeta_y v + \zeta_z w$$

The quantity $\xi_t, \eta_t,$ and ζ_t are related to the grid velocity (x_t, y_t, z_t) in the physical domain as:

$$\xi_t = -x_t \xi_x - y_t \xi_y - z_t \xi_z$$

$$\eta_t = -x_t \eta_x - y_t \eta_y - z_t \eta_z \tag{2.18}$$

$$\zeta_t = -x_t \zeta_x - y_t \zeta_y - z_t \zeta_z$$

The formulation for the Jacobian of the transformation, J, and metrics ($\xi_x, \xi_y, \xi_z,$ etc.) are given in Appendix A.

2.2 Numerical Formulation

2.2.1 Calculation of Inviscid and Viscous Fluxes

The discretized form of the governing equation, Eqn. (2.13), at a cell (i, j, k) may be written as follows using central differences:

$$\frac{\partial \bar{Q}_{i,j,k}}{\partial t} = -\left(\frac{\bar{E}_{i+\frac{1}{2},j,k} - \bar{E}_{i-\frac{1}{2},j,k}}{\Delta\xi} + \frac{\bar{F}_{i,j+\frac{1}{2},k} - \bar{F}_{i,j-\frac{1}{2},k}}{\Delta\eta} + \frac{\bar{G}_{i,j,k+\frac{1}{2}} - \bar{G}_{i,j,k-\frac{1}{2}}}{\Delta\zeta} \right) + \frac{\bar{E}_{v_{i+\frac{1}{2},j,k}} - \bar{E}_{v_{i-\frac{1}{2},j,k}}}{\Delta\xi} + \frac{\bar{F}_{v_{i,j+\frac{1}{2},k}} - \bar{F}_{v_{i,j-\frac{1}{2},k}}}{\Delta\eta} + \frac{\bar{G}_{v_{i,j,k+\frac{1}{2}}} - \bar{G}_{v_{i,j,k-\frac{1}{2}}}}{\Delta\zeta} \tag{2.19}$$

Where:

$$\Delta\xi = \xi_{i+\frac{1}{2},j,k} - \xi_{i-\frac{1}{2},j,k} = 1$$

$$\Delta\eta = \eta_{i,j+\frac{1}{2},k} - \eta_{i,j-\frac{1}{2},k} = 1 \tag{2.20}$$

$$\Delta\zeta = \zeta_{i,j,k+\frac{1}{2}} - \zeta_{i,j,k-\frac{1}{2}} = 1$$

Here, $\left(i \pm \frac{1}{2}, j \pm \frac{1}{2}, k \pm \frac{1}{2}\right)$ represents six faces of the cell. Using the central difference operator, δ, Eqn. (2.19) is re-written in following form:

$$\frac{\partial \bar{Q}_{i,j,k}}{\partial t} = -\left(\delta_\xi \bar{E} + \delta_\eta \bar{F} + \delta_\zeta \bar{G}\right) + \left(\delta_\xi \bar{E}_v + \delta_\eta \bar{F}_v + \delta_\zeta \bar{G}_v\right) \tag{2.21}$$

Equation (2.21) is the final form of the governing equation before a numerical scheme is applied. The first term on the right-hand side represents the inviscid flux, and the second term represents viscous flux. Among the many numerical schemes proposed for the computation of the inviscid fluxes, i.e. $\bar{E}_{i\pm\frac{1}{2},j,k}, \bar{F}_{i,j\pm\frac{1}{2},k}, \bar{G}_{i,j,k\pm\frac{1}{2}}$, Roe's flux-difference splitting scheme [58] is used in the present study. At a cell interface, taking into account the wave propagation direction, the numerical flux $\bar{E}$ is computed as:

$$\bar{E}_{i+\frac{1}{2}} = \frac{1}{2}\left\{\left(\bar{E}(q_L) + \bar{E}(q_R)\right) - \left|\tilde{A}\right|(q_R - q_L)\right\} \tag{2.22}$$

Where:

$$\tilde{A} = \frac{\partial \bar{E}}{\partial q} \qquad q_L = \begin{bmatrix} \rho_L \\ u_L \\ v_L \\ w_L \\ p_L \end{bmatrix} \qquad q_R = \begin{bmatrix} \rho_R \\ u_R \\ v_R \\ w_R \\ p_R \end{bmatrix}$$

$$\bar{E}_L = \begin{bmatrix} \rho_L U_L \\ \rho_L U_L u_L + p_L n_x \\ \rho_L U_L v_L + p_L n_y \\ \rho_L U_L w_L + p_L n_z \\ \rho_L U_L h_{0L} - p_L n_t \end{bmatrix} \quad \bar{E}_R = \begin{bmatrix} \rho_R U_R \\ \rho_R U_R u_R + p_R n_x \\ \rho_R U_R v_R + p_R n_y \\ \rho_R U_R w_R + p_R n_z \\ \rho_R U_R h_{0R} - p_R n_t \end{bmatrix}$$

The quantities h_0, (n_x, n_y, n_z) and n_t are the specific total enthalpy ($h_0 = (e+p)/\rho$), surface normal vector, and the grid velocity in the surface normal direction, respectively. The subscripts L and R represent the flow property at the immediate left or right side of the cell interface. The accuracy of the primitive variable computation at the left and right side determines the spatial accuracy of the solution. In the present study, the Monotone Upstream-centered Scheme for Conservation Laws (MUSCL) [59] is used. Using the MUSCL scheme, the property at the left and right side is written as:

$$q_L = q_i + \phi^l \left[\frac{(1-k)}{4}(q_i - q_{i-1}) + \frac{(1+k)}{4}(q_{i+1} - q_i) \right]$$
$$q_R = q_{i+1} - \phi^r \left[\frac{(1+k)}{4}(q_{i+1} - q_i) + \frac{(1-k)}{4}(q_{i+2} - q_{i+1}) \right] \quad (2.23)$$

Where:

$k = 1$: 2nd order central difference,

$k = 1/3$: 3rd order unwind scheme

The limiter function, ϕ, is introduced to maintain stability and to eliminate spurious numerical oscillations by reducing the order of accuracy in the regions where large gradients and discontinuities exist. In the present study, the van Albada flux limiter [60] is used:

$$\phi^l = \frac{2(q_i - q_{i-1})(q_{i+1} - q_i) + \varepsilon}{(q_i - q_{i-1})^2 + (q_{i+1} - q_i)^2 + \varepsilon}$$
$$\phi^r = \frac{2(q_{i+1} - q_i)(q_{i+2} - q_{i+1}) + \varepsilon}{(q_{i+1} - q_i)^2 + (q_{i+2} - q_{i+1})^2 + \varepsilon} \quad (2.24)$$

Here, ε is a small number to prevent indeterminacy. The third-order accurate scheme is used in this study as a baseline. An additional higher order scheme (seventh-

order) is implemented to enhance the solution accuracy. Its details are described in Chapter 3.

The second term in Eqn. (2.22), the flux Jacobian matrix $\left|\tilde{A}\right|$ multiplied by $(q_R - q_L)$, may be expressed as follows using the Vinokur and Liu [61] formula:

$$\left|\tilde{A}\right|(q_R - q_L) = \left|\tilde{\lambda}_1\right| \begin{Bmatrix} \Delta\rho \\ \Delta\rho u \\ \Delta\rho v \\ \Delta\rho w \\ \Delta \mathrm{e} \end{Bmatrix} + \delta_1 \begin{Bmatrix} \tilde{\rho} \\ \tilde{\rho}\tilde{u} \\ \tilde{\rho}\tilde{v} \\ \tilde{\rho}\tilde{w} \\ \tilde{\rho}\tilde{h}_0 \end{Bmatrix} + \delta_1 \begin{Bmatrix} 0 \\ n_x \\ n_y \\ n_z \\ \widetilde{U}_c \end{Bmatrix} \tag{2.25}$$

Where:

$$\begin{aligned}
\delta_1 &= C_1 \frac{\Delta p}{\tilde{\rho}\tilde{a}^2} + 0.5 C_2 \frac{\Delta U_c}{\tilde{a}} \\
\delta_2 &= C_1 \tilde{\rho} \Delta U_c + 0.5 C_2 \frac{\Delta p}{\tilde{a}} \\
C_1 &= -\left|\tilde{\lambda}_1\right| + 0.5\left(\left|\tilde{\lambda}_2\right| + \left|\tilde{\lambda}_3\right|\right) \\
C_2 &= \left|\tilde{\lambda}_2\right| - \left|\tilde{\lambda}_3\right| \\
\tilde{\lambda}_1 &= \widetilde{U} \\
\tilde{\lambda}_2 &= \widetilde{U} + \tilde{a} \\
\tilde{\lambda}_3 &= \widetilde{U} - \tilde{a} \\
\widetilde{U} &= n_t + n_x \tilde{u} + n_y \tilde{v} + n_z \tilde{w} \\
\widetilde{U}_c &= n_x \tilde{u} + n_y \tilde{v} + n_z \tilde{w} \\
\Delta U_c &= U_c|_R - U_c|_L = n_x(u_R - u_L) + n_y(v_R - v_L) + n_z(w_R - w_L)
\end{aligned} \tag{2.26}$$

Here, the operator Δ is defined as $\Delta(\bullet) = (\bullet)|_R - (\bullet)|_L$. The quantities with the superscript '~' represent Roe-averaged value, and are defined for any flow variable $\emptyset$ except ρ as:

$$\tilde{\rho} = \sqrt{\rho_R \rho_L}$$

$$\tilde{\emptyset} = \emptyset_L \left(\frac{1}{1 + \sqrt{\rho_R / \rho_L}} \right) + \emptyset_R \left(\frac{\sqrt{\rho_R / \rho_L}}{1 + \sqrt{\rho_R / \rho_L}} \right) \tag{2.27}$$

The viscous fluxes $(\bar{E}_v, \bar{F}_v, \bar{G}_v)$ in Eqn. (2.21) are computed using symmetric second order central difference scheme at the cell interface. Derivatives in the Eqn. (2.16) along ξ direction are computed as:

$$\emptyset_\xi \big|_{i+\frac{1}{2}} = \frac{\emptyset_{i+1} - \emptyset_i}{\Delta\xi} \qquad \emptyset_\xi \big|_{i-\frac{1}{2}} = \frac{\emptyset_i - \emptyset_{i-1}}{\Delta\xi} \tag{2.28}$$

Derivatives along η and ζ directions are computed in similar manner.

2.2.2 Time Marching Scheme

In an implicit formulation with first order backward differencing in time, Eqn. (2.21) may be written as:

$$\frac{1}{J}\frac{\Delta Q^{n+1}}{\Delta t} = -\left(\delta_\xi \bar{E}^{n+1} + \delta_\eta \bar{F}^{n+1} + \delta_\zeta \bar{G}^{n+1}\right) + \left(\delta_\xi \bar{E}_v^n + \delta_\eta \bar{F}_v^n + \delta_\zeta \bar{G}_v^n\right) \tag{2.29}$$

Here, $\Delta Q^{n+1} = Q^{n+1} - Q^n$, the superscript n and n+1 represent time level. The viscous terms are treated explicitly with flow quantities at time level n. Note that the grid Jacobian, J, is treated as a constant over a time period since the cell volume is not changed for stationary grid. However, the cell volume is continuously varied and the change should not be neglected in a moving grid with deformation. Treatment of such a case is described in Section 3.1. The inviscid flux terms are linearized using Taylor series expansion as follows:

$$\bar{E}^{n+1} \cong \bar{E}^n + [A^n]\Delta Q^{n+1}$$
$$\bar{F}^{n+1} \cong \bar{F}^n + [B^n]\Delta Q^{n+1} \tag{2.30}$$
$$\bar{G}^{n+1} \cong \bar{G}^n + [C^n]\Delta Q^{n+1}$$

Where the flux Jacobian matrices are defined as:

$$[A] = \frac{\partial \bar{E}}{\partial Q} \qquad [B] = \frac{\partial \bar{F}}{\partial Q} \qquad [C] = \frac{\partial \bar{G}}{\partial Q} \tag{2.31}$$

The detailed form of the Jacobian matrix may be written as given by Pulliam and Steger [62]:

$$[K] = \begin{bmatrix} k_t & k_x & k_y & k_z & 0 \\ k_x\phi^2 - u\theta & \Theta - k_x\sigma_2 u & k_y u - \sigma k_x v & k_z u - \sigma k_x w & \sigma k_x \\ k_y\phi^2 - v\theta & k_x v - \sigma k_y u & \Theta - k_x\sigma_2 v & k_z v - \sigma k_y w & \sigma k_y \\ k_z\phi^2 - w\theta & k_x w - \sigma k_z u & k_y w - \sigma k_z v & \Theta - k_x\sigma_2 w & \sigma k_z \\ \theta(\phi^2 - E) & k_x E - \sigma u\theta & k_y E - \sigma v\theta & k_z E - \sigma w\theta & k_t + \gamma\theta \end{bmatrix} \tag{2.32}$$

Where:

$$\begin{aligned} \phi^2 &= (\gamma - 1)\,(u^2 + v^2 + w^2)/2 \\ \theta &= k_x u + k_y v + k_z w \\ \sigma &= \gamma - 1 \\ \sigma_2 &= \gamma - 2 \\ \Theta &= k_t + \theta \\ E &= \frac{\gamma e}{\rho} - \phi^2 \end{aligned} \tag{2.33}$$

The matrix $[K]$ is $[A]$ or $[B]$ or $[C]$ when the k is chosen as ξ or η or ζ. With Eqn. (2.30), Eqn. (2.29) may be re-arranged as:

$$\left[I + \Delta t\left(\delta_\xi A^n + \delta_\eta B^n + \delta_\zeta C^n\right)\right]\Delta Q^{n+1} = (RHS)^n \tag{2.34}$$

Where I is the identity matrix and the right-hand side term, (RHS), is sometimes referred as the residual.

$$(RHS)^n = -J\Delta t\left(\delta_\xi \bar{E}^n + \delta_\eta \bar{F}^n + \delta_\zeta \bar{G}^n\right) + J\Delta t\left(\delta_\xi \bar{E}_v^n + \delta_\eta \bar{F}_v^n + \delta_\zeta \bar{G}_v^n\right) \tag{2.35}$$

Equation (2.34) is a matrix system, which is computationally very expensive to invert. To reduce the computational time, the matrix inside the bracket on the left-hand side is approximately factored using a Lower-Upper Symmetric Gauss-Seidel (LU-SGS) implicit method proposed by Yoon and Jameson [63]. In the LU-SGS scheme, Eqn. (2.34) is expressed as:

$$(L + D + U)\Delta Q^{n+1} = (RHS)^n \tag{2.36}$$

Where L is a lower block triangular matrix with null matrices on the diagonal, D is a block diagonal matrix and U is an upper block triangular matrix with null matrices on the diagonal. For the case of non-singular matrix D, Eqn. (2.36) may be re-written as:

$$D(D^{-1}L + I + D^{-1}U)\Delta Q^{n+1} = (RHS)^n \tag{2.37}$$

Using LU-factorization, Eqn. (2.37) may be approximated as:

$$D(I + D^{-1}L)(I + D^{-1}U)\Delta Q^{n+1} = (RHS)^n \tag{2.38}$$

Or

$$(D + L)D^{-1}(D + U)\Delta Q^{n+1} = (RHS)^n \tag{2.39}$$

Where:

$$\begin{aligned}
(D + L) &= I - \Delta t\left(\frac{A^-}{\Delta\xi} - \delta_\xi^- A^+ + \frac{B^-}{\Delta\eta} - \delta_\eta^- B^+ + \frac{C^-}{\Delta\zeta} - \delta_\zeta^- C^+\right) \\
D &= I + \frac{\Delta t}{\Delta\xi}(A^+ - A^-) + \frac{\Delta t}{\Delta\eta}(B^+ - B^-) + \frac{\Delta t}{\Delta\zeta}(C^+ - C^-) \\
(D + U) &= I + \Delta t\left(\frac{A^+}{\Delta\xi} + \delta_\xi^+ A^- + \frac{B^+}{\Delta\eta} + \delta_\eta^+ B^- + \frac{C^+}{\Delta\zeta} + \delta_\zeta^+ C^-\right)
\end{aligned} \tag{2.40}$$

The operator $\delta_\xi^-, \delta_\eta^-$ and δ_ζ^- are the first-order backward differences, while $\delta_\xi^+, \delta_\eta^+$ and δ_ζ^+ are the first-order forward differences. The matrices $A^\pm, B^\pm$ and $C^\pm$ are the

decomposed matrices based on the eigenvalues and eigenvectors. However, direct computing of them is computationally expensive, and an approximated approach proposed by Yoon and Jameson [63] is used in the present study.

$$\begin{aligned} A^{\pm} &= \frac{1}{2}(A \pm r_A I) & r_A &= k_A max(|\lambda_A|) \\ B^{\pm} &= \frac{1}{2}(B \pm r_B I) & r_B &= k_B max(|\lambda_B|) \\ C^{\pm} &= \frac{1}{2}(C \pm r_C I) & r_C &= k_C max(|\lambda_C|) \end{aligned} \tag{2.41}$$

Here, λ_A, λ_B and λ_C are the eigenvalues of the matrices A, B and C, respectively. The constants k_A, k_B and k_C are user-input quantities (≥ 1) to enhance stability by increasing diagonal dominance of the system of equations. However, if the values are greater than 1, the convergence ratio is reduced. In the present study, $k_A = k_B = k_C = 1$ is used. The maximum eigenvalues may be evaluated as follows:

$$\begin{aligned} max(|\lambda_A|) &= |U| + a\left(\xi_x^2 + \xi_y^2 + \xi_z^2\right)^{\frac{1}{2}} \\ max(|\lambda_B|) &= |V| + a\left(\eta_x^2 + \eta_y^2 + \eta_z^2\right)^{\frac{1}{2}} \\ max(|\lambda_C|) &= |W| + a\left(\zeta_x^2 + \zeta_y^2 + \zeta_z^2\right)^{\frac{1}{2}} \end{aligned} \tag{2.42}$$

Using Eqn. (2.40), (2.41) and (2.42), Eqn. (2.39) is sequentially solved as shown below:

$$\begin{aligned} (D + L)\Delta Q^{**} &= (RHS)^n \\ D^{-1}\Delta Q^{*} &= \Delta Q^{**} \\ (D + U)\Delta Q^{n+1} &= \Delta Q^{*} \end{aligned} \tag{2.43}$$

The matrices on the left-hand side of Eqn. (2.43) have either lower, diagonal, or upper part only with all others zero. Thus, inversion of each matrix is easily

accomplished by backward or forward substitution. Once ΔQ^{n+1} is obtained, the new Q^{n+1} is computed from $Q^{n+1} = Q^n + \Delta Q^{n+1}$.

2.3 Turbulence Models

The shear stress terms, τ_{ij}, in the Eq. (2.16) is composed of viscous stress and Reynolds stress components. An eddy viscosity model is used and the Reynolds stress term is defined as $-\overline{u_i' u_j'} = 2(\mu_t/\rho)S_{ij}$. Thus, the viscosity in the Eq. (2.16) is the sum of molecular viscosity and eddy viscosity as shown below:

$$\mu = \mu_l + \mu_t \tag{2.44}$$

The eddy viscosity is estimated using various turbulence models. Available turbulence models implemented in the code include Spalart-Allmaras (SA) [64], Spalart-Allmaras Detached Eddy Simulation (SA-DES) [65], κ–ω, a κ–ω/κ–ε blended, the κ–ω-SST (Menter) [66], the κ–ω-SST DES [67], KES [68,69], and HRKES [70,71] model. Although various turbulence models are available, SA-DES and KES models are used for rotor applications in this work.

2.3.1 Spalart-Allmaras Detached Eddy Simulation (SA-DES) model

Spalart and Allmaras [64] have proposed a one-equation transport model for eddy viscosity called the Spalart-Allmaras (SA) model. In this model, the eddy viscosity, μ_t, is computed from:

$$\mu_t = \rho \tilde{\nu} f_{v1} \tag{2.45}$$

Where the viscous damping function, f_{v1}, is given by:

$$f_{v1} = \frac{\chi^3}{\chi^3 + c_{v1}^3} \quad \text{and} \quad \chi = \frac{\tilde{\nu}}{\nu} \tag{2.46}$$

The damping function goes to zero at the wall and gradually rises to unity as the distance from the wall increases. The operating parameter $\tilde{\nu}$ is determined by the transport equation as follows:

$$\frac{D\tilde{\nu}}{Dt} = c_{b1}[1 - f_{t2}]\tilde{S}\tilde{\nu} + \frac{1}{\sigma}\left[\nabla \cdot \left((\nu + \tilde{\nu})\nabla\tilde{\nu}\right) + c_{b2}(\nabla\tilde{\nu})^2\right] - \left[c_{w1}f_w - \frac{c_{b1}}{\kappa^2}f_{t2}\right]\left[\frac{\tilde{\nu}}{d}\right]^2 + f_{t1}\Delta U^2 \tag{2.47}$$

On the right hand-side, each term represents production, diffusion, dissipation, and trasition/trip effects, respectively. The individual components are defined as:

$$\tilde{S} = S + \frac{\tilde{\nu}}{\kappa^2 d^2}f_{v2} \qquad f_{v2} = 1 - \frac{\chi}{1 + \chi f_{v1}}$$

$$f_w = g\left[\frac{1 + c_{w3}^6}{g^6 + c_{w3}^6}\right]^{\frac{1}{6}} \qquad g = r + c_{w2}(r^6 - r) \tag{2.48}$$

$$r = \frac{\tilde{\nu}}{\tilde{S}\kappa^2 d^2} \qquad f_{t2} = c_{t3}exp(-c_{t4}\chi^2)$$

$$f_{t1} = c_{t1}g_t exp\left(-c_{t2}\frac{\omega_t^2}{\Delta U^2}[d^2 + g_t^2 d_t^2]\right)$$

Where:

d_t is the distance from the field point to the trip point on the wall

ω_t is the wall vorticity at the trip

ΔU is the difference between velocity at the field point and that at the trip

$g_t \equiv min(0.1, \Delta U/\omega_t \Delta x_t)$

x_t is the grid spacing along the wall at the

And, the constants are:

$c_{b1} = 0.1355$ $\quad c_{b2} = 0.622$ $\quad \sigma = 2/3$ $\quad \kappa = 0.41$

$c_{w1} = \frac{c_{b1}}{\kappa^2} + \frac{(1 + c_{b2})}{\sigma}$ $\quad c_{w2} = 0.3$ $\quad c_{w3} = 2$ $\quad c_{v1} = 7.1$

$c_{t1} = 1$ $c_{t2} = 2$ $c_{t3} = 1.2$ $c_{t4} = 0.5$

In the current study, the trip is not applied and the flow field is assumed as full turbulent flows.

Spalart and Allmaras also proposed a Detached Eddy Simulation (DES) model [65] to improve SA model in separated flows. In the DES model, the turbulence length scale is computed in two different ways. In regions close to the wall the length scale is related to the closest distance to the wall. In regions away from the wall, this definition is replaced by the maximum cell size as follows:

$$\tilde{d} = min(d, C_{DES}\Delta), \qquad \Delta = max(\Delta x, \Delta y, \Delta z) \tag{2.49}$$

The distance, d, in the transport equation is replaced with $\tilde{d}$, and the model constant $C_{DES} = 0.65$ is used in this study. For further detailed formulation and numerical solution procedure of the implemented SA-DES model, the reader is referred to Ref. [64,65,72].

2.3.2 Kinetic Eddy Simulation (KES) model

Fang and Menon [68,69] recently developed the Kinetic Eddy Simulation (KES) model for large-eddy simulation (LES) of wall-bounded high Reynolds number flows. The model solves two PDEs, one of the sub-grid kinetic energy, k^{sgs}, and the other for $(kl)^{sgs}$ where l^{sgs} is the sub-grid length scale.

$$\frac{\partial \rho k^{sgs}}{\partial t} + \frac{\partial \rho u_i k^{sgs}}{\partial x_j} = \tau_{ij}\frac{\partial u_i}{\partial x_j} - C_k \rho \frac{(k^{sgs})^{3/2}}{l^{sgs}} + \frac{\partial}{\partial x_j}\left[\rho\left(\frac{\nu_l}{Pr} + \frac{\nu_t}{\sigma_k}\right)\frac{\partial k^{sgs}}{\partial x_j}\right] \tag{2.50}$$

$$\frac{\partial \rho (kl)^{sgs}}{\partial t} + \frac{\partial \rho u_i (kl)^{sgs}}{\partial x_j} = C_l l^{sgs} \tau_{ij} \frac{\partial u_i}{\partial x_j} - C_{kl} \rho (k^{sgs})^{\frac{3}{2}} + \frac{\partial}{\partial x_j}\left[\rho \left(\frac{\nu_l}{Pr} + \frac{\nu_t}{\sigma_{kl}}\right) \frac{\partial (kl)^{sgs}}{\partial x_j}\right] \tag{2.51}$$

Where:

$\sigma_k = 0.9$ $\quad$ $\sigma_{kl} = 2$ $\quad$ $C_k = 0.916$

$C_l = 1.06$ $\quad$ $C_{kl} = 0.58 + 2\frac{C_\nu}{\sigma_{kl}}\left(\frac{\partial l^{sgs}}{\partial x_j}\right)^2$ $\quad$ $C_\nu = 0.0667$

$\nu_l = \frac{\mu_l}{\rho}$ $\quad$ $\nu_t = \frac{\mu_t}{\rho}$ $\quad$ $Pr = 0.72$

The first term on the right-hand side of the Eqns. (2.50) and (2.51) represents production, and the second and third term represents dissipation and diffusion, respectively. The sub-grid eddy viscosity is computed from:

$$\mu_t = \rho C_\nu (k^{sgs})^{\frac{1}{2}} l^{sgs} \tag{2.52}$$

Both k^{sgs} and l^{sgs} are set to zero on the wall, and following formulation is used to determine the value on the first cell off the wall.

$$k^{sgs} = 0.25\nu (u_i u_i)_1^{0.5} / \Delta_1 \tag{2.53}$$

$$l^{sgs} = \sqrt{k^{sgs}} \Delta_1^2 / (0.53\nu) \tag{2.54}$$

When the length scale, l^{sgs}, is close to the computational grid size, Δ, the model approaches LES. When the computed length scale is much larger than the local grid size, the model smoothly approaches Very Large-Eddy Simulation (VLES). Thus, the model is considered a VLES-LES approach. For further details, the reader is referred to Ref. [68,69,71].

2.4 Parallelization of the Solution Process

Although the hybrid method is an efficient way of simulating a rotor, the computational time is still high. For example, in the CFD-CSD coupling analysis, the sequential CSD and CFD analyses takes several iterations that requires several days. Thus, the computational time should be further reduced for massive computations. In the present study, it was achieved by parallelization of the code using the Message Passing Interface (MPI) approach [73].

2.5 Initial and Boundary Conditions

2.5.1 Initial Conditions

In the beginning of the analysis, flow properties in the Navier-Stokes domain were initialized with free stream properties as:

$$\begin{aligned} \rho &= \rho_\infty \\ u &= u_\infty \\ v &= v_\infty \\ w &= w_\infty \\ p &= p_\infty \end{aligned} \tag{2.55}$$

2.5.2 Boundary Conditions

At solid walls, no-slip adiabatic wall temperature condition was applied. For this the following condition is satisfied.

$$\begin{aligned} \vec{V}_{wall} &= \vec{V}_{grid} \\ \left.\frac{\partial T}{\partial n}\right|_{wall} &= 0 \end{aligned} \tag{2.56}$$

Zero gradient of pressure at the wall was also assumed, i.e. $(\partial p/\partial n|_{wall} = 0)$.

At the block interfaces including wake-cut behind trailing edge, ghost cell was used to maintain the solution accuracy. The properties of the ghost cell were obtained from inner cell value of the opposite block. Two consecutive ghost cell properties are required for third order scheme, and four ghost cell values are required for 7th order scheme. For node-centered scheme, the flow properties at the interface were obtained by interpolating the fist inner cell value of the current block and the ghost cell value next to the interface.

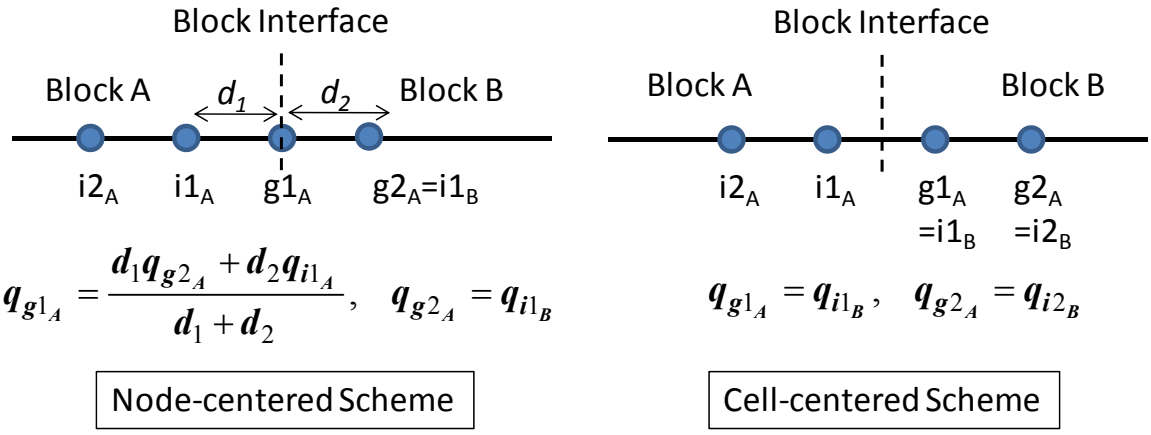

Figure 2.1 Interface boundary condition

At the outer boundaries including far-field, inboard, and outboard surfaces, characteristics based inflow/outflow boundary condition was applied to prevent non-physical wave reflection at the boundary. The details of this boundary condition may be found in classical CFD text books [74]. In this boundary condition, Riemann invariants are written as:

$$R^+ = \vec{V}_n + \frac{2a}{\gamma - 1}$$
$$R^- = \vec{V}_n - \frac{2a}{\gamma - 1} \tag{2.57}$$

And the characteristic velocities are

$$\lambda_1 = \vec{V}_n + a$$
$$\lambda_2 = \vec{V}_n - a \tag{2.58}$$

Here, $\vec{V}_n$ is the normal velocity directing outward from the computational domain. In the current hybrid method, the velocity at the outer boundary surface is defined as:

$$\vec{V} = \vec{V}_{wind} + \vec{V}_{wake\ induce} \tag{2.59}$$

Here, $\vec{V}_{wake\ induce}$ is the induced velocity by all the wake filaments.

If $\vec{V}_n$ is a negative value, so is λ_2, inflow condition is applied. In this case, if the value of λ_1 is also negative, all the information comes from the free stream. If λ_1 value is positive, one piece of information comes from the interior and others come from the free stream.

If $\vec{V}_n$ is a positive value, so is λ_1, outflow condition is applied. In such a case, if the value of λ_2 is positive, all the information comes from the interior. If the value of λ_2 is negative, one piece of information comes from the free stream and others come from the interior of the domain. Detailed computation of flow properties may be found in reference [74].

2.6 Inflow Modeling

Because the calculations of rotors require an accurate modeling of inflow, a hybrid three-dimensional Navier-Stokes/free wake method is used in this study. In this hybrid approach, the time-consuming Navier-Stokes simulations are carried out only for a single blade, in a small region surrounding this "reference blade" (Figure 2.2-a). The wake structure behind this reference blade and those of the other blades is modeled using a free wake vortex model (Figure 2.2-b). Only the trailing vortices from the blade tips are modeled. The vortex strength of the most recently generated tip vortex segment was

assumed to be peak bound circulation at the instance the vortex segment was generated. The tip vortices were propagated in time at a local velocity, calculated as the induced velocity due to all vortex filaments plus the freestream velocity. Biot-Savart law is used to compute the induced velocity. The induced velocities due to wake structure are also calculated at the outer surface of the Navier-Stokes computational domain and applied as an inflow boundary condition. This allows the vortices to reenter the computational domain. If the rotor is in steady flight, only a single blade is modeled by the Navier-Stokes solver since the solution is periodic.

At start of the calculations, for the very first iteration, the wake is prescribed for 4~5 full revolutions. This initial guess reduces Navier-Stokes domain revolution required to reach steady state (periodic) solution. Subsequently, 3 to 6 additional revolutions were made to reach steady solution. The proper time step was chosen after time step convergence study. The wake structure was updated at every 5 degrees. For details of the free wake model, the reader is referred to reference [50] and [52].

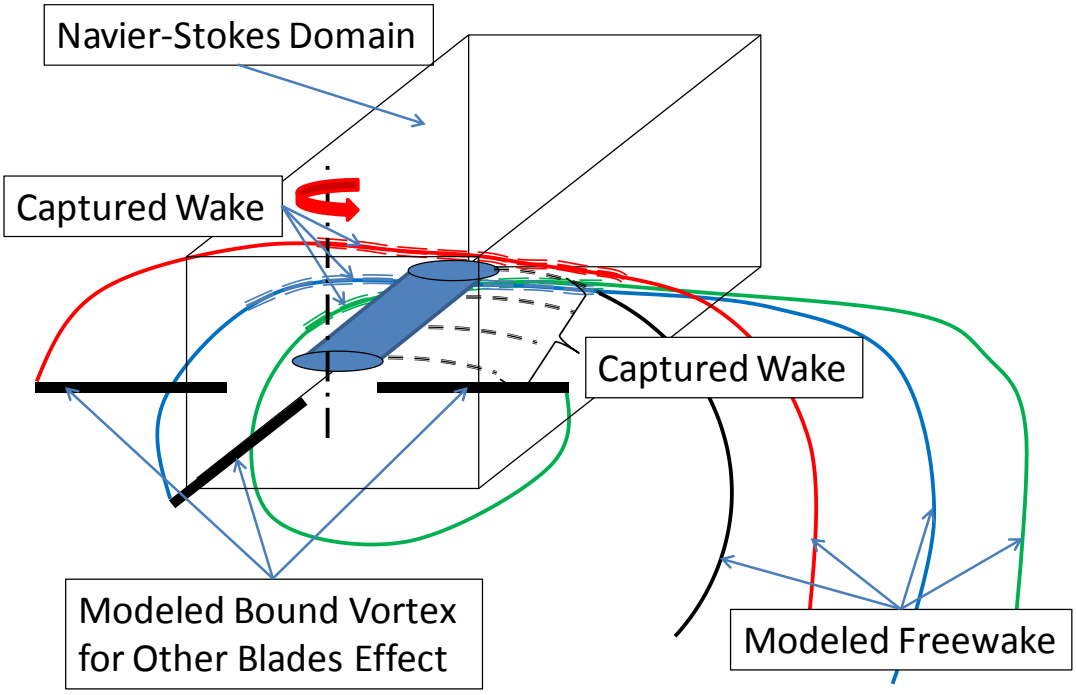

a) Illustration of the hybrid method

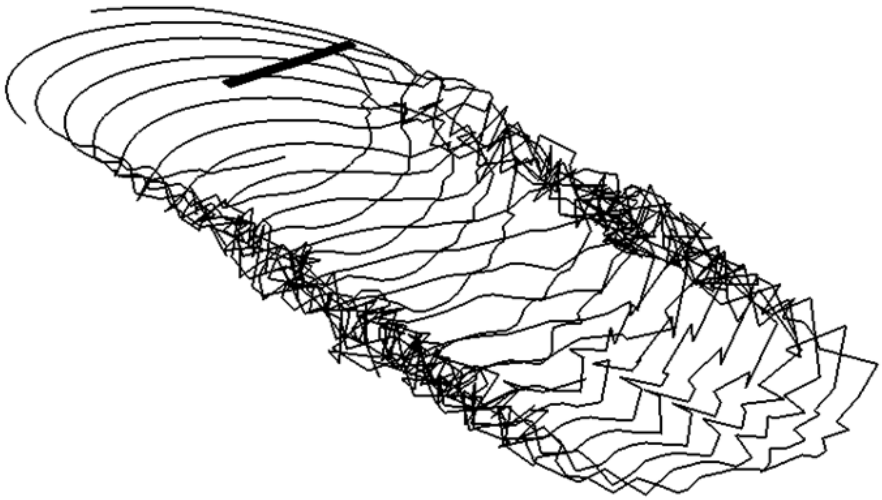

b) Simulated free wake

Figure 2.2 A schematic view of the hybrid method

2.7 Rigid Blade Rotor Trim

The elastic blade response was modeled using a comprehensive CSD (Computational Structure Dynamics) code, DYMORE. The rotor is trimmed internally with its own lifting line aerodynamic model or with external airloads from a CFD solver. The CFD-CSD coupling method is explained in the next section. In this section, a trim methodology used for a rigid blade rotor is introduced.

2.7.1 Flapping Equation Solver

Considering blade flapping motion shown in Figure 2.3, the equation of flapping motion can be derived as Eqn. (2.60) by taking moment balance about the flap hinge.

$$\int_e^R \acute{r}^2 \ddot{\beta} m dr - \int_e^R \acute{r} F_1 dr + \int_e^R \acute{r} \sin\beta (e + \acute{r}\cos\beta)\, \Omega^2 m dr + \int_e^R \acute{r}\cos\beta\, g m dr + k_\beta(\beta - \beta_p) = 0 \tag{2.60}$$

Here, each term on the left hand side represents moment due to the inertial force, aerodynamic force, centrifugal force, gravity force, and the hinge spring force, from left to right. In general, the gravity force can be neglected in the steady state condition. Using chain rule, the time derivative of β can be expressed as follows.

$$\dot{\beta} = \frac{d\beta}{dt} = \frac{d\beta}{d(\psi/\Omega)} = \Omega \frac{d\beta}{d\psi} = \Omega\beta^*$$
$$\ddot{\beta} = \frac{d^2\beta}{dt^2} = \Omega^2 \frac{d^2\beta}{d\psi^2} = \Omega^2\beta^{**} \tag{2.61}$$

Substituting Eqn. (2.61) into Eqn. (2.60), dividing by $(\Omega R)^2 = V_{tip}^2$, and neglecting gravity term yields following flapping equation.

$$\beta^{**}\int_e^R\left(\frac{\acute{r}}{R}\right)^2 mdr-\int_e^R \acute{r}\frac{F_1}{V_{tip}^2}dr+\int_e^R\left(\frac{1}{R}\right)^2 \acute{r}\sin\beta(e+\acute{r}\cos\beta)\,mdr + k_\beta(\beta-\beta_p)\frac{1}{V_{tip}^2}=0 \tag{2.62}$$

The aerodynamic force term is further extended as follows (see Figure 2.4 for terminology).

$$\frac{F_1}{V_{tip}^2}=\frac{1}{V_{tip}^2}[L'\cos\phi-D'\sin\phi] \tag{2.63}$$

Where:

$$L'=\tfrac{1}{2}\rho V^2 cC_l \qquad D'=\tfrac{1}{2}\rho V^2 cC_d$$

$$\phi\cong\frac{U_p}{U_t} \qquad C_l, C_d\cong f(\alpha)$$

$$\alpha=\theta-\phi$$

$$\frac{U_p}{V_{tip}}=\frac{V_\infty}{V_{tip}}\sin\alpha_s\cos\beta+(r-e)\beta^*+\lambda_i\cos\beta+\frac{V_\infty}{V_{tip}}\cos\alpha_s\sin\beta\cos\psi \tag{2.64}$$

$$\frac{U_t}{V_{tip}}=(r-e)\cos\beta+e+\frac{V_\infty}{V_{tip}}\cos\alpha_s\sin\psi$$

$$\theta=\theta_0+\theta_{tw}\left(\frac{r}{R}-0.75\right)+\theta_{1c}\cos\psi+\theta_{1s}\sin\psi$$

The Glauert's model was used to determine the uniform inflow, λ_i. A simple thin airfoil theory based linear aerodynamic model is used for lift and drag estimation.

Two approaches are available for solving the flapping equation. The first is a time-marching scheme where Eqn. (2.62) is solved by marching in time. This procedure is continued until the blade motion reaches steady periodic state for one revolution. The other approach is a harmonic balance approach. The flapping angle and its 2nd derivative are expressed as:

$$\beta = \beta_0 + \beta_{1c}\cos\psi + \beta_{1s}\sin\psi$$
$$\frac{\partial^2\beta}{\partial\psi^2} = \beta^{**} = -\beta_{1c}\cos\psi - \beta_{1s}\sin\psi \tag{2.65}$$

The higher harmonics are neglected. By substituting β and β^{**} in the Eqn. (2.62) with small angle assumptions, i.e. $\cos\beta = 1, \sin\beta = \beta$, expressions for β_0, β_{1c} and β_{1s} may be obtained in a closed form. An alternative method without small angle assumption is to solve the flapping equation as:

$$\sum_{\psi=0}^{2\pi} \mathcal{F}\,(\beta_0, \beta_{1c}, \beta_{1s}) = 0$$
$$\sum_{\psi=0}^{2\pi} \mathcal{F}\,(\beta_0, \beta_{1c}, \beta_{1s})\sin\psi = 0 \tag{2.66}$$
$$\sum_{\psi=0}^{2\pi} \mathcal{F}\,(\beta_0, \beta_{1c}, \beta_{1s})\cos\psi = 0$$

This gives three equations with three unknowns$(\beta_0, \beta_{1c}, \beta_{1s})$. The Newton-Raphson iterative method is used in this study to solve the system of equation.

2.7.2 Trim Controller

Trimmed state is achieved such that all the trim targets are met with a set of pilot control inputs. Rotor is trimmed for the desired thrust and zero hub moments.

$$C_T = C_T(\theta_0, \theta_{1c}, \theta_{1s})$$
$$C_{PM} = C_{PM}(\theta_0, \theta_{1c}, \theta_{1s}) \tag{2.67}$$
$$C_{RM} = C_{RM}(\theta_0, \theta_{1c}, \theta_{1s})$$

A Newton-Raphson iterative method is used to find the trimmed solution. Using the given initial value of the control inputs, $[\theta_0^0, \theta_{1c}^0, \theta_{1s}^0]$, and the trim

targets, $\left[C_T^d, C_{PM}^d, C_{RM}^d\right]$, a new estimate for the control variables are obtained by solving following linearized system of equations:

$$\begin{bmatrix} C_T \\ C_{PM} \\ C_{RM} \end{bmatrix}^0 + \begin{bmatrix} \partial C_T/\partial\theta_0 & \partial C_T/\partial\theta_{1c} & \partial C_T/\partial\theta_{1s} \\ \partial C_{PM}/\partial\theta_0 & \partial C_{PM}/\partial\theta_{1c} & \partial C_{PM}/\partial\theta_{1s} \\ \partial C_{RM}/\partial\theta_0 & \partial C_{RM}/\partial\theta_{1c} & \partial C_{RM}/\partial\theta_{1s} \end{bmatrix}^0 \begin{bmatrix} \Delta\theta_0 \\ \Delta\theta_{1c} \\ \Delta\theta_{1s} \end{bmatrix}^0 = \begin{bmatrix} C_T \\ C_{PM} \\ C_{RM} \end{bmatrix}^d \tag{2.68}$$

The trim Jacobian matrix is obtained using small perturbations to the control variables$(\Delta\theta_0^0, \Delta\theta_{1c}^0, \Delta\theta_{1s}^0)$.

$$\left[\frac{\partial C_T}{\partial\theta_0}\right]^0 \approx \frac{\Delta C_T^0}{\Delta\theta_0^0}, \qquad \left[\frac{\partial C_T}{\partial\theta_{1c}}\right]^0 \approx \frac{\Delta C_T^0}{\Delta\theta_{1c}^0}, \qquad \left[\frac{\partial C_T}{\partial\theta_{1s}}\right]^0 \approx \frac{\Delta C_T^0}{\Delta\theta_{1s}^0}, \tag{2.69}$$

The other derivatives may be obtained in the similar manner. Once the above linear system of equations is solved for $[\Delta\theta_0^0, \Delta\theta_{1c}^0, \Delta\theta_{1s}^0]^T$, the updated estimates for the control variables are obtained as follows.

$$\begin{bmatrix} \theta_0 \\ \theta_{1c} \\ \theta_{1s} \end{bmatrix}^1 = \begin{bmatrix} \theta_0 \\ \theta_{1c} \\ \theta_{1s} \end{bmatrix}^0 + \begin{bmatrix} \Delta\theta_0 \\ \Delta\theta_{1c} \\ \Delta\theta_{1s} \end{bmatrix}^0 \tag{2.70}$$

With the new control variables, the flapping equation is solved and the rotor performance metrics are obtained. This procedure is iterated until the computed rotor performance metrics meet the desired trim targets.

2.7.3 Rigid Blade Rotor Trim Coupled with CFD Solver

The flapping equation solver employs simple thin-airfoil-theory-based linear aerodynamic model to save computational time. However, above trim controller and the flapping equation solver can be coupled with a CFD solver to include high fidelity aerodynamic model. Delta-airloads approach was utilized for this coupling analysis. In

the beginning of the analysis, a trimmed state is estimated with linear aerodynamic model (LM) and the blade motion in terms of β_0, β_{1c}, β_{1s}, θ_0, θ_{1c} and θ_{1s} is obtained. A CFD solver is utilized to obtain sectional normal $\left(C_n M_{tip}^2\right)$ and chord-wise $\left(C_c M_{tip}^2\right)$ forces with the estimated flapping and feathering angles. Then, lift and drag forces in the flapping equation are provided in the following manner:

$$C_l^i = C_{l,LM}^i + \Delta C_l^i, \qquad C_d^i = C_{d,LM}^i + \Delta C_d^i \tag{2.71}$$

Where:

$$\begin{aligned} \Delta C_l^i &= C_{l,CFD}^{i-1} - C_{l.LM}^{i-1} \\ \Delta C_d^i &= C_{d,CFD}^{i-1} - C_{d.LM}^{i-1} \\ C_{l,CFD} &= C_{n,CFD}\cos\alpha - C_{c,CFD}\sin\alpha \\ C_{d,CFD} &= C_{n,CFD}\sin\alpha + C_{c,CFD}\cos\alpha \end{aligned} \tag{2.72}$$

The coupling iteration is repeated until the desired target state is achieved.

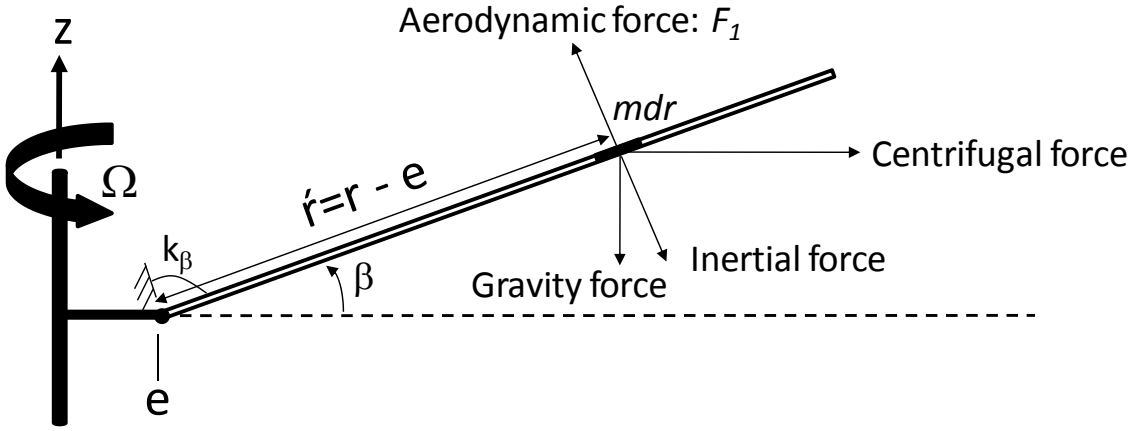

Figure 2.3 Flapping motion

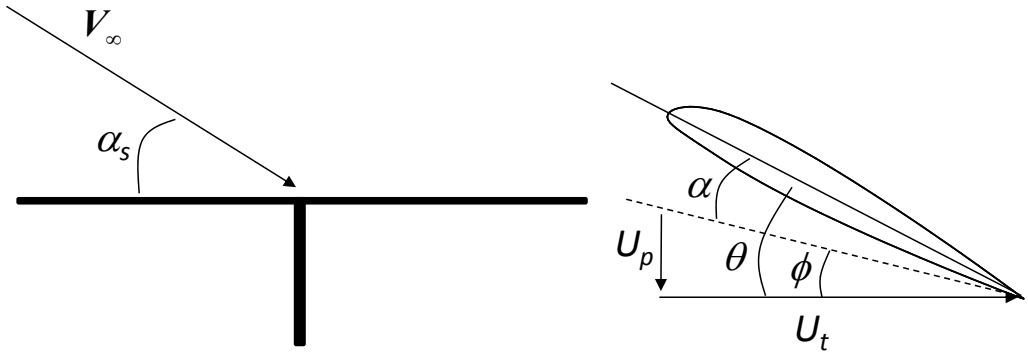

Figure 2.4 Terminology for flapping equation

2.8 CFD-CSD Coupling Analysis

2.8.1 Coupling Analysis Strategy

A finite element solver called DYMORE is used in this study for modeling the aeroelastic response of the blades. DYMORE uses a multi-body dynamics approach for the modeling of the rotor as a nonlinear elastic multi-body system. This approach allows modeling of complex rotor configurations with emphasis on detail. The code incorporates robust and efficient time integration algorithms for integrating the resulting large scale, nonlinear, differential or algebraic equations. Figure 2.5 shows a multi-body representation of a bearingless and articulated rotor system in DYMORE.

The calculations presented in this study exchange aerodynamic loads and deflections between the CFD and CSD solvers at periodic intervals. The CFD-CSD coupling methodology framework is also shown in Figure 2.5 for a loose coupling strategy. The coupling between DYMORE and the present CFD analysis uses the original Fluid Structure Interface (FSI) format to exchange data [75]. The first step involves running the CSD code that computes airloads using its internal lifting line (LL) based aerodynamic model. These airloads are applied on the rotor structural model to compute the elastic deformations. The deformation data consists of linear deformations ($\Delta x, \Delta y, \Delta z$) and rotational deformations ($\Delta\phi, \Delta\theta$ and $\Delta\psi$ corresponds to x, y, and z as a rotational axis in blade frame respectively) defined at each blade span section quarter chord points as a function of azimuthal angle and radial location. The solver also trims the rotor to match the specified hub loads by adjusting the pitch controls. The periodic blade deformations obtained from this run are transferred to the CFD solver using a fluid structure interface. The CFD solver deforms the blade mesh and computes the periodic

air loads, which is subsequently transferred to the structural dynamics system using the delta air loads method. The delta air loads method, explained in detail in references [76-79], provides immediate aerodynamic damping force against elastic blade structural deformation and is shown to drive the solver to robust convergence. The delta air loads is computed as follows:

$$\Delta L_i = L_{i-1}^{CFD} - L_{i-1}^{LL} = L_{i-1}^{CFD} - L_{i-1}^{CSD} + \Delta L_{i-1} \tag{2.73}$$

Where:

$$L_{i-1}^{LL} = L_{i-1}^{CSD} - \Delta L_{i-1} \tag{2.74}$$

And the resultant airloads in the CSD code will be:

$$L_i^{CSD} = L_i^{LL} + \Delta L_i \tag{2.75}$$

When the trimmed state is established and steady periodic condition is achieved, the air loads in CSD code become identical to CFD air loads, i.e. $L_i^{CSD} = L_i^{CFD}$. The delta air loads are first recast in a shaft fixed frame as three components of forces and moments at each radial location prior to its use in the CSD analysis.

The coupling iterations are executed till convergence is observed in the hub loads obtained from the CFD solver and pitch controls obtained from the CSD solver.

For the configuration considered in this study, a wind tunnel trim was employed which requires specification of the shaft angle and the thrust setting. The pitching and the rolling moments were trimmed to zero at the hub. The comprehensive analysis is capable of handling other trim settings, e.g. propulsive trim.

The Gurney flap is considered as a part of the airfoil, thus the structural analysis does not model the Gurney flap separately. Since the size and weight of the Gurney flap

is small, the structural property of the airfoil was assumed same as the baseline airfoil. Thus, the effect of the gurney flap is accounted in the form of air loads variation only.

2.8.2 Grid Deformation

The unsteady moving grid including pilot control input and local blade deformation due to elastic behavior of the blade is simulated in the following manner.

The blade motion obtained from the CSD analysis includes linear (Δx, Δy, Δz) and rotational deformations ($\Delta\phi$, $\Delta\theta$, $\Delta\psi$). The definition of the local deformation is shown in Figure 2.6. The deformation includes not only elastic deformation, but also pilot control input and flapping motion.

Once the deformations are obtained from the CSD analysis, an interpolation technique is employed to obtain deformations at desired radial and azimuthal location. The rotational deformation is applied to the initial un-deformed grid following x-y-z sequence of the Euler angle rotation around the reference point as follows.

$$\begin{bmatrix} x \\ y \\ z \end{bmatrix}_r = L_r \left[\begin{bmatrix} x \\ y \\ z \end{bmatrix}_{initial} - \begin{bmatrix} x \\ y \\ z \end{bmatrix}_{ref} \right]$$

$$L_r = L_3(-\Delta\psi)L_2(-\Delta\theta)L_1(-\Delta\phi) \tag{2.76}$$

$$= \begin{bmatrix} CS \cdot CT & -SS \cdot CF + ST \cdot CS \cdot SF & SS \cdot SF + ST \cdot CS \cdot CF \\ SS \cdot CT & CS \cdot CF + SS \cdot ST \cdot SF & -CS \cdot SF + SS \cdot ST \cdot CF \\ -ST & CT \cdot SF & CT \cdot CF \end{bmatrix}$$

Where:

$$CS = \cos\Delta\psi\,, CT = \cos\Delta\theta\,, CF = \cos\Delta\phi$$

$$SS = \sin\Delta\psi\,, ST = \sin\Delta\theta\,, SF = \sin\Delta\phi \tag{2.77}$$

Here, $[x \quad y \quad z]^T_{initial}$ is the initial grid coordinates placed at 0 degree azimuth without pre-cone, elastic deformation, flapping and pitch control input, but with built-in

twist angle. The point, $[x \quad y \quad z]_{ref}^{T}$, is the reference point, where the deformations were obtained after interpolation. Note that the expression above represents rotation applied to the grid point with positive $\Delta\phi$, $\Delta\theta$, and $\Delta\psi$ angles. Thus, the angles in the rotational matrixes (L_1, L_2, L_3) for the axis have negative sign. The final grid at the desired azimuthal angle is then obtained after applying linear transformation, pre-cone angle and rotation to the azimuthal location as follows.

$$\begin{bmatrix} x \\ y \\ z \end{bmatrix} = L_{IB} \left[\begin{bmatrix} x \\ y \\ z \end{bmatrix}_r + \begin{bmatrix} x \\ y \\ z \end{bmatrix}_{ref} + \begin{bmatrix} \Delta x \\ \Delta y \\ \Delta z \end{bmatrix} \right]$$

$$L_{IB} = L_3(-\Psi)L_2(\theta_p) \tag{2.78}$$

$$= \begin{bmatrix} \cos\Psi\cos\theta_p & -\sin\Psi & -\cos\Psi\sin\theta_p \\ \sin\Psi\cos\theta_p & \cos\Psi & -\sin\Psi\sin\theta_p \\ \sin\theta_p & 0 & \cos\theta_p \end{bmatrix}$$

Where, Ψ is the azimuthal angle (+, counterclockwise from top view), and θ_p is the pre-cone angle (+, flap up). Again, note that the angles in the rotational matrixes have the opposite sign of the grid rotation. The positive pre-cone angle is defined as flap-up direction, which is the opposite of the right hand rule. Thus, its sign in the rotational matrix is positive.

The grid deformation may be gradually reduced from the blade surface to the outer boundary of the computational domain, so that the outer boundary is remained un-deformed. However, deformations observed in this study were small, and the same deformation has been applied at a radial location throughout the constant span-wise plane.

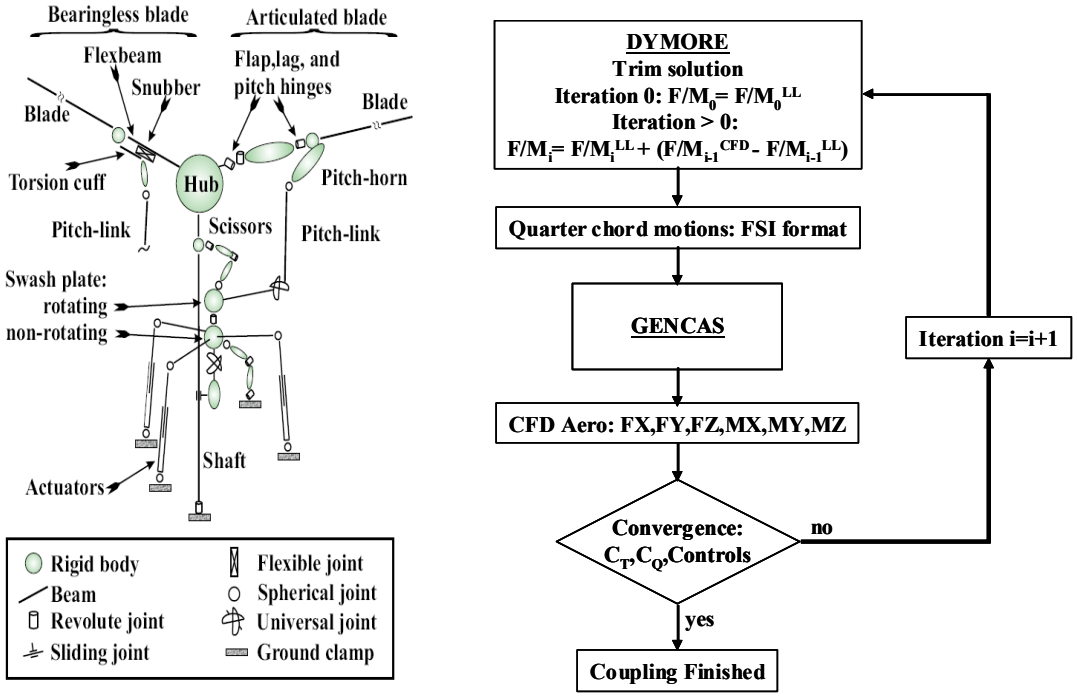

Figure 2.5 Details of the Multi-Body Representation of a Rotor System and the CFD/CSD Coupling Process

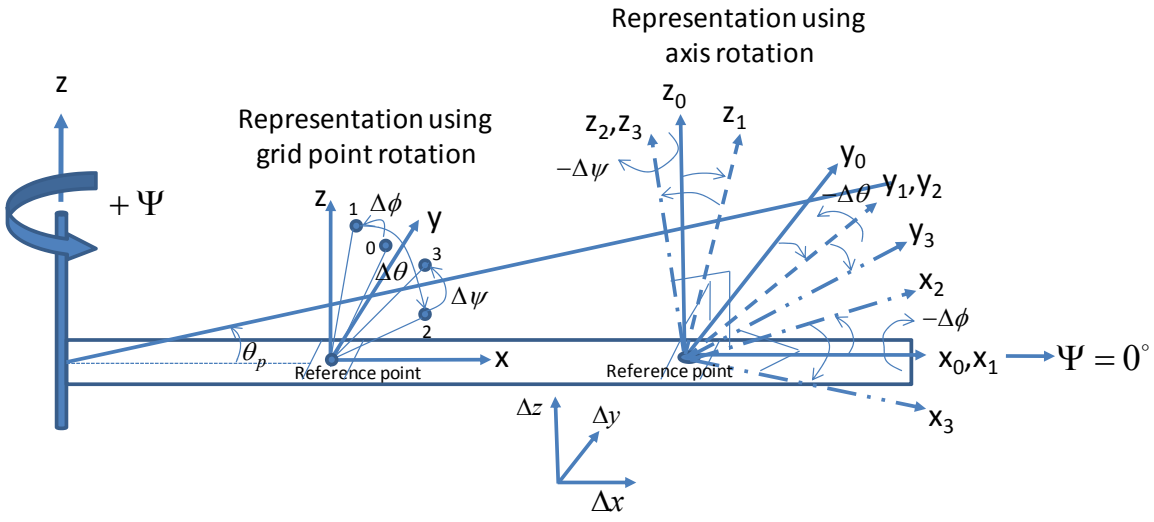

Figure 2.6 Definition of the deformation

2.9 Gurney Flap Simulation

Dynamic deployment of Gurney flap was simulated using the dynamic wall boundary condition shown in Figure 2.7 (GF installed at T.E) and Figure 2.8 (GF installed at both lower and upper surfaces near T.E). When the Gurney flap is not deployed, the vertical portion behind the trailing edge (Figure 2.7) or the vertical block interface portions on the lower and upper surfaces (between block 1 and 2, and block 2 and 3 in Figure 2.8) become a fluid interface. Boundary conditions enforcing continuity of the flow properties are applied.

If the Gurney flap is installed at the trailing edge, the flap is deployed and no slip boundary conditions are employed when the reference blade reaches a pre-specified azimuthal interval. The length of the deployed Gurney flap is assumed to follow a sinusoidal variation over the azimuthal interval where the flap is deployed. Figure 2.7 shows an example of Gurney flap schedule, deployed over two different azimuthal locations per revolution.

If the Gurney flap is installed at both lower and upper surfaces, the Gurney flap is deployed either on the lower or upper surface as scheduled. At points on the Gurney flap, on either sides of the interface, no slip boundary conditions are employed, while the pressure and temperature gradients are set to zero. Figure 2.8 shows an example of the Gurney flap schedule, deployed four per revolution (4P). The boundary condition modules allow deployment of partial span Gurney flaps over multiple radial segments, user specified boundary conditions at run time. The Gurney flap length is adjusted by changing the amplitude and frequency of the user-specified flap schedule.

If the Gurney flap is used to minimize rotor vibration, the schedule of the Gurney flap is determined so that the interested vibratory load is minimized by adjusting the phase angle, ϕ, and the amplitude, A. The mechanism of the vibration reduction is shown in Figure 2.10. If the Gurney flap is deployed on the lower surface, the local lift is increased due to enhanced circulation. On the other hand, if the Gurney flap is deployed on the upper surface, the local lift is decreased. This delta-load is tailored to cancel out the vibratory loads on the baseline rotor by providing desired additional load at a proper phase angle. A Fourier analysis is performed on the baseline hub load to extract the vibratory load components of most concern. From the baseline simulations the phase angle and amplitude, and/or the radial location of the Gurney flap is manually adjusted. Multiple analyses are done until minimum vibration is achieved. Figure 2.9 and Figure 2.10 illustrates four per revolution vibration reduction.

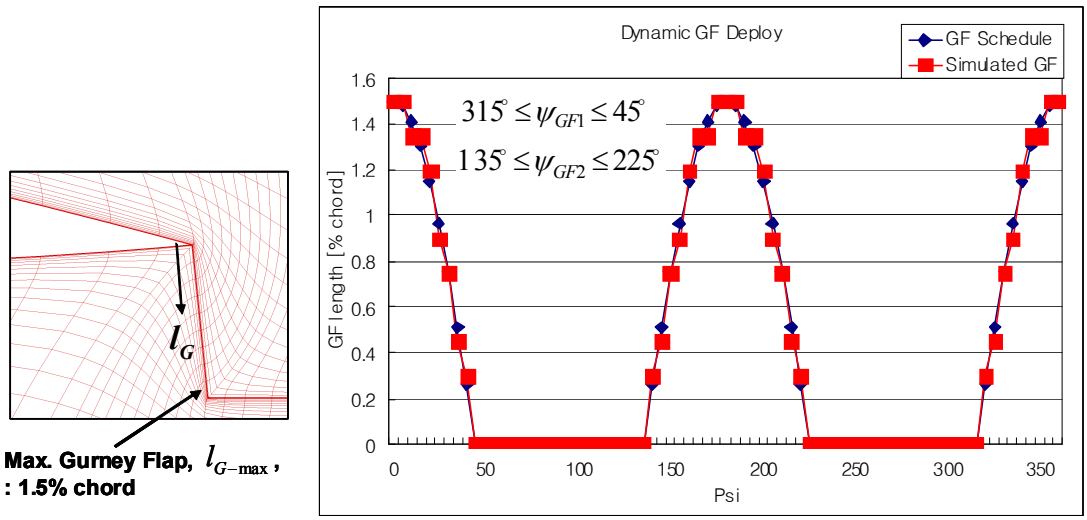

Figure 2.7 Gurney flap deployment at specified locations

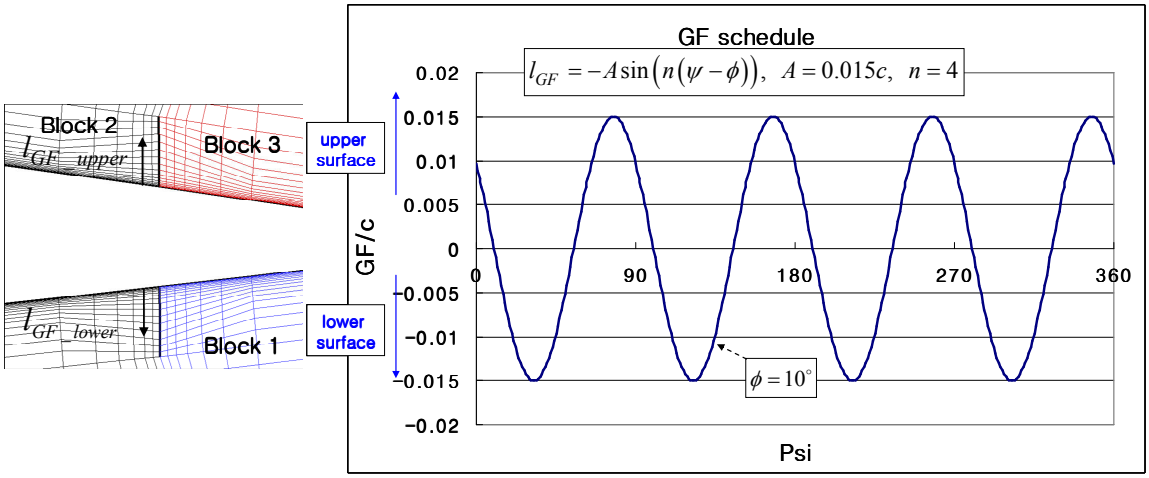

Figure 2.8 Harmonic Gurney flap deployment (4P)

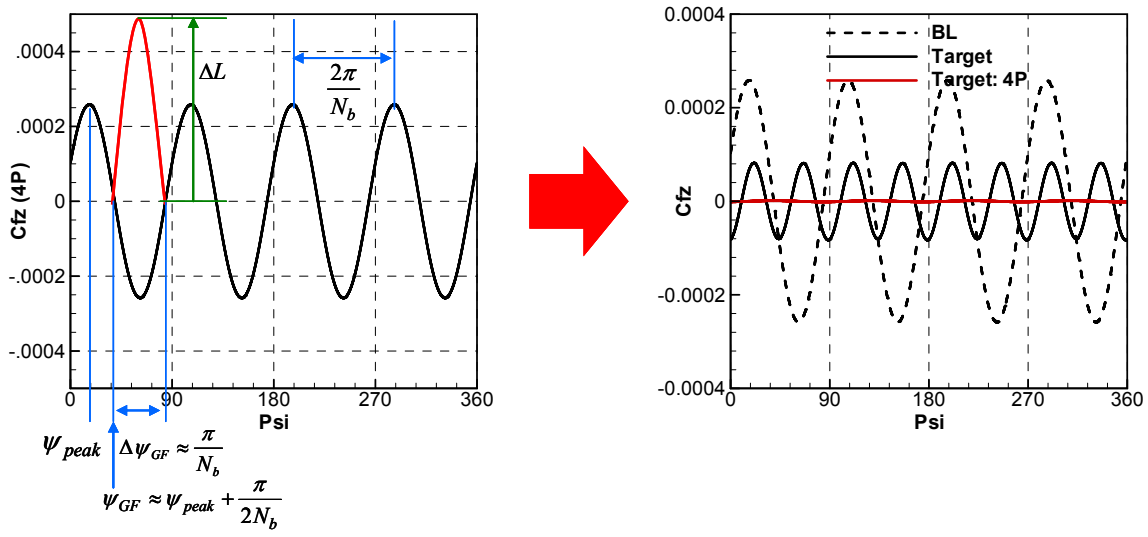

Figure 2.9 Vibration reduction mechanism: GF installed at lower side T.E

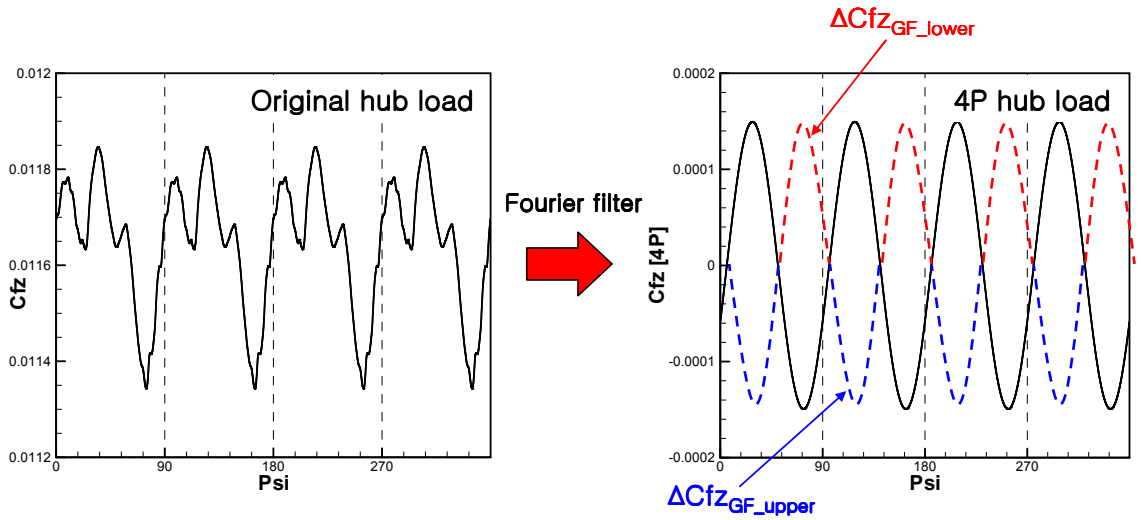

Figure 2.10 Vibration reduction mechanism: GF installed at both lower and upper surfaces

CHAPTER 3

ENHANCEMENTS TO THE HYBRID METHOD

3.1 Geometric Conservation Law

The Navier-Stokes equations may be written on a curvilinear coordinate system as follows:

$$\frac{\partial \bar{Q}}{\partial t}+\frac{\partial \bar{E}}{\partial \xi}+\frac{\partial \bar{F}}{\partial \eta}+\frac{\partial \bar{G}}{\partial \zeta}=\frac{\partial \bar{E}_v}{\partial \xi}+\frac{\partial \bar{F}_v}{\partial \eta}+\frac{\partial \bar{G}_v}{\partial \zeta} \tag{3.1}$$

Where, $\bar{Q}=(1/J)Q$. Current study involves aeroelastic deformation of the blade, which results in grid system deformation and cell volume changes for each of the cells, every time step. The Jacobian of the coordinate transformation, which is the inverse of the cell volume, is a function of both time and space. The first term of the Eqn. (3.1) becomes:

$$\frac{\partial \bar{Q}}{\partial t}=\frac{\partial \forall Q}{\partial t}=\forall \frac{\partial Q}{\partial t}+Q\frac{\partial \forall}{\partial t} \tag{3.2}$$

The second term on the right side of Eqn. (3.2) must be properly modeled to satisfy GCL (Geometric Conservation Law) [80,81]. Neglecting this term is equivalent to placing an equivalent numerical source or sink in the flow field. The magnitude of the second term on the right may be quite large far away from the rotor. These sources and sinks will affect the conservation of momentum, and thus the conservation of vorticity. To mitigate this error, a properly formulated GCL has been included in the present numerical method.

The differential form of the GCL term in generalized coordinate system may be expressed as:

$$\frac{\partial \forall}{\partial t} = -\left[\frac{\partial}{\partial \xi}\left(\frac{\xi_t}{J}\right) + \frac{\partial}{\partial \eta}\left(\frac{\eta_t}{J}\right) + \frac{\partial}{\partial \zeta}\left(\frac{\zeta_t}{J}\right)\right] \tag{3.3}$$

The details of the GCL term derivation is given in Appendix A. Rearranging Eqn. (3.1) using Eqn. (3.2) and (3.3) results in following governing equation.

$$\frac{1}{J}\frac{\partial Q}{\partial t} + \frac{\partial \bar{E}}{\partial \xi} + \frac{\partial \bar{F}}{\partial \eta} + \frac{\partial \bar{G}}{\partial \zeta} = \frac{\partial \bar{E}_v}{\partial \xi} + \frac{\partial \bar{F}_v}{\partial \eta} + \frac{\partial \bar{G}_v}{\partial \zeta} + RHS_{GCL} \tag{3.4}$$

Where,

$$RHS_{GCL} = Q\left[\frac{\partial}{\partial \xi}\left(\frac{\xi_t}{J}\right) + \frac{\partial}{\partial \eta}\left(\frac{\eta_t}{J}\right) + \frac{\partial}{\partial \zeta}\left(\frac{\zeta_t}{J}\right)\right] \tag{3.5}$$

This term has been implemented in the present hybrid analysis.

3.2 Higher Order Calculation of Grid Jacobian and Metric

The errors associated with the computation of the Jacobians, (the inverse of the cell volume), and metrics (which represent surface areas of the cell), may produce additional numerical sources or sinks. This error may be small and safely neglected if the cell size is small or the grid is nearly orthogonal. However, the error may not be negligible in the far-field, where the grid is coarse. The errors in the calculation of cell volumes and cell face areas may become more significant if a disturbance such as an entering vortex is introduced at the far-field. An effort has made to refine the calculation of the Jacobian and associated metrics of transformation as follows.

For every cell, the node-centered hexahedron is split into 8 sub-hexahedra as shown in Figure 3.1-a. Each of the hexahedra is further split into 6 tetrahedra (Figure 3.1-b). The volume of a node centered cell is computed using Eqn. (3.6)

$$\forbidden{V} = \sum_{m=1}^{8} \sum_{l=1}^{6} \forbidden{V}_{Tetrahedron\_l} \tag{3.6}$$

Where:

$$\forbidden{V}_{Tetrahedron} = \left| \frac{1}{6} \vec{a} \cdot \left(\vec{b} \times \vec{c} \right) \right| \tag{3.7}$$

And $J = 1/\forbidden{V}$.

Figure 3.2 illustrates the procedure for computing the cell face areas. As shown in the Figure 3.2-a, conventional approaches for area computations using the 4 points may introduce significant errors on a highly skewed grid. To mitigate these errors, the surface area is expressed in the present work as the sum of four smaller areas as shown in Figure 3.2-b.

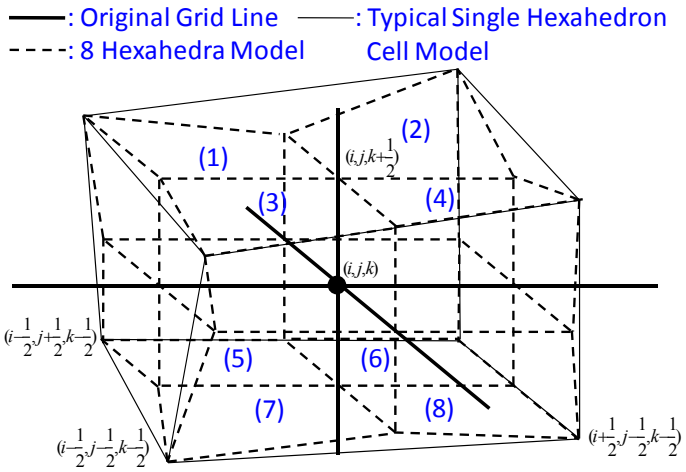

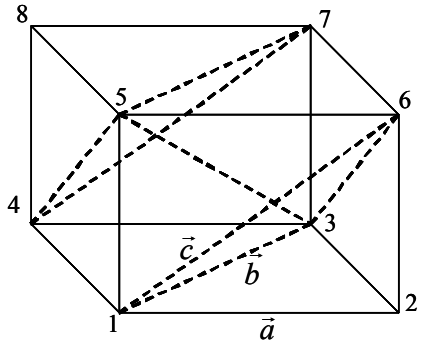

(a) A node-centered cell into 8 hexahedra on a skewed grid

(b) A hexahedron into 6 tetrahedra

Figure 3.1 Cell split

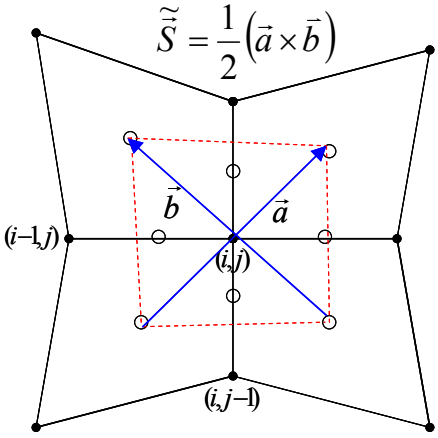

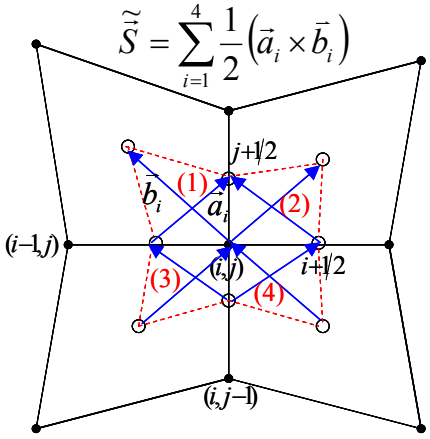

(a) Conventional Single Quadrangle model

(b) Refined Interface Area

Figure 3.2 Surface vector computation

3.3 7th Order Weighted Essentially Non-Oscillatory (WENO) Scheme

A spatially higher order scheme is utilized to reduce artificial viscosity. The WENO scheme introduced by Shu [82,83], a cell interface reconstruction scheme developed from ENO (Essentially Non-Oscillatory) scheme for inviscid flux calculation, is used. The WENO scheme uses all available combination of stencils, with nonlinear weighting factors, to achieve a high order non-oscillatory interpolation of the flow properties at cell faces. The conventional ENO scheme in contrast uses only one combination of stencils out of many possible candidates. The 7th order WENO scheme used in the present work employs a weighted average of cell interface values, computed using 4 different combinations of 7 points (Figure 3.3) as shown in Eqn. (3.8).

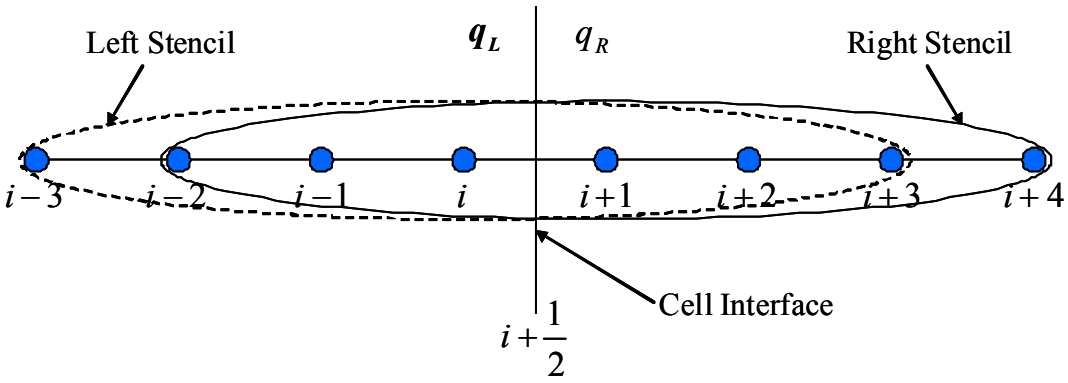

Figure 3.3 Stencils used in 7th order WENO scheme

$$
\begin{aligned}
q_L &= w_L^{(1)}\hat{q}_{i+1/2}^{(1)} + w_L^{(2)}\hat{q}_{i+1/2}^{(2)} + w_L^{(3)}\hat{q}_{i+1/2}^{(3)} + w_L^{(4)}\hat{q}_{i+1/2}^{(4)} \\
q_R &= w_R^{(1)}\tilde{q}_{i+1/2}^{(1)} + w_R^{(2)}\tilde{q}_{i+1/2}^{(2)} + w_R^{(3)}\tilde{q}_{i+1/2}^{(3)} + w_R^{(4)}\tilde{q}_{i+1/2}^{(4)}
\end{aligned}
\tag{3.8}
$$

Where:

$$
\begin{aligned}
\hat{q}^{(1)}_{i+1/2} &= \frac{1}{4}q_i + \frac{13}{12}q_{i+1} - \frac{5}{12}q_{i+2} + \frac{1}{12}q_{i+3} \\
\hat{q}^{(2)}_{i+1/2} &= -\frac{1}{12}q_{i-1} + \frac{7}{12}q_i + \frac{7}{12}q_{i+1} - \frac{1}{12}q_{i+2} \\
\hat{q}^{(3)}_{i+1/2} &= \frac{1}{12}q_{i-2} - \frac{5}{12}q_{i-1} + \frac{13}{12}q_i + \frac{1}{4}q_{i+1} \\
\hat{q}^{(4)}_{i+1/2} &= -\frac{1}{4}q_{i-3} + \frac{13}{12}q_{i-2} - \frac{23}{12}q_{i-1} + \frac{25}{12}q_i
\end{aligned}
\tag{3.9}
$$

$$
\begin{aligned}
\widetilde{q}^{(1)}_{i+1/2} &= \frac{1}{4}q_{i+1} + \frac{13}{12}q_i - \frac{5}{12}q_{i-1} + \frac{1}{12}q_{i-2} \\
\widetilde{q}^{(2)}_{i+1/2} &= -\frac{1}{12}q_{i+2} + \frac{7}{12}q_{i+1} + \frac{7}{12}q_i - \frac{1}{12}q_{i-1} \\
\widetilde{q}^{(3)}_{i+1/2} &= \frac{1}{12}q_{i+3} - \frac{5}{12}q_{i+2} + \frac{13}{12}q_{i+1} + \frac{1}{4}q_i \\
\widetilde{q}^{(4)}_{i+1/2} &= -\frac{1}{4}q_{i+4} + \frac{13}{12}q_{i+3} - \frac{23}{12}q_{i+2} + \frac{25}{12}q_{i+1}
\end{aligned}
\tag{3.10}
$$

The nonlinear weights are defined as:

$$
w^{(i)}_L = \frac{\widetilde{w}^i_L}{\sum_{k=1}^{4}\widetilde{w}^k_L}, \quad \text{and} \quad w^{(i)}_R = \frac{\widetilde{w}^i_R}{\sum_{k=1}^{4}\widetilde{w}^k_R} \tag{3.11}
$$

Where:

$$
\begin{aligned}
&\widetilde{w}^k_L = \frac{\gamma_k}{\left(\varepsilon + \beta^k_L\right)^2}, \quad \text{and} \quad \widetilde{w}^k_R = \frac{\gamma_k}{\left(\varepsilon + \beta^k_R\right)^2} \\
&\gamma_1 = \frac{4}{35}, \gamma_2 = \frac{18}{35}, \gamma_3 = \frac{12}{35}, \gamma_4 = \frac{1}{35}
\end{aligned}
\tag{3.12}
$$

And the smoothness indicators, β^k_L and β^k_R, are defined as follows:

$$
\begin{aligned}
\beta_L^{(1)} &= 2107q_i^2 - 9402q_{i+1}q_i + 7042q_iq_{i+2} - 1854q_iq_{i+3} - 17246q_{i+1}q_{i+2} \\
&\quad - 3882q_{i+2}q_{i+3} + 11003q_{i+1}^2 + 7043q_{i+2}^2 + 547q_{i+3}^2 + 4642q_{i+1}q_{i+3} \\
\beta_L^{(2)} &= 267q_{i+2}^2 - 1642q_{i+2}q_{i+1} + 1602q_{i+2}q_i - 494q_{i+2}q_{i-1} - 2522q_iq_{i-1} \\
&\quad + 3443q_i^2 + 547q_{i-1}^2 - 5966q_{i+1}q_i + 2843q_{i+1}^2 + 1922q_{i+1}q_{i-1} \\
\beta_L^{(3)} &= 267q_{i-2}^2 - 494q_{i+1}q_{i-2} - 1642q_{i-1}q_{i-2} + 1602q_iq_{i-2} - 5966q_iq_{i-1} \\
&\quad + 3443q_i^2 - 2522q_{i+1}q_i + 2843q_{i-1}^2 + 547q_{i+1}^2 + 1922q_{i+1}q_{i-1} \\
\beta_L^{(4)} &= 2107q_i^2 + 7042q_iq_{i-2} - 1854q_iq_{i-3} - 9402q_iq_{i-1} - 17246q_{i-1}q_{i-2} \\
&\quad + 4642q_{i-1}q_{i-3} + 547q_{i-3}^2 - 3882q_{i-2}q_{i-3} + 11003q_{i-1}^2 + 7043q_{i-2}^2
\end{aligned}
\tag{3.13}
$$

$$
\begin{aligned}
\beta_R^{(1)} &= 2107q_{i+1}^2 + 7042q_{i+1}q_{i-1} - 1854q_{i+1}q_{i-2} - 9402q_{i+1}q_i - 17246q_iq_{i-1} \\
&\quad + 4642q_iq_{i-2} + 547q_{i-2}^2 - 3882q_{i-1}q_{i-2} + 11003q_i^2 + 7043q_{i-1}^2 \\
\beta_R^{(2)} &= 267q_{i-1}^2 - 494q_{i+2}q_{i-1} - 1642q_{i+3}q_{i+1} + 1602q_{i+1}q_{i-1} - 5966q_{i+1}q_i \\
&\quad + 3443q_{i+1}^2 - 2522q_{i+2}q_{i+1} + 2843q_i^2 + 547q_{i+2}^2 + 1922q_{i+2}q_i \\
\beta_R^{(3)} &= 267q_{i+3}^2 - 1642q_{i+3}q_{i+2} + 1602q_{i+3}q_{i+1} - 494q_{i+3}q_i - 2522q_{i+1}q_i \\
&\quad + 3443q_{i+1}^2 + 547q_i^2 - 5966q_{i+2}q_{i+1} + 2843q_i^2 + 1922q_{i+2}q_i \\
\beta_R^{(4)} &= 2107q_{i+1}^2 - 9402q_{i+2}q_{i+1} + 7042q_{i+1}q_{i+3} - 1854q_{i+1}q_{i+4} - 17246q_{i+2}q_{i+3} \\
&\quad - 3882q_{i+3}q_{i+4} + 11003q_{i+2}^2 + 7043q_{i+3}^2 + 547q_{i+4}^2 + 4642q_{i+2}q_{i+4}
\end{aligned}
\tag{3.14}
$$

The weights depend on smoothness of the q values, such that the scheme prevents from oscillation by proper selection of the weight. The reader is referred to reference [83] for details. The scheme gradually reduces to 5th order WENO and 3rd order MUSCL interpolations near the boundaries. The 7th order WENO scheme was successfully implemented in TURNS and showed stronger blade tip vortex capturing capability [84].

3.4 2nd Order Time Accuracy with Newton Sub-iteration

In the baseline GENCAS analysis, an implicit two point backward difference scheme is used to advance the solution in time. This scheme is only first order in time. To assess the effects of temporal differencing scheme on the solutions, the analysis was enhanced with a 2nd order accurate time marching scheme, with Newton sub-iterations. The governing equation in implicit form is given as follows:

$$\left[\frac{(1+\phi)}{J\Delta t}I + \delta_\xi A + \delta_\eta B + \delta_\zeta C\right]\Delta Q^m = \frac{\phi\Delta Q^{n-1}}{J^{n-1}\Delta t} - \frac{(1+\phi)(Q^m - Q^n)}{J\Delta t} + R(Q^m) \quad (3.15)$$

Where:

$$\begin{gathered} \Delta Q^m = Q^{m+1} - Q^m \\ \Delta Q^{n-1} = Q^n - Q^{n-1} \\ A = \frac{\partial E}{\partial Q}, B = \frac{\partial F}{\partial Q}, C = \frac{\partial G}{\partial Q} \\ R(Q^m) = RHS^m_{GCL} + RHS^m \end{gathered} \quad (3.16)$$

If ϕ is 0, the discretization is 1st order in time, and if ϕ is 0.5, it becomes 2nd order accurate in time. The superscript *m* indicates the sub-iteration level. Use of Newton sub-iterations improves convergence and stability at the expense of computer time, because of the need to re-compute the residual on the right hand side once every iteration.

3.5 Embedded Grid

The artificial viscosity associated with the coarse grid at the outer boundary is one of the primary causes of dissipation of the tip vortex strength. The artificial viscosity is of the order of Δ^n, where Δ is the grid spacing and n is determined by the order of spatial accuracy. To reduce artificial diffusion, the grid has to be fine enough in the region the vortex travels through. For a structured grid, global refinement may increase the grid

points to several millions. In the present study, local refinement was used. This was achieved with an embedded grid.

The embedded grid, shown in Figure 3.4, is nested inside global grid. It is placed only in regions where high gradients are expected. It is treated as another computational block, and the property,q_p, at the boundary points are obtained using linear interpolation from nearby global grid points as illustrated in Figure 3.5. Here, *a*, *b*, *c* and *d* are nearby global grid points forming a tetrahedron surrounding the boundary point, *p*. The surrounding global grid points are found in the beginning of the computation such that the factors $\alpha, \beta,$ and γ satisfy following conditions.

$$\text{2-D: } \overrightarrow{ap} = \alpha\left(\overrightarrow{ab}\right) + \beta(\overrightarrow{ac}), \qquad \alpha + \beta \leq 1, \qquad \text{and } \alpha, \beta \geq 0 \tag{3.17}$$

$$\text{3-D: } \overrightarrow{ap} = \alpha\left(\overrightarrow{ab}\right) + \beta(\overrightarrow{ac}) + \gamma\left(\overrightarrow{ad}\right), \ \alpha + \beta + \gamma \leq 1, \text{and } \alpha, \beta, \gamma \geq 0 \tag{3.18}$$

After every time step, the properties of the nodes within the global grid where the embedded grid are placed are updated using the properties on the embedded grid block. The embedded grid is re-generated every time step by refining the global grid after the global grid is translated in space (to account for blade rotation) and deformed (to account for elastic deformations, blade flapping, and pitching). Figure 3.4 illustrates a level 1 embedded grid.

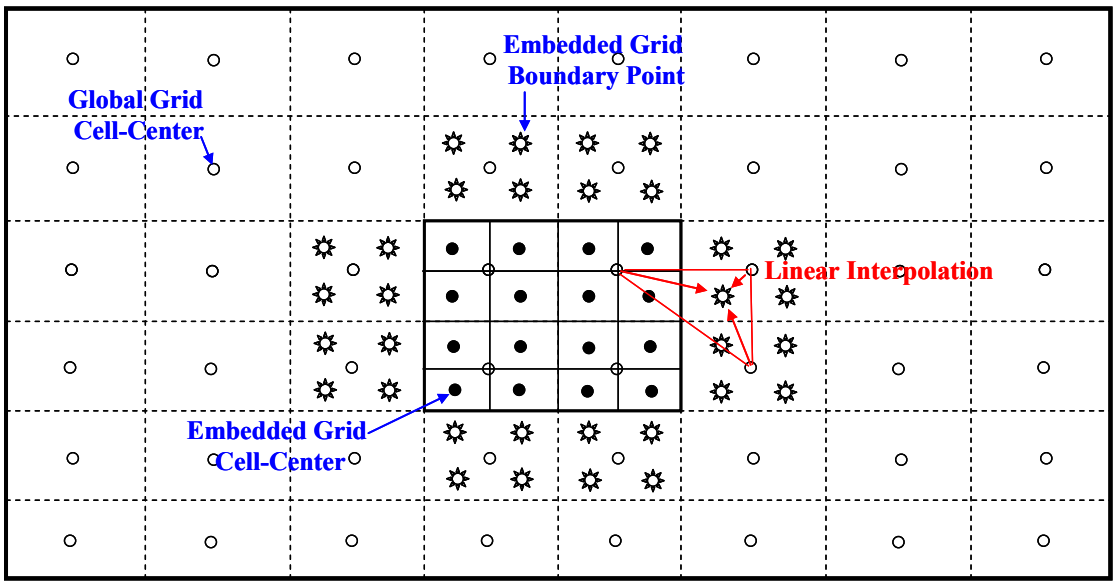

Figure 3.4 Illustration of an embedded grid

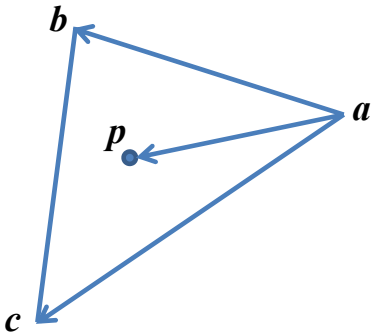

$$q_p = q_a + \alpha(q_b - q_a) + \beta(q_c - q_a)$$

(a) 2-Dimensional grid

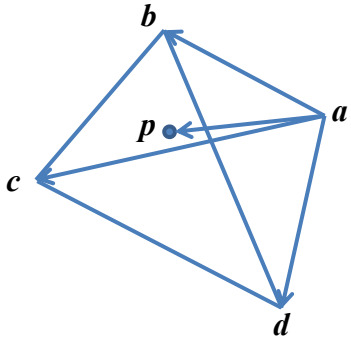

$$q_p = q_a + \alpha(q_b - q_a) + \beta(q_c - q_a) + \gamma(q_d - q_a)$$

(b) 3-Dimensional grid

Figure 3.5 Linear interpolation

CHAPTER 4

VALIDATION AND FEASIBILITY STUDIES

Several simulations have been done validate the ability of the code to capture key flow features related to rotor and Gurney flap. The selected cases include 2-D airfoil under attached and stalled flows, 2-D airfoil undergoing dynamic stall, 2-D flow over hump, 3-D turbine vane, 3-D finite wing, and the HART-II data. A Gurney flap-equipped airfoil has also been simulated and compared with experimental data. Validity of the infinitely thin Gurney flap model is studied as well. Reference [55] includes additional validation case for turbulence models.

4.1 Steady 2-D Airfoil

4.1.1 RAE 2822 Airfoil

The RAE 2822 airfoil from the AGARD test data base [85] was chosen for transonic flow regime validation of the Navier-Stokes solver, GENCAS. This test case is commonly accepted as a standard CFD code validation case. The freestream Mach number is 0.729, at a Reynolds number of 6.5 million, and an angle of attack 2.31 degree. Figure 4.1-a) shows the baseline C-type grid and Figure 4.1-b) shows an embedded grid placed on the upper surface. The embedded grid was introduced for enhanced resolution of the flow acceleration along suction side and a crisp resolution of the shock wave. The surface C_p compared in Figure 4.2 shows excellent agreement with the measured data on the lower surface. The leading edge suction peak and the shock wave formed on the upper surface due to transonic flow are also well captured for both turbulence models.

Both turbulence models predicted the shock wave location slightly ahead of the measured data, with the KES model predicting the shock wave earlier than the S-A model. With an embedded grid, better resolution along the suction surface led to the prediction of the shock wave location closer to the measured data.

4.1.2 NACA 0015 Airfoil including Stall

The load prediction capability of the code has been validated for a static airfoil covering wide range of angle of attack including stall regime. The computed loads of NACA0015 airfoil were compared with the measured data by Piziali [86]. An O-type grid was used (Figure 4.3). Figure 4.4 shows the variation of static loads as a function of angle of attack. The Mach and Reynolds number for this case are 0.29 and 1.955 million, respectively.

Several turbulence models have been tested. These include k-ω SST, KES, and a hybrid RANS-KES (HRKES) [70] model. All three turbulence models showed good correlation with measured data for static airload characteristics.

4.1.3 NACA 0015 Airfoil with Gurney Flap

Prior to the study of Gurney flaps in a 3-D case, a number of 2-D simulations were done to assess the computational grid effects and the turbulence model on airloads. Since the deployment of Gurney flap normal to the chord line causes flow separation behind the flap, the numerical method should be able to capture such phenomena, and predict the airloads properly.

Troolin et al. [17] have investigated the effect of Gurney flap via wind tunnel test. The configuration tested is a NACA 0015 airfoil equipped with several heights of Gurney flap at the trailing edge. An angle of attack sweep was performed and the lift coefficients

were reported. The flap height of 2% of the chord length was chosen for the present validation study. The Mach number and Reynolds number were 0.05 and 2.1×10^5, respectively. The O-type grid with zoomed trailing edge, where the Gurney flap is installed, is shown in Figure 4.5. The lift coefficient, compared with the experimental data in Figure 4.6, shows very good correlation. Comparing with the previously studied lift data in Figure 4.4, it is apparent that the Gurney flap increases lift force over the baseline clean airfoil and this effect was well predicted with current methodology.

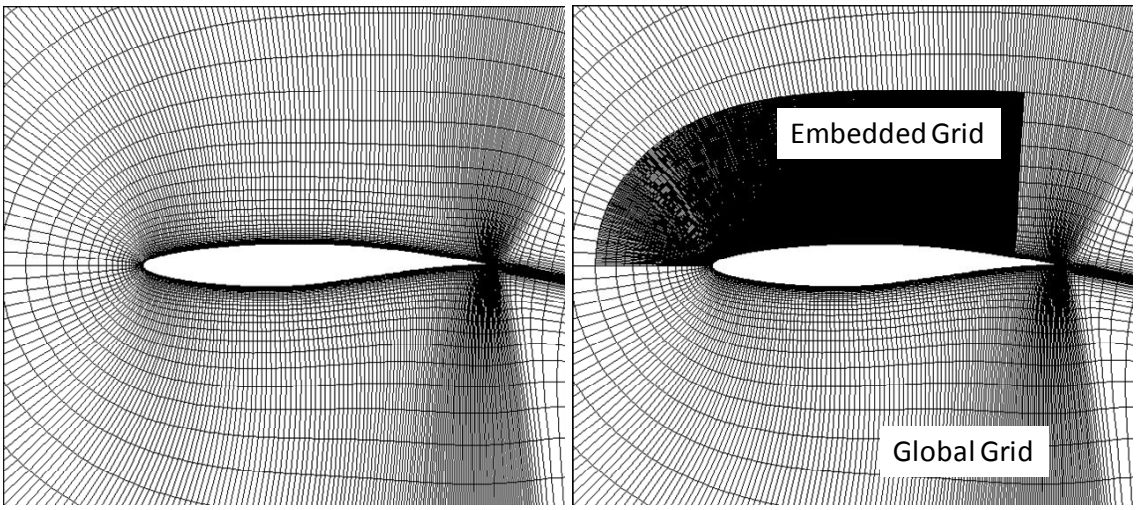

a) Baseline grid [369×65] b) With embedded grid[841×89]

Figure 4.1 RAE 2822 grid

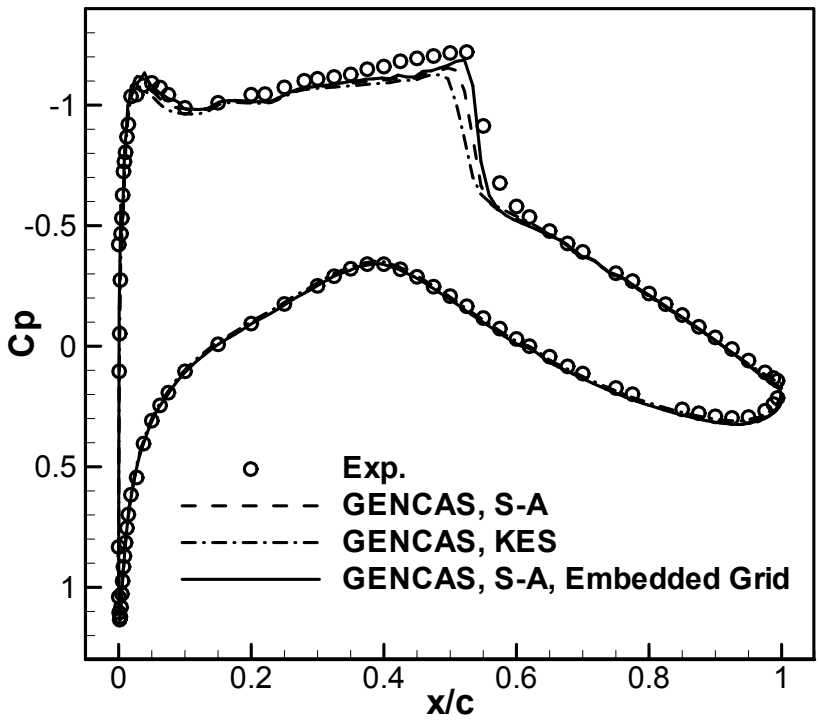

Figure 4.2 Comparison of surface C_p: RAE 2822

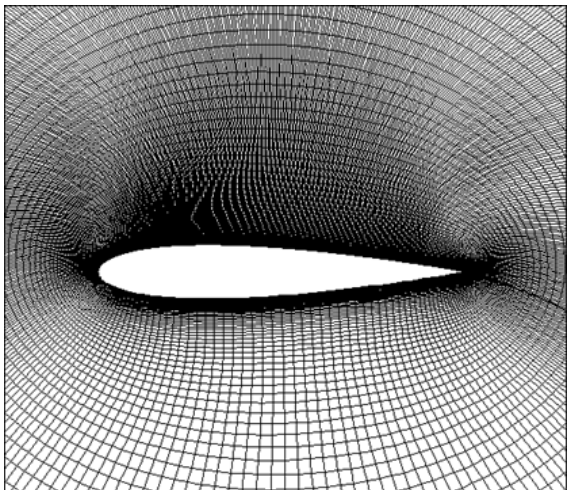

Figure 4.3 NACA 0015 grid [499×137]

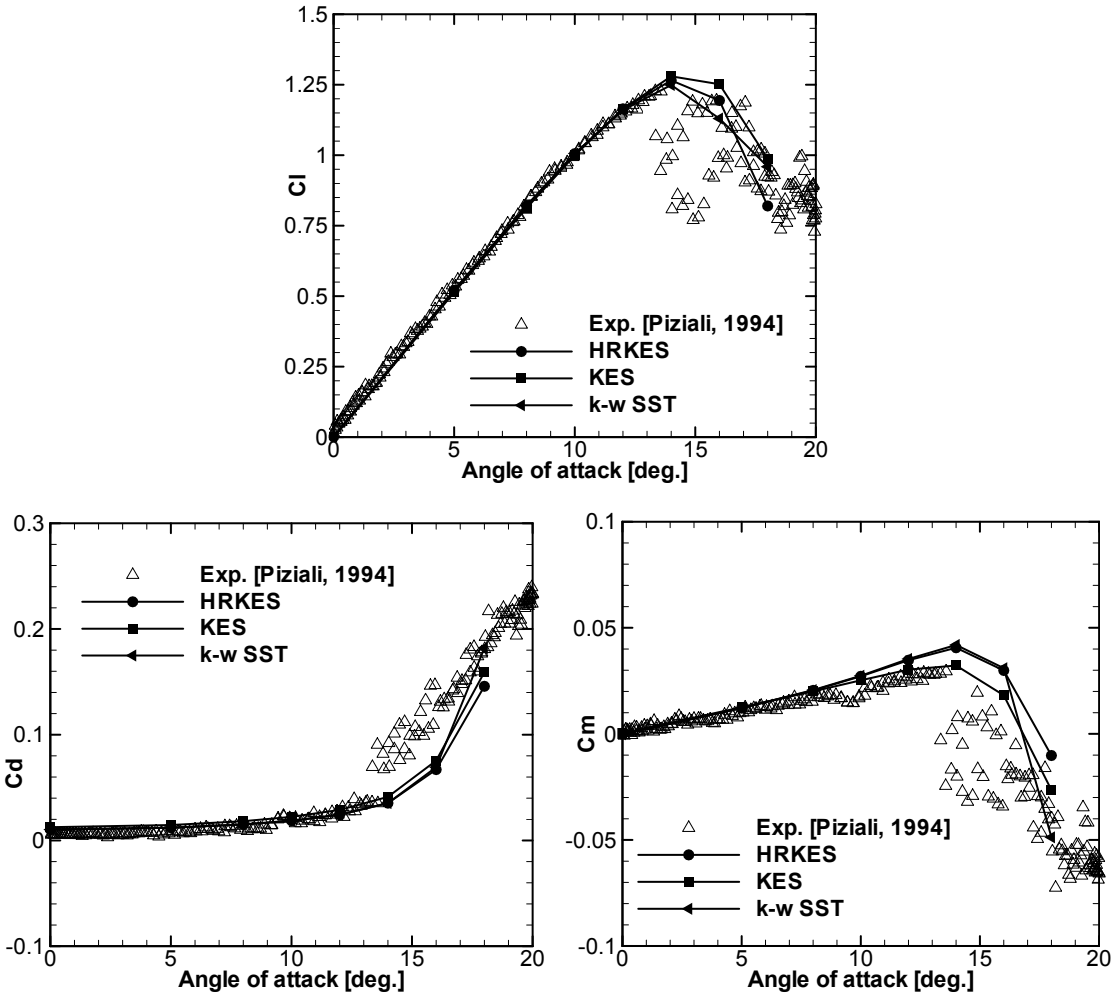

Figure 4.4 Comparison of loads and moment: NACA 0015

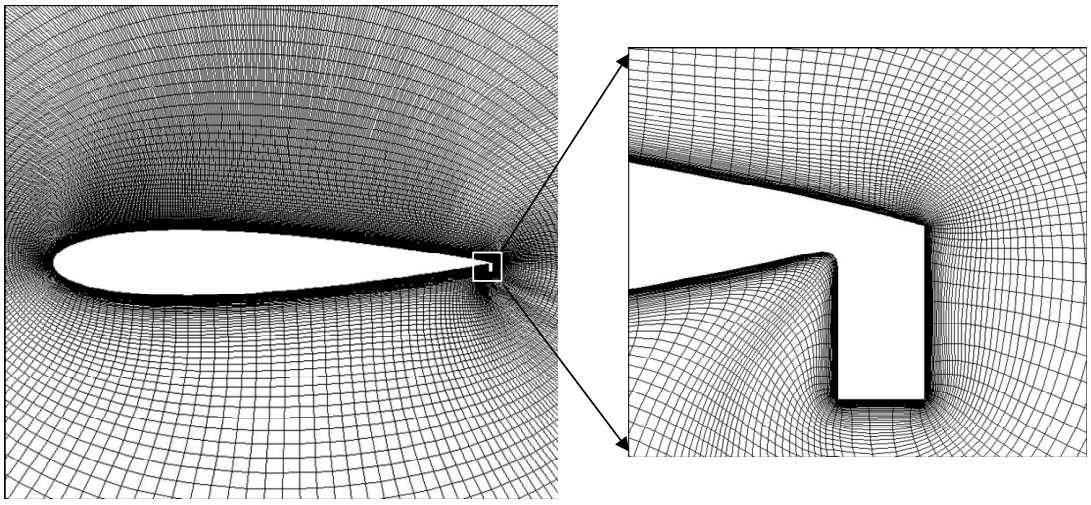

Figure 4.5 Grid system for NACA 0015 with 0.02c GF [524×134]

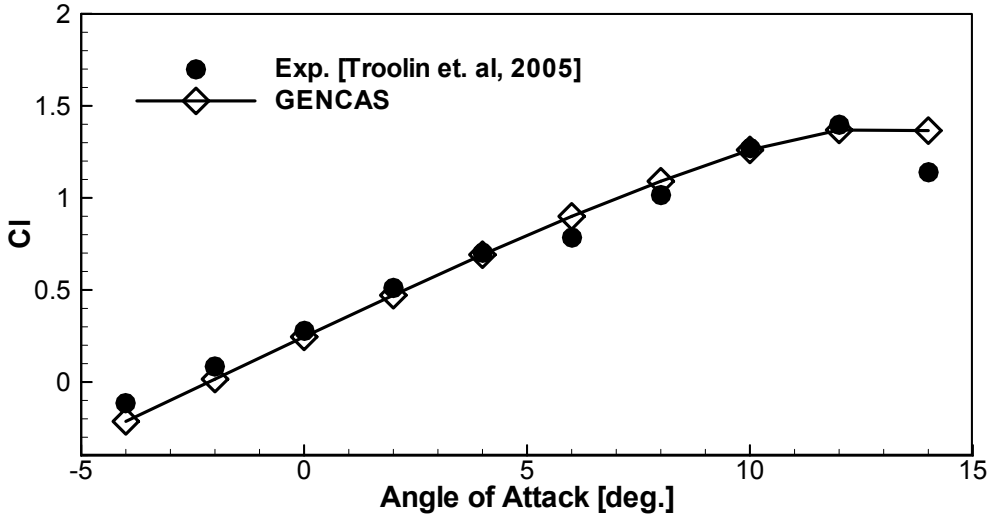

Figure 4.6 Comparison of lift coefficient: NACA 0015 with GF

4.2 Airfoil undergoing Dynamic Stall

4.2.1 NACA 0015 Airfoil

An oscillating NACA 0015 airfoil was simulated and compared with measured data. The flow condition was same with the static stall case addressed above, i.e. M=0.29, and Re=1.955 million. The reduced frequency, k, was 0.096. The pitch angle was varied as follows:

$$\alpha = 15.04^{\circ} + 4.16^{\circ} \sin\left(2kM_{\infty}t + \frac{3}{2}\pi\right) \tag{4.1}$$

Approximately 113000 time steps took place per one cycle. The grid system shown in Figure 4.3 was used. Figure 4.7 shows the resultant loads and moment compared to the measured data by Piziali [86]. Although the peak values of drag and moment coefficients were under-predicted, the predicted result shows overall good agreement with the measured data.

Turbulence models play a more significant role in the prediction of stall onset, leading edge vortex development, its convection of the upper surface, and its ultimate shedding into the wake. Among the models tested, the KES model was found to best capture these events.

4.2.2 NACA 0012 Airfoil

Calculations have also been done for an oscillating NACA0012 airfoil using KES and HRKES turbulence models. The C-type grid system is shown in Figure 4.8, and the predicted loads are compared with experimental data by McAlister et al. [87] in Figure 4.9. The flow Mach number was 0.28 and Reynolds number was 3.52 million. The reduced frequency is 0.1. The angle attack of the airfoil varies with time as:

$$\alpha = 14.84^{\circ} + 9.87^{\circ} \sin\left(2kM_{\infty}t + \frac{3}{2}\pi\right) \tag{4.2}$$

Lift and moment stall occur in the computation at higher angles of attack compared to experiments. The maximum lift, drag and moment were over-predicted. However, the overall hysteresis loop is in good agreement.

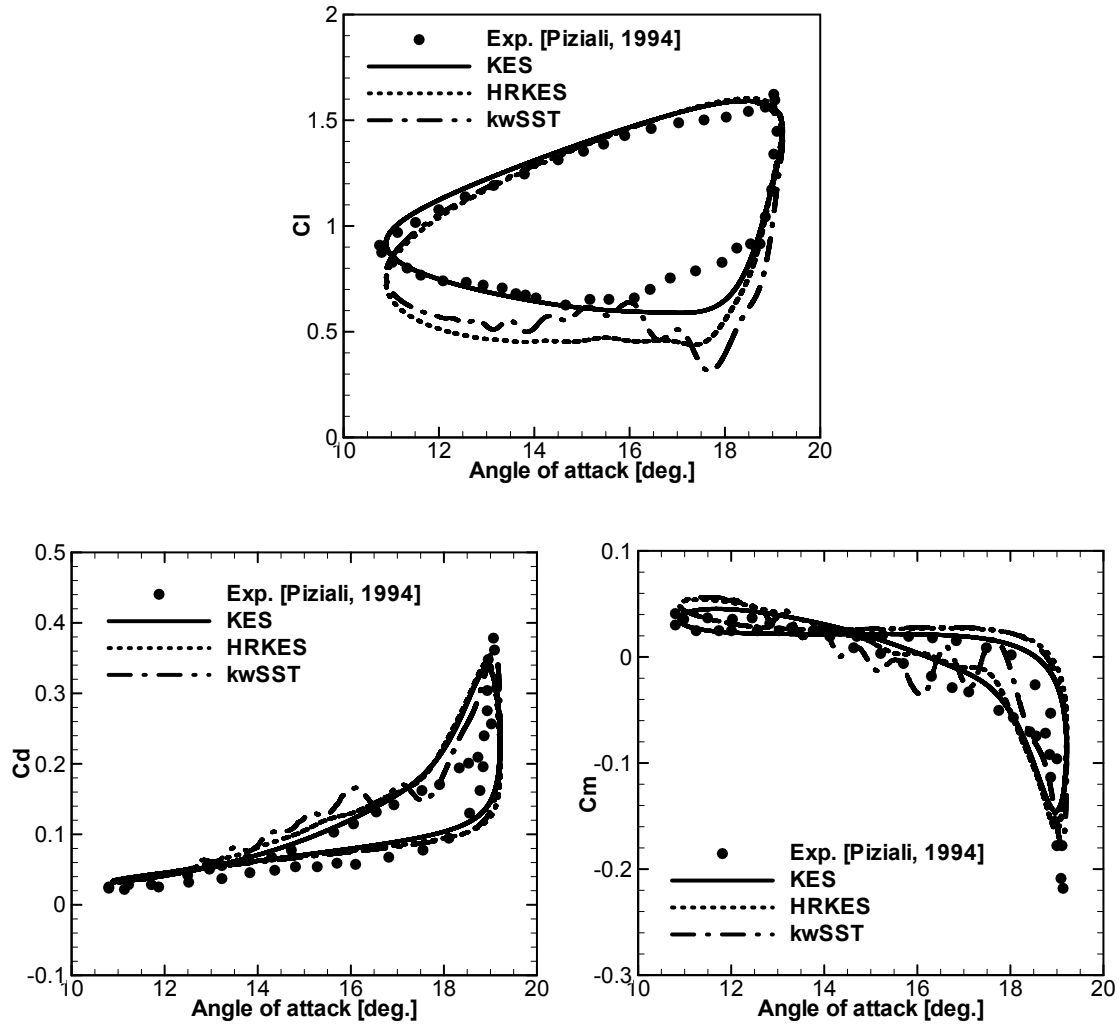

Figure 4.7 Comparison of loads and moment in dynamic stall: NACA 0015

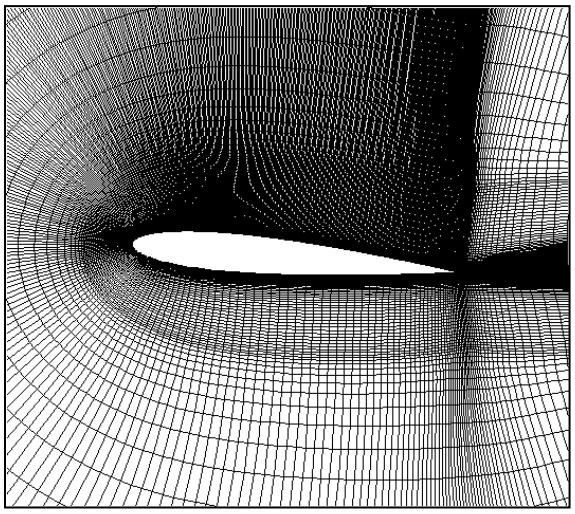

Figure 4.8 NACA 0012 grid [547×105]

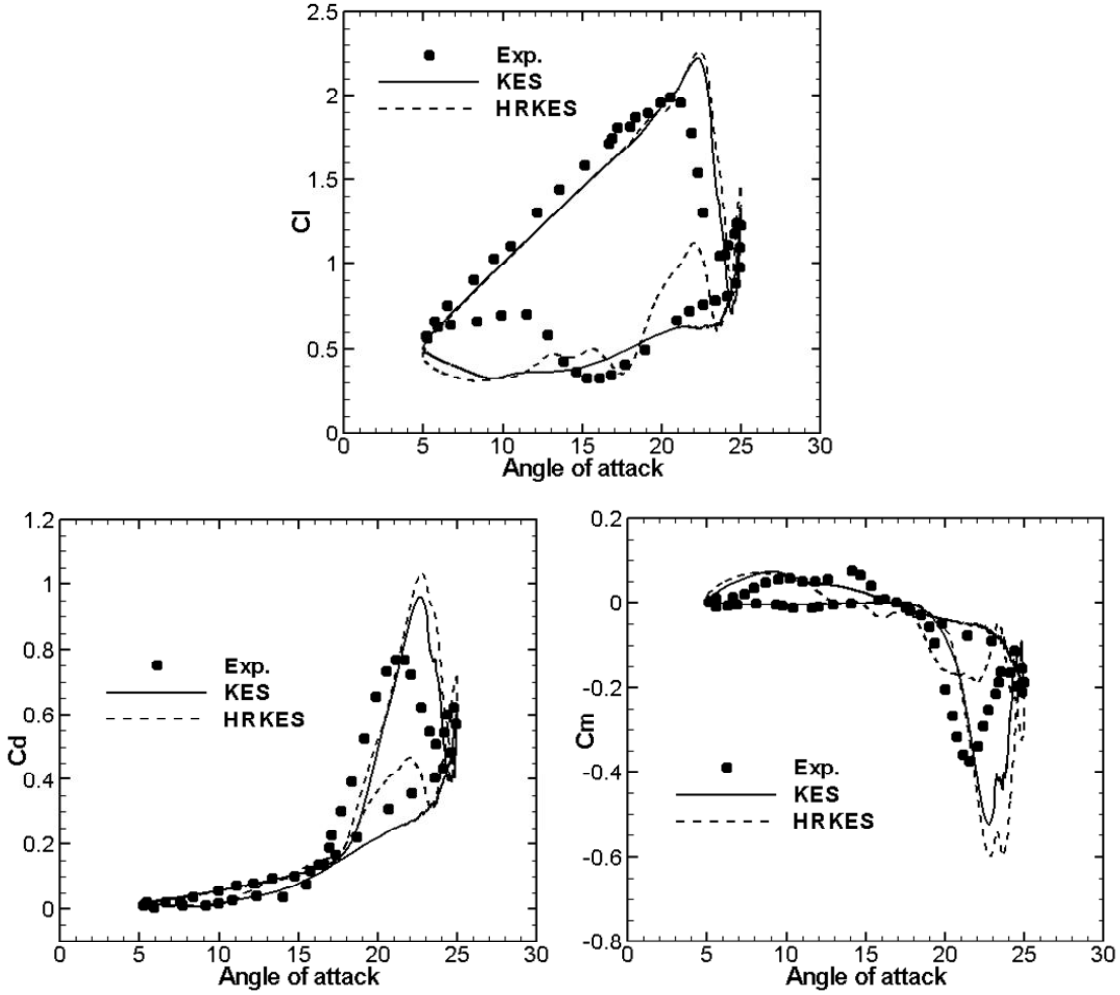

Figure 4.9 Comparison of loads and moment in dynamic stall: NACA 0012

4.3 Flow over Hump

A wall mounted 2-D hump geometry (Figure 4.10) tested by Greenblatt et al. [88] has been simulated with the current method and compared with the experimental data.

The flow feature includes separation due to adverse pressure gradient at the short concave section in the aft part of the body. In the experiment, a thin slot was placed immediately upstream of the concave surface for active flow control by means of suction or blowing. However, the current validation case corresponds to a steady flow condition. Slip-wall boundary conditions were applied at the bottom of block 4. The upper surfaces of block 1 and 2 were modeled with a slip-wall boundary condition to account for wind tunnel blockage effect. Block 1 extends forward to -6.39c to model the developed boundary layer in actual experiment. The freestream Mach number was 0.1, Reynolds number based on the hump chord length was 9.36×10^5. The pressure and temperature at the inlet was set to 101325 pa and 298 K, and the back pressure at the exit was set to 101271.3 pa. Additional details of the test are available in references [88,89].

Predicted surface C_P and streamlines using SA and KES turbulence models are compared with measured data in Figure 4.11 and Figure 4.12. The peak pressure drop at the top of the hump and the flow reattachment point was better predicted with SA model, while the onset of separation and following delay of pressure recovery was slightly better with KES model. Overall, simulations with both turbulence models show very good correlation with measured data.

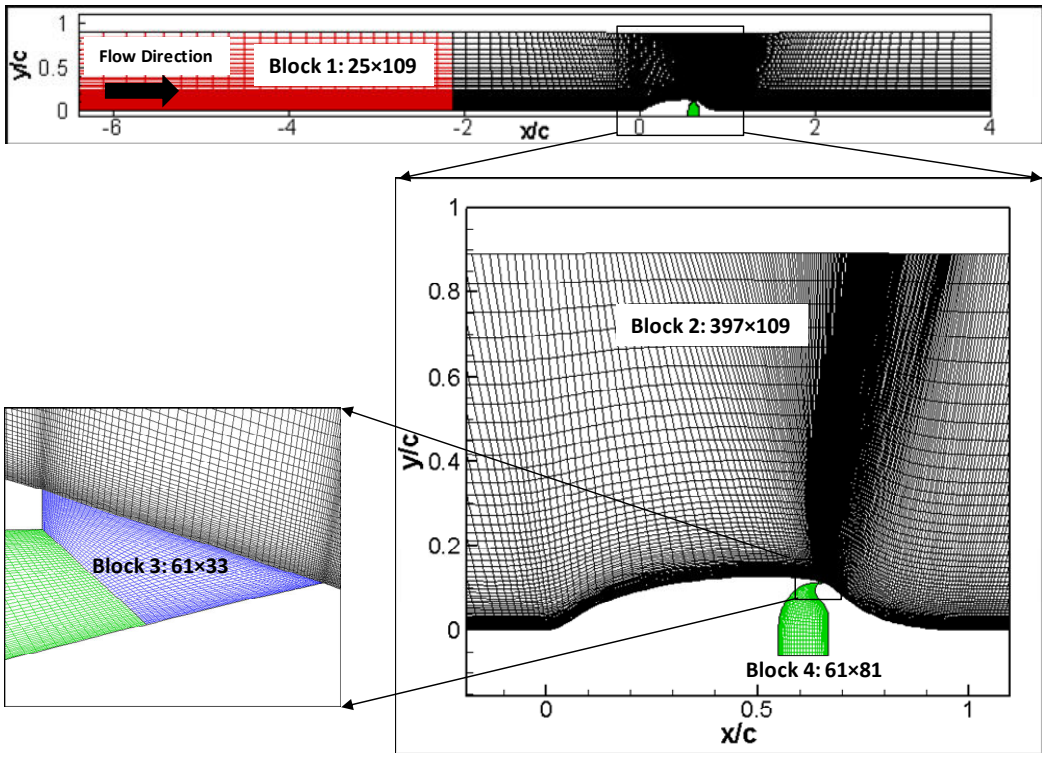

Figure 4.10 2-D hump geometry and grid system

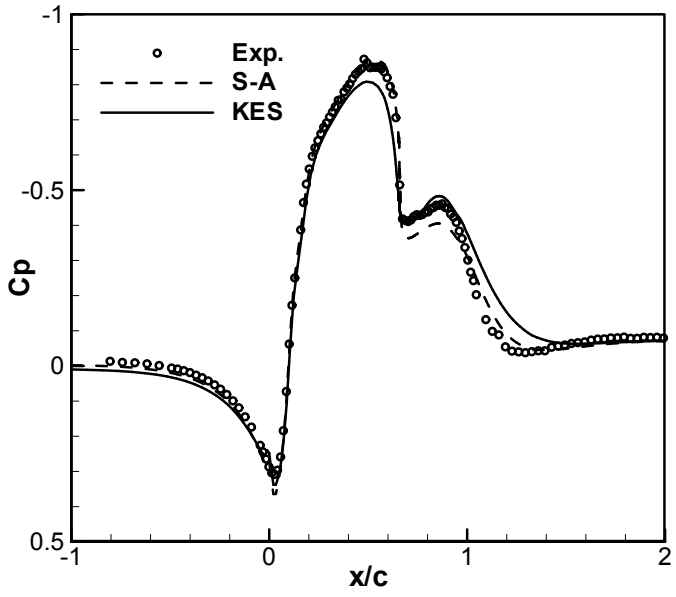

Figure 4.11 Surface C_P comparison

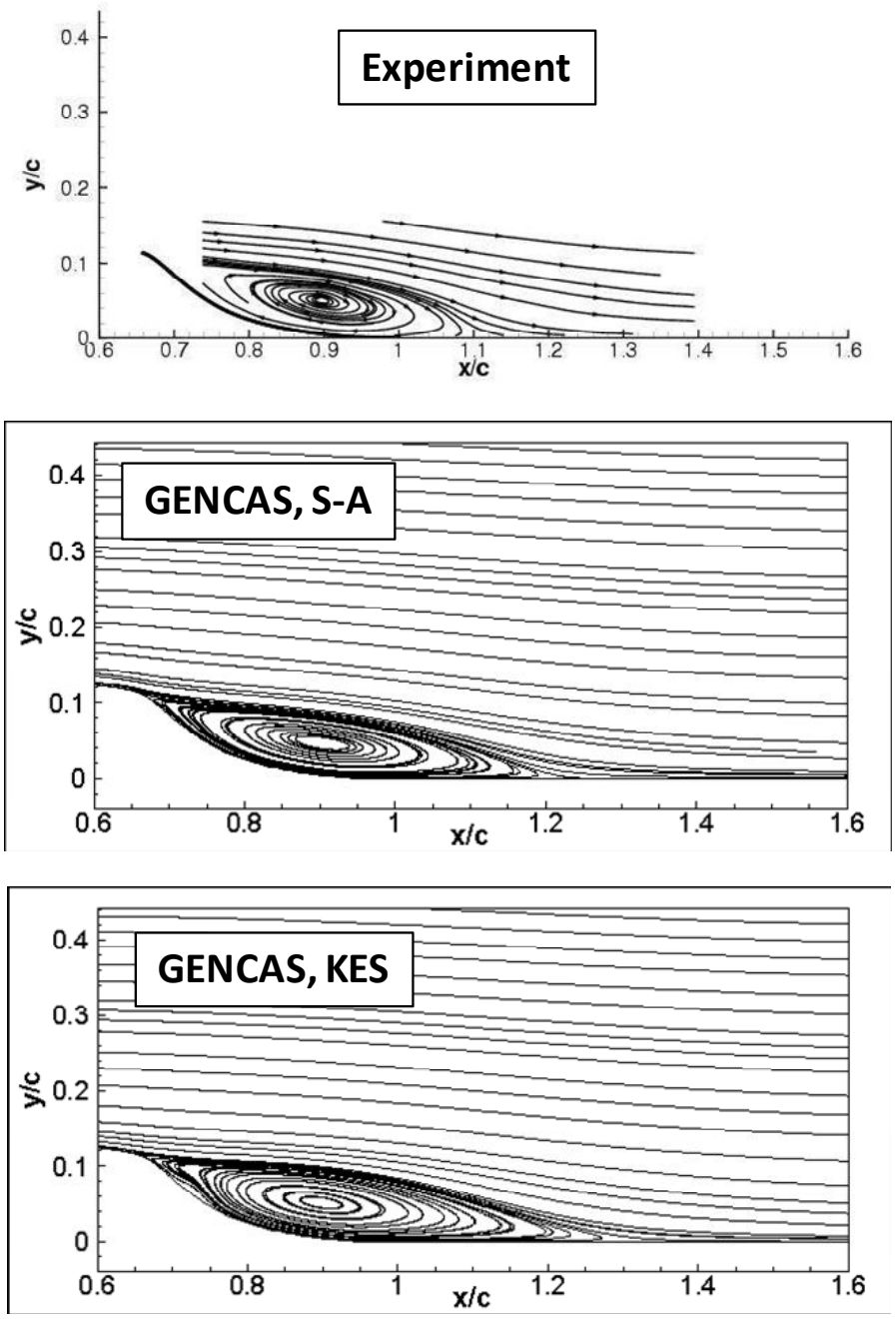

Figure 4.12 Streamline comparison with experiment [89]

4.4 Goldman Turbine Vane

An annular turbine stator developed and tested at NASA Glenn Research Center by Goldman et al. [90] has been selected as a validation case. The stator has 36 vanes. The vanes have an axial chord length of 0.03823 m, a span (between the hub and the tip) of 0.0381 m, a 0.508 m tip diameter, and a hub-to-tip radius ratio of 0.85. The inlet Mach number is 0.211. It has a design pressure ratio of 0.6705, exit Mach number of 0.665 and Reynolds number based on the axial chord of 173,000.

A single vane is modeled with periodic boundary conditions at the upper and lower grid surfaces. Figure 4.13 shows the C-type grid used in this study. A characteristic based inflow/outflow condition is applied at the inlet, and the design pressure ratio is applied at the exit surface. No-slip wall boundary conditions are applied at the vane surface, hub and tip side walls.

Computed pressure ratios along the chord-wise vane surface at the mid-span are compared with measured data. Figure 4.14 shows good agreement of the predicted values. The one equation S-A turbulence model did not do as well at the separated region near the upper surface trailing edge. However, the S-A DES model was as good as two equation models (κ-ω and κ-ω SST).

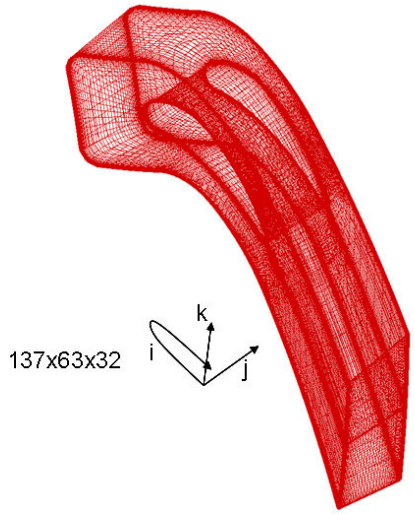

Figure 4.13 C-type grid for Goldman turbine vane

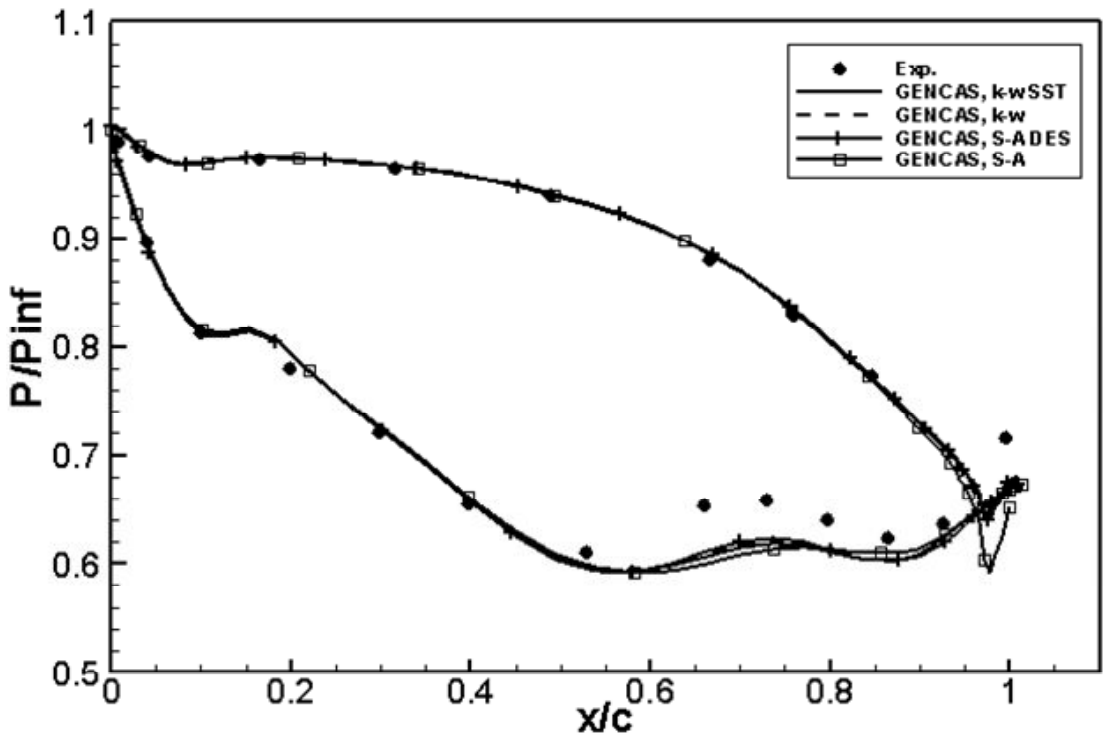

Figure 4.14 Pressure distributions along Mid-span

4.5 ONERA M6 Wing

A half-wing model ONERA-M6 reported in AGARD test data base [91] is a classical three dimensional validation case suitable for CFD code assessment. The model is a swept back wing with an aspect ratio of 3.8 and taper ratio of 0.562. The mean aerodynamic chord length is 0.64607m and the semi-span is 1.1963m. The wing has been tested in the ONERA S2MA wind tunnel at transonic Mach numbers and the surface pressure distributions were obtained at several span sections. Figure 4.15 shows the single block grid system. The selected case was tested at Mach number of 0.84 with angle of attack of 3.06 degrees. The chord length based Reynolds number is 11.72 million. The λ shape shock wave on the upper surface was well captured with both S-A and KES turbulence models (Figure 4.16). The C_p distributions showed in Figure 4.17 at seven span sections show good correlation with test data for both the S-A and KES turbulence models. The leading edge suction and following shock wave locations were well predicted.

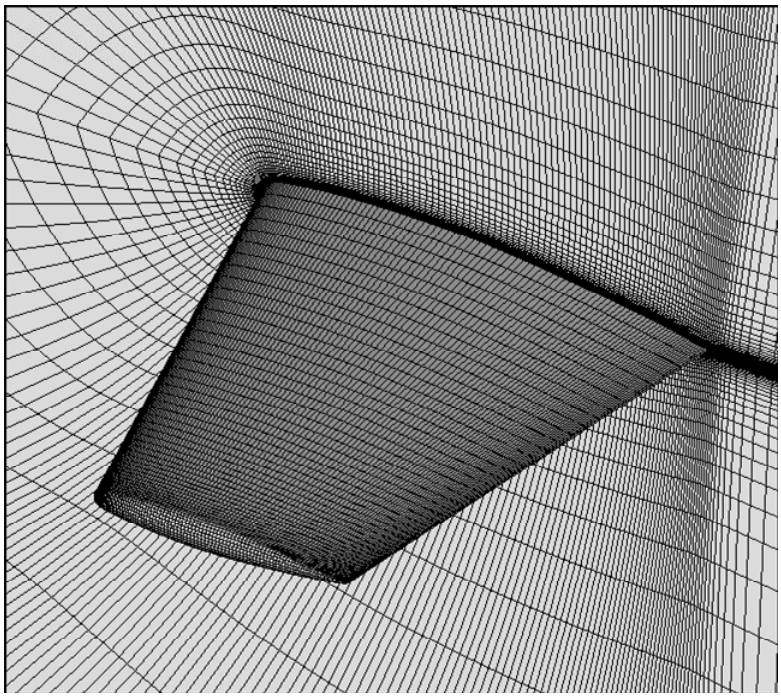

Figure 4.15 ONERA-M6 wing grid [289×65×49]

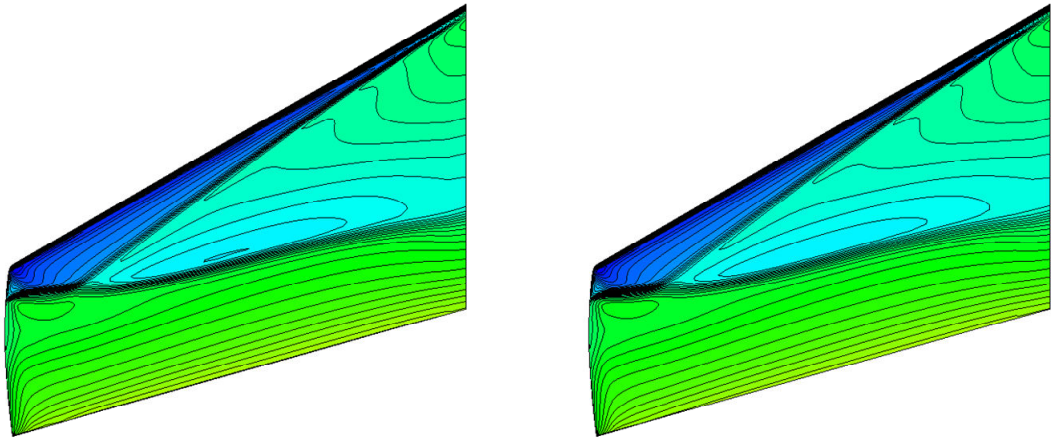

a) S-A model b) KES model

Figure 4.16 Surface pressure contour

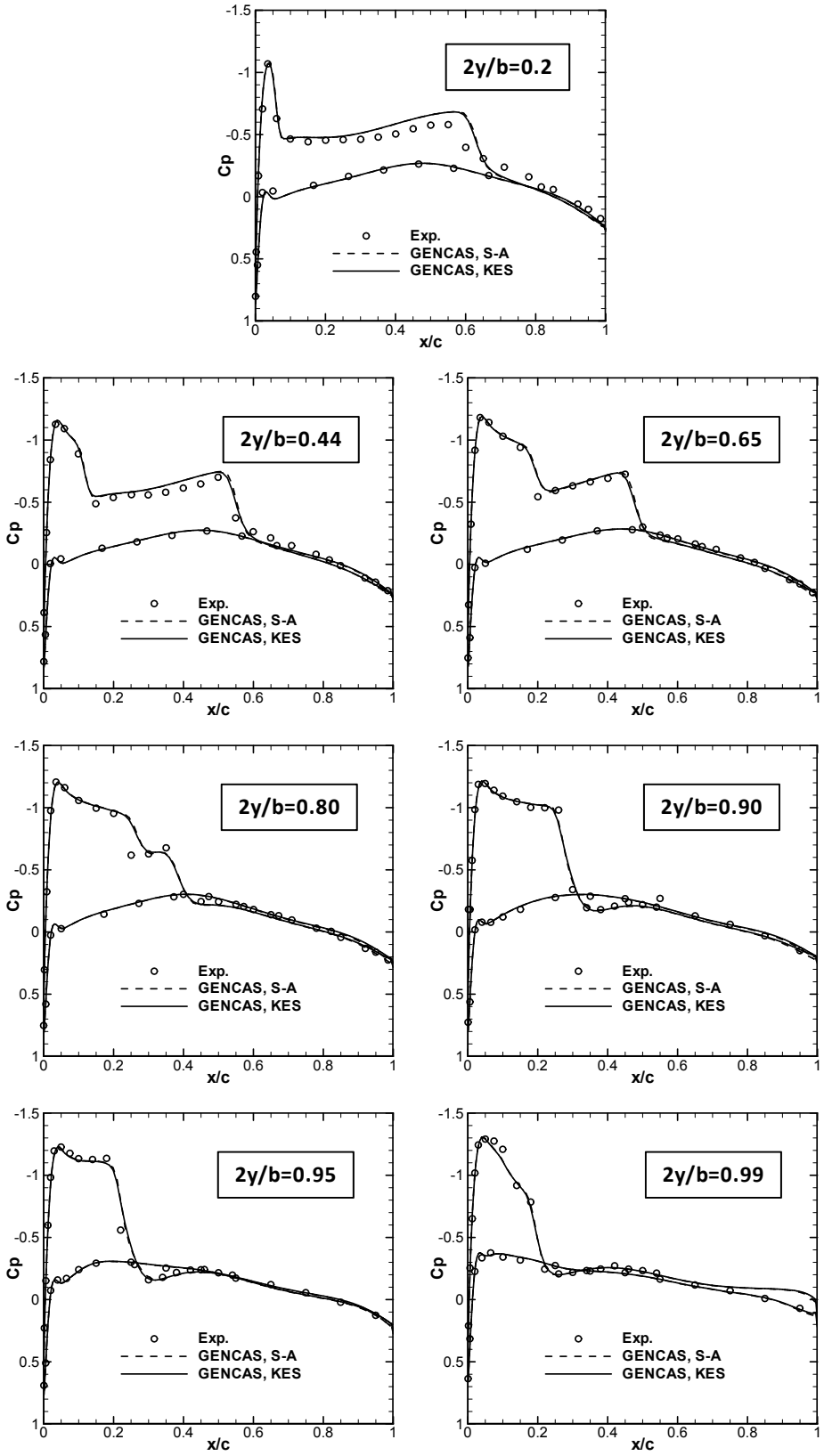

Figure 4.17 Surface C_P distribution

4.6 HART-II: 3-D Rotor with CFD/CSD Coupling Analysis

The methodology used in this study has also been validated for the HART-II (Higher harmonic control Aeroacoustics Rotor Test) for which experimental data is available [92,93]. The HART program is a common project of US Army AFDD, NASA Langley, DLR, ONERA and DNW to investigate physics of HHC on vibration reduction/increase and noise emission.

The rotor is a 40% scaled replica of the four-bladed hingeless Bo-105 main rotor. The rotor radius is 2m, chord length is 0.12m, and has rectangular blade with NACA23012 airfoil and 5.4mm trailing edge tap of 0.8mm thickness. The rotor has an -8 degree of linear twist, 2.5 degree of pre-cone angle, and a solidity of 0.077. The rotor rotational speed was 1040 rpm (corresponding to hover tip Mach number 0.638), and nominal thrust coefficient was 0.00457.

The available test data include the baseline descent case, as well as higher harmonic control studies for minimum noise and minimum vibration. The baseline descent mode flight condition at advance ratio 0.15 without higher harmonic control was chosen for comparison. The wind-tunnel corrected shaft angle was 4.5 degree backward tilt.

An elastic blade motion pre-obtained by Lim et al. [94] using OVERFLOW2-CAMRAD-II coupling analysis was used to assess the ability to model BVI phenomena of the enhanced method compared to the baseline hybrid method. The baseline hybrid method serves as the reference. It is 3^{rd} order in space (Roe's FDS scheme with MUSCL), 1^{st} order in time with LUSGS scheme, with no GCL terms, and a conventional metric and Jacobian computation. KES turbulence model was used.

Finally, GENCAS-DYMORE coupling analysis was carried out to model the elastic blade deformation and air loads variation simultaneously, and to validate the current methodology.

4.6.1 Near-wall Grid Independence Study

Sensitivity of the solution to near-wall grid density was studied using two sets of grid system. Figure 4.18 shows the baseline C-type grid system with 131×65×45 grid points (0.383 Million) in chord wise, span wise, and surface normal direction. The fine grid has doubled chord wise and surface normal direction grid points (261×65×90 = 1.527 Million), thus the computational time with the fine grid is about four times more than the baseline grid. The baseline hybrid method described earlier was utilized in this study. A characteristic based inflow/outflow boundary condition combined with vortex induced velocity is applied on all the outer boundary surfaces, and no-slip conditions are applied on the blade surface. Figure 4.19 compares normal force predicted by the two sets of grid systems at three radial locations. It is seen that there is no essential difference in the prediction. Furthermore, the predicted thrust coefficient from the baseline grid (4.33×10^{-3}) has a difference of less than 1% compared to the fine grid prediction (4.36×10^{-3}). Therefore, the baseline grid system was used in modeling HART-II blade in the rest of this study, unless otherwise specified.

4.6.2 Time Step Convergence Study

A time step convergence study has been performed to determine time steps needed to obtain time step independent solution. Four different time steps with baseline hybrid method were tested at the baseline descent mode flight condition. The sectional normal forces at three radial locations are compared in Figure 4.20. The normal force of

all four time steps at 0.65 and 0.87R locations seems to be nearly identical. However, solutions with a 0.1 degree time step deviates from other solutions with smaller time steps at fourth quadrant near the tip, r/R=0.99. Based on this study, a time step of 0.05 degree per step was used in the rest of computations, unless otherwise specified.

4.6.3 The Effect of Higher Order Metric and Jacobian, and GCL

Figure 4.21 compares C_nM^2 of baseline hybrid method with measured data. Results with the GCL case are also shown. First, it is observed that the baseline hybrid method predicts low frequency load reasonably, but it completely misses the high frequency BVI load variations in the first and fourth quadrants. Even after the metric and Jacobian computation is refined, and the GCL term is included, the BVI phenomena were not captured. This indicates that the errors in volume and surface area computation are not the significant sources of the vortex dissipation in this particular instance. However, without GCL term in the governing equation, a non-physical mass accumulation or loss was observed at the outer surface due to large cell deformation. Figure 4.22 shows density contours plot obtained after analysis without any blade geometry, but with the grid deformation. In the absence of a body that disturbs the flow field, the flow properties should be equal to freestream values within machine round-off errors. The density variation shown in Figure 4.22-a is well above what is anticipated due to machine round-off. This non-physical phenomenon was eliminated once GCL is applied.

4.6.4 The Effect of Spatial and Time Accuracy

Figure 4.23 shows a comparison of normal force history for the 3rd order and 7th order scheme against test data. On the grid shown in Figure 4.18, the use of the 7th order scheme did not improve BVI prediction significantly. While spatially high order schemes

do have excellent accuracy and superior dissipation characteristics on uniform grids and fine curvilinear grids, these benefits unfortunately do not always carry over to highly stretched or distorted grids. The magnitude of the truncation errors and numerical viscosity are of orderΔ^n, where n=1,3,5,7 for first through seventh order WENO schemes. On highly stretched grids, Δ is large away from the body and higher order schemes may have increased dissipation. It was observed that the 7th order scheme was not stable with a conventional metric and Jacobian computation, especially near the blade tip region where the grid is highly skewed. It appears that the inaccuracy of the conventional metric and Jacobian computation is large enough to destabilize the higher order scheme on highly skewed grids. For this reason, the refined metric and grid Jacobian computations, along with GCL, were used in all the subsequent HART-II validation studies.

The effect of time accuracy on BVI prediction was minor when an azimuthal time step of 0.05 degree is used, as shown in Figure 4.24 . The 2nd order time scheme with Newton sub-iteration would allow larger time steps with added robustness and better convergence. However, since the computational time increases substantially with sub-iterations, and since the 2nd order temporal scheme does not improve BVI prediction significantly, the subsequent HART-II validation studies used a first order in time scheme without sub-iterations.

4.6.5 The Effect of Finer Grid using an Embedded Grid

Figure 4.25 shows the embedded grid placed upstream of the blade in the region that captures entering wakes. The embedded grid was generated with a two-level split of the global grid, thus 64 (4×4×4) cells are located inside one global cell. Total 0.895M

cells are placed in the computational domain including 0.383M cells from the baseline global grid and 0.512M cells from embedded grid. The computation was done using 3rd order MUSCL and 1st order time accuracy with GCL, and with refined metric and Jacobian computations.

The embedded grid results shown on Figure 4.26 more clearly show BVI encounters at the first and fourth quadrant. This confirms that the coarseness of the grid and the high attendant artificial viscosity is a significant contributor to tip vortex dissipation and the inability of the baseline grid to resolve BVI events. For the completeness of the study, the spatially higher order scheme was re-examined with the embedded grid. In the previous spatial accuracy study with the baseline coarse grid, the BVI prediction capability was not improved with 7^{th} order WENO scheme (Figure 4.23). However, Figure 4.27 shows that the 7^{th} order WENO scheme predicted higher BVI peak loads compared to the 3^{rd} order MUSCL scheme. Thus, it was confirmed that the spatially higher order scheme improves BVI prediction capability with fine grid.

Contour plots of sectional loads, or even local pressures at representative locations on the blade may be used to visually identify both the location and intensity of BVI events. In the HART-II experiment, leading edge pressure difference was measured and plotted over the disk to identify the BVI. The high pass filtered measured pressure differential is shown in Figure 4.28. For comparison, computed normal force differentials from all the studies described above are also shown. The baseline grid simulations do not pick up the distinct BVI patterns seen in experiments. On the other hand, simulations on the embedded grid show clear BVI patterns in the first quadrant as in the measured data.

However, the BVI events in the fourth quadrant were only weakly captured compared to the experiment.

The conservation of tip vortices in the embedded grid is more clearly observed from Q value [95] iso-surfaces in Figure 4.29. Here Q is defined as a balance between vorticity and strain rate. Thus boundary layer regions, where both vorticity and strain rate are high, are excluded and tip vortices are identified. It is clear that the baseline grid does not conserve the tip vortex for long once it is introduced in the computational domain. In particular, when the reference blade is located at the 0 degree azimuthal position, the entering tip vortices were quickly and artificially dissipated in the baseline grid. The embedded grid conserves the vortex strength relatively better, leading to an improved capture of BVI events in the first quadrant. A similar improvement in the capture of tip vortices and associated BVI events were observed as well on the retreating side, with embedded grids.

4.6.6 CFD Validation with Measured Blade Motion

In all the computations shown above, a motion file for the blade (which includes cyclic pitch and flap, along with the torsional and bending deformations) obtained from OVERFLOW2 loosely coupled to a comprehensive analysis (CAMRAD-II) was used. The cyclic pitch and collective pitch were from the internal trim done in the above CFD-CSD approach. It is observed in all the results presented earlier that the mean value of the normal force is under-predicted and the loads over the fourth quadrant showed large deviation especially around $\psi = 340$ degree.

To determine how much of these differences are attributable to the blade motion and the trim settings, a prescribed motion obtained from measured blade deflection data

[96] was used. The deflection data of the reference (instrumented) blade was used in this study. The same algorithm options (first order in time, 3rd order MUSCL, GCL, improved cell volume and cell area calculations) were used. An embedded grid was employed. The mode shapes of the blade were pre-computed and the blade motion is defined such that the reconstructed data matches the measured deflection data in a least square sense. Up to 3 modes were needed for flap, and 2 modes were used for lead-lag and torsion.

Figure 4.30 indicates that the mean value of the load is shifted close to the experimental data compared to earlier results using prescribed motions (e.g. Figure 4.26). The low frequency load prediction at the fourth quadrant has been improved and correlates better against measured data. However, some of BVI events and low frequency peak load are not predicted well, and phase differences between computed and measured air loads exist. A main contributor to these BVI phase and strength deviations is the inaccurate free wake trajectory as seen in Figure 4.31 and Figure 4.32. From the top view, the wake position at the advancing side, especially over the second quadrant, showed a relatively poor correlation with test data. From Figure 4.31-b, it is seen that the tip vortex shedding point is located more towards the outboard near the tip than the predictions. The current predictions used a bound circulation weighted radial location as the position where the free wake is released into the flow. The vertical position of the tip vortex was also under-predicted. The wake trajectory prediction of the free wake and the estimates of the radial location where the trailing tip vortices are released should be improved for a more accurate BVI prediction.

A further reason for the discrepancy is the pressure sensor instrumentation which modifies the dynamic characteristics of the reference blade, compared to the other three

un-instrumented blades on this four-bladed system. Reference [97] compared the results using four different blade motions, and showed an overshoot around 90 degree azimuth angle similar to Figure 4.30 for the reference blade (which was instrumented) while the overshoot was absent for other blades.

4.6.7 GENCAS-DYMORE Coupled Analysis

The GENCAS-DYMORE loosely coupled analysis was performed to model elastic blade deformation and aerodynamic force variation simultaneously while the rotor is trimmed. Figure 4.33 shows pitch control and trim target history compared to the measured data during the coupling iterations. It is seen that the pitch control settings quickly converge after iteration 4 and meet the trim targets. The predicted collective pitch angle closely matches the measured data, but the cyclic pitch controls deviate by 0.7~1 degree relative to the measurements.

The normal force at the 87% radial location is compared in Figure 4.34. Compared to the prescribed OVERFLOW and measured motion file seen in Figure 4.30, the mean value was shifted close to the measured data, and the low frequency load was better matched. However, the BVI amplitude at the first quadrant was weaker than for the previous results. The BVI phase difference still exists. The top view of the wake trajectory seen in Figure 4.35 is very similar to the measured motion result, Figure 4.31 . However, the side view seen in Figure 4.36 indicates that the predicted wake from the coupled analysis has a lower trajectory than the measured motion results, Figure 4.32 .

Figure 4.37 compares computed normal force differentials with high pass filtered measured pressure differential to identify BVI pattern. In both measured motion and coupled analysis cases, clean BVI patterns are seen in the first quadrant, although the

pattern is weaker with the coupled analysis. The BVI events in the fourth quadrant were only weakly captured in both simulations, compared to the experiment.

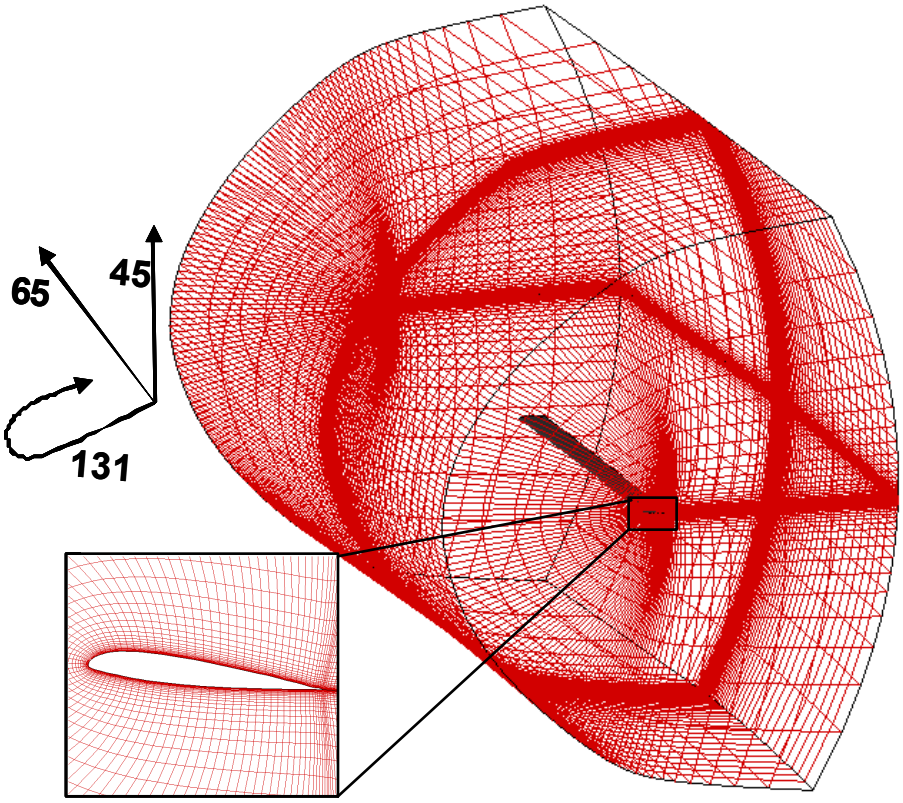

Figure 4.18 HART-II baseline grid system

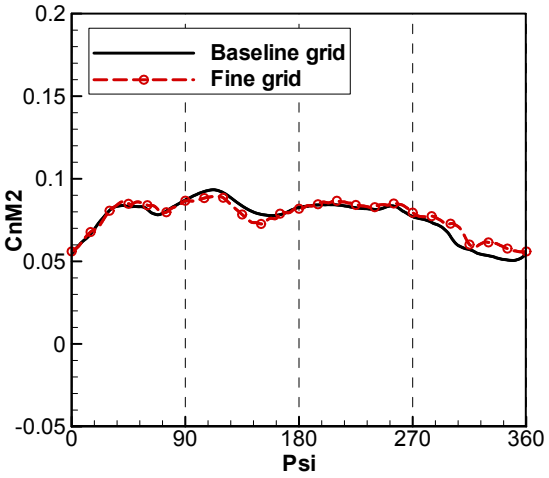

a) $r/R = 0.65$

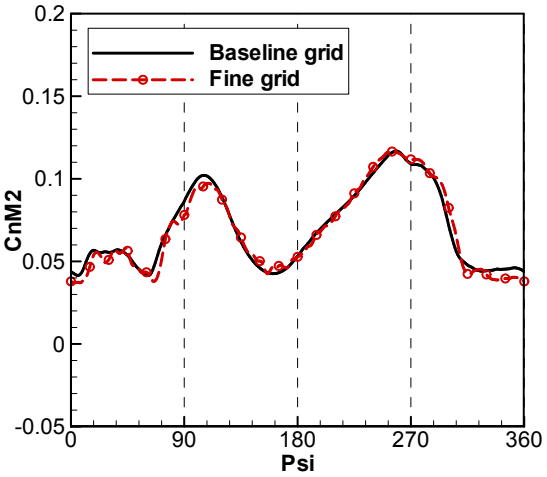

b) $r/R = 0.87$

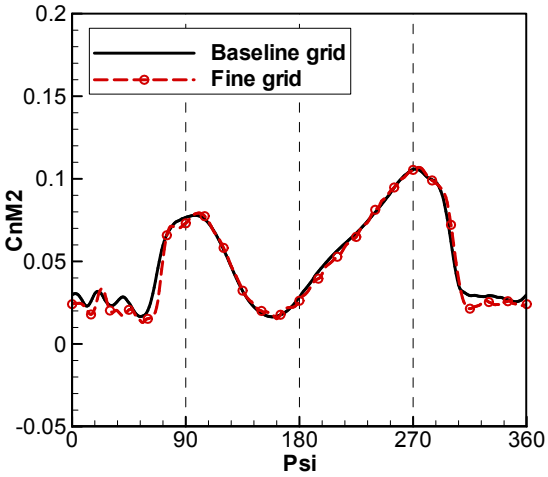

c) $r/R = 0.95$

Figure 4.19 Near-wall grid density test

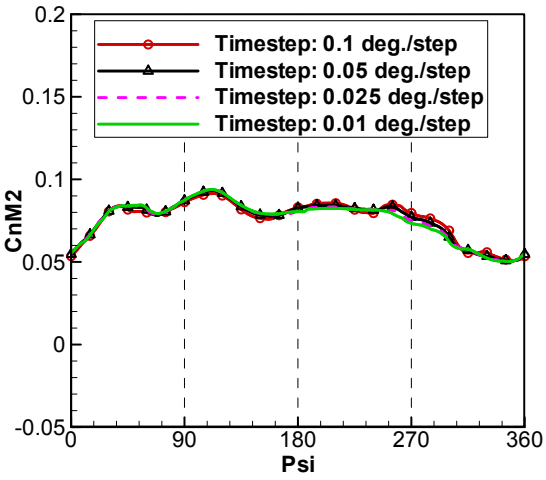

a) $r/R = 0.65$

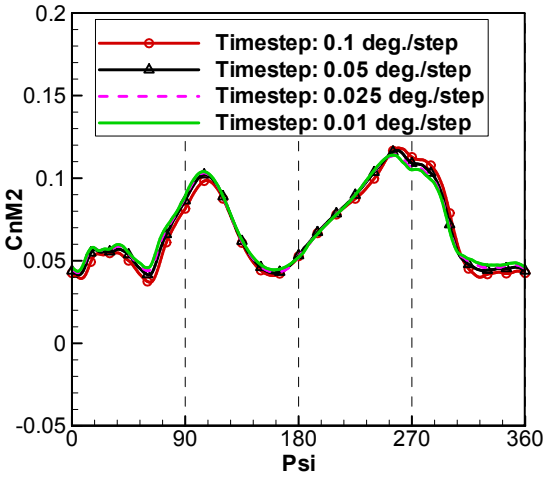

b) $r/R = 0.87$

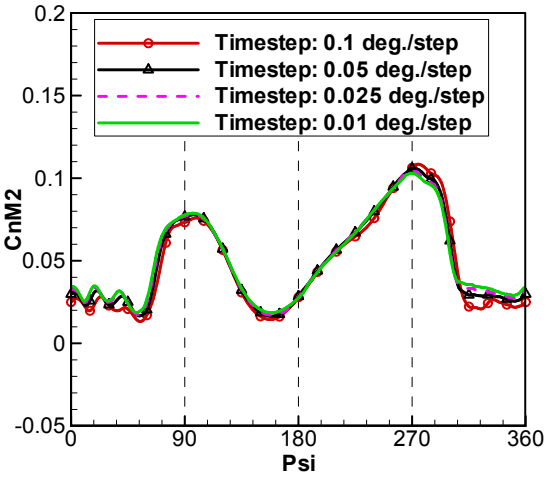

c) $r/R = 0.95$

Figure 4.20 Time step convergence study

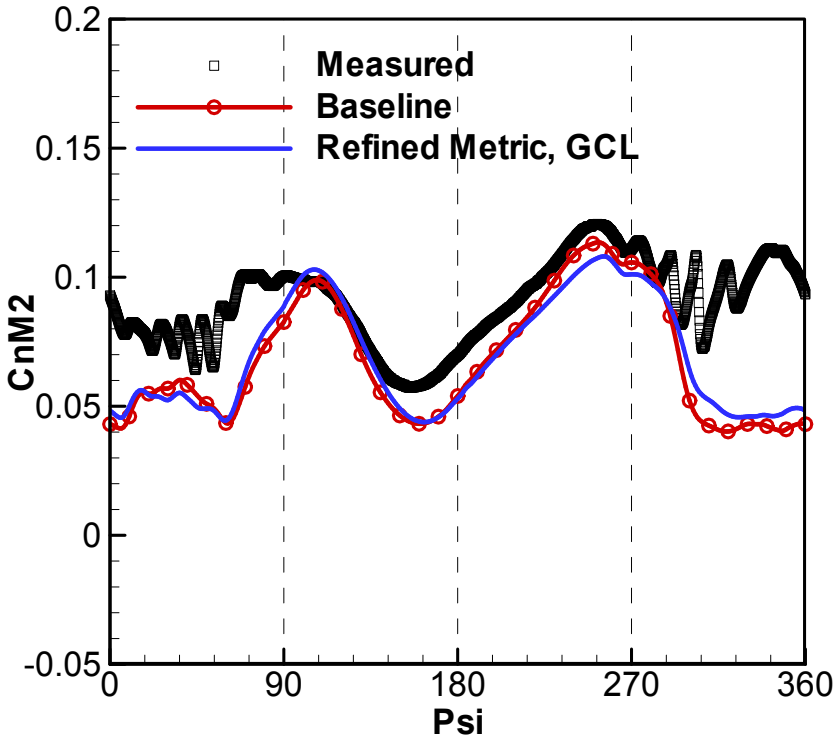

Figure 4.21 Comparison of $C_n M^2$ at r/R=0.87, baseline vs. refined metric and GCL

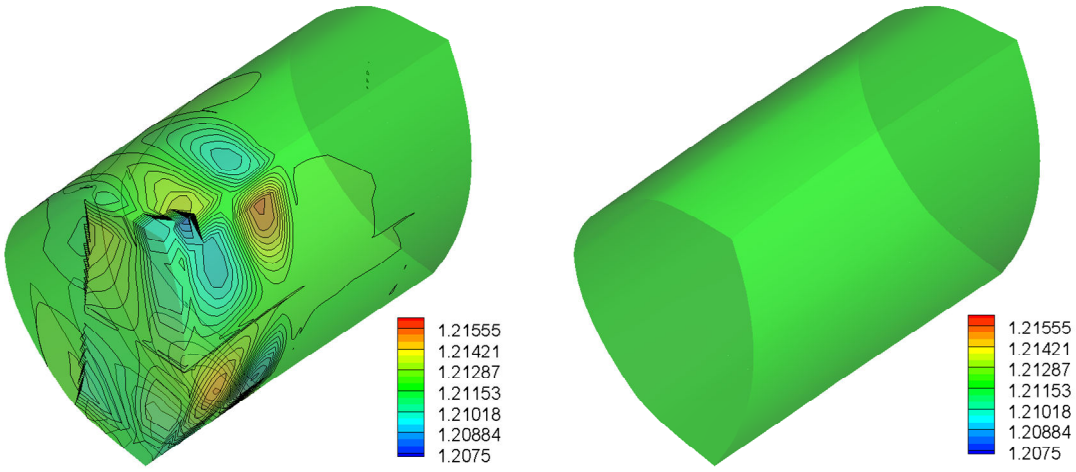

a) Baseline hybrid b) Hybrid with GCL

Figure 4.22 Density contours at the outer surface
(Analysis without blade, but with deforming grid)

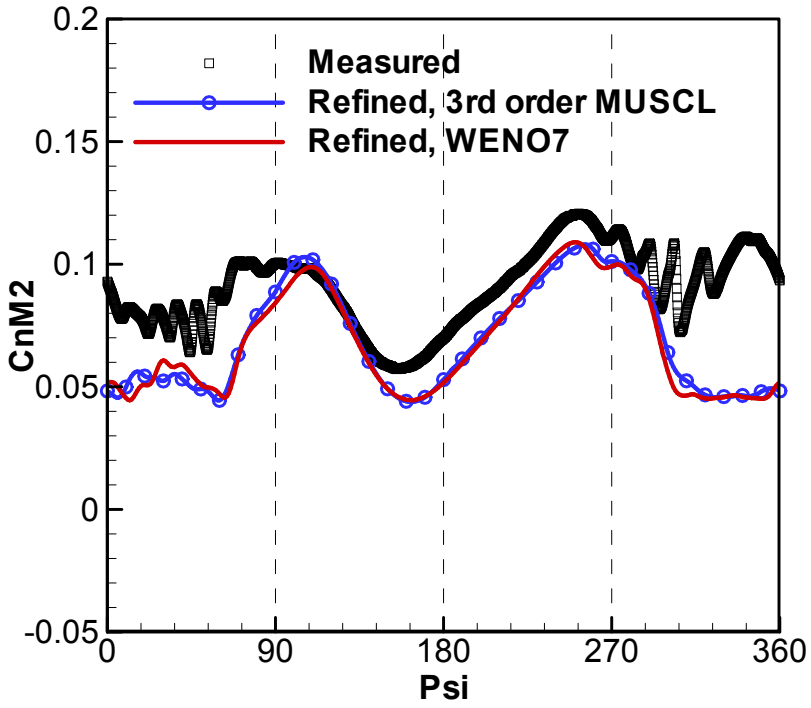

Figure 4.23 Comparison of $C_n M^2$ at *r*/*R*=0.87. 3rd order MUSCL vs. 7th order WENO, Coarse Grid

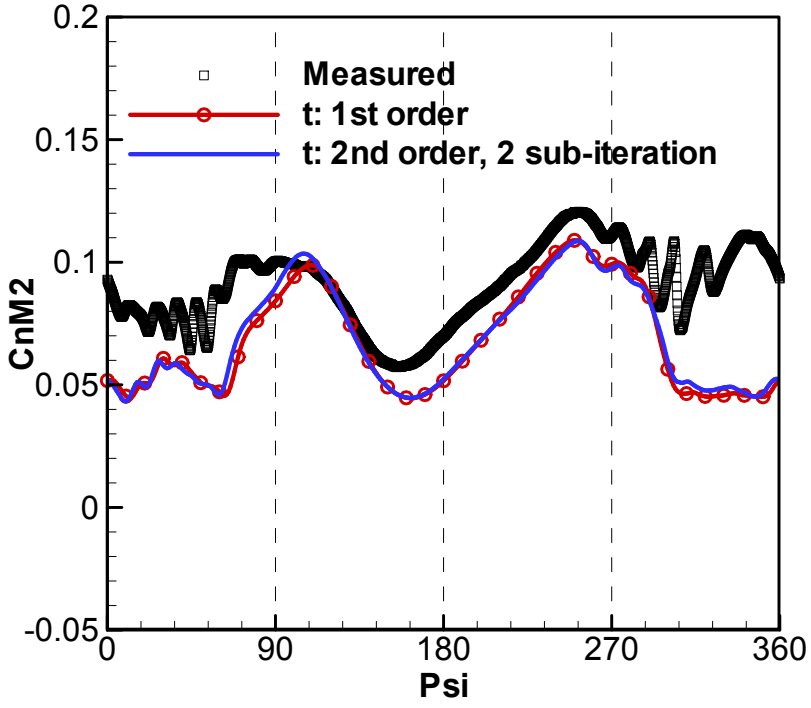

Figure 4.24 Comparison of $C_n M^2$ at *r*/*R*=0.87 for time accuracy. 1st order vs. 2nd order with 2 sub-iterations

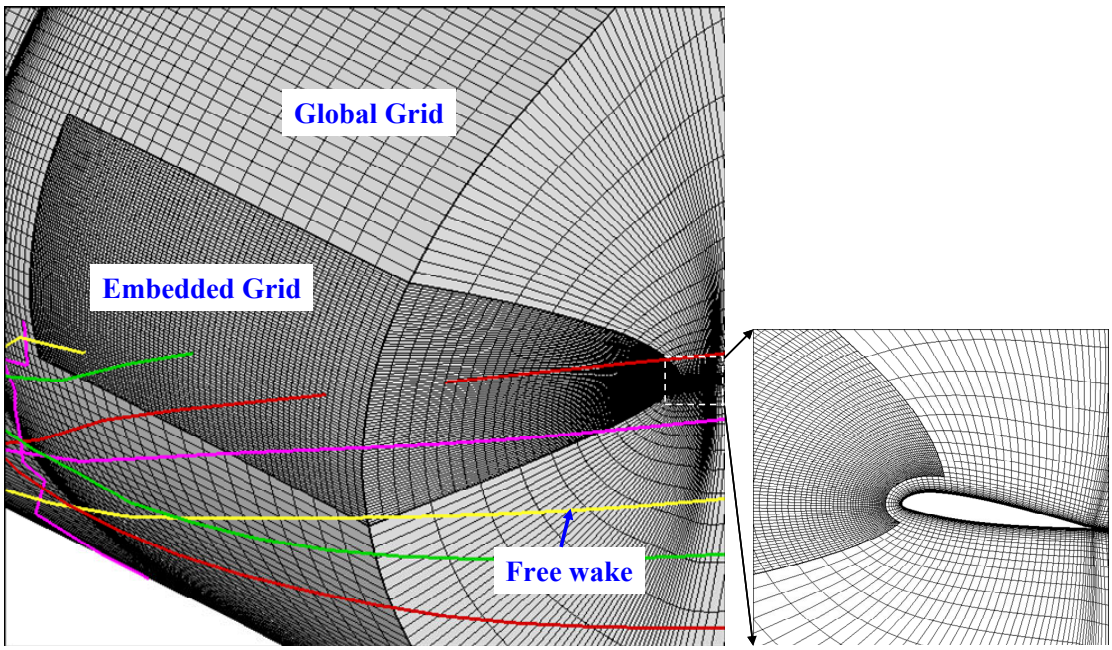

Figure 4.25 Embedded grid

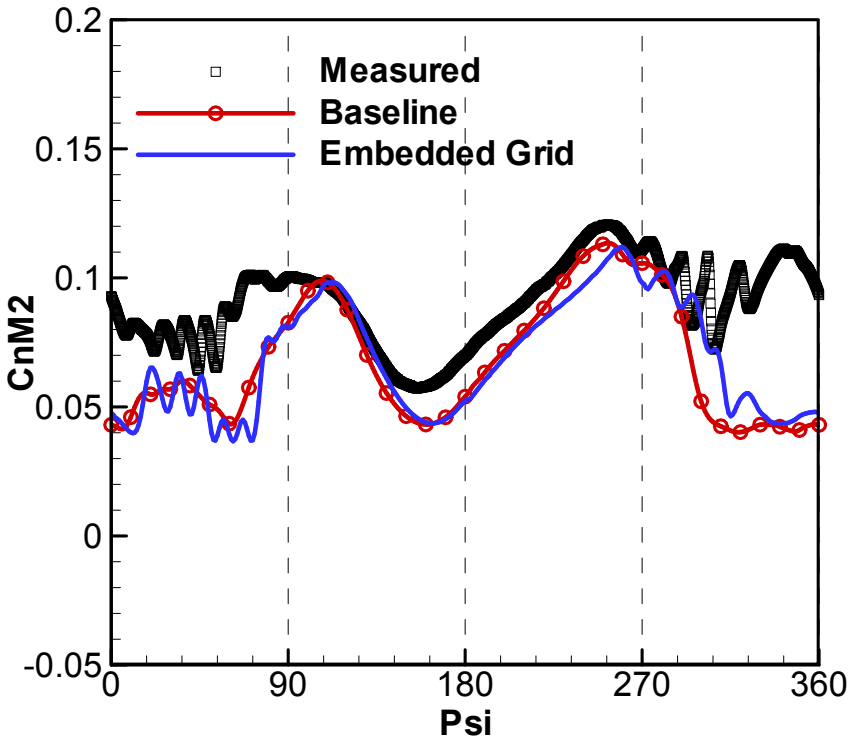

Figure 4.26 Comparison of $C_n M^2$ at r/R=0.87, baseline grid vs. embedded grid

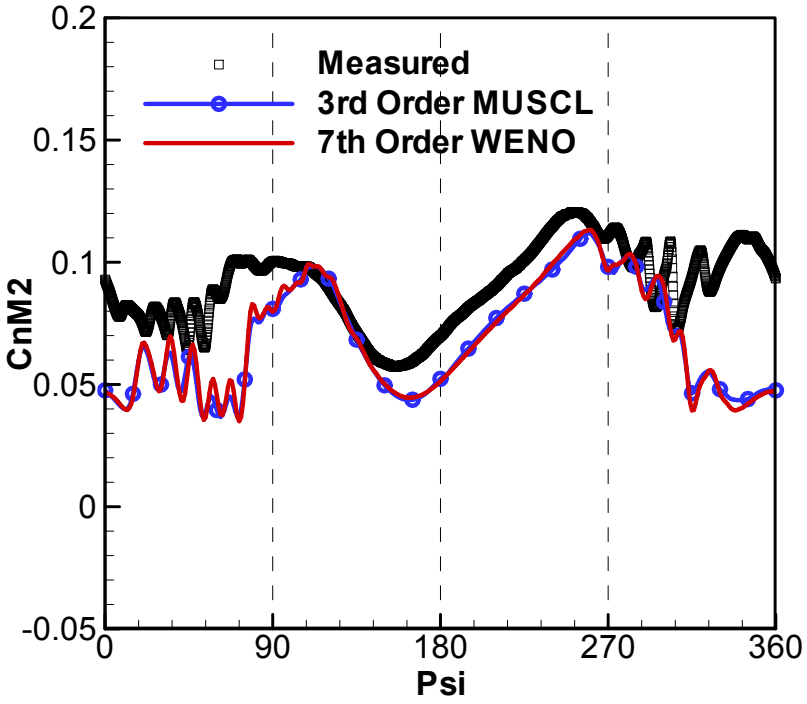

Figure 4.27 Comparison of C_nM^2 at r/R=0.87. 3rd order vs. 7th order with embedded grid

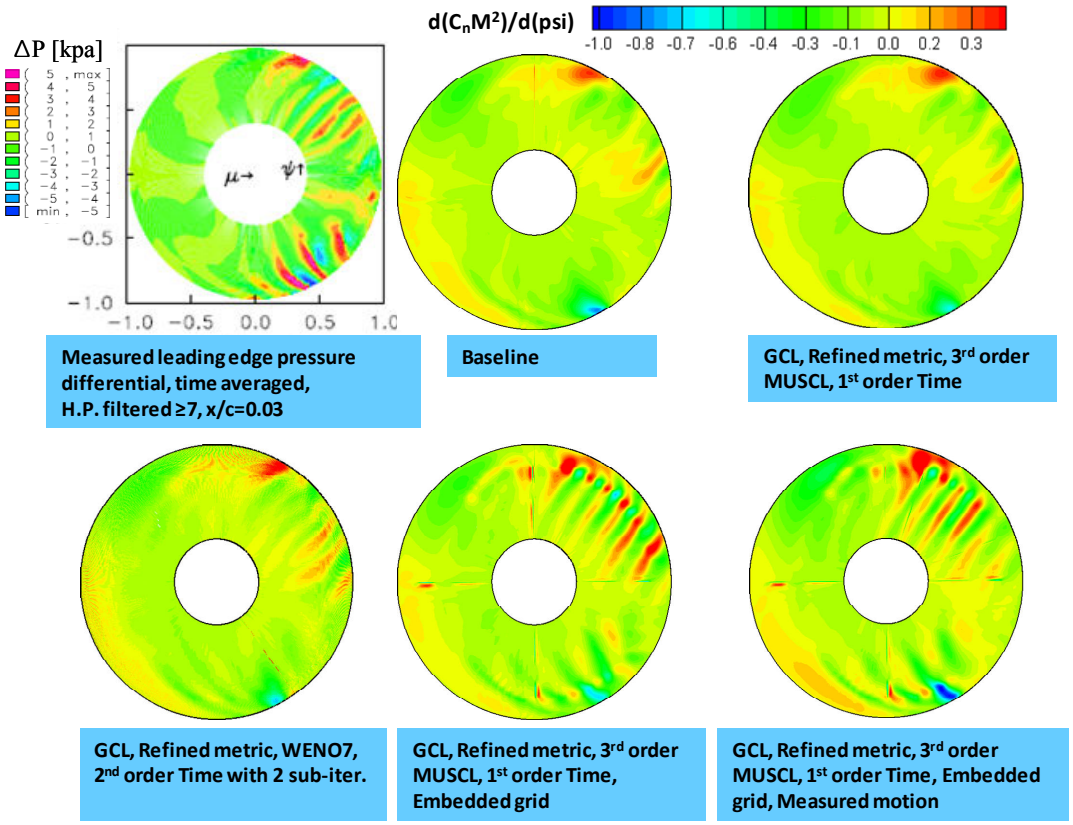

Figure 4.28 Comparison of BVI pattern over the disk with measured data [93]

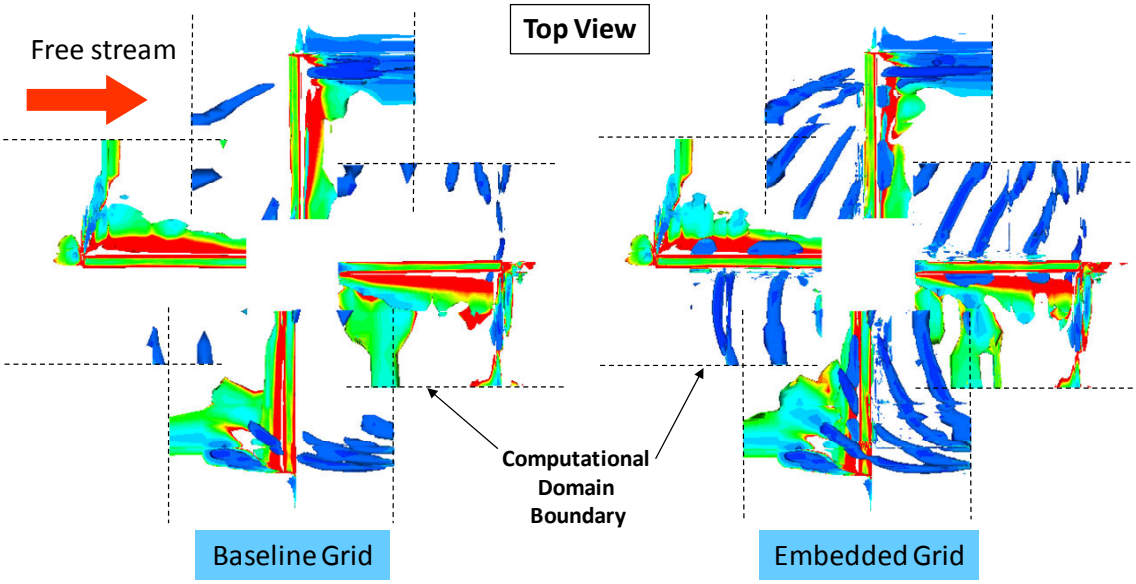

Figure 4.29 Iso-surfaces of Q at 4 azimuth positions, colored by vorticity magnitude

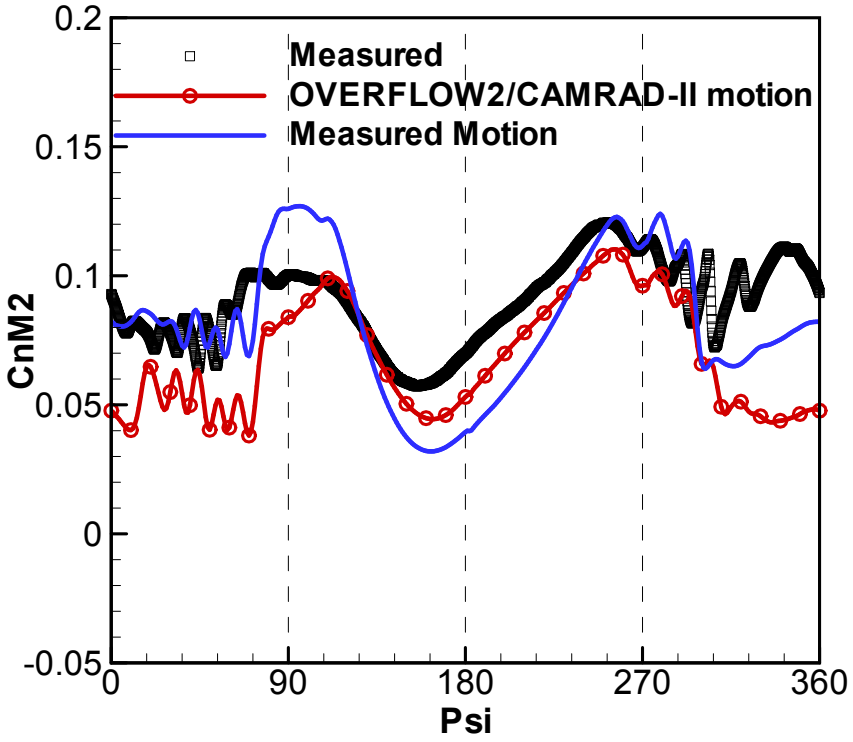

Figure 4.30 Comparison of $C_n M^2$ at r/R=0.87. OVERFLOW motion [94] vs. Measured motion [96]

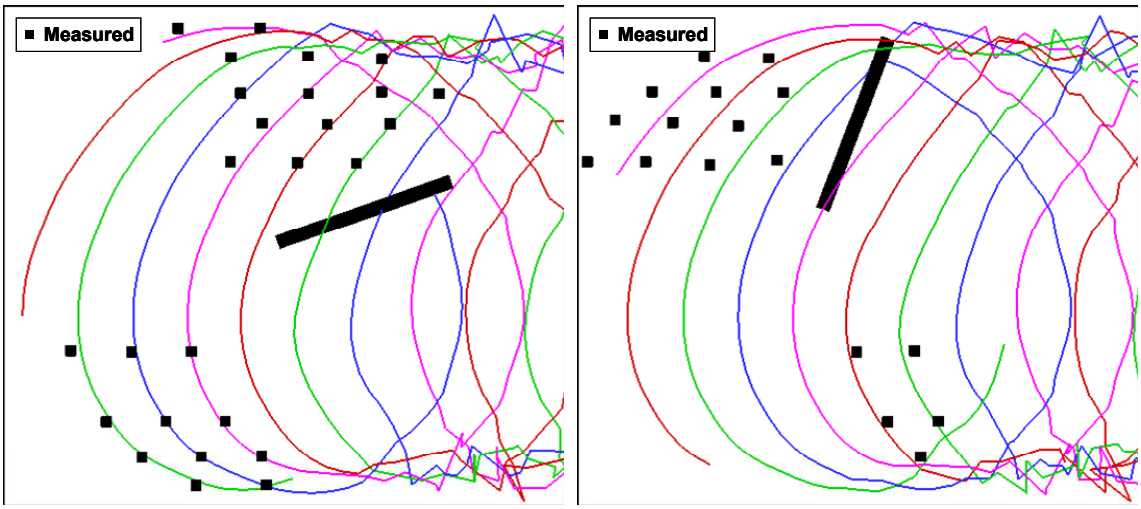

a) $\psi = 20°$ b) $\psi = 70°$

Figure 4.31 Tip vortex geometry, top view

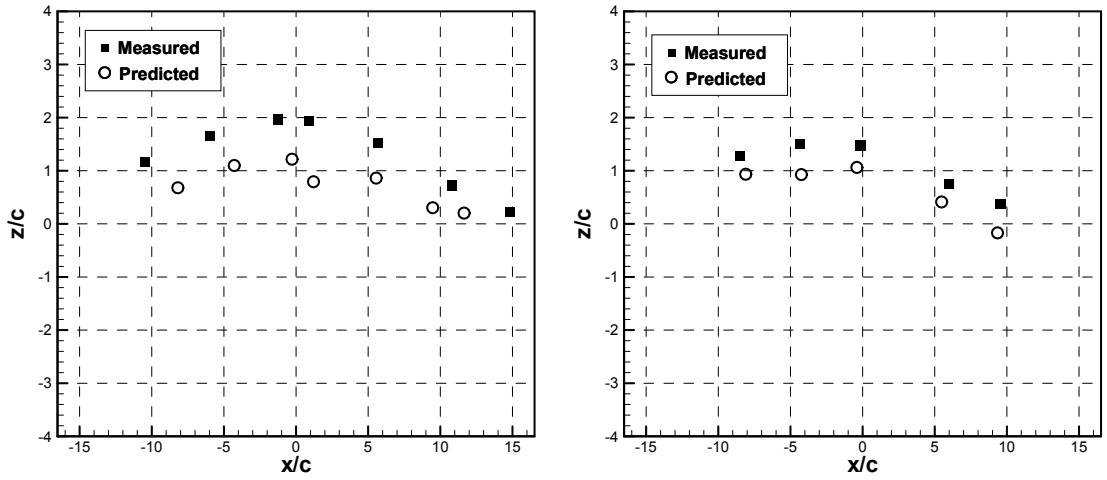

a) y=1.4 m (Advancing side) b) y=-1.4 m (Retreating side)

Figure 4.32 Tip vortex, side view

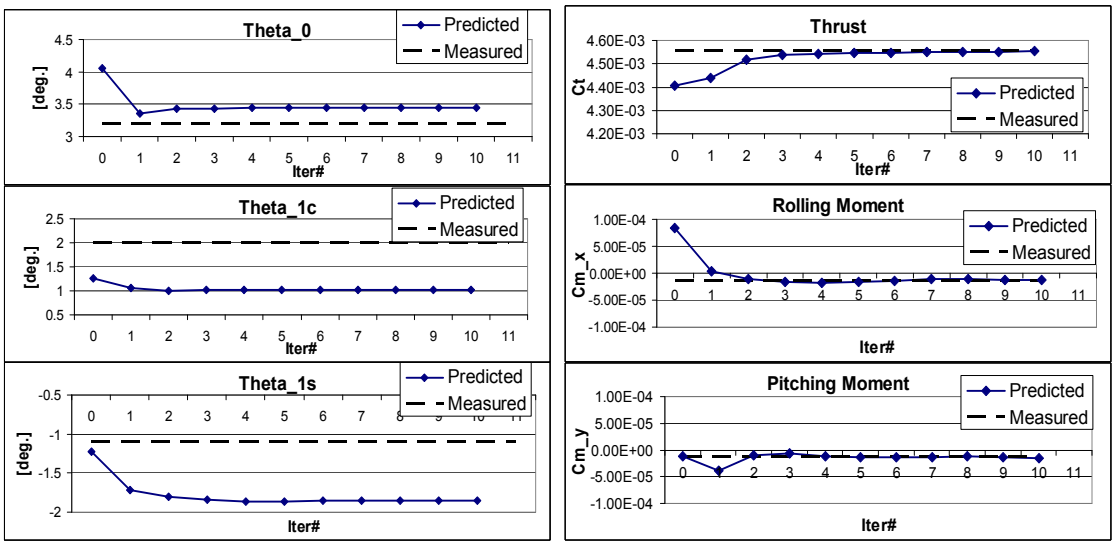

a) Pitch control history b) Trim target history

Figure 4.33 Trim history

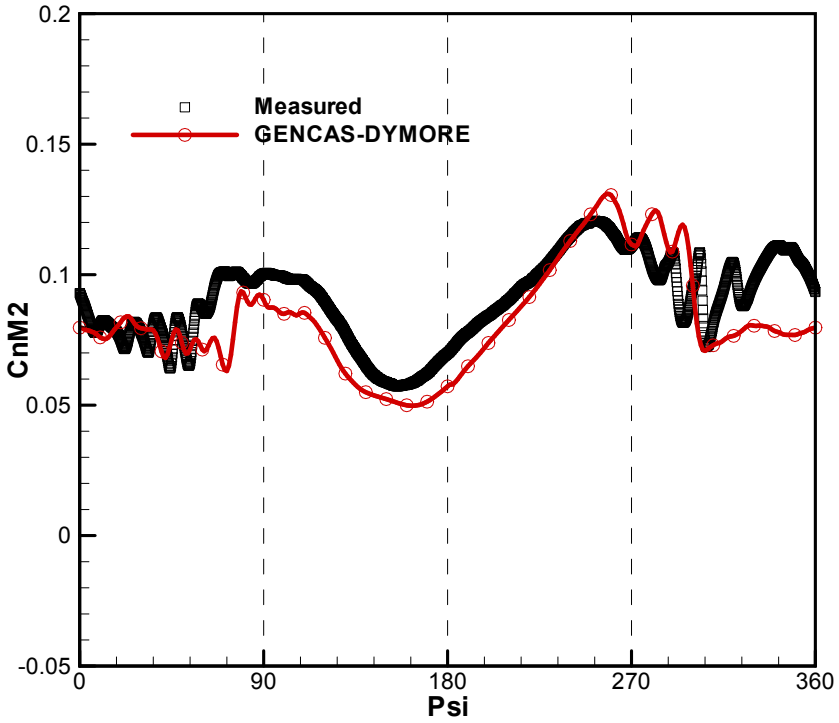

Figure 4.34 C_nM^2 at *r/R*=0.87, coupled analysis

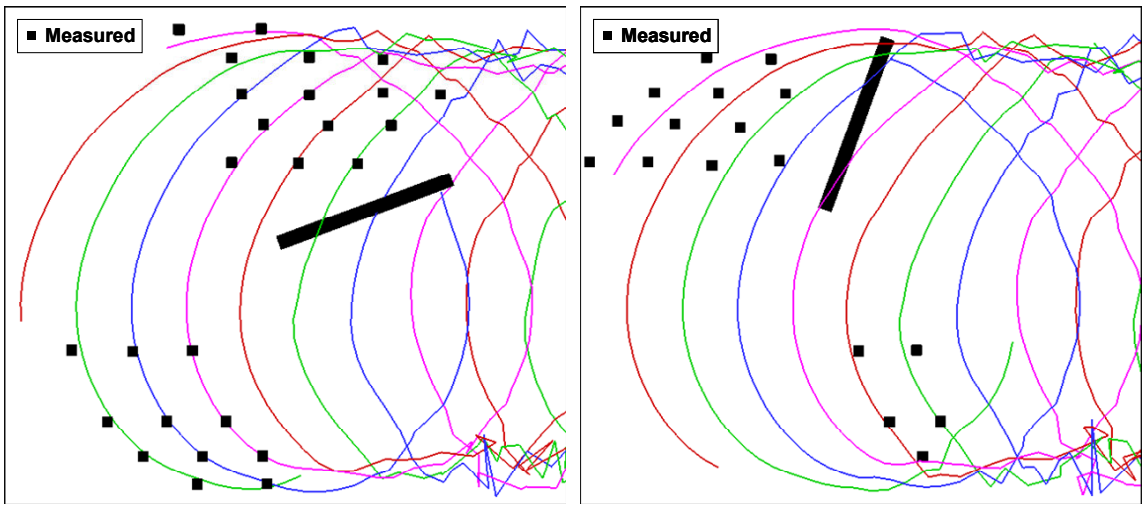

a) $\psi = 20°$ b) $\psi = 70°$

Figure 4.35 Predicted tip vortex geometry from coupled analysis, top view

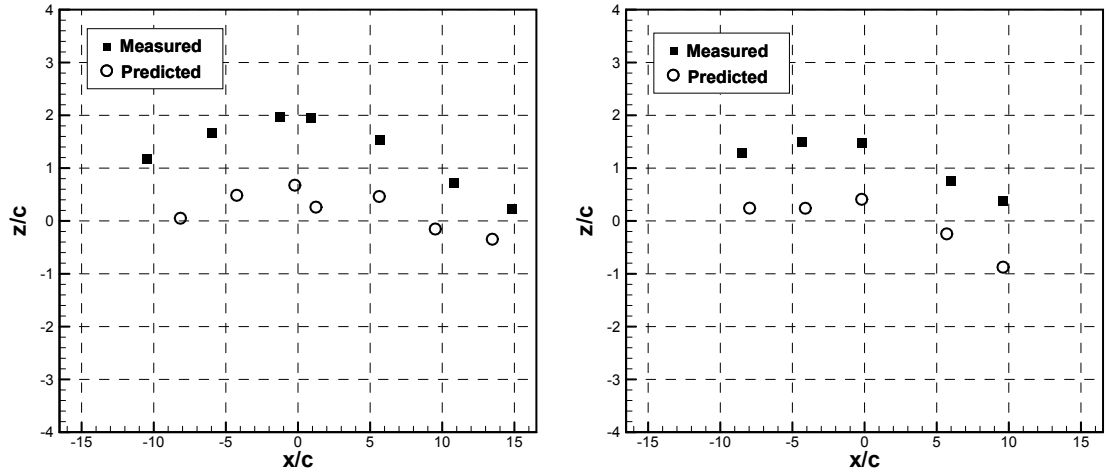

a) y=1.4 m (Advancing side) b) y=-1.4 m (Retreating side)

Figure 4.36 Predicted tip vortex geometry from coupled analysis, side view

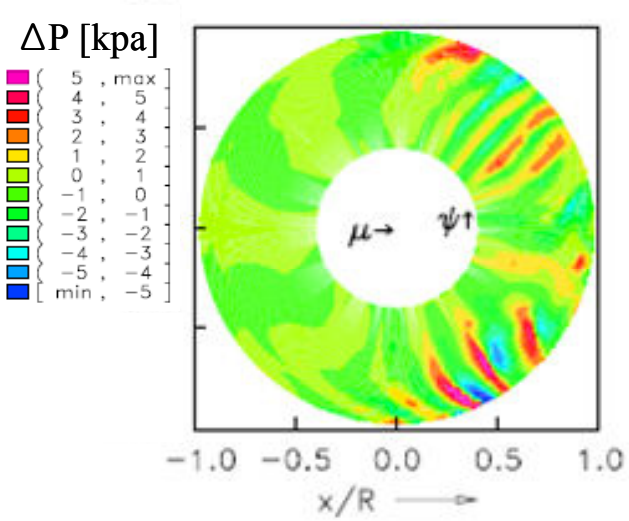

Measured leading edge pressure differential, time averaged, H.P. filtered ≥7, x/c=0.03

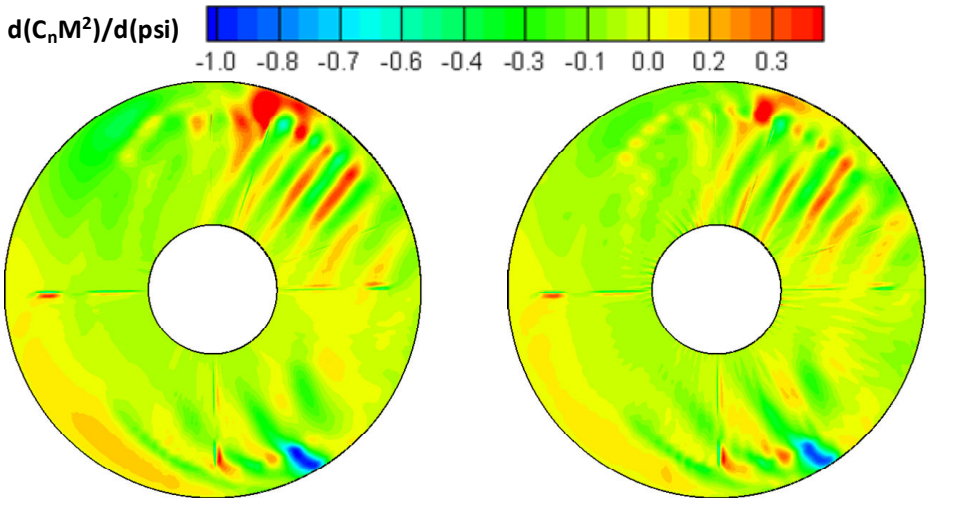

Measured motion (Embedded grid)

GENCAS-DYMORE (Embedded grid)

Figure 4.37 Comparison of BVI pattern over the disk with measured data [93]

4.7 Thickness Effect of the Gurney Flap

In section 4.1.3, the validation study of the current CFD method for a Gurney flap was carried out. The airfoil model was NACA 0015 with the Gurney flap installed at the trailing edge. In this section, the same condition is tested with an infinitely thin Gurney flap model, i.e. a line representation of the Gurney flap. The Gurney flap installed ahead of the trailing edge was tested as well.

4.7.1 Gurney Flap Installed at Trailing Edge

Figure 4.38 compares the original Gurney flap model (used in section 4.1.3) with a line representation of the flap at the trailing edge. The thickness and height of the original model was 1% and 2% of the chord length, respectively. The angle of attack sweep was made and the lift coefficients are compared in Figure 4.39. The pure computational result comparison shows that the line representation of the Gurney flap resulted in slightly higher lift. The flat bottom surface of the finite thickness Gurney flap keeps the flow attached and holds the flow to the surface tangential direction (Figure 4.41-a), whereas the infinitely thin flap model lets the flow leave in the downward direction to satisfy the Kutta condition (Figure 4.41-b). Therefore, the infinitely thin flap model increases the flow deflection effect of the Gurney flap, and produces more circulation and lift. However, the drag difference was minor, as shown in Figure 4.40.

4.7.2 Gurney Flap Installed ahead of Trailing Edge

The flap installed at a certain distance from the trailing edge will be more realistic in terms of engineering installation of the flap, if deployable. A Gurney flap with a height of 2% and thickness of 1% chord length was installed at 90% of the chord from the leading edge. NACA 0015 airfoil was used, but pure computational results were

compared since experimental data is not available. Modified airfoils with finite and infinitely thin thickness of the Gurney flap model are shown in Figure 4.42. Figure 4.43 compares the computed lift coefficient and drag is compared in Figure 4.44. Unlike the previous trailing edge installation case, the lift from both models coincided together, and the drag difference was only small. As shown in Figure 4.45, the flow deflection effect, and thus the camber effect of the Gurney flap comes from the flap and large separation bubble behind it. The effect of the flow turning angle at the tip of the Gurney flap is minor in this separation bubble dominant region, and the resultant circulation and lift difference was negligible.

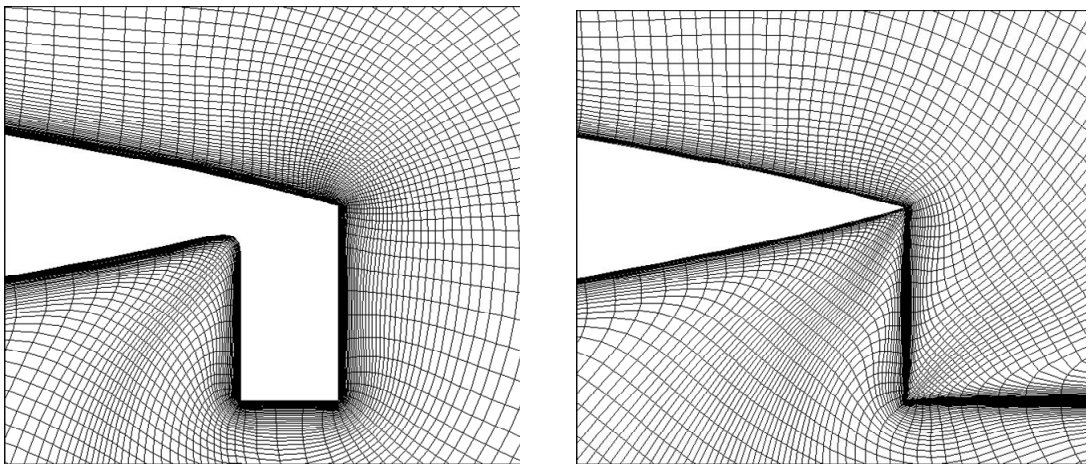

a) Flap thickness of 0.01c [524×134] b) Infinitely thin flap [615×130]

Figure 4.38 Gurney flap model and grid: Installed at tailing edge

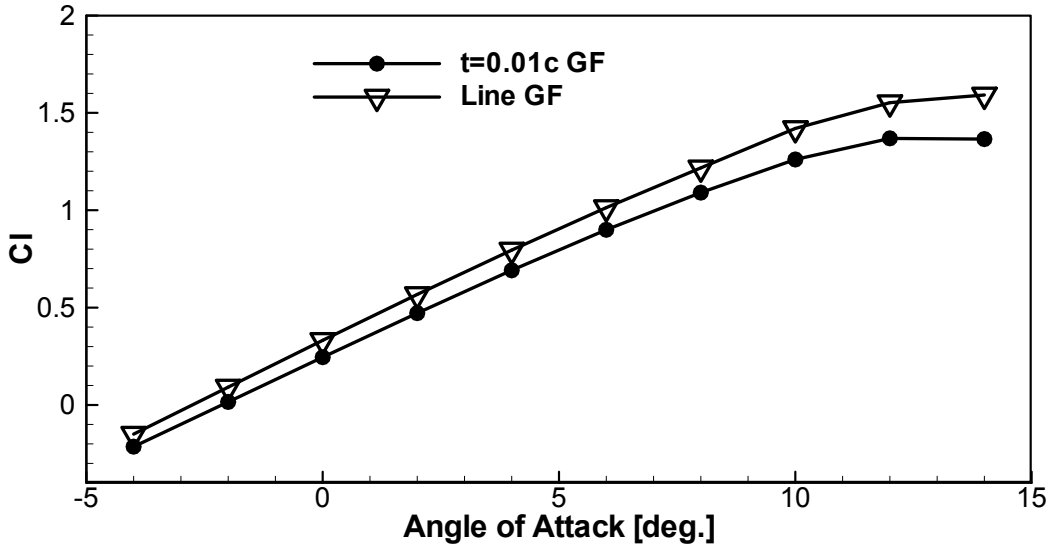

Figure 4.39 Lift coefficient comparison

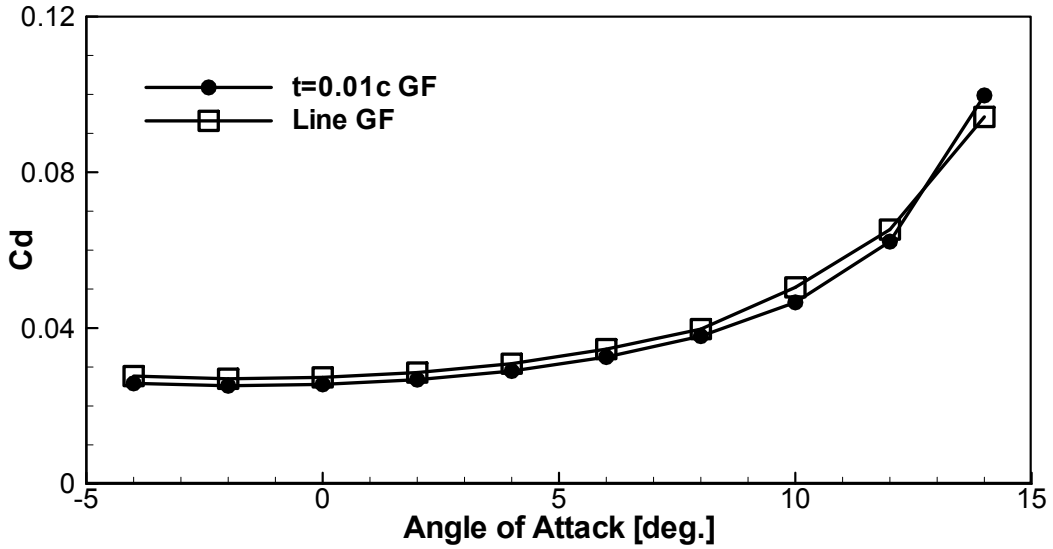

Figure 4.40 Drag coefficient comparison

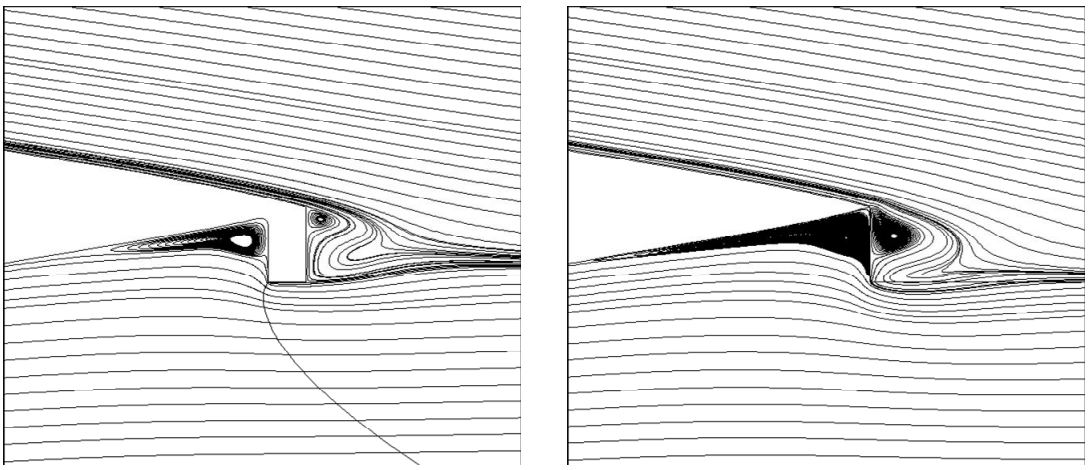

a) Flap thickness of 0.01c b) Infinitely thin flap

Figure 4.41 Streamline near the trailing edge ($\alpha = 0^{\circ}$)

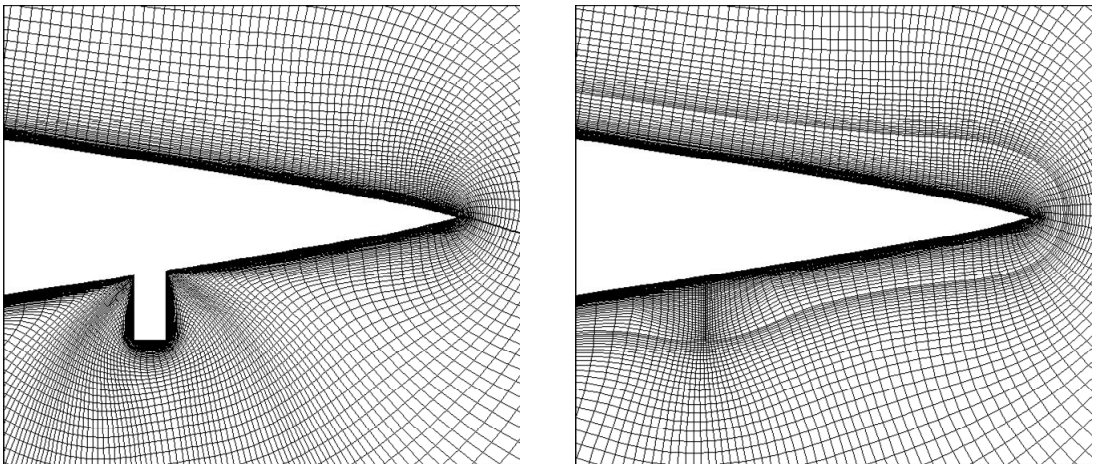

a) Flap thickness of 0.01c [559×131] b) Infinitely thin flap [521×140]

Figure 4.42 Gurney flap model and grid: Installed at 0.9c

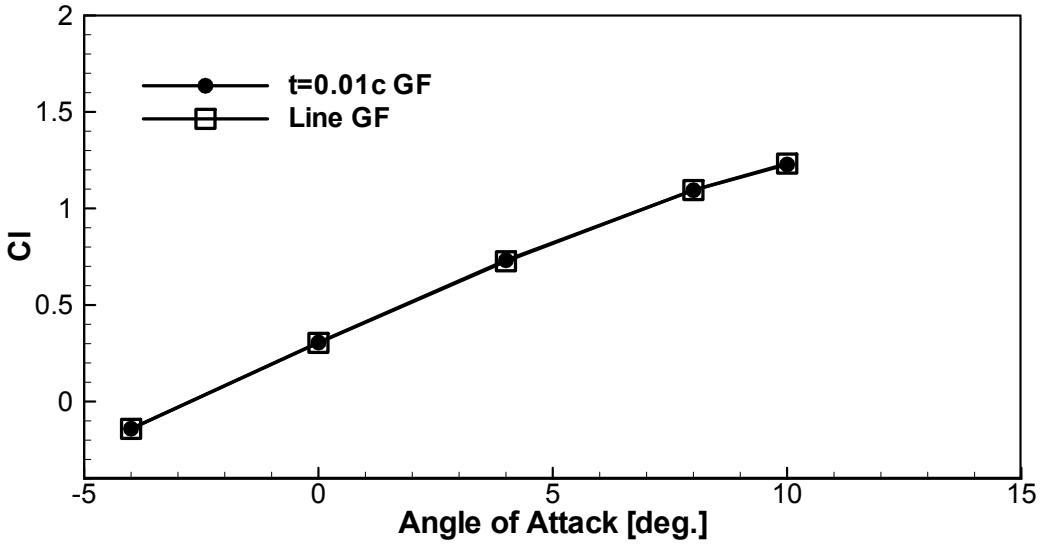

Figure 4.43 Lift coefficient comparison

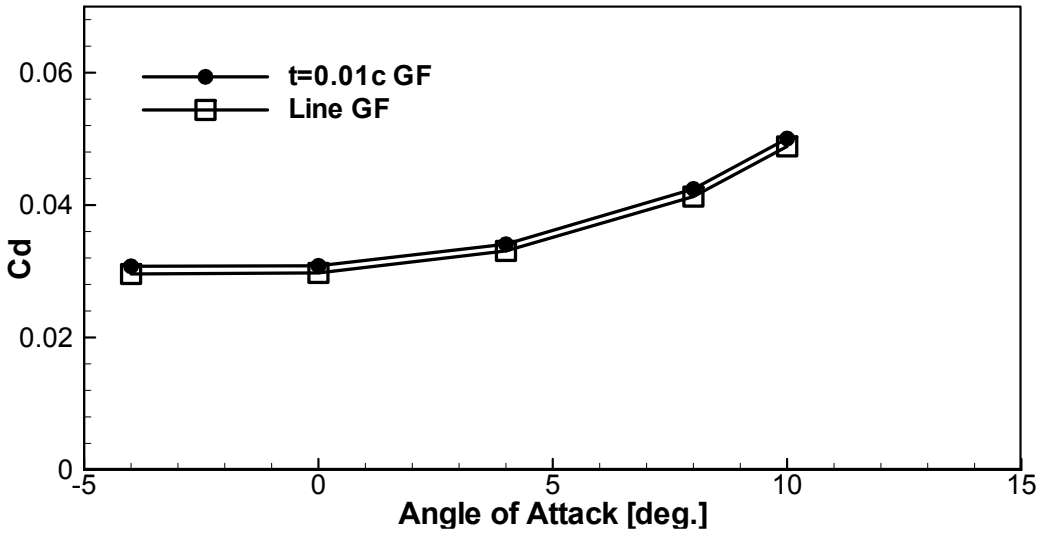

Figure 4.44 Drag coefficient comparison

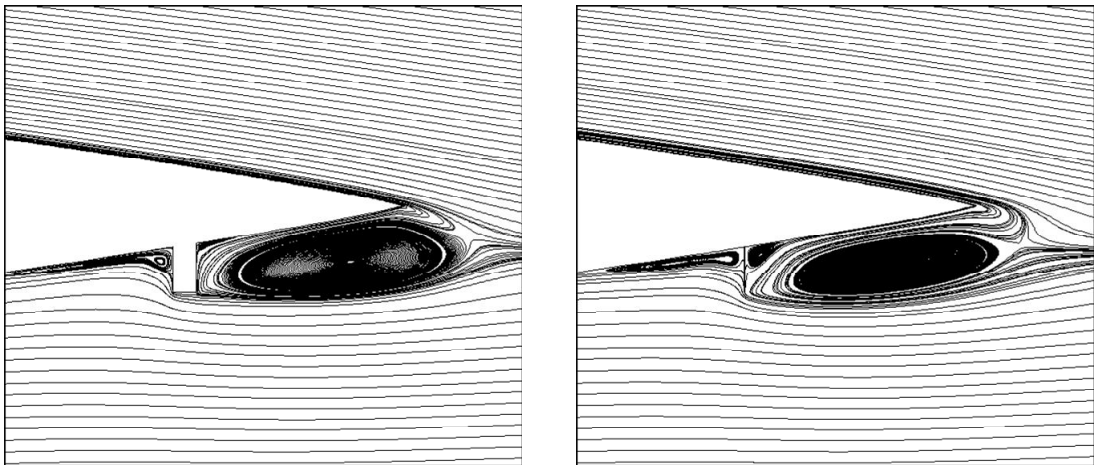

a) Flap thickness of 0.01c

b) Infinitely thin flap

Figure 4.45 Streamlines near the Gurney flap ($\alpha = 0^{\circ}$)

CHAPTER 5

THE EFFECT OF GURNEY FLAP IN AUTOROTATION

In this chapter, the modification of the autorotative characteristics of rotors by the retrofit addition of a Gurney flap is studied.

To understand how autorotation works, consider an airfoil section shown in Figure 5.1. Here V_{wind} is the descent speed. When the descent speed, the in-plane velocity Ωr, and the induced velocity are combined as shown in the Figure 5.1, the lift vector is tilted forward. The propulsive force in the plane of rotation is $L\sin\phi$ - $D\cos\phi$. Using simple trigonometry, for small values of ϕ,

$$\text{Propulsive Force} \cong L\left[\frac{V_{wind}-V_{induced}}{\Omega r}\right] - D$$
$$\text{Torque} = \int_0^R r\left\{L\left[\frac{V_{wind}-V_{induced}}{\Omega r}\right] - D\right\} dr \tag{5.1}$$

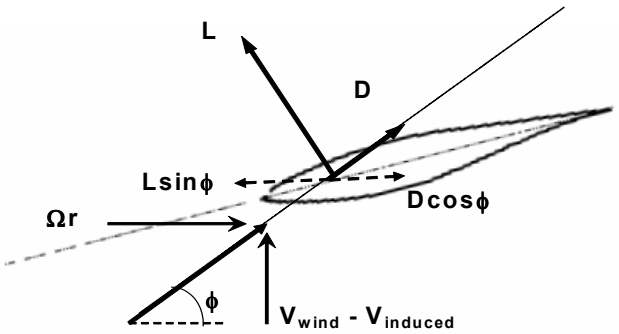

Figure 5.1 Autorotation of a rotor in descent

For autorotation to occur, the integrand must be positive over most of the rotor disk. This can be achieved by high descent rate (high wind speed), high L, low D, or a

combination of the above. It is clear that a high *L/D* will give a positive integrand permitting autorotation, even at low descent speeds.

The HART-II rotor, which is a representative of rotors found on modern commercial rotorcraft, was chosen for this study, with the trailing edge tab removed. The Gurney flaps were permanently deployed. In autorotative descent without power, there will not be enough control power available for periodic deployment of these devices. In order to simplify the analysis, all the calculations were done for a rigid rotor with a rigid Gurney flap. Figure 5.2 illustrates definitions of terminologies used in this section.

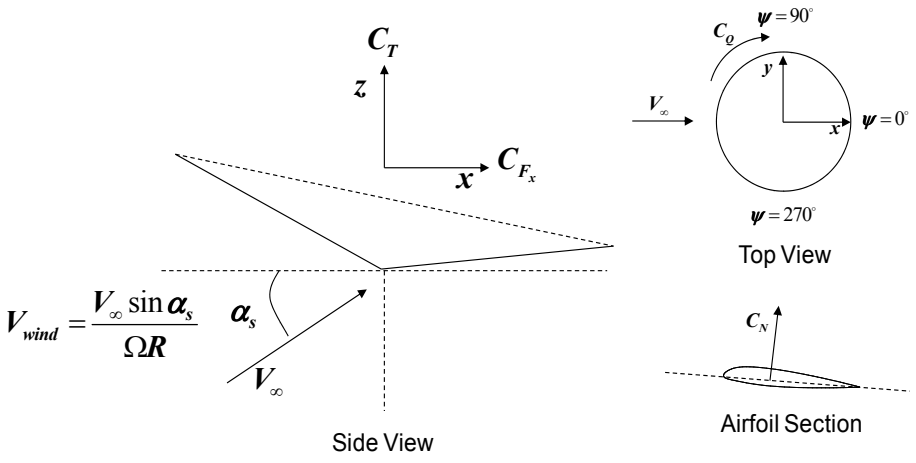

Figure 5.2 Terminology in autorotation study

5.1 Grid System and Time Step Selection

Figure 5.3 shows the body-fitted grid for the baseline configuration without trailing edge tab, and for the rotor blades equipped with Gurney flap. The Gurney flap was simulated as an infinitesimally thin plate installed at the lower side of the trailing edge with a 1.5% chord length. Based on the grid independence study shown in section 4.6.1, the grid has dimensions of 131×65×45 and 143×65×45 (chord-wise × span-wise × surface normal) for baseline and flap-equipped rotor, respectively. The y^+ value at the first point of the wall was varied with the radial and azimuthal location on the blade as well as operating conditions (advance ratio, shaft angles of attack). Post-processing of the simulations indicated that much of the first layer of points had a y^+ of 5.5 or below. In autorotative descent, average rotor performance metrics, such as thrust and torque, are of most concern rather than higher harmonic BVI phenomena. Therefore, time consuming embedded grid based simulations were not done.

The baseline schemes (Roe's FDS with 3rd order MUSCL, 1st order LUSGS time marching scheme without sub-iteration) with GCL terms were used. The conventional grid metric and Jacobian computations were used to save computational time. The KES turbulence model was used to model eddy viscosity.

In high descent rate autorotative mode, up to 6 revolutions of simulations were required to reach steady periodic solution. A time step convergence study of thrust and torque was performed for the baseline configuration at an advance ratio of 0.13 and a representative high descent angle of 30 degree. The blade pitch control inputs were obtained using the rigid blade trim solver introduced in section 2.7 for zero torque. Predicted thrust and torque are plotted in Figure 5.4 as a function of time step.

Asymptotically converged thrust were obtained after $1/\Delta\psi$=5, and 10 for torque. Based on this study, a time step of 0.1 degree ($1/\Delta\psi$=10) was used.

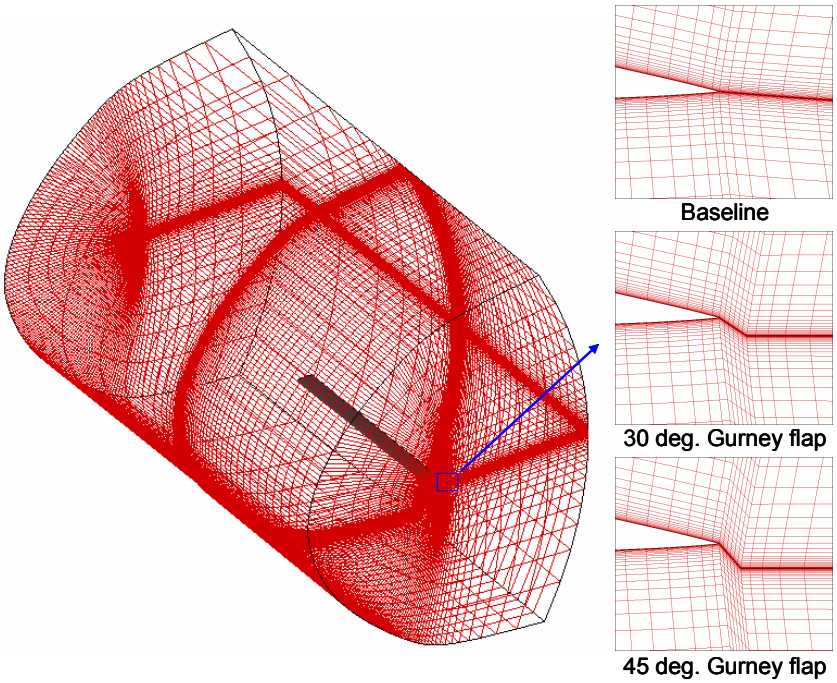

Figure 5.3 Grid system and Gurney flap modeling ($l_{GF} = 0.015c$)

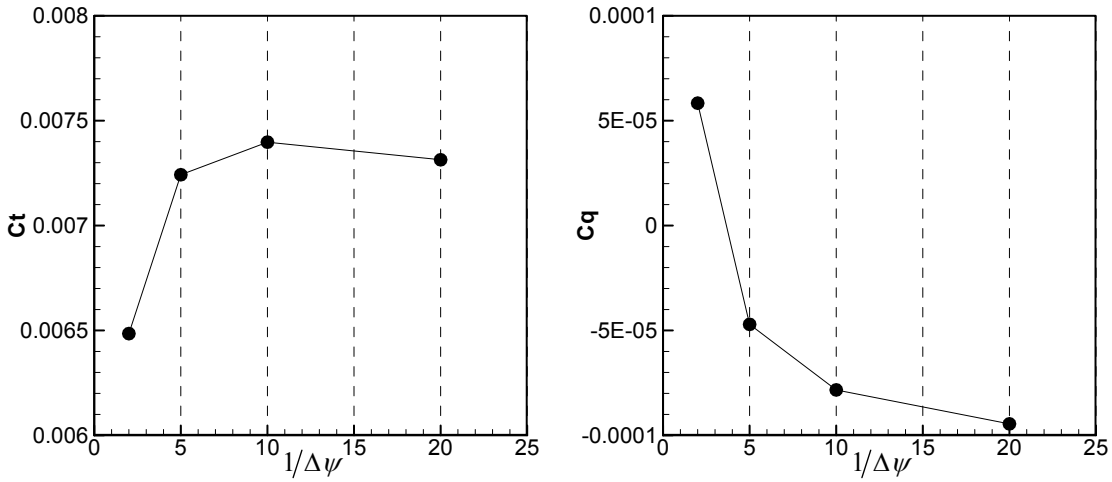

Figure 5.4 Time step convergence study for autorotation ($\Delta\psi$ in degree)

5.2 Fixed Control Setting

The baseline rotor was trimmed as follows. The rotor RPM (and hence the tip Mach number of the rotor) was left unchanged from the HART-II test case discussed in the validation chapter. Flights at two advance ratios were tested. The target C_T/σ of the baseline rotor (i.e. without a Gurney flap) was nominally set at 0.083, representative of the typical operating condition of a helicopter. Note that this is approximately 50% higher than the thrust setting for the validation case. To reduce computational time required for trimming, a simple rigid blade trim solver (section 2.7) was employed prior to the CFD simulation to obtain the collective and the cyclic pitch angles that satisfy the target C_T/σ, zero hub moments, and zero torque with a simple linear aerodynamic model. Once the control settings were obtained, a sweep of the shaft angle of attack (positive with the shaft tilted rearwards) was done using CFD simulations and the required torque was computed. Autorotative state was established at the shaft angle of attack at which the torque is zero.

The shaft angle of attack sweep simulations were repeated for the rotors equipped with a Gurney flap for the same collective and cyclic pitch settings. In other words, the baseline rotor and the two Gurney flap equipped rotors (as shown in Figure 5.3) operate at the same control settings, and not at the same trimmed C_T/σ. In a fixed wing terminology, this is similar to comparing a wing and a wing-flap configuration at the same geometric alpha rather than the same C_L. Two different angles of the flap (30 degree and 45 degree) were investigated and compared with the baseline blade. The blade pitch control inputs obtained from the rigid blade trim solver is shown in Figure 5.5. In this fixed control setting approach, the Gurney flap was permanently deployed at

70~90% radial location with 1.5% chord length by selectively applying wall boundary condition (Figure 5.6).

Figure 5.7 shows the variation of the computed torque with shaft angle of attack for two advance ratios, for each of the three configurations (baseline rotor, rotor with a 30 degree Gurney flap, rotor with a 45 degree Gurney flap). It should be kept in mind that the flap equipped rotor simulations were run for the same control setting as the baseline rotor, and not for the same C_T/σ. As may be expected, as the shaft angle of attack increases, the induced angle of attack ϕ decreases in magnitude and eventually reverses the sign over large portions of the rotor. The torque required to operate the rotor decreases and eventually reverses sign. At high enough shaft angles of attack [equivalently, at high enough descent rates quantified as $\mu \tan(\alpha_s)$], the torque goes negative indicating that the rotor is being driven by the airstream as in a wind turbine. It was found that the Gurney flap equipped rotors, for the same control and collective settings as the baseline rotor (trimmed at C_T/σ of 0.083), establish autorotation at a lower descent rate than does the baseline rotor at an advance ratio of 0.13. The rotor with moderate deflection angle of the Gurney flap (30 degree) was more efficient than the high flap angle (45 degree). In high advance ratio flight ($V_\infty/\Omega R = 0.2$), the efficiency of the high deflection angle Gurney flap decreased further and the descent rate was higher than the baseline.

Figure 5.8 and Figure 5.9 compares in-plane drag force and thrust distribution over the rotor disk of each rotor configuration at two examined advance ratios. The comparison was made at the same descent rate, where the rotor with 30 degree Gurney flap is in autorotation state, so that the effect of Gurney flap can be equally examined. In

all cases, most of the front half of the rotor disk (driving region) produced propulsive forces, whereas aft half of the rotor disk (driven region) produced drag forces. The increased sectional lift, and thus a higher thrust due to Gurney flap, is evident compared to the baseline rotor over the radial locations where the Gurney flap is installed (0.7~0.9R). In terms of the in-plane forces, the Gurney flap installed radial location is highlighted with strong propulsive forces in the driving region. However, over the driven region, the drag force also increases with Gurney flap deployment. The streamlines at the 0 degree azimuth angle shown in Figure 5.10 and Figure 5.11 show that the local velocity combined with forward flight velocity, descent velocity, vortex induced velocity, and the blade rotational velocity forms near zero or slight negative angle of attack with respect to the airfoil chord line. It is believed that this increase in drag is caused by the higher induced velocity over the aft section of the disk. Thus, the lift vector is directed normal or slight backward. Furthermore, a close view near the Gurney flap shows flow separation with a high angle of flap. The attendant flow separation at high flap angle increases drag and decreases Gurney flap efficiency. On the other hand, the local velocity at the front disk (Figure 5.12) was inclined upward with the airfoil at near zero pitch angles. Thus, the lift vector was tilted forward and produced strong propulsive forces with increased lift due to Gurney flap. The lift increase is high as well compared to the driven region.

Table 5.1 shows the descent rates for zero torque condition, extracted from Figure 5.7. Table 5.2 summarizes the corresponding thrust settings. Figure 5.13 shows the azimuthal variation of normal force and sectional pitching moment at 81% radial location. As may be expected, the Gurney flap equipped rotors, for the same collective and control settings, operate at higher sectional lift coefficients even though the descent

rate is lower than the baseline rotor. However, it is also observed that the high pressure on the windward side of the Gurney flap caused a large nose down sectional pitching moments.

Table 5.1 Estimated zero-torque descent rates

	$V_\infty/\Omega R = 0.13$		$V_\infty/\Omega R = 0.2$	
	α_s	$\mu\tan(\alpha_s)$	α_s	$\mu\tan(\alpha_s)$
Baseline	22.5	0.0498	12.85	0.0445
30 deg. GF	20.9	0.0464	12.7	0.0440
45 deg. GF	21.2	0.0470	13.0	0.0450

Table 5.2 Computed thrust coefficients at the estimated zero-torque descent rates

	Baseline	30 deg. GF	45 deg. GF
$V_\infty/\Omega R = 0.13$	6.41×10^{-03}	7.46×10^{-03}	8.02×10^{-03}
$V_\infty/\Omega R = 0.2$	6.92×10^{-03}	8.09×10^{-03}	8.79×10^{-03}

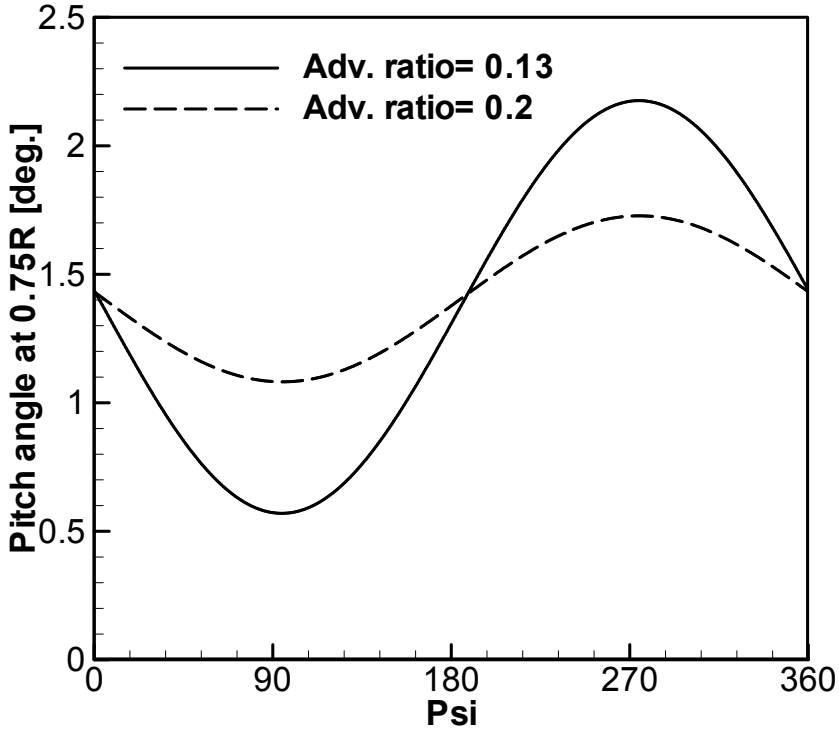

Figure 5.5 Blade pitch angle schedule obtained from the rigid blade trim solver

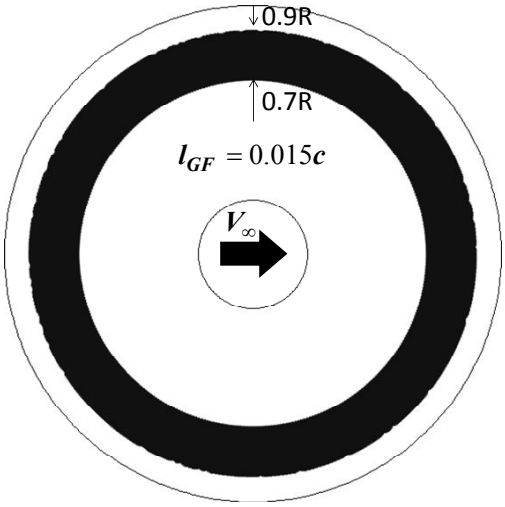

Figure 5.6 Installed Gurney flap location

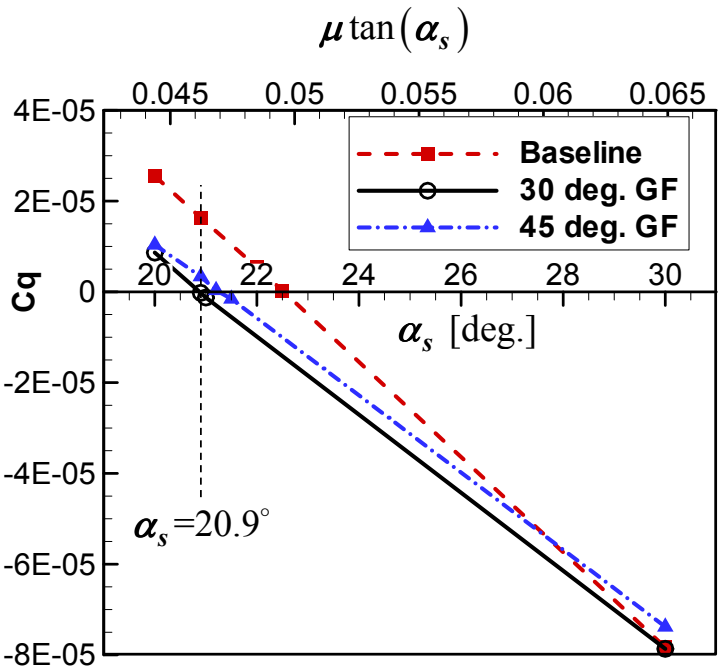

a) $V_\infty/\Omega R = 0.13$

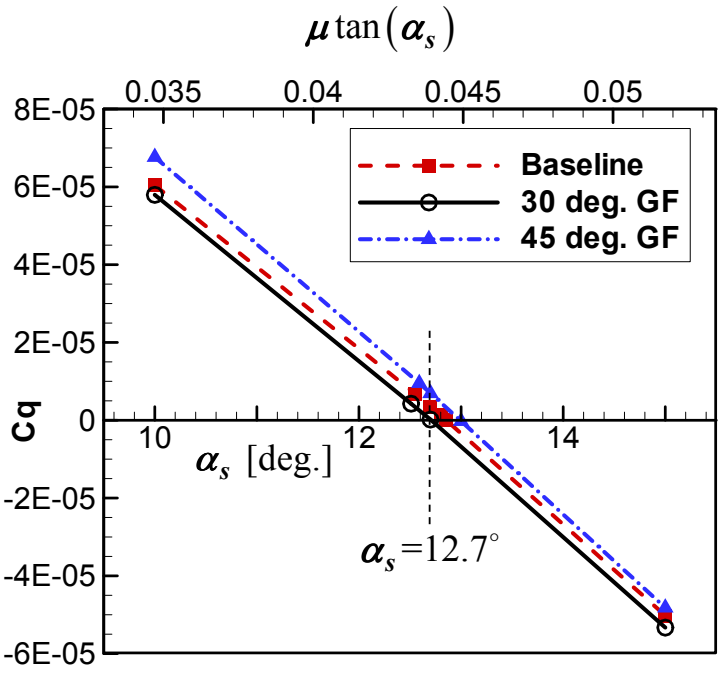

b) $V_\infty/\Omega R = 0.2$

Figure 5.7 Variation of rotor torque coefficient with descent rate

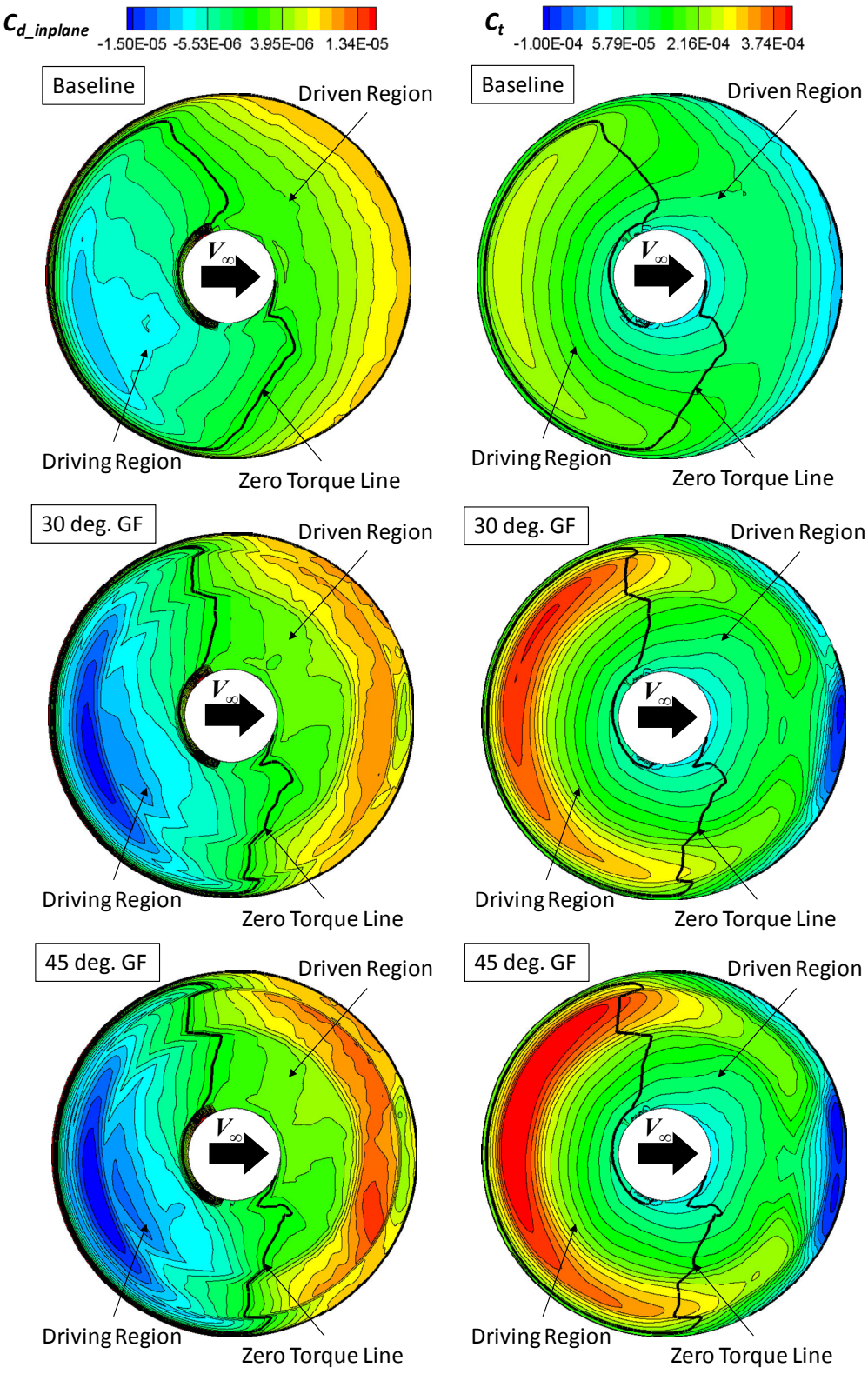

a) In-plane drag b) Thrust

Figure 5.8 In-plane drag and thrust distribution
($V_\infty/\Omega R = 0.13$, $\alpha_s = 20.9$ deg., Top View)

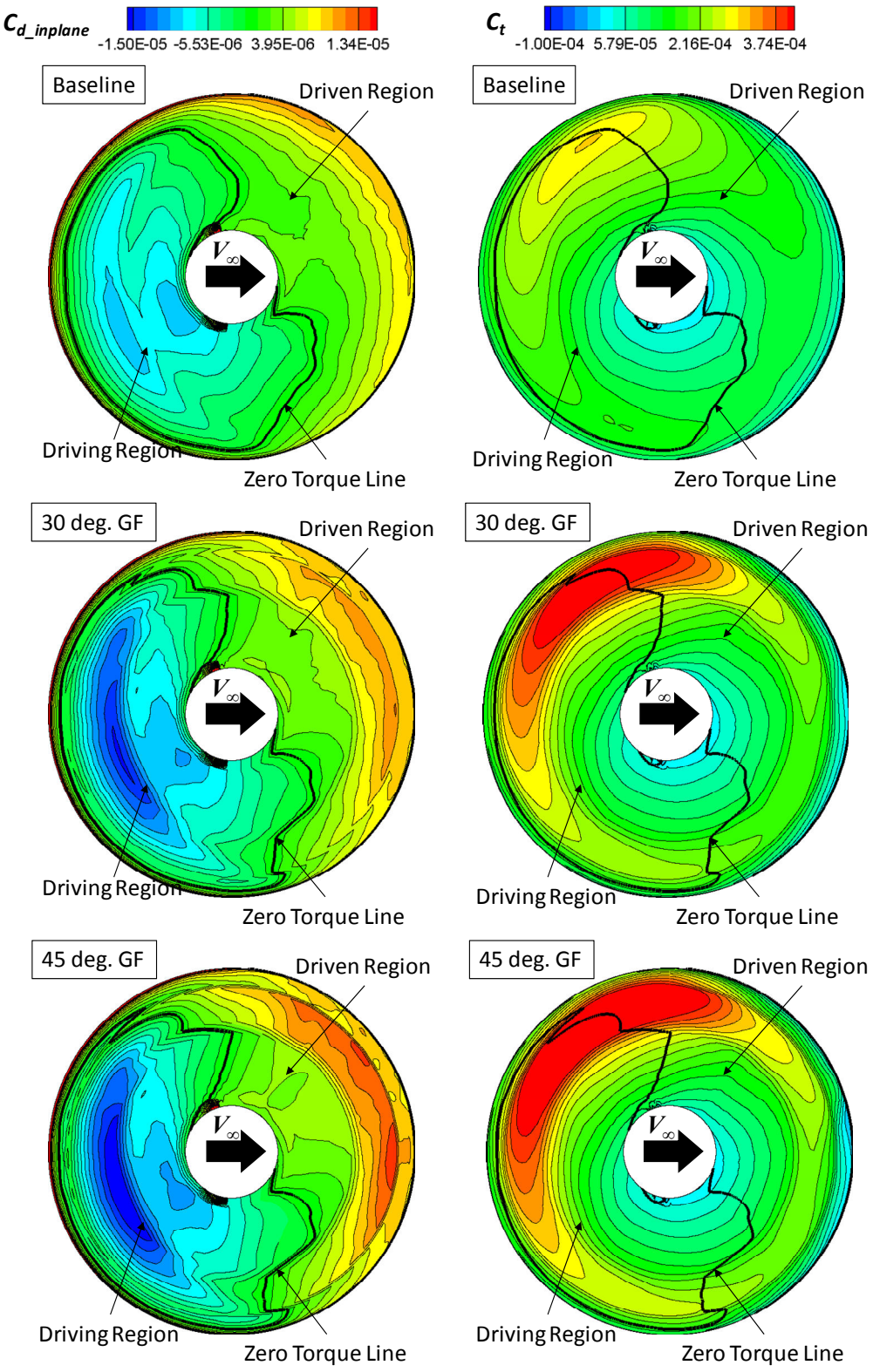

a) In-plane drag b) Thrust

Figure 5.9 In-plane drag and thrust distribution
($V_\infty/\Omega R = 0.2$, α_s = 12.7 deg., Top View)

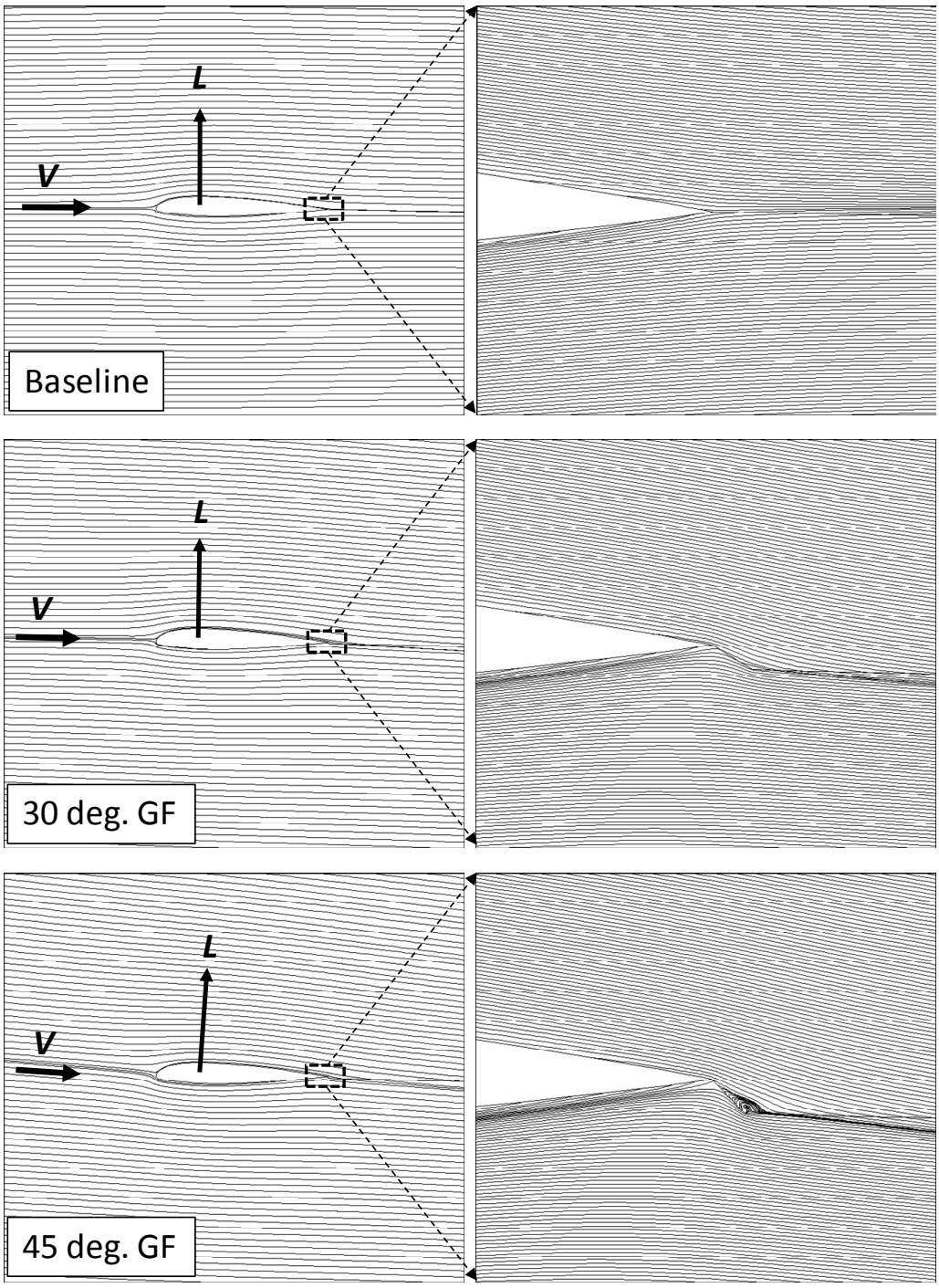

Figure 5.10 Streamlines around airfoil and in the vicinity of Gurney flap
($V_\infty/\Omega R = 0.13$, α_s = 20.9 deg., ψ = 0 deg, r/R=0.85)

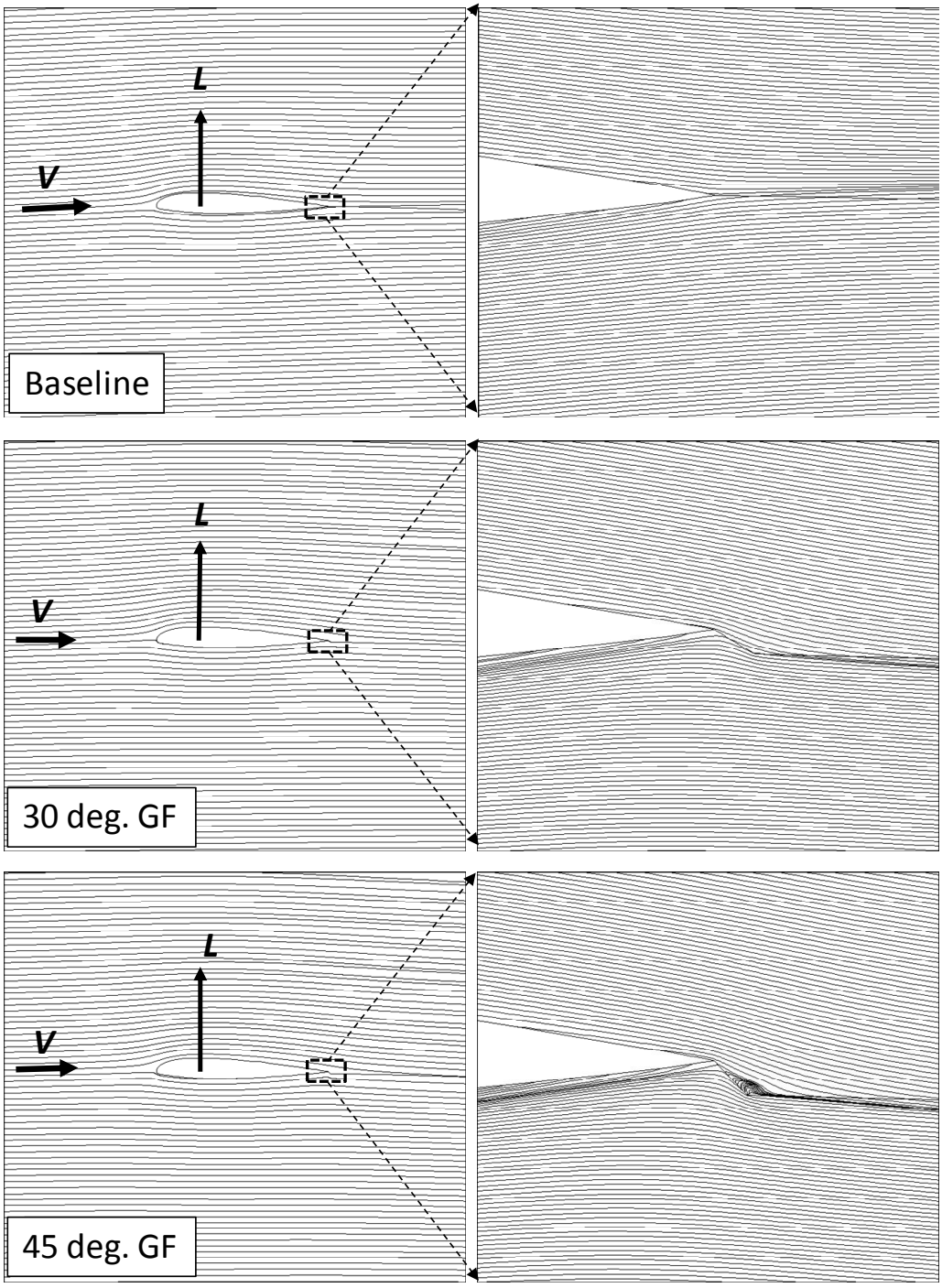

Figure 5.11 Streamlines around airfoil and in the vicinity of Gurney flap
($V_\infty/\Omega R = 0.2$, α_s = 12.7 deg., ψ = 0 deg, r/R=0.85)

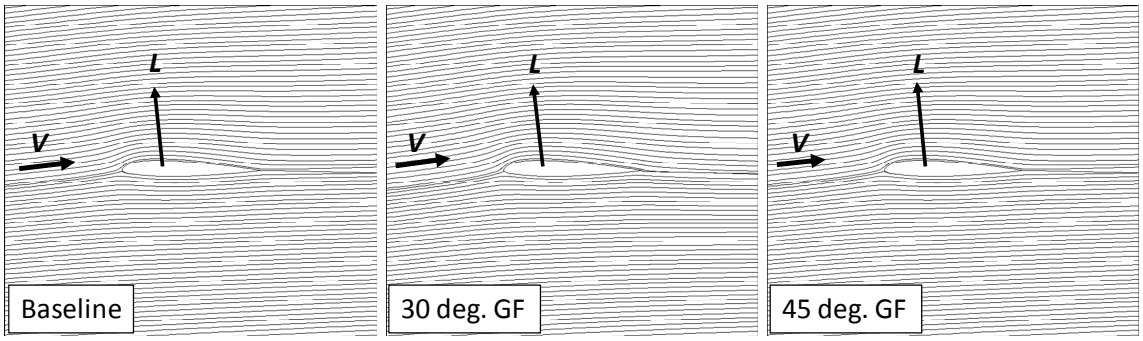

a) $V_\infty/\Omega R = 0.13$, α_s = 20.9 degree

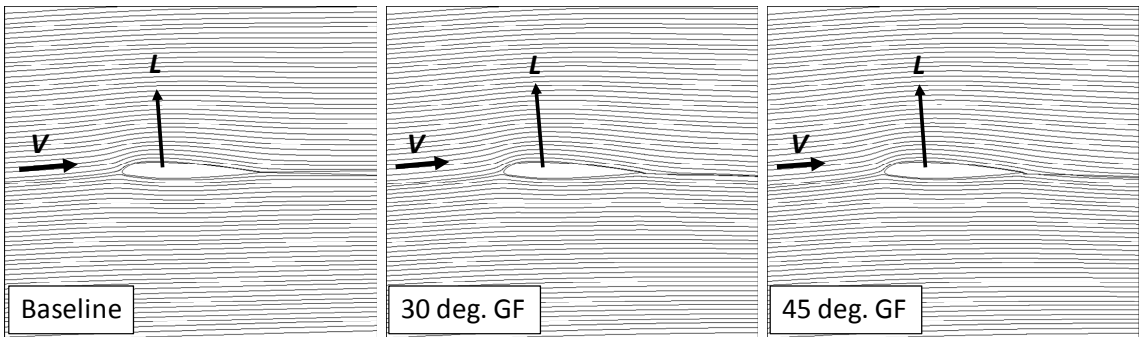

b) $V_\infty/\Omega R = 0.2$, α_s = 12.7 degree

Figure 5.12 Streamlines around airfoil, ψ = 180 deg, r/R=0.85

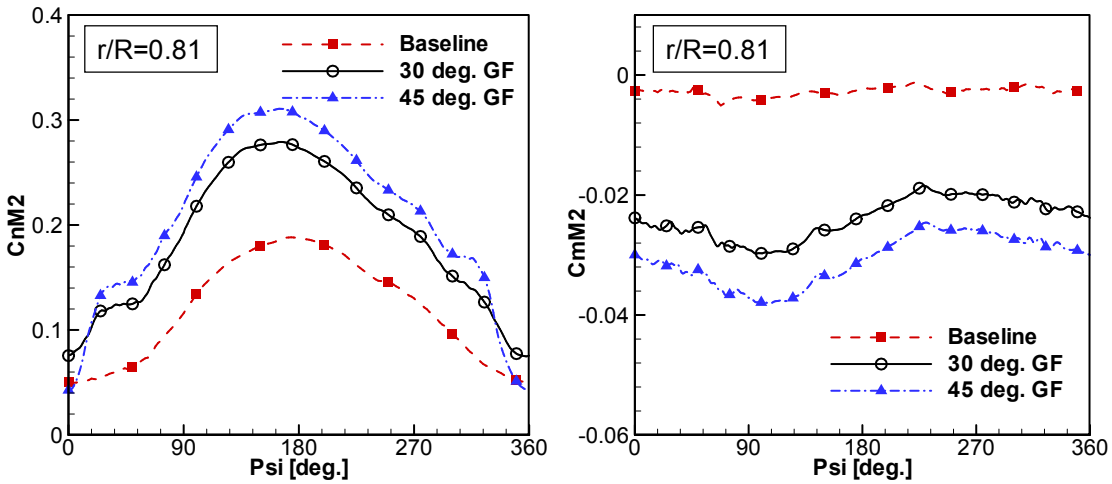

Figure 5.13 Variation of sectional normal forces and sectional pitching moment along azimuth angle, zero-torque condition, $V_\infty/\Omega R = 0.13$

5.3 Identical C_T/σ Trim

The previous study was done with the control settings locked, with the thrust coefficient allowed to vary. A subsequent study where the rotors are trimmed to identical C_T/σ was carried out to examine the effectiveness of the Gurney flap for a steady descent condition. The target C_T/σ of the baseline rotor (i.e. without a Gurney flap) was nominally set at 0.0584. For both the baseline and the Gurney flap equipped rotors, the collective pitch and the cyclic pitch were iteratively adjusted using the trim procedure described in section 2.7 until the C_T/σ reached the target value, and the azimuthally averaged rotor rolling and pitching moments at the hub were driven to zero. The trim procedure was repeated at several shaft tilt angles, and the autorotation state was estimated as the shaft angle at which the net torque is zero. As in the previous study, the elastic deformations were ignored, and the calculations were carried out in the rigid rotor mode. From the previous study, it was found that a highly deflected Gurney flap increases sectional drag. Thus, only a rotor with a 30 degree Gurney flap was studied. The Gurney flap was permanently deployed over the same radial locations as shown in Figure 5.6. The freestream velocity was held constant as $V_\infty/\Omega R = 0.13$.

The numerical schemes, grid system, and time steps were identical to the previous study. However, since the multiple cases of numerical trim procedure requires huge computational time, a one-equation SA-DES turbulence model was used instead of the two-equation KES model.

The resultant torque coefficients obtained from the trimmed state are plotted in Figure 5.14 as a function of shaft tilt angle. Unlike the previous study, with the rotor trimmed for zero hub moments and target thrust, the estimated descent rate required to

sustain autorotation was higher for the Gurney flap equipped rotor than for the baseline rotor. The estimated shaft tilt angle required for the autorotation state was 25 degree for the baseline rotor and 27 degree for the Gurney flap equipped rotor. Figure 5.15, Figure 5.16 and Figure 5.17 compares torque, thrust and in-plane drag distribution over the disk at the shaft tilt angle of 25 degrees, where the baseline rotor is in the autorotation state while the Gurney flap rotor still requires a shaft torque input. It is observed that the Gurney flap equipped blade section produces higher thrust and that the rotor with the Gurney flap experiences dramatic change in the in-plane drag from negative over the front half of the disk (driving region) to positive over the aft side of the disk (driven region). To investigate the reason for the high propulsive and drag forces, flow field around the blade at the driving and driven region was examined. Streamlines shown in Figure 5.18 at driving region reveals that the lift vector tilted forward, thus propulsive force is produced. On the contrary, Figure 5.19 shows the lift vector is almost normal or tilted slightly backward, thus the local lift contributes to the induce drag on top of the profile drag. In the previous fixed control setting study, the thrust increase was mainly generated over the front section of the disk, thus the lift contribution to the propulsive force was greater than its contribution to the drag force. However, when the rotor is trimmed for zero hub moments and specified thrust, the increased thrust was more evenly distributed over the disk to balance the hub moments. Note that the effective angles of attack in both the driving (Figure 5.18) and the driven (Figure 5.19) regions are similar. Therefore, the difference of the lift force contributions to the propulsive and drag forces is less than the case when the control setting is fixed. Since the Gurney flap increases profile drag as well, the net effect of the flap in the driven region is to increase the total

drag. The integrated effect of these high in-plane forces with the Gurney flap resulted in more drag and smaller driving region. As a result, faster descent rate was required to establish autorotation state with the current configuration of the Gurney flap equipped rotor.

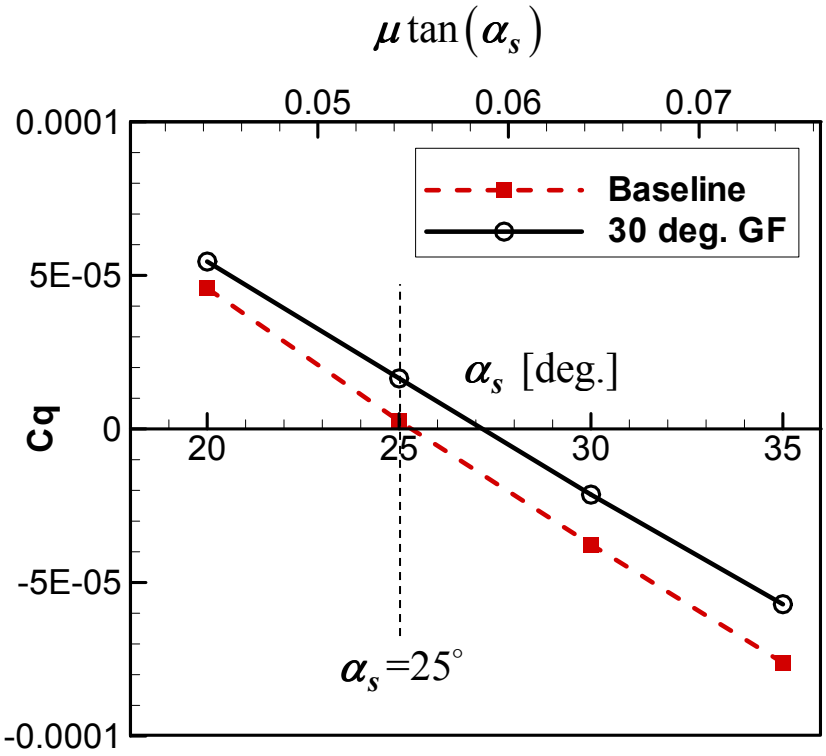

Figure 5.14 Estimation of autorotation state

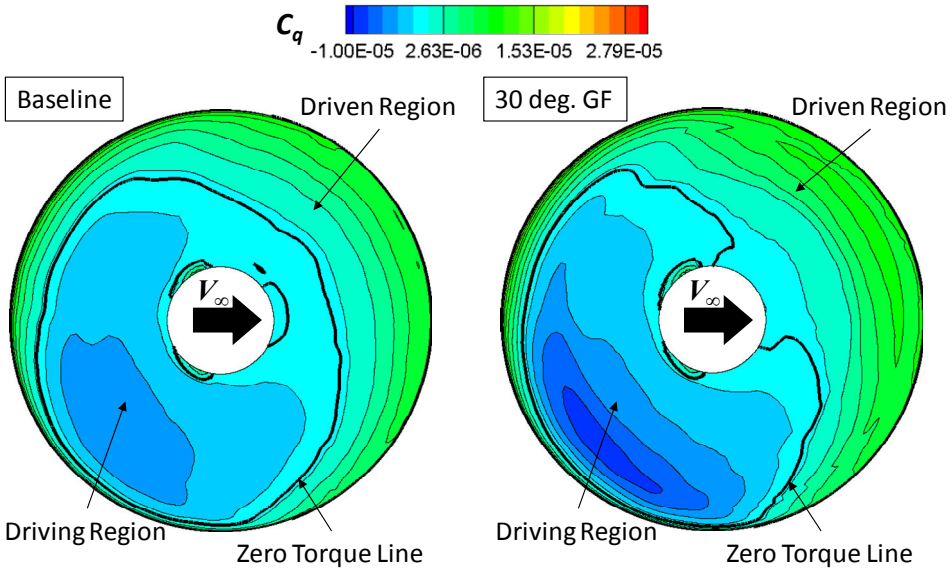

Figure 5.15 Torque distribution ($V_\infty/\Omega R = 0.13$, $\alpha_s = 25$ deg., Top View)

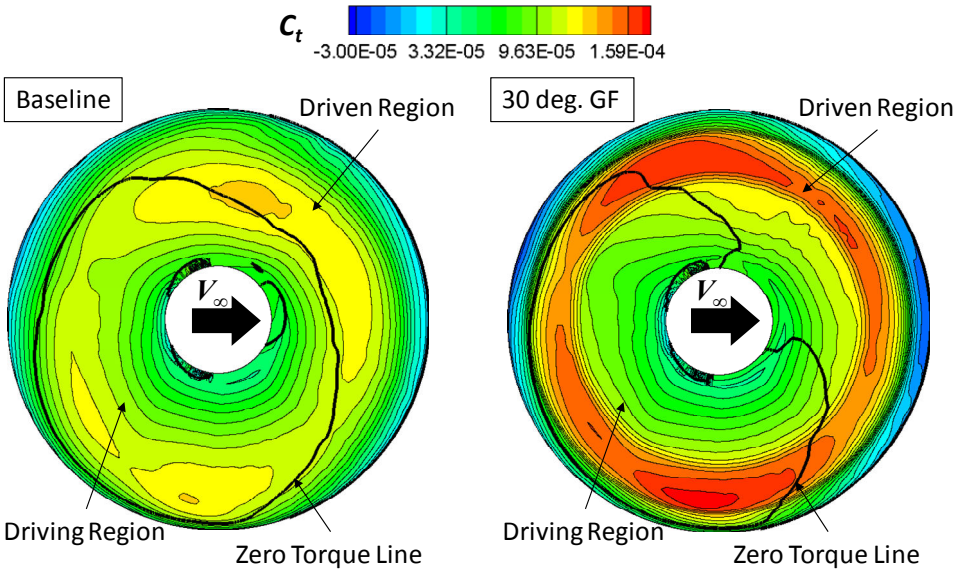

Figure 5.16 Thrust distribution ($V_\infty/\Omega R = 0.13$, α_s = 25 deg., Top View)

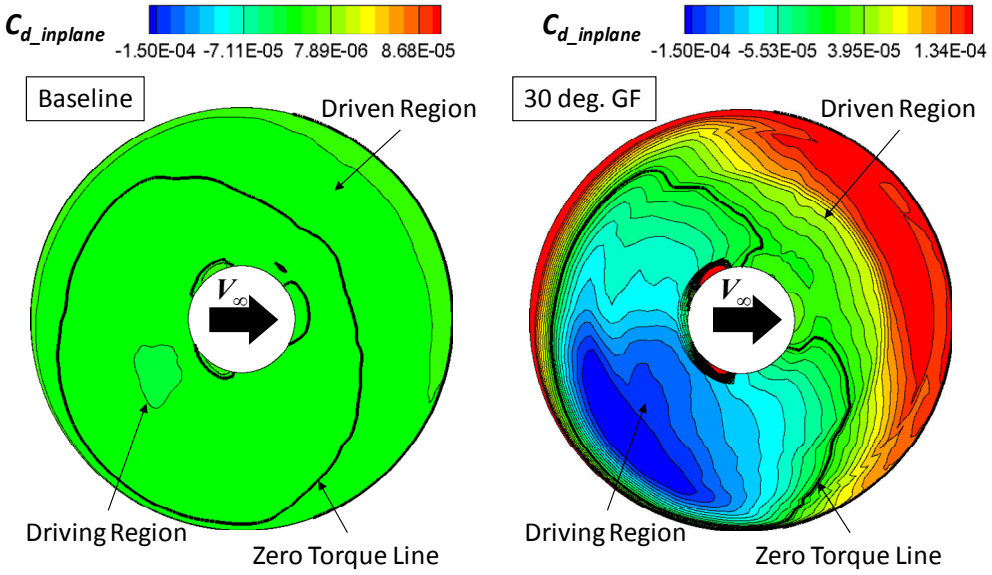

Figure 5.17 In-plane drag distribution ($V_\infty/\Omega R = 0.13$, α_s = 25 deg., Top View)

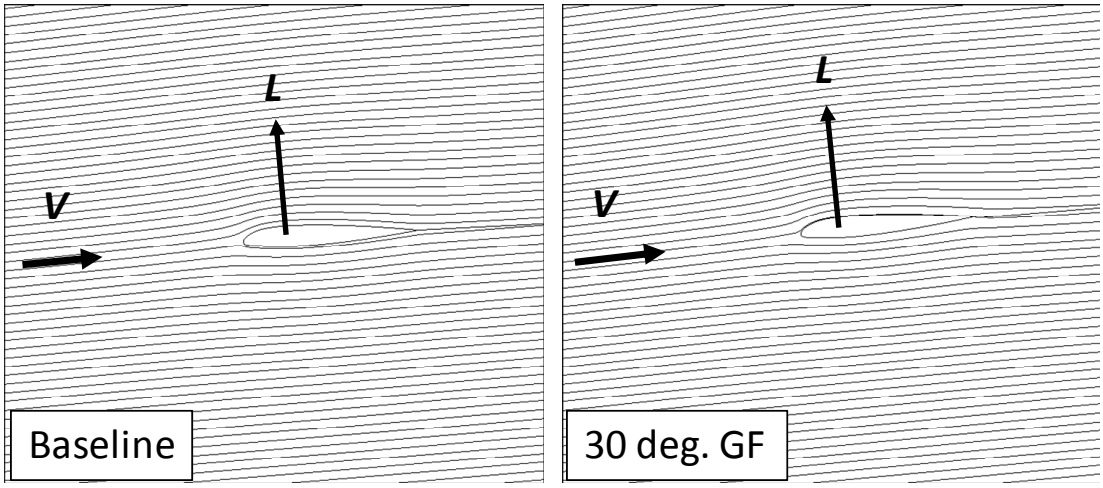

Figure 5.18 Streamlines around blade at driving region
($\psi = 225\ deg.,\ r/R = 0.85$)

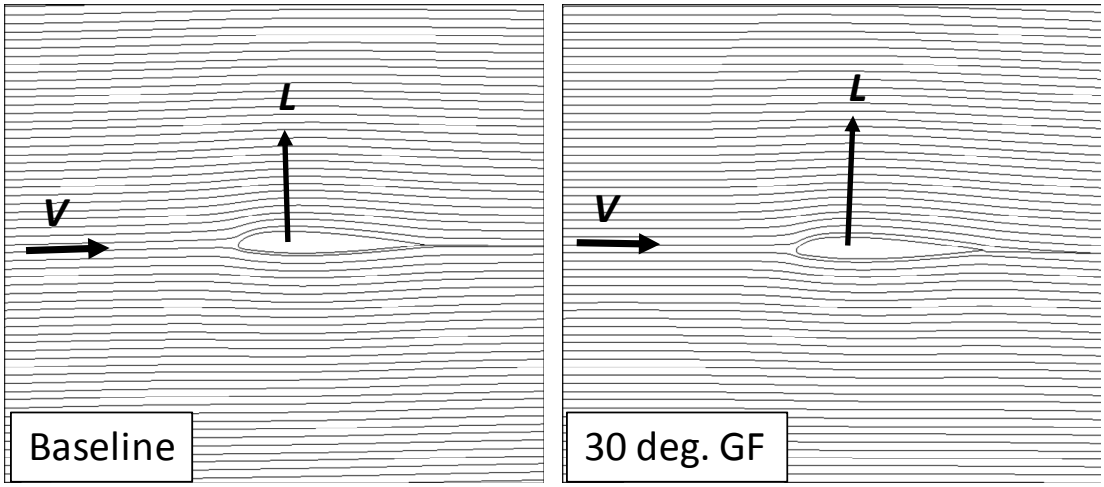

Figure 5.19 Streamlines around blade at driven region
($\psi = 45\ deg.,\ r/R = 0.85$)

5.4 Chapter Summary

When the baseline rotor and the Gurney flap equipped rotor are operated at identical control setting, autorotation conditions were established by a series of shaft angle sweeps that produce zero torque with the same collective and cyclic pitch input for all rotors including baseline, a rotor equipped with a 30 degree Gurney flap, and a rotor with a 45 degree Gurney flap. It was found that the deployment of the flap with a moderate 30 degree deflection angle simultaneously increased rotor thrust and decreased the descent rate needed to maintain autorotation. However, a highly deflected 45 degree Gurney flap caused flow separation and the attended drag rise reduced its beneficial effect. Although a more detailed study is needed, it appears that a properly designed Gurney flap deployment could be useful in flare-type autorotation prior to touch-down by increasing thrust especially for high disk loading or hovering autorotation.

Next, all the rotors were trimmed to an identical thrust and zero hub moments by iteratively adjusting collective and cyclic pitch controls using CFD-coupled numerical trim procedure. The trim procedure was carried out for several shaft angles of attack, and the autorotation state was estimated where the torque is zero. With the careful trim procedure, it was found that the current model of Gurney flap equipped rotor required faster descent rate than the baseline rotor to maintain autorotation state. Although the flap installed portions of the blade produce a higher propulsive force in the driving region, the profile and induced drag rise in the driven region was higher, and the net effect increased shaft torque.

However, the study indicates that if a small amount of power is available to deploy Gurney flaps under engine failure conditions, deploying the flap in the driving

region may accelerate autorotation state and slow down the descent rate. Similarly, deployable Gurney flap may be used in an auto-gyro. The flap deployed in the driving region may enable the auto-gyro to operate at a lower backward disk tilt angle, reducing vehicle drag and increasing lift.

However, the study indicates that if a small amount of power is available to deploy Gurney flaps under engine failure conditions, deploying the flap in the driving region may accelerate autorotation state and slow down the descent rate. Similarly, deployable Gurney flap may be used in an auto-gyro. The flap deployed in the driving region may enable the auto-gyro to operate at a lower backward disk tilt angle, reducing vehicle drag and increasing lift.

CHAPTER 6

STUDY OF DEPLOYABLE GURNEY FLAP FOR ROTOR VIBRATION REDUCTION

The effect of a Gurney flap is to increase sectional lift by forcing flow to follow the increased airfoil curvature near the trailing edge, so that the circulation is enhanced. The Gurney flap may be deployed either lower or upper sides of an airfoil to increase lift or act as a spoiler. Gurney flaps are an attractive active control mechanism due to their simplicity, small size, and light weight.

In this chapter, use of dynamically deployed Gurney flaps is explored as an OBC concept to reduce rotor vibration. The four-bladed HART-II rotor model [92,93] is used as a representative rotor. The flight condition corresponds to a forward flight descent mode with advance ratio of 0.15 and a hover tip Mach number of 0.64. The HART-II program includes higher harmonic control (HHC) test for minimum vibration and noise. The test was repeated with 3P HHC input superposed over the baseline control at the same descent condition. Among those test cases, baseline and the minimum vibration cases with HHC were simulated in the present work, and compared against the Gurney flap OBC concept.

In all subsequent computations in this chapter, the baseline scheme (Roe's FDS with 3^{rd} order MUSCL, 1^{st} order LUSGS time marching scheme without sub-iteration) with KES turbulence model is used. Since low frequency vibratory loads are of more concern rather than high frequency BVI events, the embedded grid option, which requires more memory and CPU time, was not utilized in this chapter. Based on the near-wall grid

independence and time step convergence study performed for the validation of HART-II rotor in section 4.6, the same grid density along surface normal direction was maintained as in Chapter 4. The blade was rotated 0.05 degrees azimuth per time step.

6.1 Preparatory 2-D studies

Prior to its application to the three dimensional rotor blades, the dynamically deployed Gurney flap was tested in a 2-D airfoil to determine the air load response. The NACA 23012 airfoil, the airfoil used in the HART-II blade, was selected. Gurney flaps were deployed on the lower and upper surfaces of the airfoil at 90% chord with the following function:

$$l_{GF} = l_{GF-max} \sin(2kM_{\infty}t) \tag{6.1}$$

Where, M_{∞} is the reference Mach number, and k is the reduced frequency. A positive value for l_{GF} represents a lower side deployment, while a negative value indicates an upper side deployment. The reference Mach number and reduced frequency were selected so that the analysis simulates the baseline descent mode of the HART-II rotor. The corresponding reference Mach number was 0.64 (hover tip Mach number of the blade). The reduced frequency was 0.121 for 4P deployment and 0.242 for 8P deployment. The maximum Gurney flap length was limited to 1% of the airfoil chord length to reduce the sectional drag penalty and reduce nose-down sectional pitching moments.

6.1.1 Grid Independence Study for the Modeling of Deployable Gurney Flap

Since the deployable Gurney flap is simulated using dynamic wall boundary condition, the grid resolution along the Gurney flap is of concern in establishing the model's accuracy. Two sets of grids in the vicinity of the Gurney flap were tested. Figure

6.1 shows the grid around Gurney flap. The fine grid system has more than twice the grid points along the flap as the baseline grid, and more grid points were placed upstream and downstream of flap in the airfoil chordwise direction. Figure 6.2 compares predicted delta-airloads from two grid sets. Here, delta-airloads is the airloads difference between Gurney flap deployed airfoil and the clean airfoil. The predictions from both grids compare well with each other. Spikes were observed in the drag coefficient, and it was greater with the coarse baseline grid. This is caused by the step change in the number of grid points on the flap from one time step to the next. The spikes are reduced with a finer grid since the cell size is smaller, the step changes are small and the wall boundary condition is turned on in more smooth and gradual manner. However, the low frequency content of the drag values on the two grid systems is quite similar. The lift variation was smooth in both grid systems, and the pitching moment variation shows a small fluctuation due to the drag oriented moment. Based on this study, a grid similar to the baseline grid was used in all subsequent 2-D and 3-D computations.

6.1.2 Unsteady Airloads Response to the Dynamically Deployed Gurney Flap

The dynamic deployment of Gurney flap causes unsteady variations in the sectional loads. This includes phase lag and delta magnitude of airloads relative to the steady state air loads. Identifying the temporal (or phase) lag between the Gurney flap deployment and the air load response is important in establishing a Gurney flap schedule.

Figure 6.3 and Figure 6.4 shows air loads with deployed Gurney flap scheduled for reduced frequency of 0.121 and 0.242. In the delta-C_l plot for k=0.121, it is clearly seen that the zero, maximum and minimum lift occur with a 38.5 degree (0.1069 cycle) phase lag from the flap schedule. In comparison, the phase lag was about 55 degree

(0.153 cycle) for the k=0.242 case. However, drag variation follows the flap schedule without noticeable phase lag because the flap deployed normal to the flow leads to a nearly instantaneous loss in momentum, unlike the lift generation that requires flow settling time needed to build circulation. The phase-lag for the pitching moment was somewhat between the lift and drag phase lags due to both of their contribution to the moment. A noticeable decrease in the magnitude of the lift is also observed with the higher frequency flap deployment, similar to classical unsteady aerodynamics where an increase in frequency leads to a reduced lift and moment response.

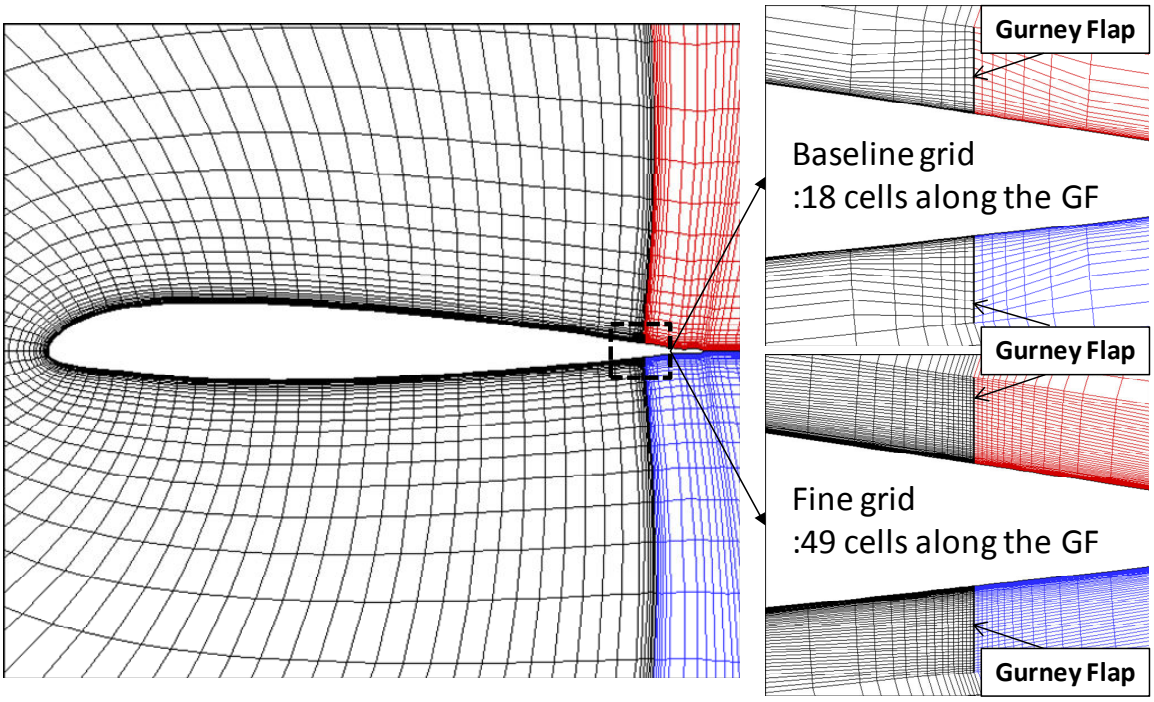

Figure 6.1 Gurney flap grid resolution

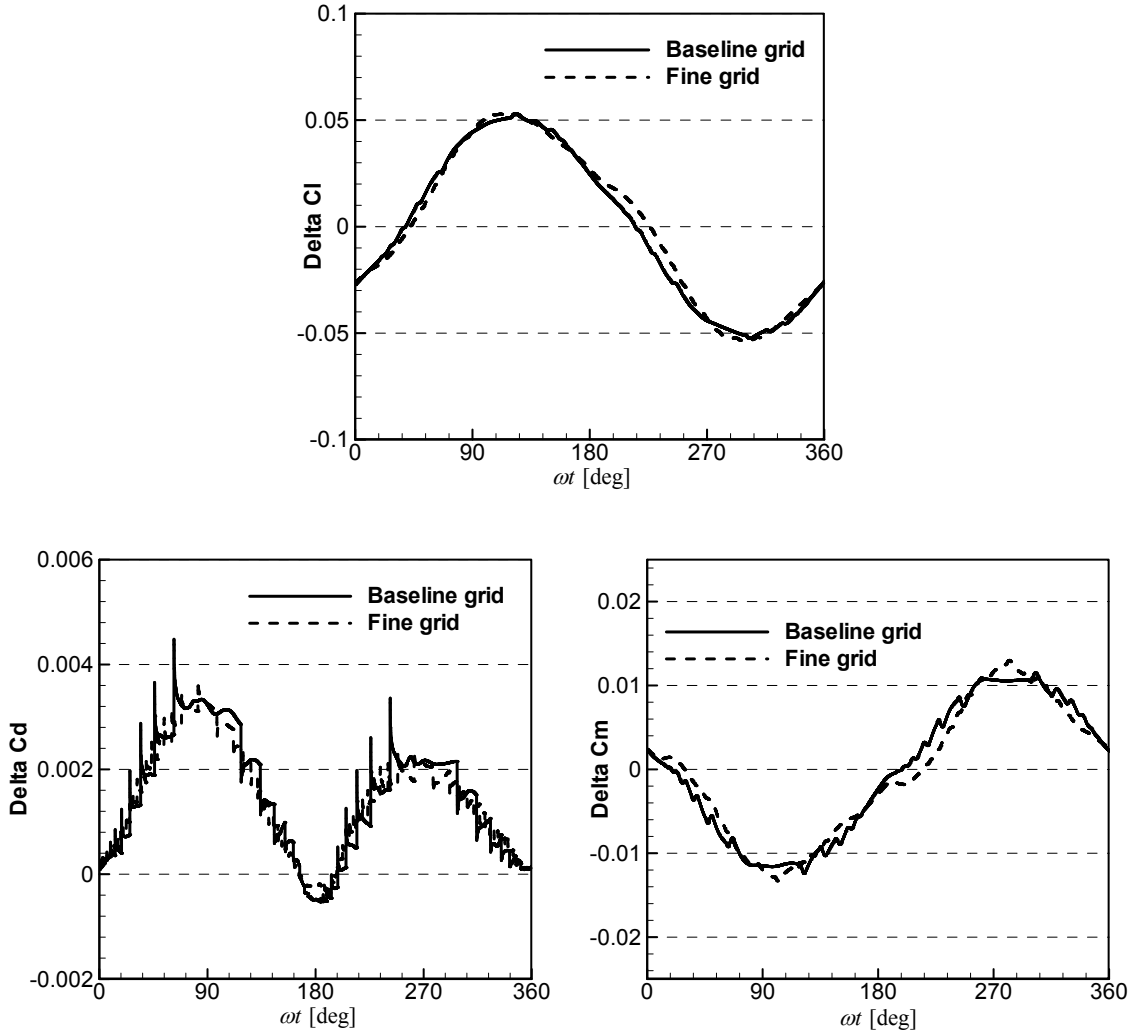

Figure 6.2 Delta-airloads comparison

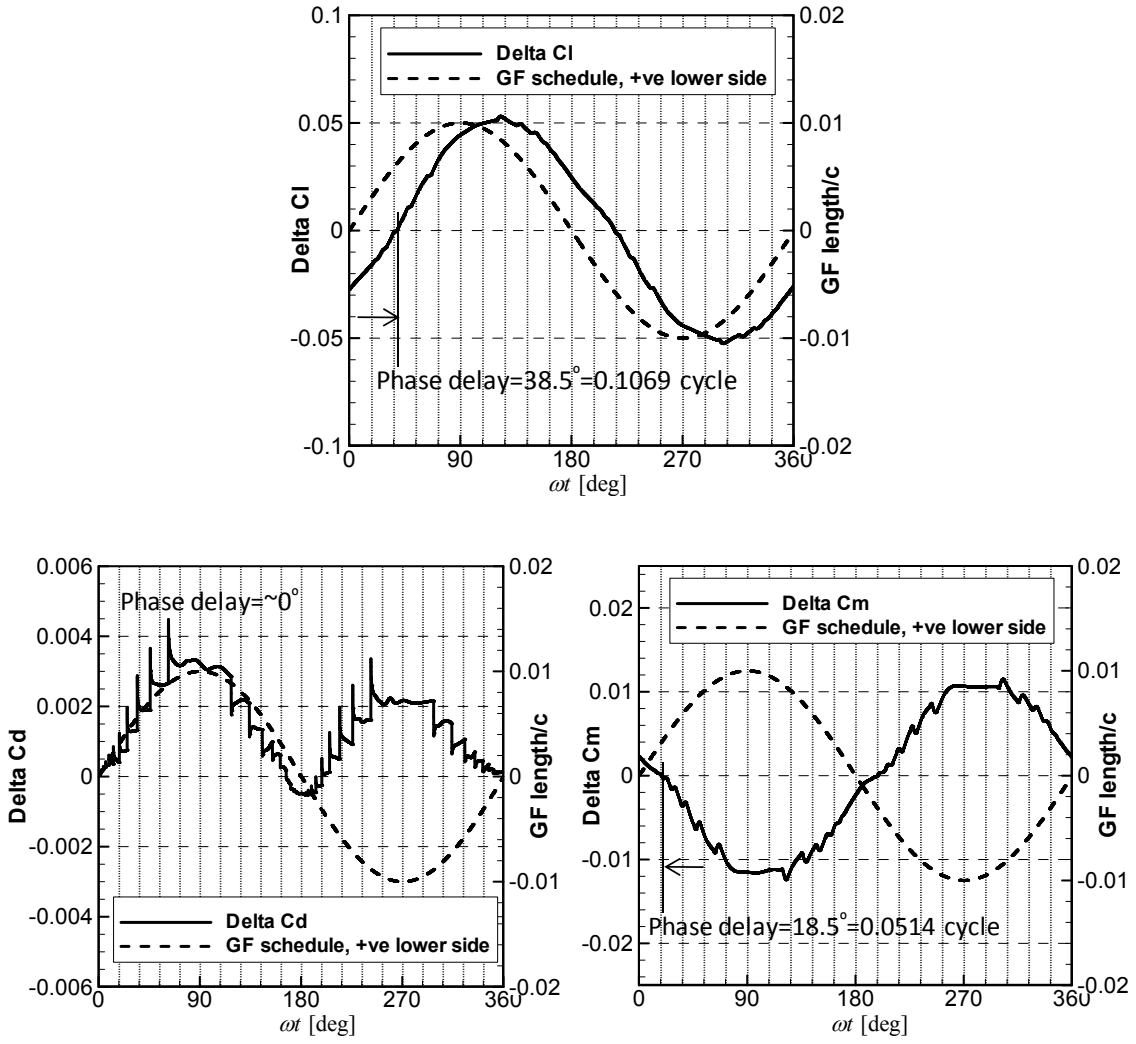

Figure 6.3 Airloads phase lag: k=0.121 (4P)

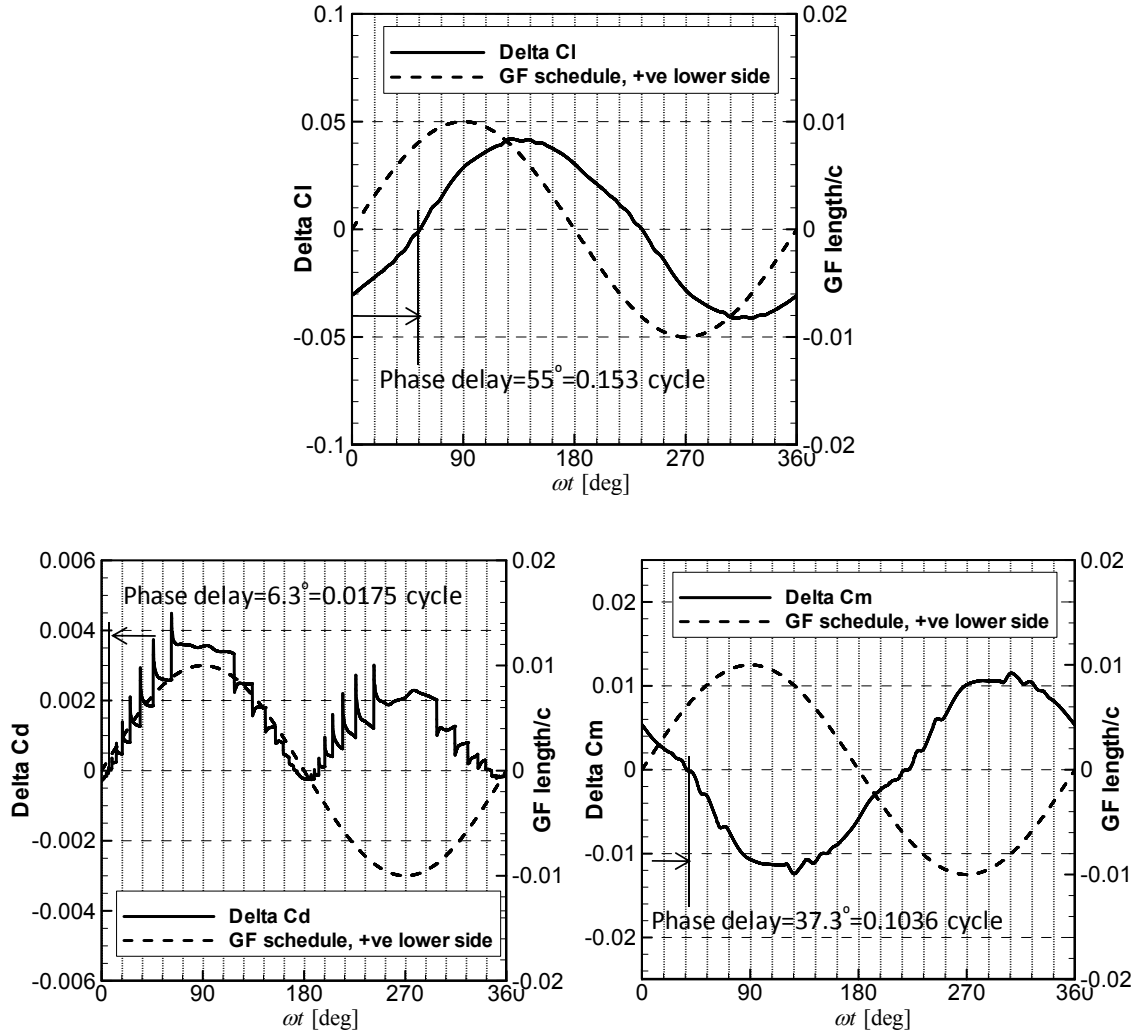

Figure 6.4 Airloads phase lag: k=0.242 (8P)

6.2 HART-II Rotor: Gurney Flap Deployed at the Lower Side of Trailing Edge

In this configuration, Gurney flap is installed at the lower side of trailing edge with 1.5% chord length as shown in

Figure 6.5. Note that the trailing edge tab was removed. The dynamic deployment of Gurney flap was simulated via dynamic wall boundary condition addressed in section 2.9. In this preliminary study, the azimuthal and span-wise location of the Gurney flap deployment was manually adjusted to minimize 4P vertical hub vibration. However, the determining of the deployment schedule was based on the following procedure.

1. The baseline rotor, HART-II model without trailing edge tab, was analyzed prior to the Gurney flap simulation for a flow condition identical to the descent state experiment [92,93].
2. The hub load was filtered and the 4P harmonic load, which is the highest vertical vibration source in this 4 blades rotor, was obtained using Fourier analysis.
3. The lift increment due to Gurney flap was assumed as a sinusoidal function over the deployment interval, and one time deployment was assumed.
4. The lift increment is added to the baseline rotor, and an optimizer is used to find the minimum 4P normal force vibration. The azimuthal angle where the Gurney flap begins to deploy, the deployment interval, and the magnitude of the lift increment are considered as independent variables.
5. The flow solver is then used with the Gurney flap schedule obtained at step 4 as an initial guess. The span-wise deployment location is manually adjusted by trial and error to achieve reductions in vibratory loads. The azimuthal

location was also adjusted to account for the input and output phase difference in unsteady flow phenomena.

The procedure is shown in Figure 6.6. A prescribed blade motion, obtained from OVERFLOW2-CAMRAD-II coupling analysis [94] for HART-II model was used to quickly examine the possibility of the Gurney flap as an OBC concept for vibration reduction.

Several Gurney flap deployments were examined, and one of these was selected for examination. Note that this is not an optimum schedule. The Gurney flap was deployed at the first quadrant, in the outboard region from 70 to 90% of radius as shown in Figure 6.7. Figure 6.8 compares the Z force (normal to hub plane) distributions of the baseline, HHC, and Gurney flap OBC cases, and Figure 6.9 compares filtered vibratory load of each cases. The higher harmonic control case has superposed HHC amplitude of 0.79 degree ($\theta_3 = 0.79^\circ$), and 180 degree ($\psi_3 = 180^\circ$) phase angle on top of the baseline motion. The comparison with the measured data could not be made because the measured hub loads are not available. The baseline rotor shows distinct peak values over the advancing side and the retreating side, which contribute to 4P vibrations. The HHC rotor shows that the peak values are slightly extended to rear side with another peak value at the front disk, where maximum 3P higher harmonic pitch angles occur. The combined effect of this extended peak value smoothes out the distinct normal force peak, and reduces the 4P vibratory loads. With the Gurney flap deployed over the first quadrant, additional peak thrust is introduced in the first quadrant. Figure 6.10 shows that the flow around the Gurney flap is deflected downward like a cambered airfoil, and the lower surface near the trailing edge is pressurized at the windward side of the flap. The

combined effects increases lift generation over the baseline airfoil. Notice that the additional thrust peak in the first quadrant occurs about 45 degree, which is the phase difference between high peak and low peak of the 4P vibratory load, earlier than the original thrust peak in the advancing side. This additional thrust cancels out the low peak of the baseline rotor vibratory load. As a result, the Gurney flap OBC reduces 4P vibratory loads even more than the HHC result. Figure 6.9-a shows the 3P~10P loads, while Figure 6.9-b shows the 4P vibratory loads. The Gurney flap OBC is seen to reduce the 4P normal vibration by 80%, while the HHC achieves a 53% reduction (Table 6.1). The equivalent L/D_e ($= L/[D + M_z\Omega/V_\infty]$) of the Gurney flap OBC was slightly less than others in this identical blade motion analysis due to flow separation behind flap and attended drag rise (Figure 6.10).

The side force, H force, and hub moments variations are compared in Figure 6.11. The magnitude of the vibratory loads is small and all cases (baseline, HHC, Gurney) yielded comparable results. The roll and pitching moment vibrations of the Gurney flap OBC were the lowest and HHC showed the highest variations of these moments.

The pressurized wind-ward side of the Gurney flap (Figure 6.10) and separation behind the flap introduces a large nose-down pitching moment at the local blade section as indicated in Figure 6.12. This may cause large torsional deformations of the rotors and lead to blade fatigue. Another issue is the hub moment imbalance. Since the Gurney flap was deployed at the first quadrant only, the additional lift from the Gurney flap caused higher roll and pitching moments at the hub. The roll moment was almost doubled and the pitching moments was changed about 20% with the Gurney flap. The changes to the hub moments of the HHC rotor were negligible.

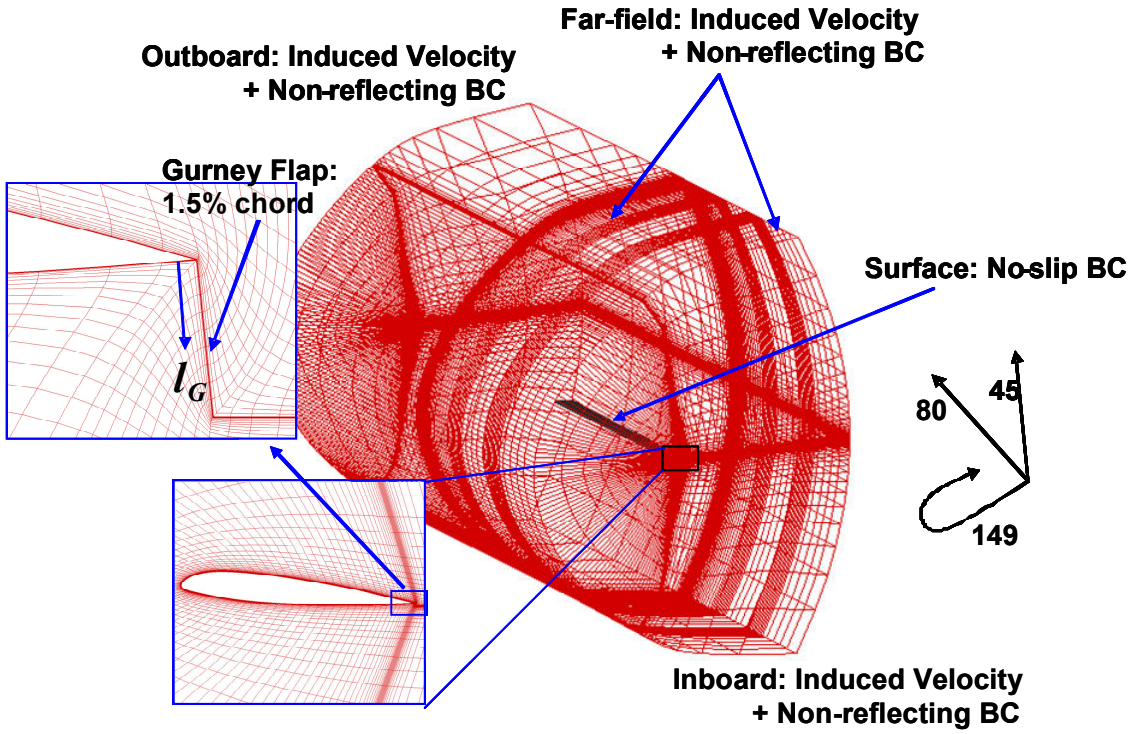

Figure 6.5 Grid system for lower side Gurney flap simulation [149×80×45]

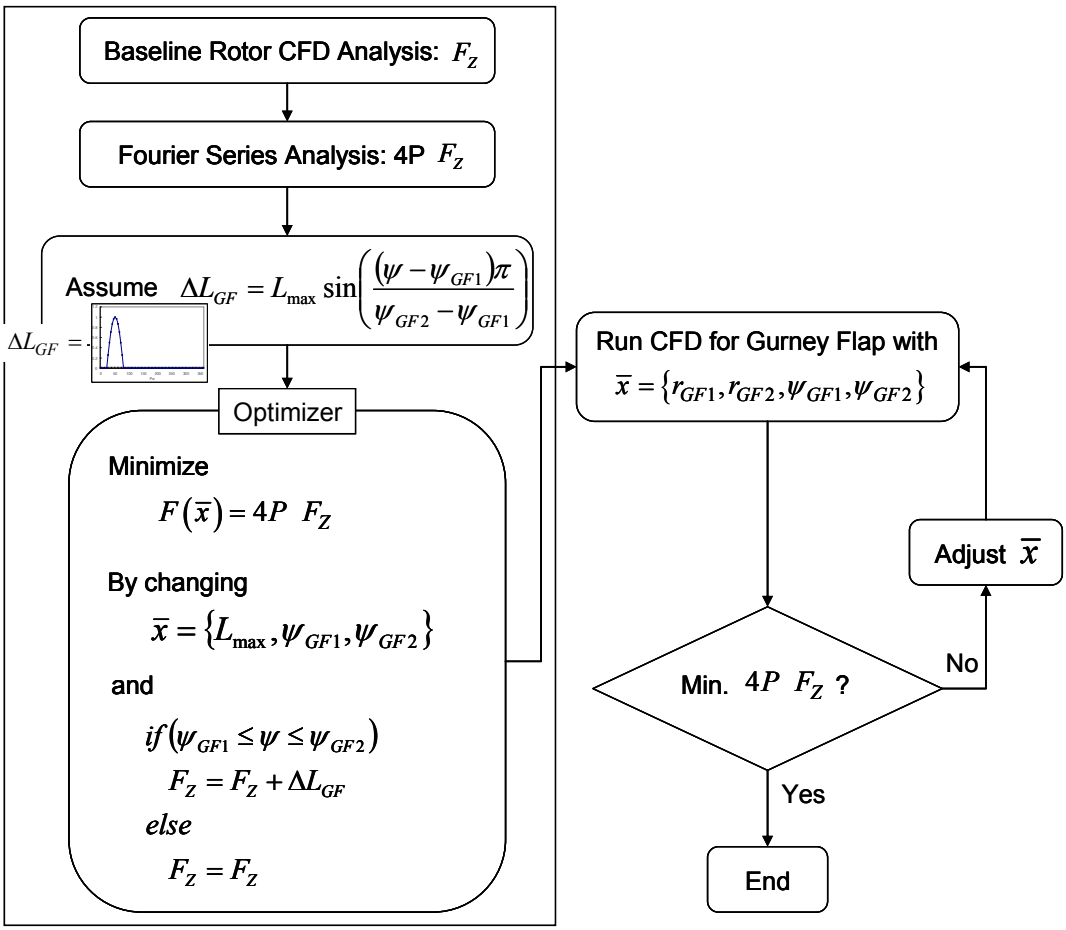

Figure 6.6 Gurney flap schedule determination

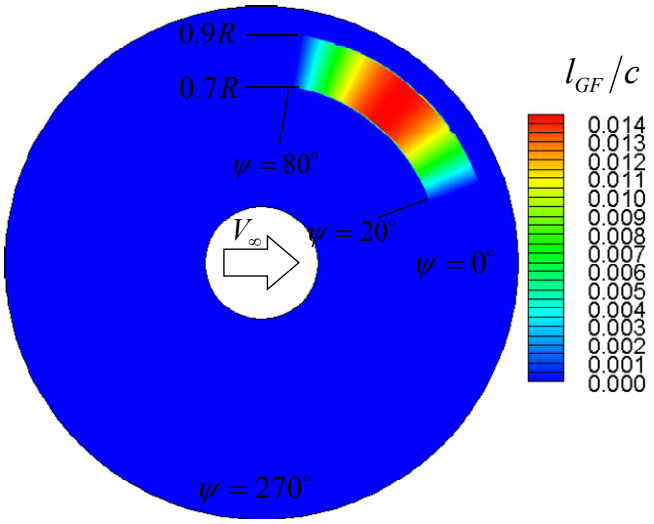

Figure 6.7 Determined Gurney flap schedule

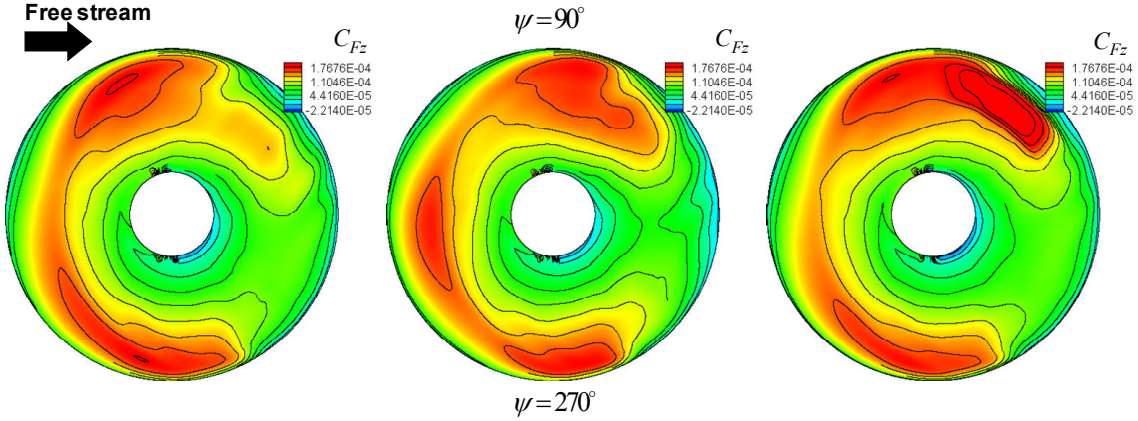

a) Baseline b) HHC c) GF OBC

Figure 6.8 Vertical force distributions

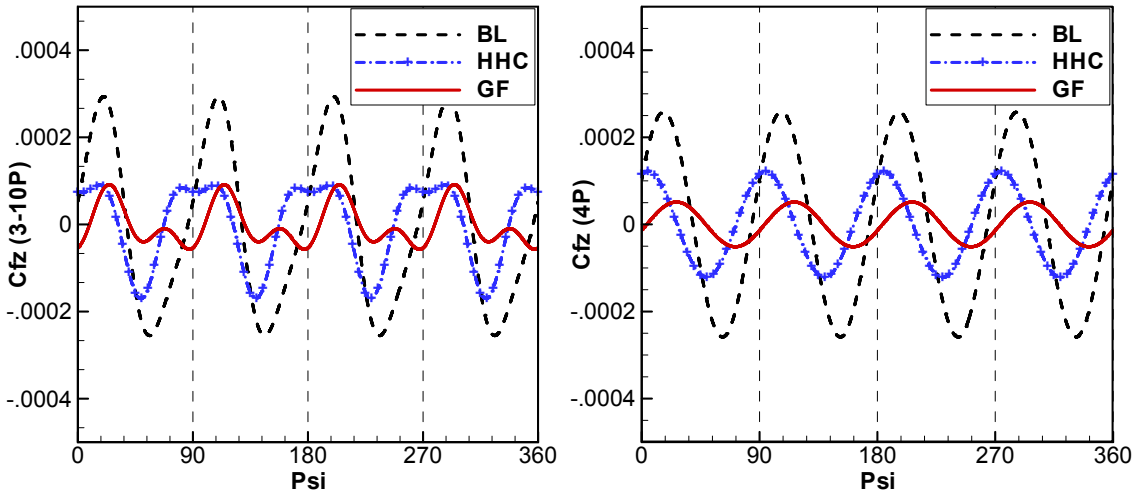

a) 3-10P frequency b) 4P frequency

Figure 6.9 Vertical hub load

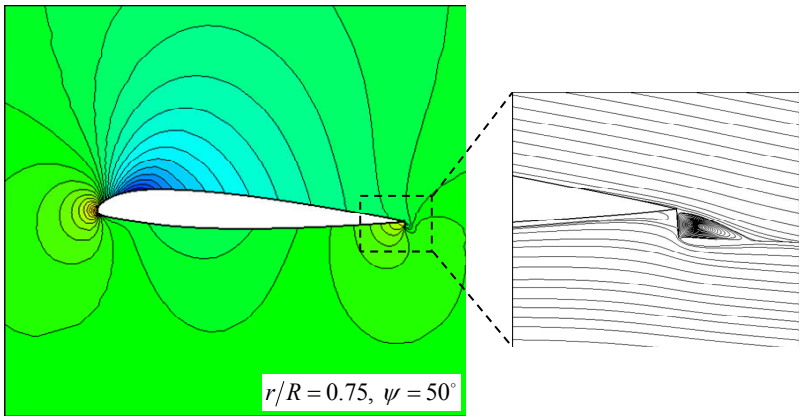

Figure 6.10 Pressure contour and streamline near the Gurney flap

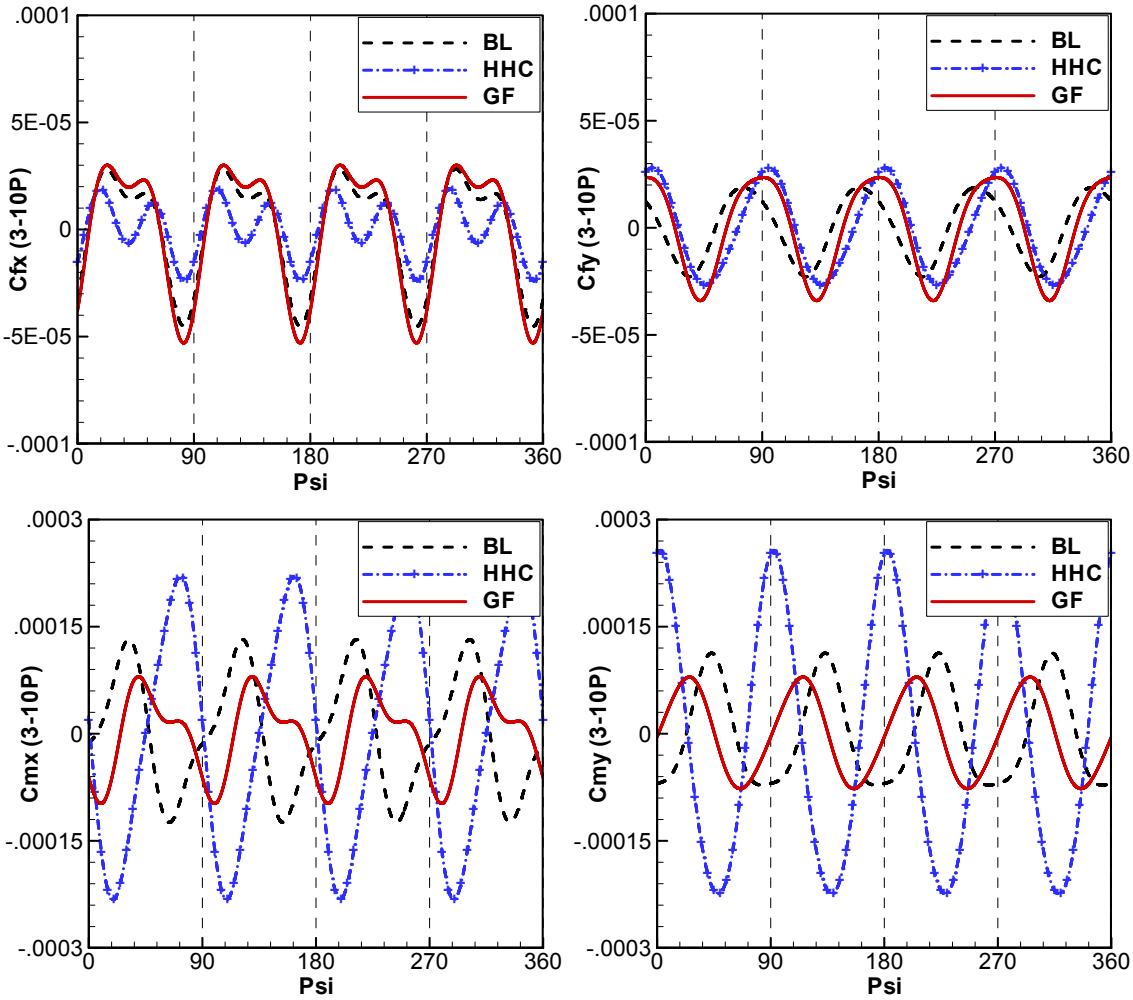

Figure 6.11 H force, Y force, roll and pitching moment vibration

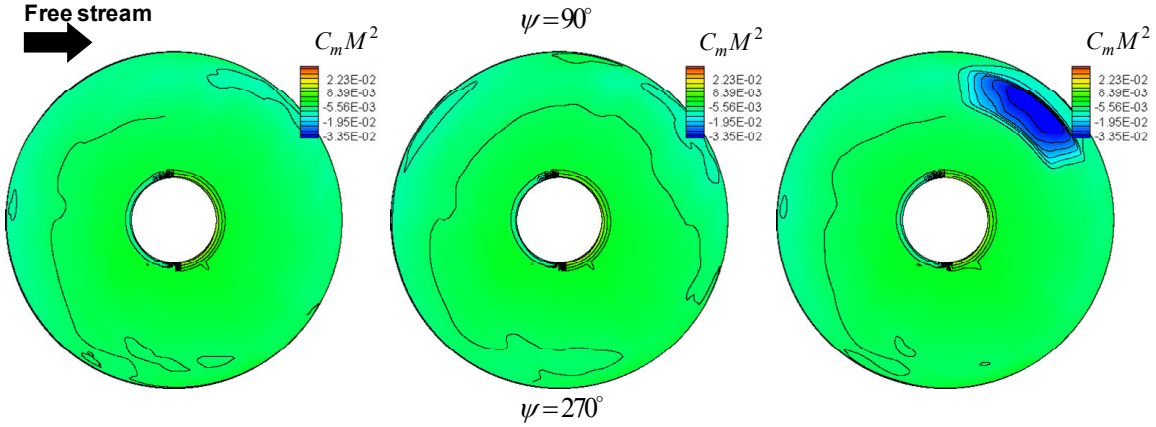

a) Baseline b) HHC c) GF OBC

Figure 6.12 Local pitching moment distributions

Table 6.1 4P vibration and performance characteristics

	Baseline	HHC	GF OBC
4P Vertical load reduction	0	53 %	80 %
$(L/D_e)/(L/D_e)_{BL}$	1	1.01	0.94

Table 6.2 Thrust and moments deviation

	C_T/C_{T_BL}	$\Delta C_{m\_x}=C_{m\_x}-C_{m\_x\_BL}$	$\Delta C_{m\_y}=C_{m\_y}-C_{m\_y\_BL}$
HHC	1.010	0.099×10^{-4}	0.026×10^{-5}
GF OBC	1.016	1.36×10^{-4}	-7.64×10^{-5}

6.3 HART-II Rotor: Gurney Flap Deployed at Both Lower and Upper Surfaces of Airfoil

In the previous section, a suitably chosen schedule for the Gurney flap deployment was shown to reduce the 4P vertical hub vibratory loads up to 80% for the HART-II descent condition with negligible performance penalty. However, these studies were carried out for a prescribed blade motion obtained from a baseline rotor analysis, with a fixed control setting. The resultant thrust and hub moments differed from the baseline rotor. High local pitch down moment due to the Gurney flap was also observed, but the effect to the elastic blade twist was not modeled.

In this section, a harmonic deployment of Gurney flaps is studied, aimed at minimizing the 4P harmonic vertical vibratory load while mitigating adverse effects such as high sectional pitching moments and hub moments observed in the previous study. A CFD-CSD coupled analysis was carried out to model the elastic blade deformation and to maintain trim state, while the Gurney flap is dynamically deployed.

A multi-block grid system shown in Figure 6.13 is used, with Gurney flap installed at 90% chord-wise location. Dynamic wall boundary condition is applied at the block interfaces between block 1 and 2 (lower surface flap) and block 2 and 3 (upper surface flap). The grid was built so that the deployed flap height can reach up to 1.5% times the local chord. Note that the trailing edge tab is included for closer modeling of HART-II rotor.

6.3.1 HART-II Baseline Rotor

Prior to deploying the Gurney flap, the baseline descent condition was simulated using GENCAS-DYMORE coupled analysis and the trimmed state was established.

Figure 6.14 shows the convergence history of the CFD-CSD coupled analysis. It is seen that the GENCAS-DYMORE loosely-coupled analysis successfully and quickly converges. The pitch control settings quickly converged after iteration 4 and met the trim targets. The predicted collective pitch angle closely matches the measured data, and the cyclic pitch controls deviate less than 1 degree relative to the measurements. Figure 6.15 shows that the overall trend (low frequency load variation, which is the main concern in this study) of the normal force is well predicted. In this study, the relatively time consuming embedded grid was not utilized since the dominant low frequency vibratory load is the main concern. The result was referenced as a baseline to be compared with the Gurney flap OBC concept.

6.3.2 4P Deployment of Gurney Flaps

Starting with the trimmed baseline rotor flow field as the initial condition, Gurney flap was deployed and the coupled analysis was continued to reach trimmed state. The phase angle of the Gurney flap schedule was specified based on the 2-D studies discussed earlier, so that the delta-lift due to Gurney flap aims to cancel out the 4P vibratory load of the baseline rotor (Figure 6.16). A phase lag was based on the 2-D analyses discussed earlier was included in the specification of the flap deployment. The radial placement of the flap was adjusted to minimize the target vibratory loads. The final Gurney flap schedule was obtained after several adjustments and is shown in Figure 6.17.

The GENCAS-DYMORE loosely-coupled analysis was continued in time from the trimmed baseline rotor with the scheduled Gurney flap deployment. The rotor was re-trimmed after every few rotor revolutions, and the blade elastic motion updated. Figure

6.18 shows the trim history of the rotor with Gurney flap. It is seen that the trim process drives the rotor hub loads (thrust and moments) to the same values as the baseline rotor.

Although the Gurney flap schedule was rigorously determined by including the response time lag, the resultant hub load at the beginning of Gurney flap deployment will somewhat differ from the desired load distribution. This is seen in Figure 6.19, which compares the 4P vertical load for the baseline rotor and the Gurney flap-equipped rotor before a re-trim. The desired 4P load cancellation was not achieved. This is attributable to the non-uniform delta-load production from the Gurney flap at each azimuth angle in forward flight due to varying dynamic pressure. It may be noted that the force coefficients are non-dimensionalized based on the blade tip speed, not the local flow velocity. Figure 6.20 shows delta-load distributions after Gurney flap is deployed, before (Iter #11) and after the rotor is re-trimmed (Iter #17). On the advancing side, the high dynamic pressure produces a large delta-load. On the retreating side, the Gurney flap is not as effective due to the lower dynamic pressure even though the flow is fully attached to the blade (Figure 6.21). As a result, moment unbalance occurs as shown in the trim history plot (Figure 6.18). The re-trimming process re-distributes the load so that the adjusted pitch control compensates for the delta-load differences in the advancing/retreating and fore/aft sides of the disk due to Gurney flap. Once the rotor is re-trimmed, the delta-loads following the re-trimming is shown in Figure 6.20-b.

The summation of delta-load of four blades, located with 90 degree azimuth angle phase shift is shown in Figure 6.22. Before the re-trim, Gurney flap produced a skewed and phase shifted delta-load instead of the expected clean sinusoidal shape. After the re-trim, the desired delta-loads with proper phase angle and a near sinusoidal shape was

obtained. Figure 6.23 and Figure 6.24 show the vertical hub loads at the hub and the filtered 4P hub load, respectively. It is evident that the vertical hub load is more evenly distributed and 4P vertical hub load is greatly reduced from the original state.

Additional studies have been done to adjust the width and radial position of the Gurney flap. In Figure 6.24, an alternative flap schedule, with the flap spanning the 70% to 74% radius is shown. With this radial placement, a small increment in the delta-loads was seen compared to the original flap placement (between 70% and 73% radius). The sensitivity of the vertical hub loads to the span of the flap and the radial placement indicates that the 4P vertical load may be virtually eliminated with an optimized flap placement and flap length.

Gurney flaps are known to generate high nose-down local pitching moments. In the current study, the local pitching moments and their effect on the blade torsional deflection were examined. Figure 6.25 shows the local pitching moment distribution. As a result of the small size of the flap coupled with 3-D relief effects, the effect of Gurney flaps on elastic torsional deflection (in the vicinity of $r/R = 0.7{\sim}0.73$) was negligible as shown in Figure 6.26.

Figure 6.27 compares vibratory side forces and hub moments. The incremental changes in H-force, Y-force and pitching moments at the hub, attributable to the Gurney flaps, were negligible. Although the vibratory rolling moment increased relative to the baseline rotor, the Gurney flaps had one order of magnitude less impact on hub rolling moment coefficients than on vibratory vertical hub load coefficient.

It was observed that a vortical flow forms behind the flap and shed into the wake as the flap is retracted. The vortices shed periodically from the lower and upper sides of

the blade. Figure 6.28 shows streamline around lower side flap when the flap was fully deployed and retracted, showing vortex shedding. Because of centrifugal force, the vortex flow propagates from inboard to outboard direction. The shed vortex may interact with the following blade and influence load and noise. However, current numerical method is not able to examine this interaction effect because only a single blade is modeled by the Navier-Stokes solver and the shed vortex was not modeled.

6.3.3 On-Board Control of 4P & 8P Vibratory Loads

A further benefit of deployable Gurney flap as a control concept is that the segmented flap can be controlled individually. This section examines the potential for Gurney flaps for reducing higher harmonic components of vibratory loads.

As shown in Figure 6.29, the change in the 8P vertical hub load of the 4P Gurney flap deployed rotor was minor compared the baseline rotor, and the amplitude was similar to the reduced 4P hub load (Figure 6.24). In an attempt to reducing the 8P components of the vertical hub loads, the previous 4P deployment at separated flap segments was modified with the addition of an 8P schedule of the flap. The radial placement of the flaps, and the flap schedule was adjusted. The final schedule is shown in Figure 6.30. Since the resultant change in the thrust and hub moments was negligible with this additional eight-per-rev deployment, re-trimming process was not necessary.

The 8P vertical hub loads shown in Figure 6.31 demonstrate a significant reduction in vibratory loads compared to the previous cases. Table 6.3 summarizes rotor performance and vibration level of the 4P and 4P+8P concepts. The 4P vertical hub load of the 4P Gurney flap deployed rotor was reduced to the 17% of the baseline rotor, and the 8P vertical load of the simultaneous 4P and 8P Gurney flap deployed rotor was

reduced to the 4% of the baseline rotor. These improvements were achieved while the trim state was maintained with negligible performance penalty (L/D_e).

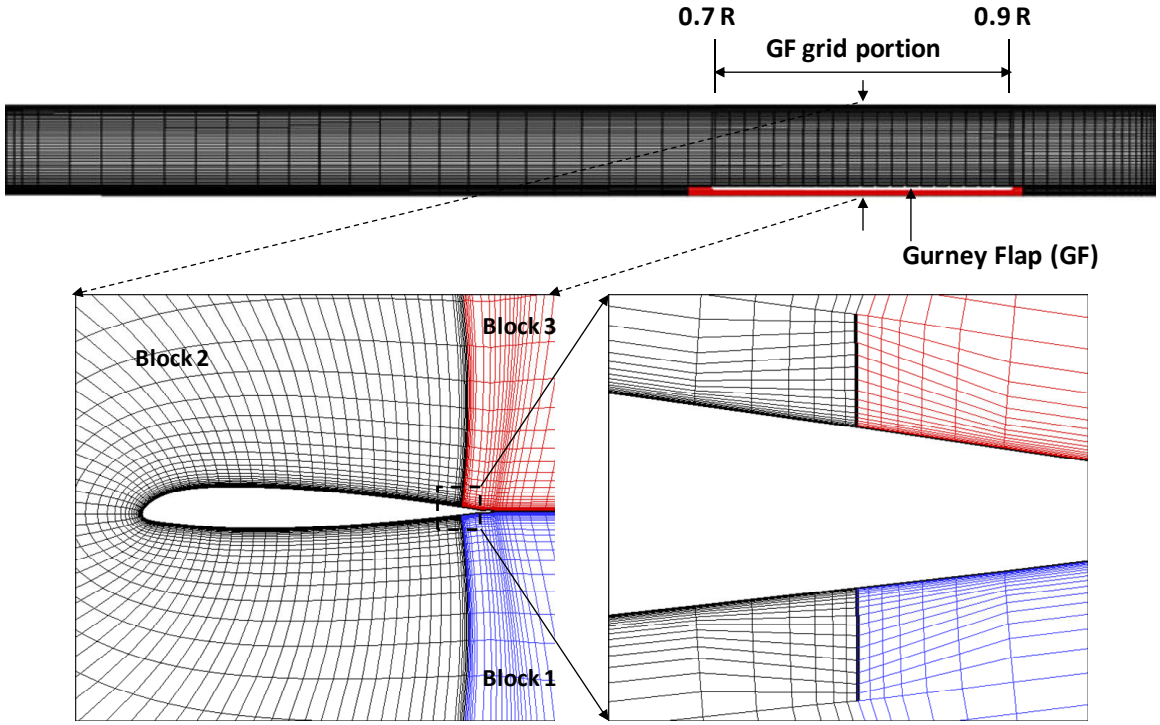

Figure 6.13 Grid system for Gurney flap simulation

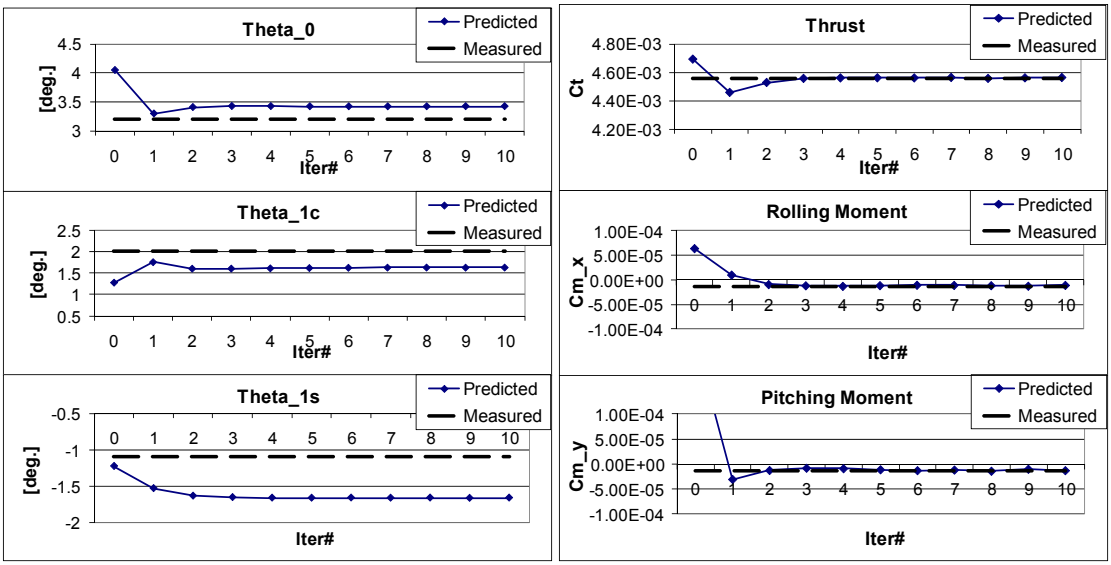

Figure 6.14 CFD-CSD coupling convergence history for the HART-II baseline rotor

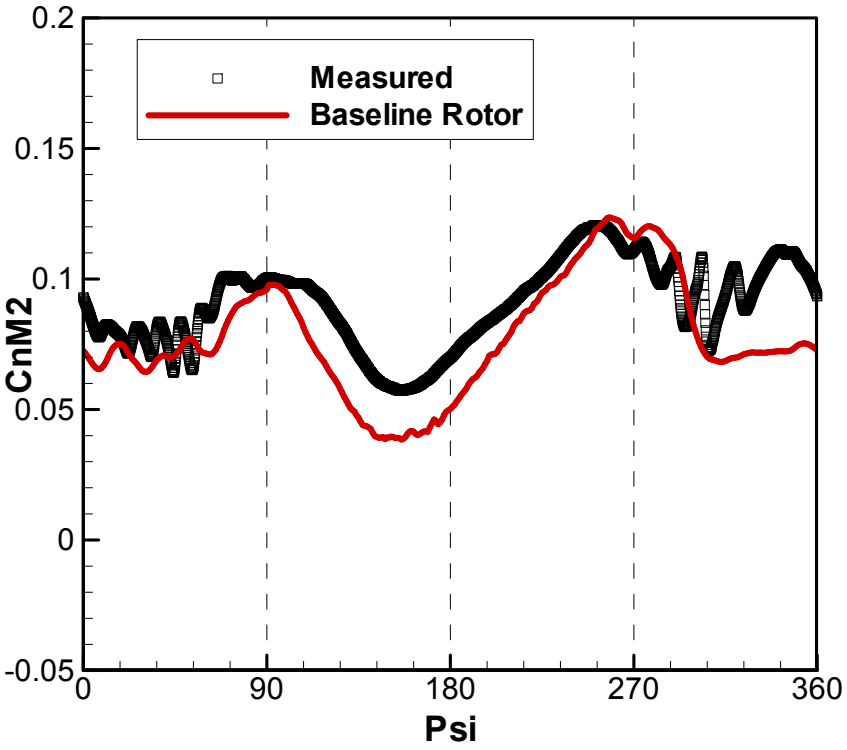

Figure 6.15 Normal force (r/R=0.87), CFD-CSD coupled simulations, HART-II baseline rotor

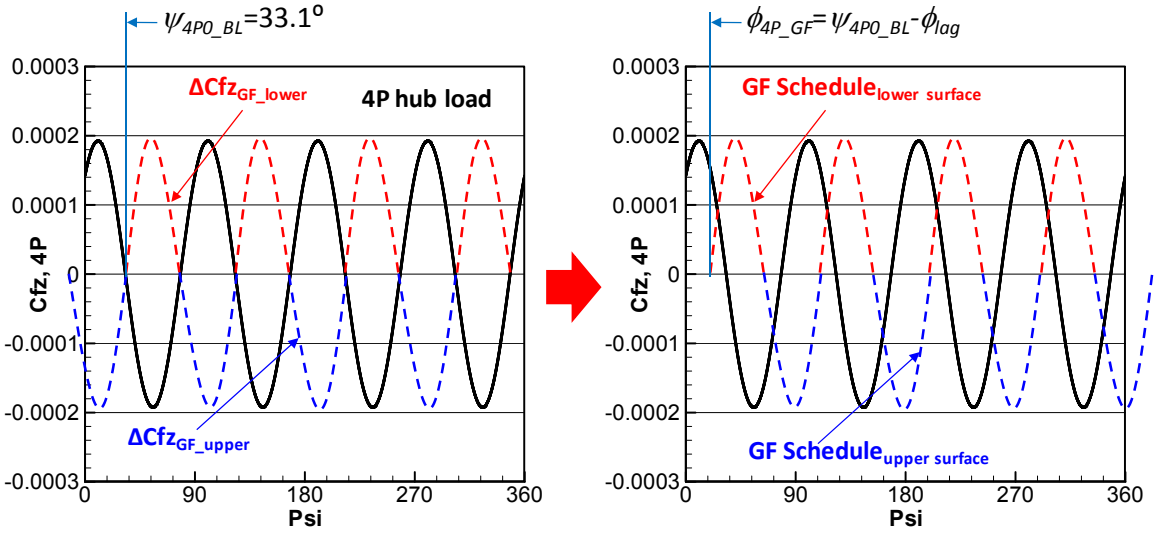

Figure 6.16 4P vertical hub load of the baseline rotor and initial Gurney flap schedule

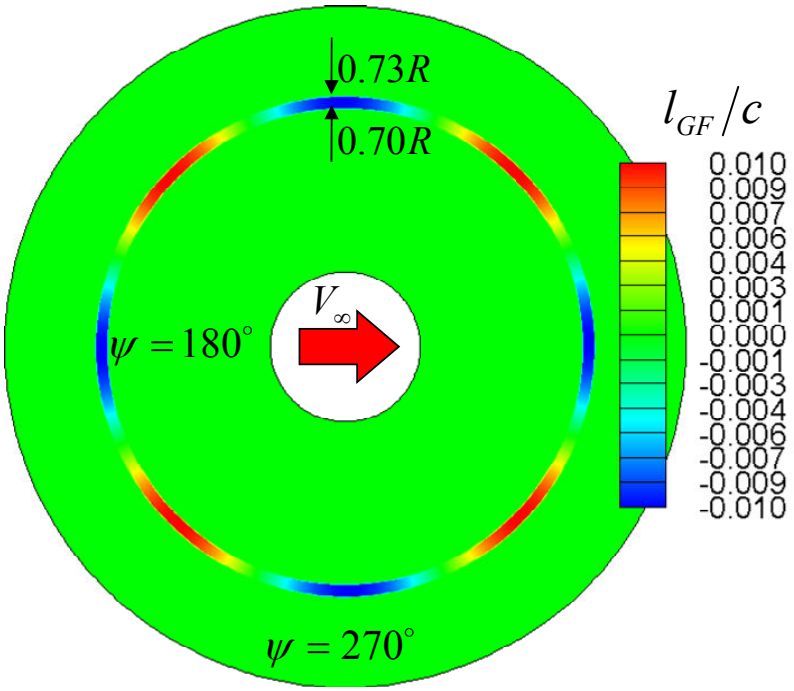

Figure 6.17 4P Gurney flap schedule (+: lower surface, -: upper surface)
($l_{GF} = A\sin\left(n\left(\psi - \phi_{4P\_GF}\right)\right)$, where n=4, A=0.01c, and $\phi_{4P\_GF} = 23.5°$)

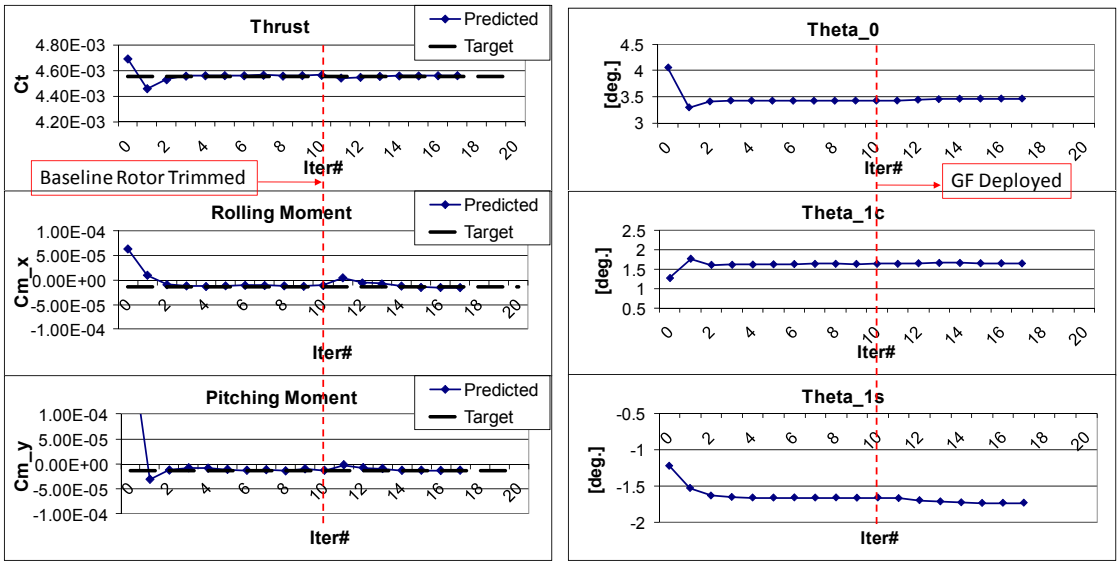

Figure 6.18 Trim history of the Gurney flap deployed rotor

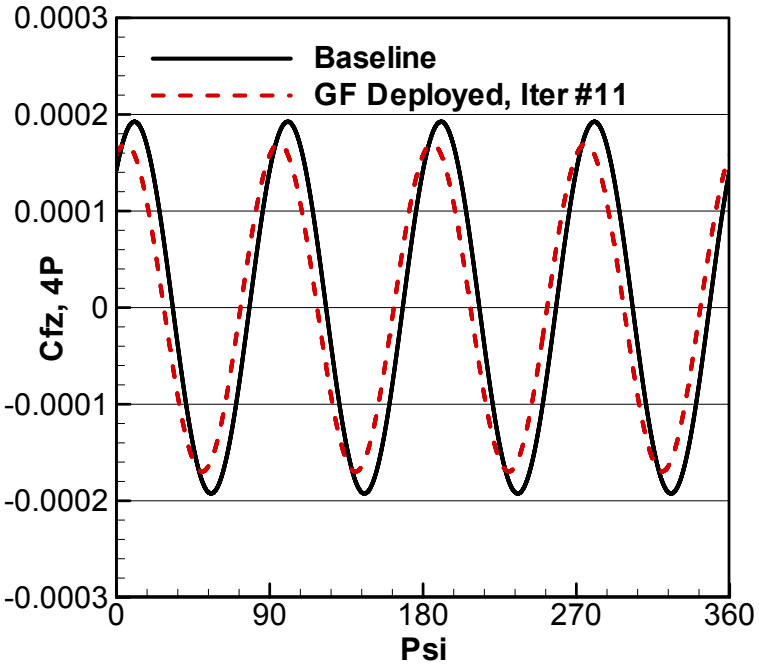

Figure 6.19 4P vertical hub load comparison,
(Baseline vs. GF rotor before re-trimming)

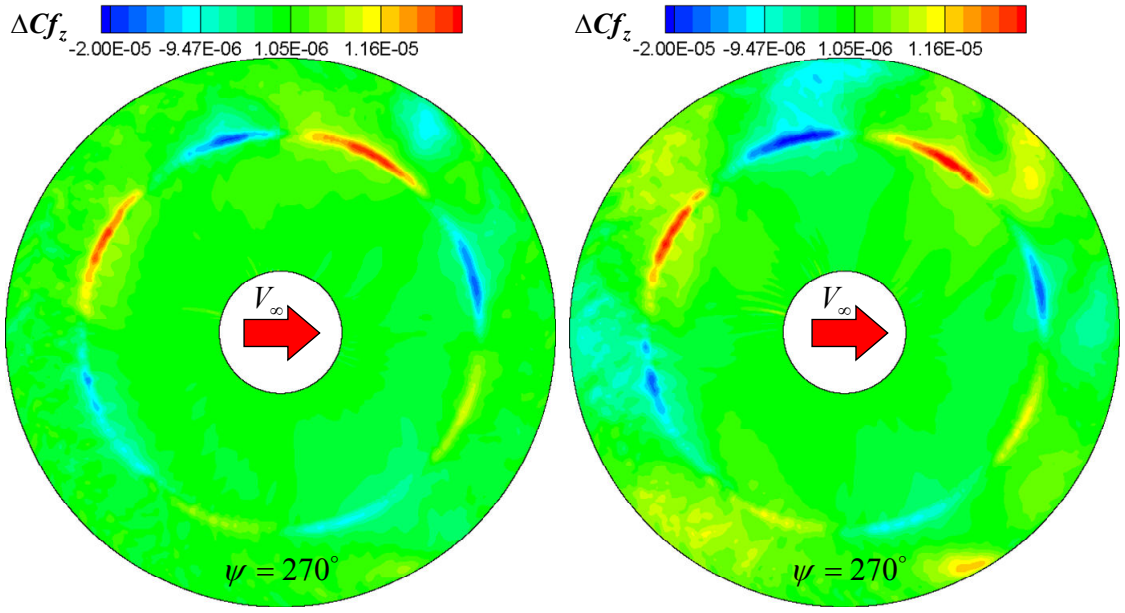

a) Before re-trimming (Iter. #11) b) After re-trimming (Iter. #17)

Figure 6.20 Delta vertical force due to Gurney flap ($\Delta Cf_z = Cf_z - Cf_{z\_Baseline}$)

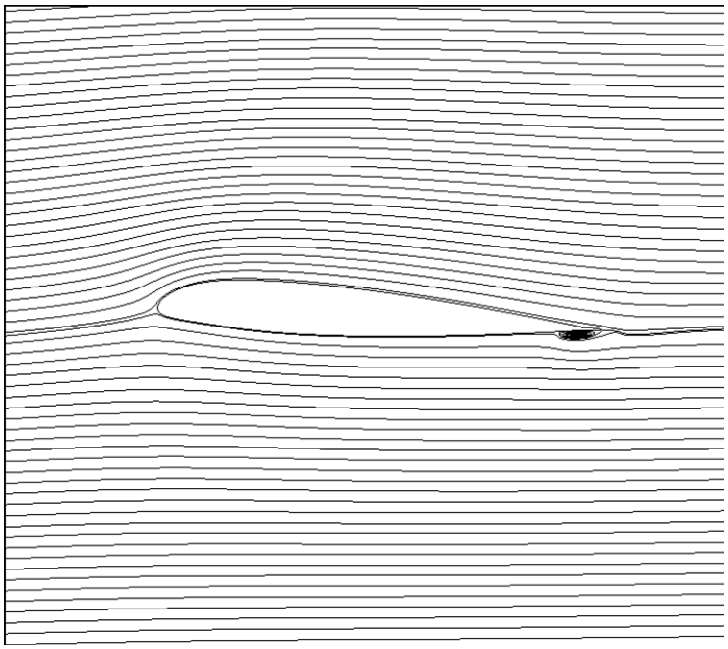

Figure 6.21 Streamlines around Gurney flap at retreating side
(After re-trimmed, $\psi = 226°, r/R = 0.72$)

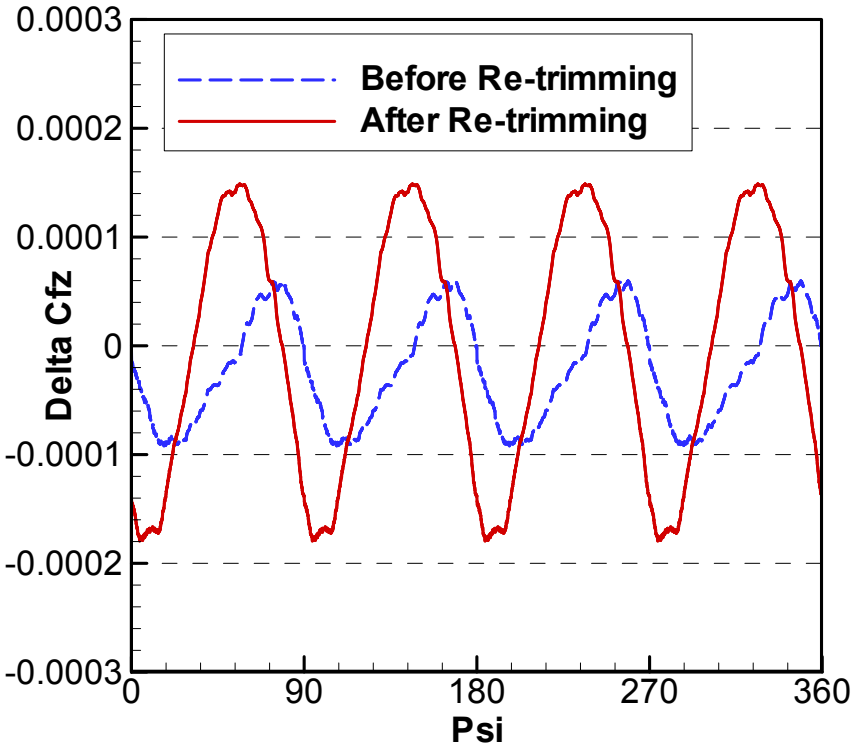

Figure 6.22 Delta hub load due to Gurney flap before/after re-trimming

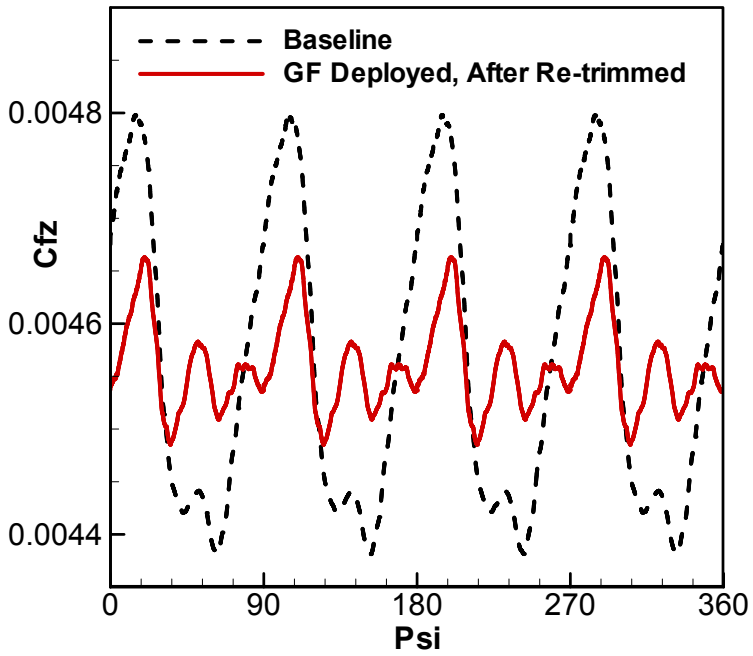

Figure 6.23 Vertical hub load comparison, baseline vs. GF rotor after re-trimmed

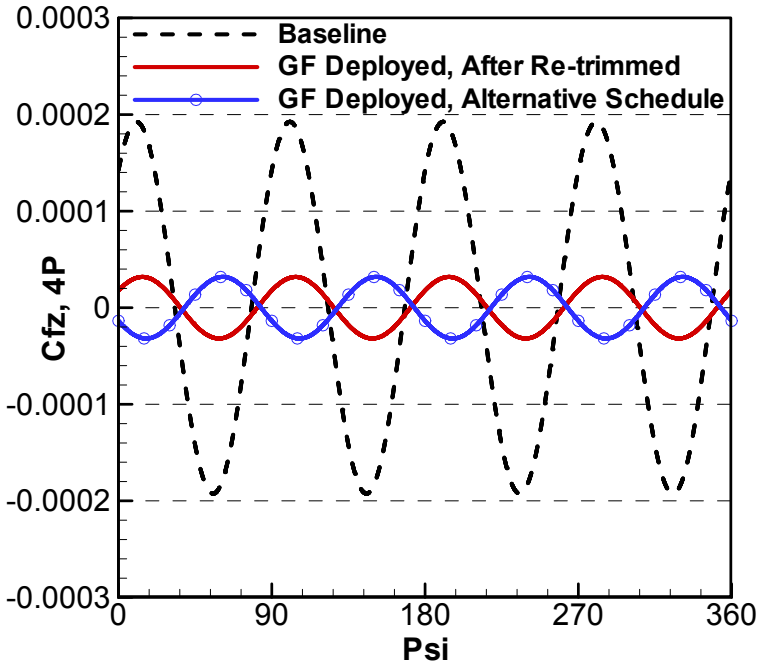

Figure 6.24 4P vertical hub load comparison, baseline vs. GF rotor after re-trimmed (Alternative GF schedule: $\phi_{4P\_GF} = 25°, r/R_{GF} = 0.7\sim0.74$)

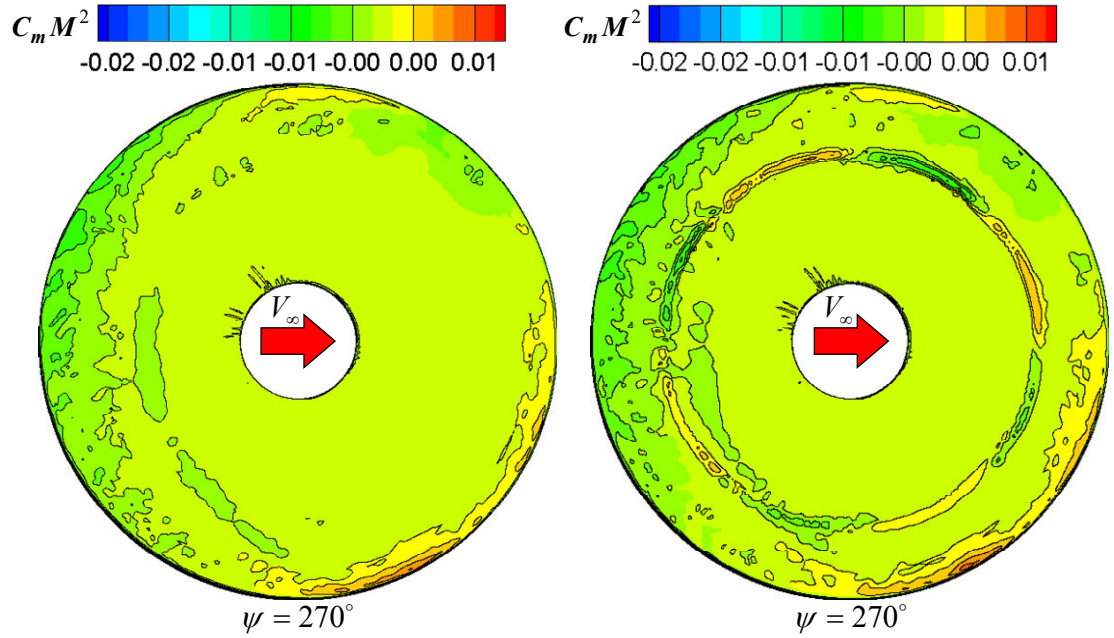

a) Baseline b) 4P GF deployed

Figure 6.25 Local pitching moment distribution

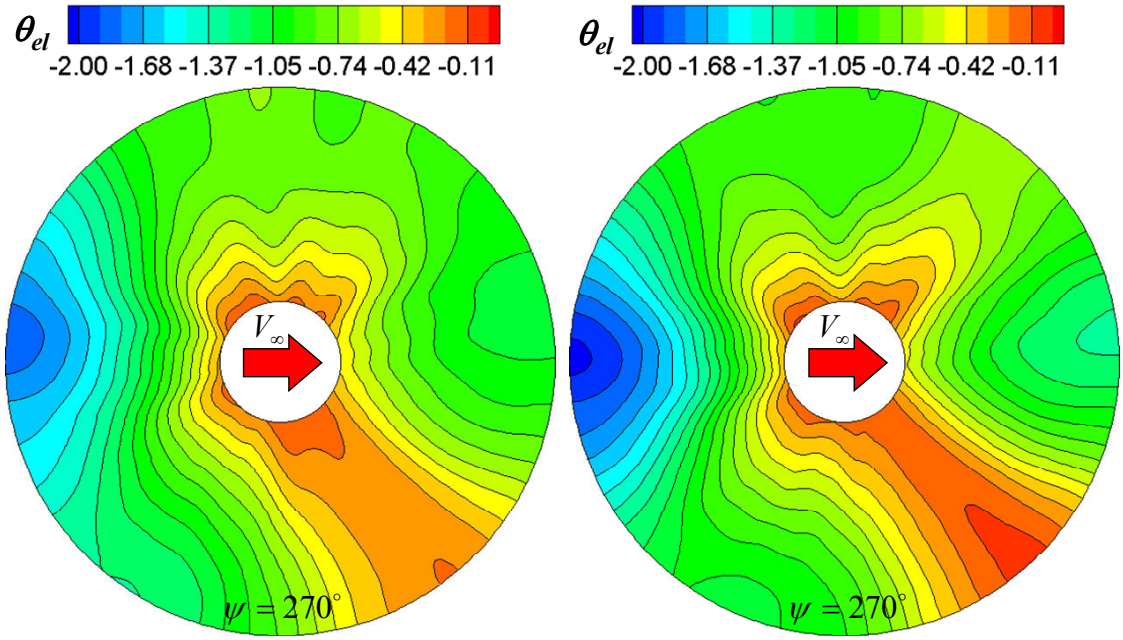

a) Baseline b) 4P GF deployed

Figure 6.26 Blade torsional deflection comparison
(Elastic deformation only, angle in degree)

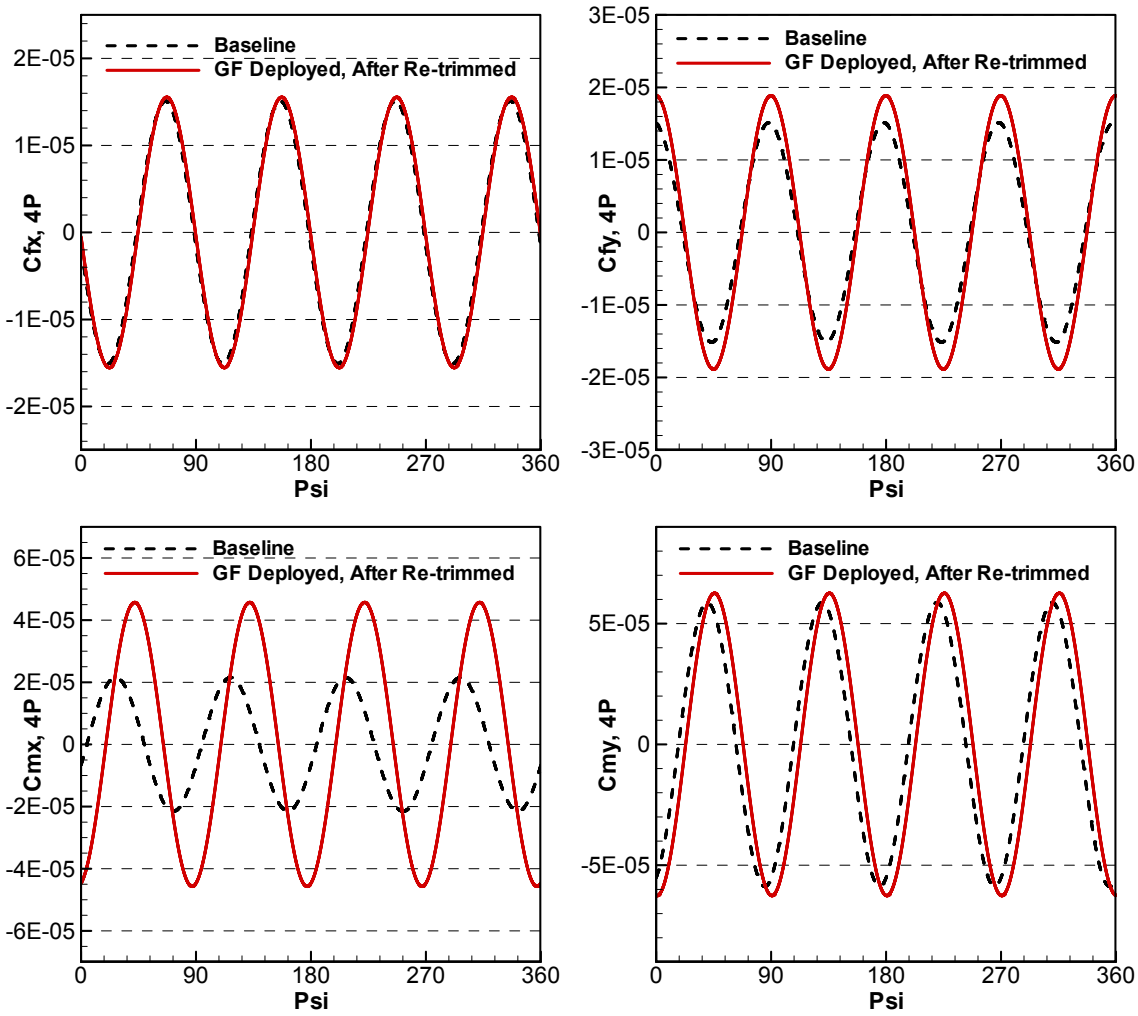

Figure 6.27 4P hub load comparison

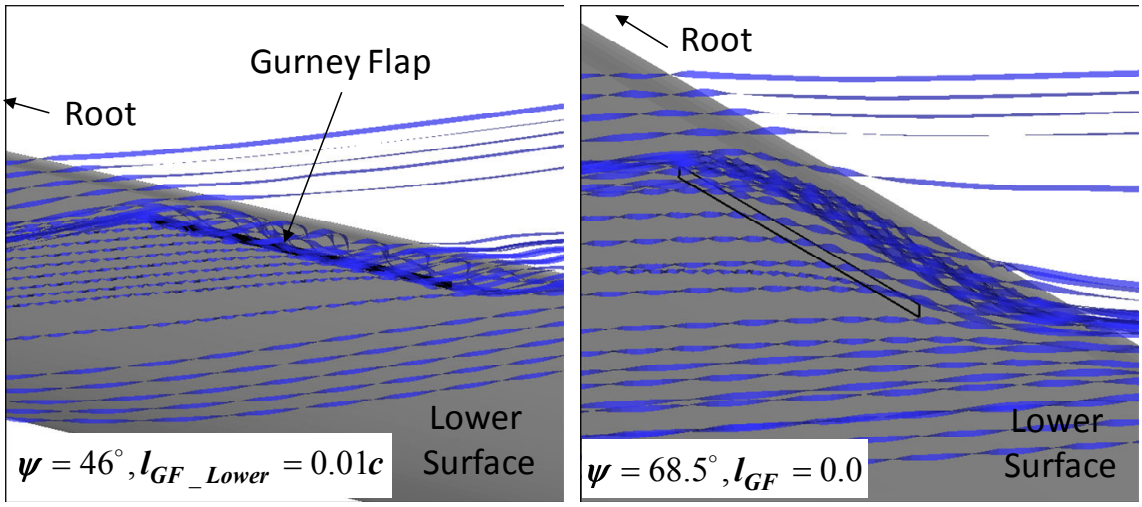

Figure 6.28 Vortex shedding due to Gurney flap, view from rear lower.

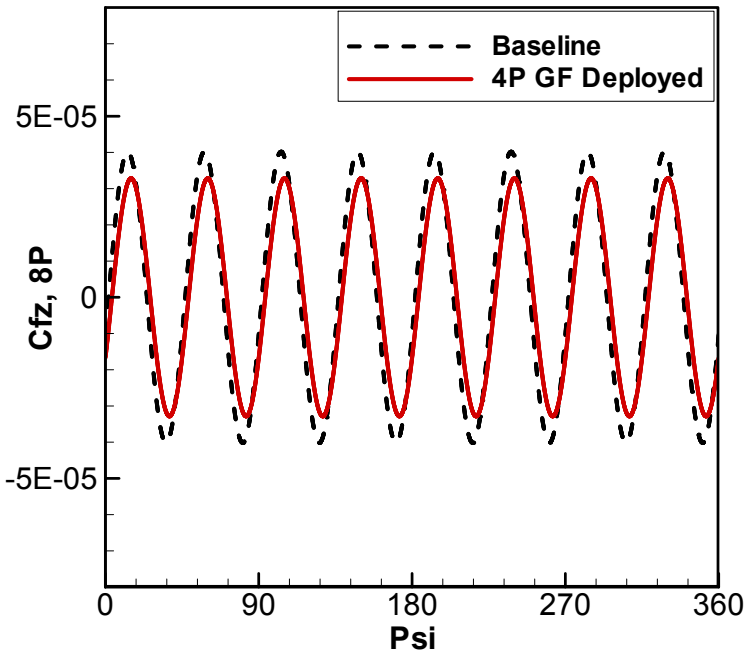

Figure 6.29 8P vertical hub load comparison

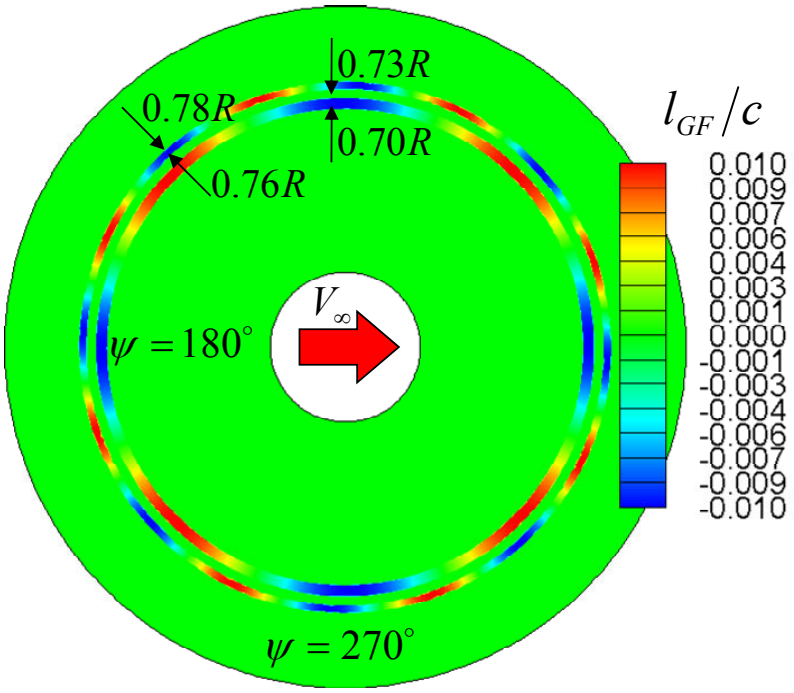

Figure 6.30 4P and 8P Gurney flap schedule (+: lower surface, -: upper surface)
($l_{GF\_4P} = A\sin\left(n_{4P}\left(\psi - \phi_{4P\_GF}\right)\right)$, $l_{GF\_8P} = A\sin\left(n_{8P}\left(\psi - \phi_{8P\_GF}\right)\right)$
Where, $n_{4P} = 4$, $n_{8P} = 8$, A=0.01c, $\phi_{4P\_GF} = 23.5°$, and $\phi_{8P\_GF} = 8°$)

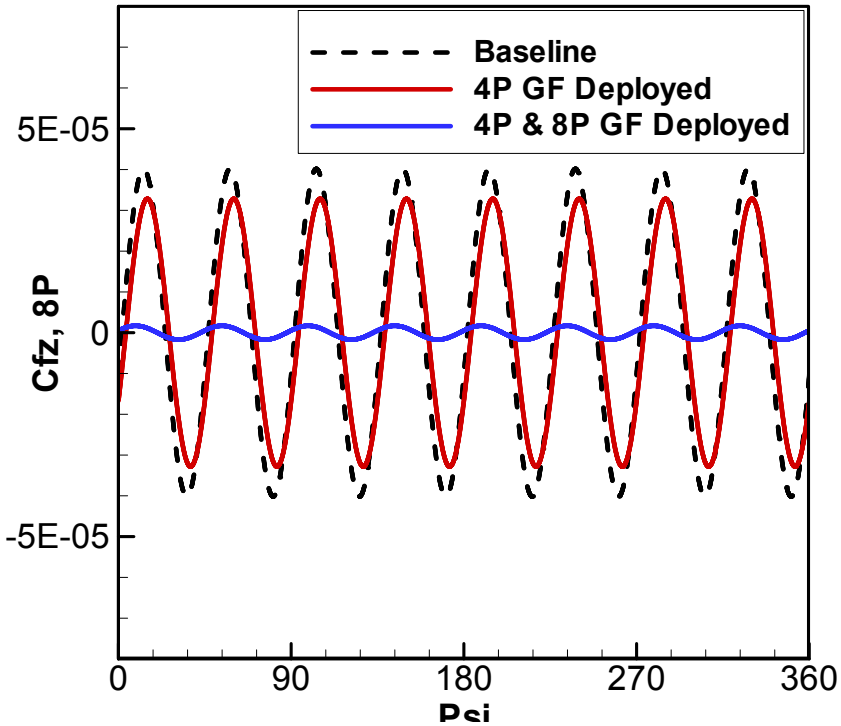

Figure 6.31 8P vertical hub load comparison

Table 6.3 Rotor performance and vibratory load $\left(L/De = L/\left(D + \frac{M_z\Omega}{V_\infty}\right)\right)$

	GF Deployed (4P Harmonic)	GF Deployed (4P & 8P Harmonic)
C_T/C_{T_BL}	1	1
$\Delta C_{M\_x} = C_{M\_x} - C_{M\_x\_BL}$	-4.21×10^{-6}	3.54×10^{-6}
$\Delta C_{M\_y} = C_{M\_y} - C_{M\_y\_BL}$	1.29×10^{-7}	4.84×10^{-6}
$(L/De)/(L/De)_{BL}$	0.99	0.98
$\left(F_{z\_4P}\right)/\left(F_{z\_4P}\right)_{BL}$	**0.17**	0.18
$\left(F_{z\_8P}\right)/\left(F_{z\_8P}\right)_{BL}$	0.82	**0.04**

6.4 Chapter Summary

The deployable Gurney flap was examined as an OBC concept for rotor vibration reduction. The HART-II rotor in descent mode was used as a baseline case. Prior to the three-dimensional rotor studies, a two dimensional study was carried out to understand the unsteady air loads response of the dynamically deployed Gurney flap. The results from the 2-D study were used to determine the initial Gurney flap schedule.

The Gurney flap deployed at the lower side of blade trailing edge demonstrated its potential in reducing hub vertical vibratory loads. However, high nose-down sectional pitching moments were observed.

A more realistic simulation of Gurney flap was performed by installing the flap at 90% chord wise location on both the lower and upper surfaces. The flap was harmonically deployed. The effects of Gurney flap at the retreating side were relatively small due to low dynamic pressure, and a re-trimming process was required. For this configuration, the study showed improved vertical vibration reduction (more than 80%) while maintaining trimmed state with negligible performance penalty. The high local pitching moment issue was relieved with harmonic deployment and its effects on the blade torsional deflection were negligible.

The 4P and 8P harmonics of vibration were successfully suppressed simultaneously using individually controlled segmented flaps along the blade span.

The deployable Gurney flap shed vortices periodically as the flap is deployed and retracted. However, the effect of the shedding vortex to the noise and interaction with following blade was not captured in the current methodology.

CHAPTER 7

BVI AVOIDANCE USING DEPLOYABLE GURNEY FLAP

The HART-II program includes rotor test for maximum BVI condition in the descent mode, and then the test was repeated with HHC control superposed over the baseline control at the same flow condition, aimed to minimum noise and vibration. In this chapter, the effect of the deployable Gurney flap to the blade motion, BVI event and noise is studied.

7.1 Strategy to Avoid BVI Phenomena using Deployable Gurney Flap

Deployable Gurney flap produces additional load at the selected azimuthal and radial location. The increased load at certain locations may lift the blade up, providing an alternate trim state. This provides the potential to avoid interactions with strong tip vortices from the preceding blades.

A GENCAS-DYMORE coupled analysis was carried out to examine the deployable Gurney flap as an alternate trim state provider while avoiding BVI events. The grid system shown in Figure 6.13 was used with the HART-II rotor structural properties. The Gurney flap was deployed from lower surface over a pre-specified range of azimuth locations. The maximum flap height was set to 0.015*c* and the flap was deployed at 70~90% of the blade radial location. The flap was deployed at two pre-specified azimuth locations where the BVI events mostly occur at the baseline condition, and the flap schedule is shown in Figure 7.1.

The same numerical schemes used in Chapter 6 were utilized with identical time steps. Once a trim state is obtained with the coupled analysis, an embedded grid (Figure 7.2) is employed to better capture the incoming vortices.

7.2 Results and Discussion

As shown in Section 4.6, most of the BVI events occur in the first and fourth quadrants in the baseline condition. Thus, the deployment schedule was determined so that the flap was deployed a little earlier and over those azimuth locations to account for phase delay in the blade motion response due to gyroscopic precession. After trimmed state was established from the coupled analysis with the Gurney flap, an alternate blade motion was obtained and shown in Figure 7.3 (the entire blade motion) and Figure 7.4 (the tip position). The new trim state lowered the blade position in the aft section. As intended, the increased lift force (Figure 7.5) in the aft section moved the blade upward in the first quadrant. The Gurney flap effect in the retreating side was small due to low dynamic pressure as discussed in Section 6.3.2. Instead, another peak thrust was introduced in the second quadrant as a result of the trim procedure. The tip vortices encountering the blade in the first quadrant are released in the second quadrant and travels downstream. Notice that the lower tip position of the Gurney flap deployed rotor in the second quadrant (Figure 7.4) may release the tip vortices in the lower trajectory. In Figure 7.5, note that the distinguishable thrust fluctuation due to BVI observed in the first quadrant of the baseline rotor has been removed in the Gurney flap deployed rotor. However, the retreating side load fluctuations became more distinguishable. The sudden span-wise change of the load across the Gurney flap deployed radial location may release

other vortices as well, and the interaction of the following blade with these vortices is not captured with the current hybrid method.

Figure 7.6 shows the wake strength as a function of wake age. The periodicity of the wake strength ensures that the rotor is in steady periodic condition. As described in section 2.6, the wake strength was assumed to be peak bound circulation at the time the wake is shed from the blade. The local high thrust, due to Gurney flap (aft section) and new trim state (second quadrant), produces strong tip vortices (two additional spikes near wake age of 225 and 360 degree) as seen in Figure 7.6. The change in the wake strength may alter the wake geometry. Although the free wake geometry does not directly interact with the blade inside the Navier-Stokes domain, its structure and strength affect the wake initiation at the boundary of the computational domain. The wake geometry near the rotor disk, which contributes to the BVI events, shows a small difference due to its altered blade motion and corresponding shedding point (Figure 7.7).

Figure 7.8 compares local normal force at three typical radial locations, and Figure 7.9 shows normal force differentials over the disk, which is an indirect indicator for the BVI events. It is evident that the BVI events (indicated as high frequency force fluctuations in Figure 7.8 and stripe pattern in Figure 7.9) in the outboard section of the first quadrant have been relieved noticeably. The small red dots and stripes seen in the Gurney flap deployed region are numerical noise due to the step deployment of the Gurney flap using dynamic wall boundary condition.

Figure 7.10 compares vortex position at the cross section 'A-B' indicated in Figure 7.9, when the reference blade is located at $\psi = 20^{\circ}$. At this instance, the baseline rotor blade is in flapping down motion whereas the Gurney flap deployed rotor is in

flapping up motion (Figure 7.4). In addition, the vortex is traveling in the downward direction as the vortices (1), (2), (3) and (4) are aligned. The vortex trajectory of the Gurney flap deployed rotor is even lower than the baseline due to lower blade tip position in the second quadrant. Taking into account these factors, vortex (3) encounters the baseline rotor blade at this instance (indicated as a stripe pattern at the end of the cross section near the tip in Figure 7.9), but it is passing below the Gurney flap deployed rotor with relatively large miss-distance. Furthermore, the baseline rotor encounters vortices (1) and (2) as the blade rotates, indicated in Figure 7.9 as two stripe patterns located inboard of the cross section, whereas BVIs are weak with the Gurney flap deployed rotor due to larger blade-vortex miss-distance.

However, the BVI phenomena over the inboard stations were not changed much. This may be attributable to the small flapping distance changes, attributable to Gurney flaps, as plotted in Figure 7.11. Due to the decreased dynamic pressures over the retreating side, the effectiveness of the Gurney flap on the BVI events in the fourth quadrant was small, as well.

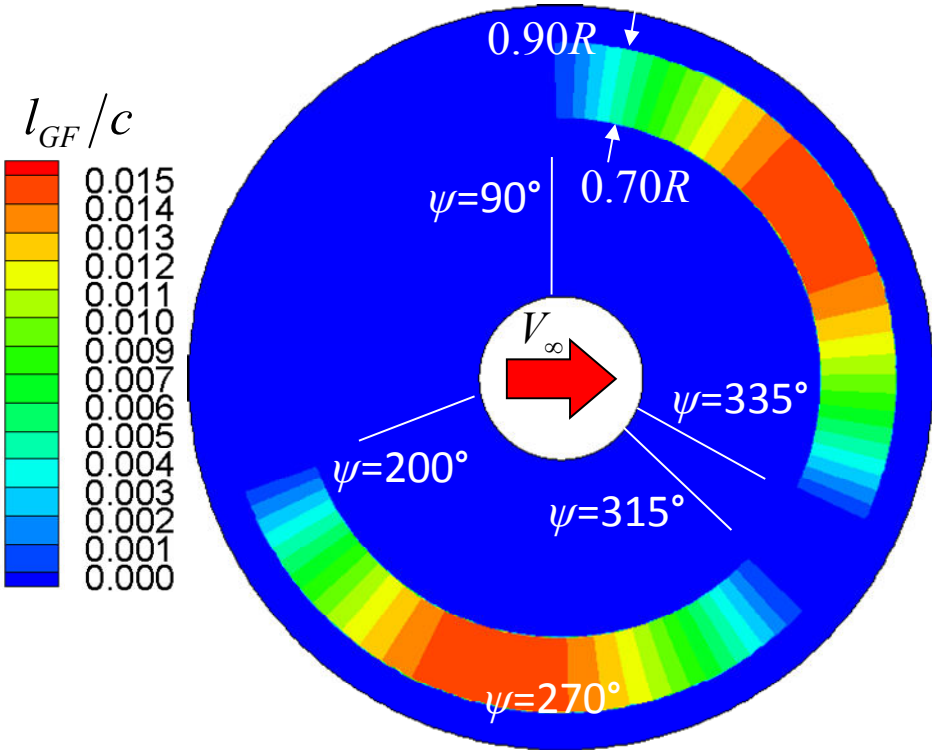

Figure 7.1 Gurney flap schedule for BVI avoidance

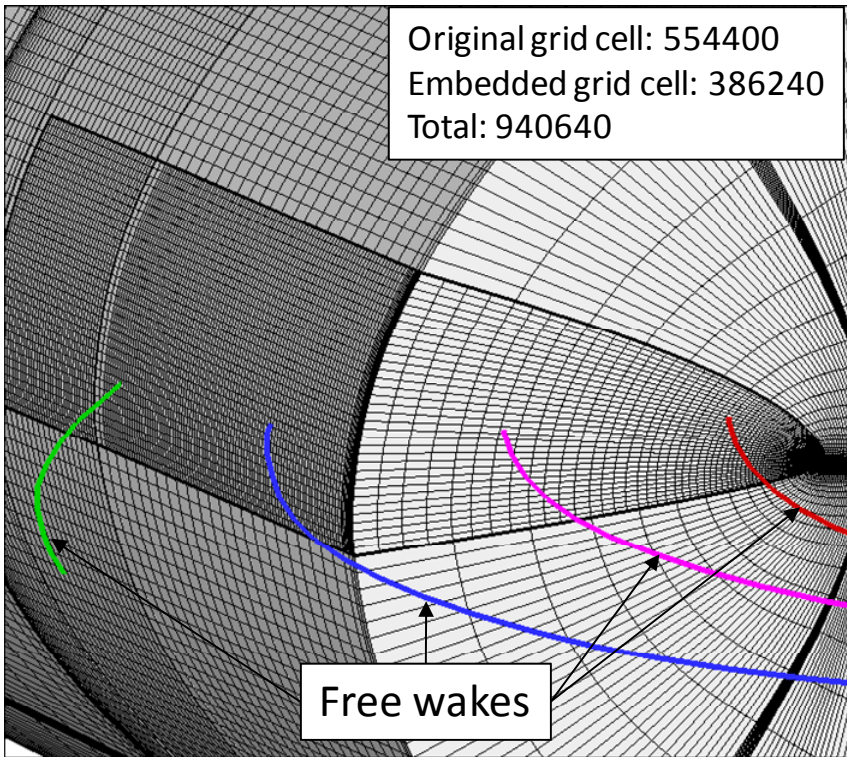

Figure 7.2 Employed embedded grid

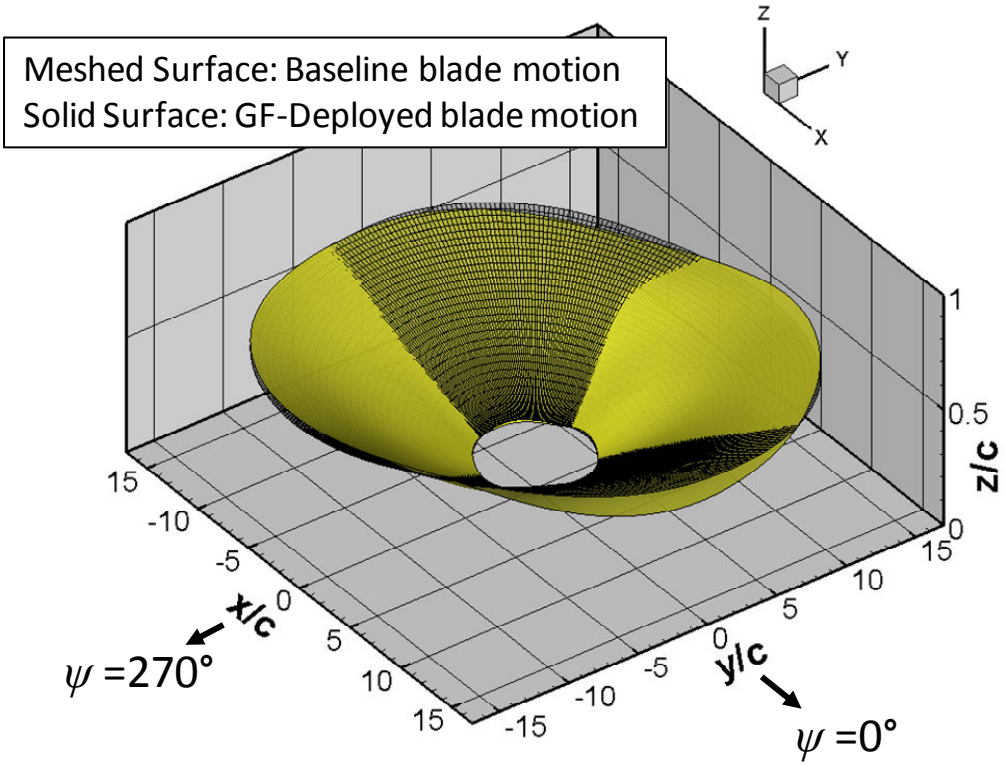

Figure 7.3 Blade motion comparison

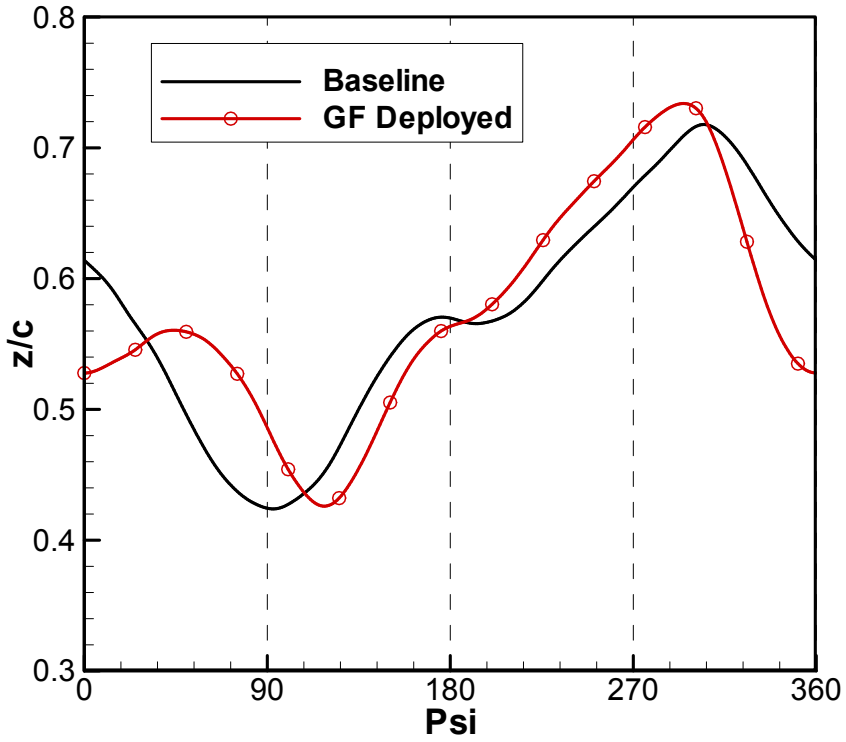

Figure 7.4 Blade tip motion (measured from hub)

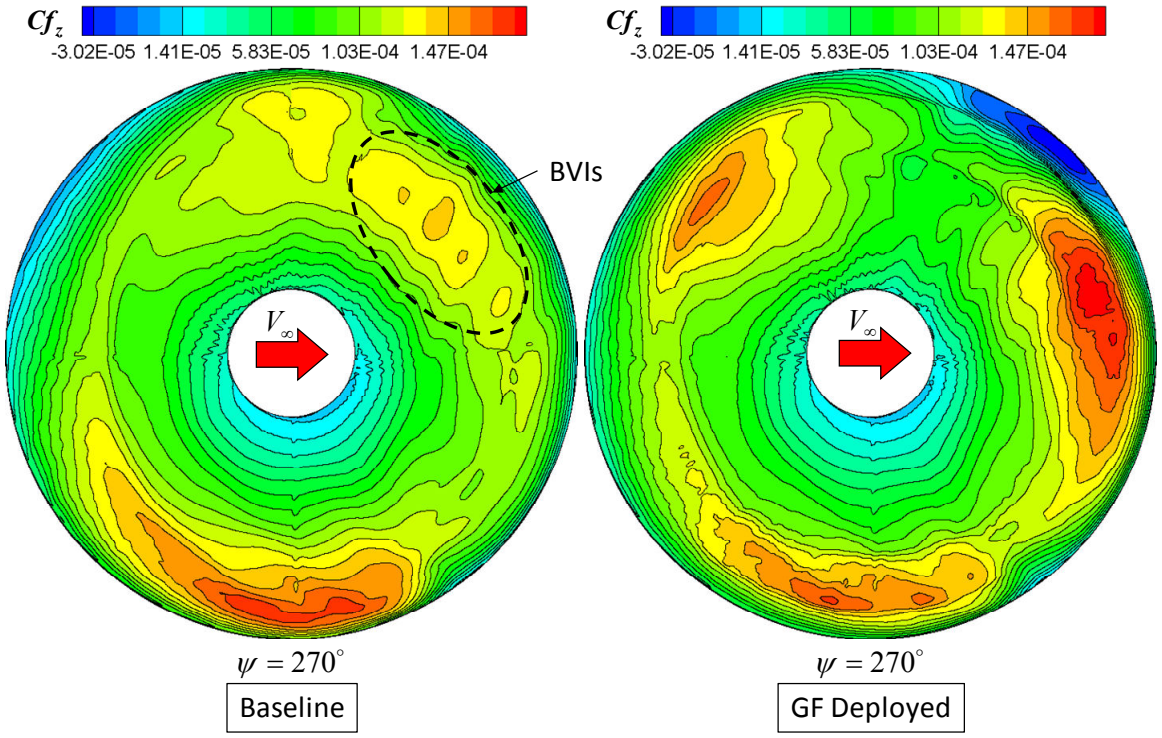

Figure 7.5 Vertical force distribution

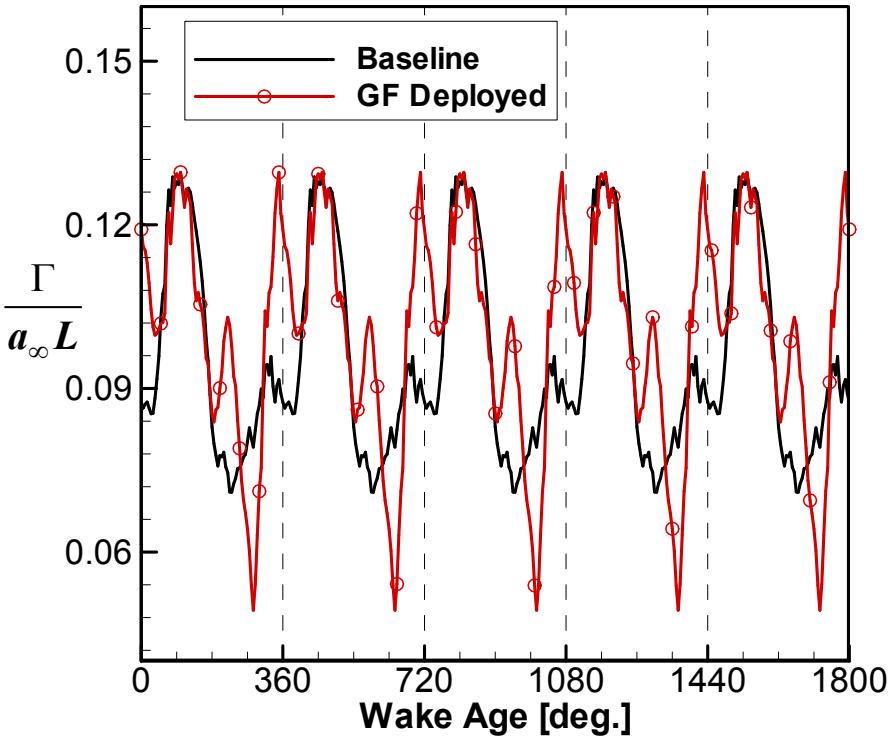

Figure 7.6 Tip-vortex strength (reference blade at 0 degree)

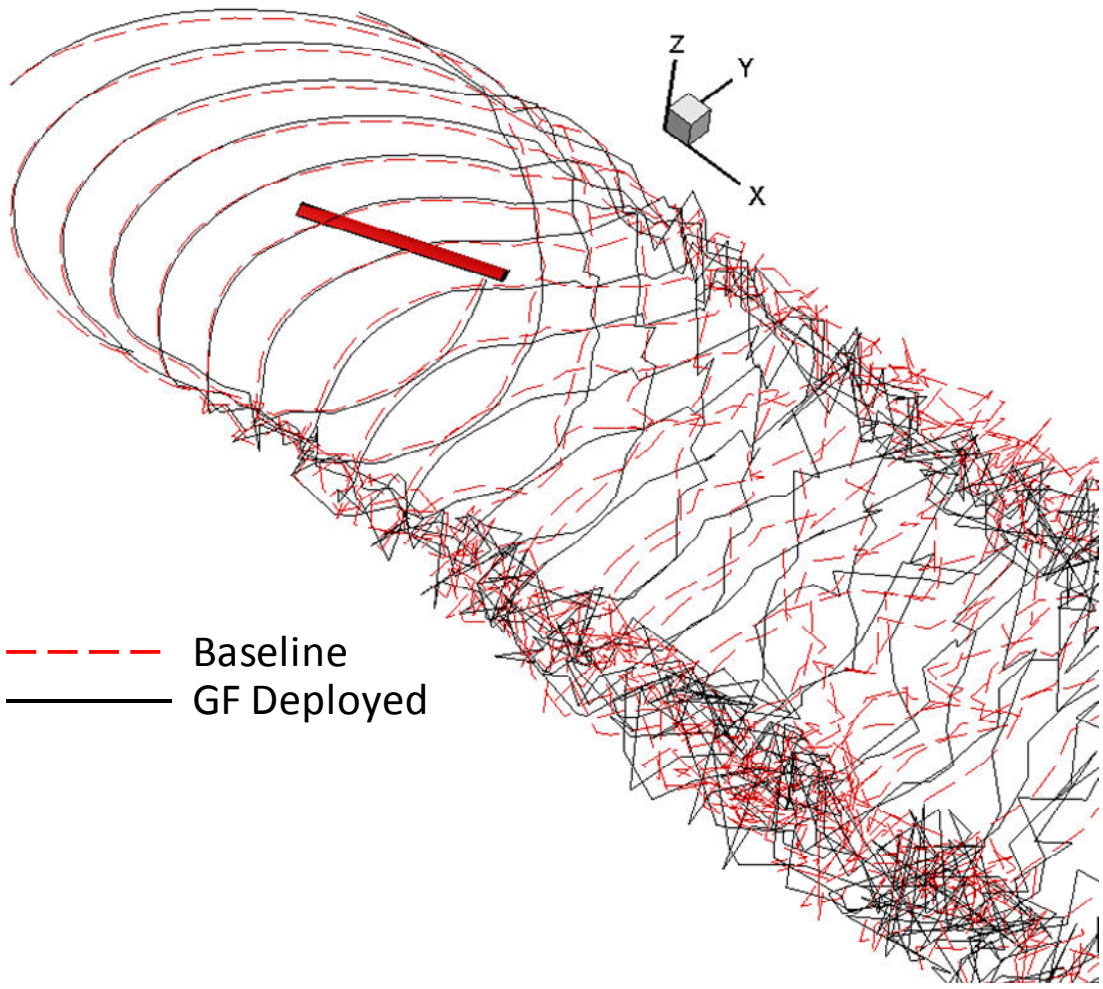

Figure 7.7 Wake geometry comparison, reference blade at $\psi = 20^{\circ}$

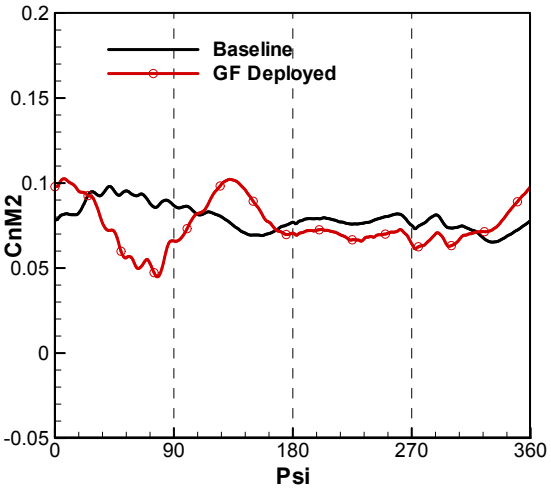

a) r/R=0.655

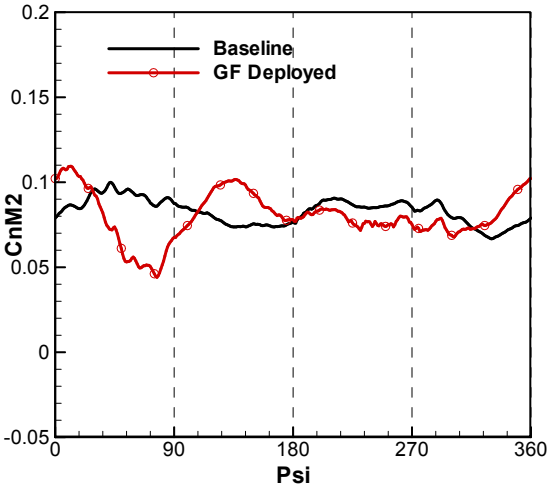

b) r/R=0.7

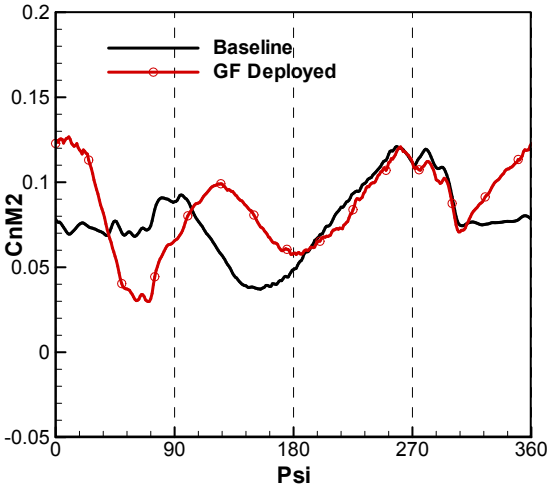

c) r/R=0.87

Figure 7.8 $C_n M^2$ at three radial locations

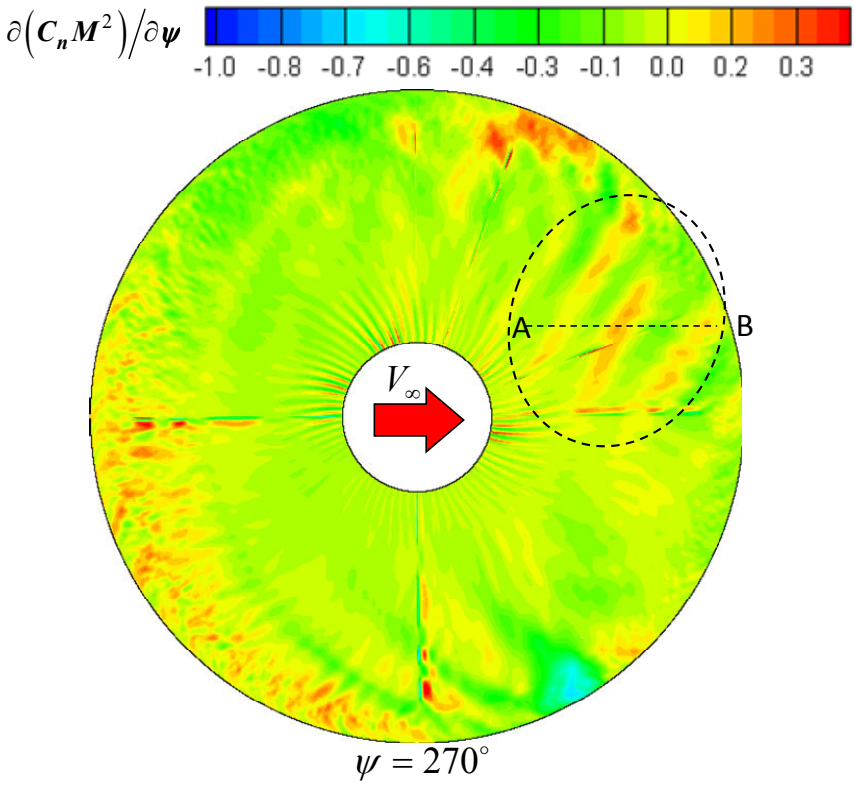

a) Baseline rotor

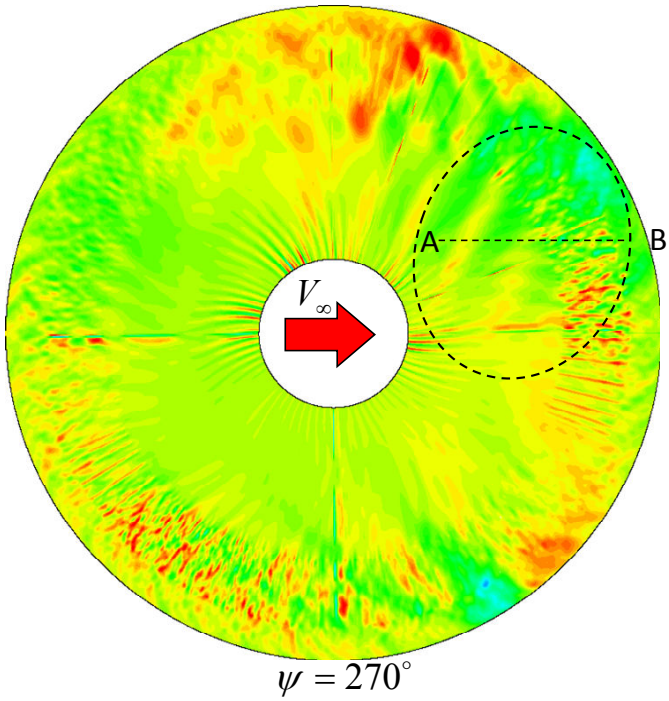

b) Gurney flap deployed rotor

Figure 7.9 BVI identification with $\Delta C_n M^2$

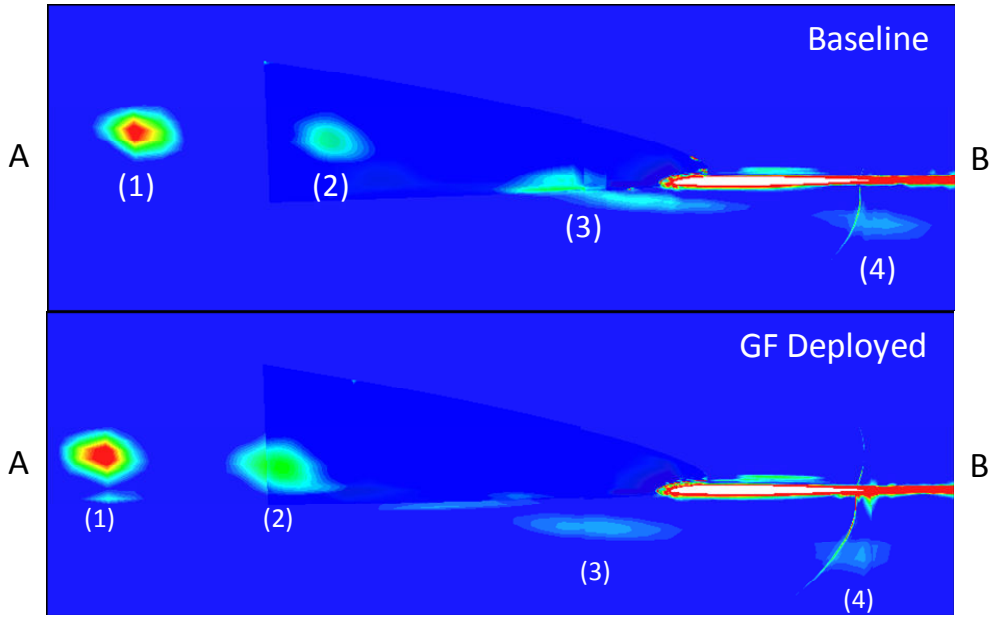

Figure 7.10 Vorticity contour ($y/c = 4.5$, reference blade at $\psi = 20^{\circ}$)

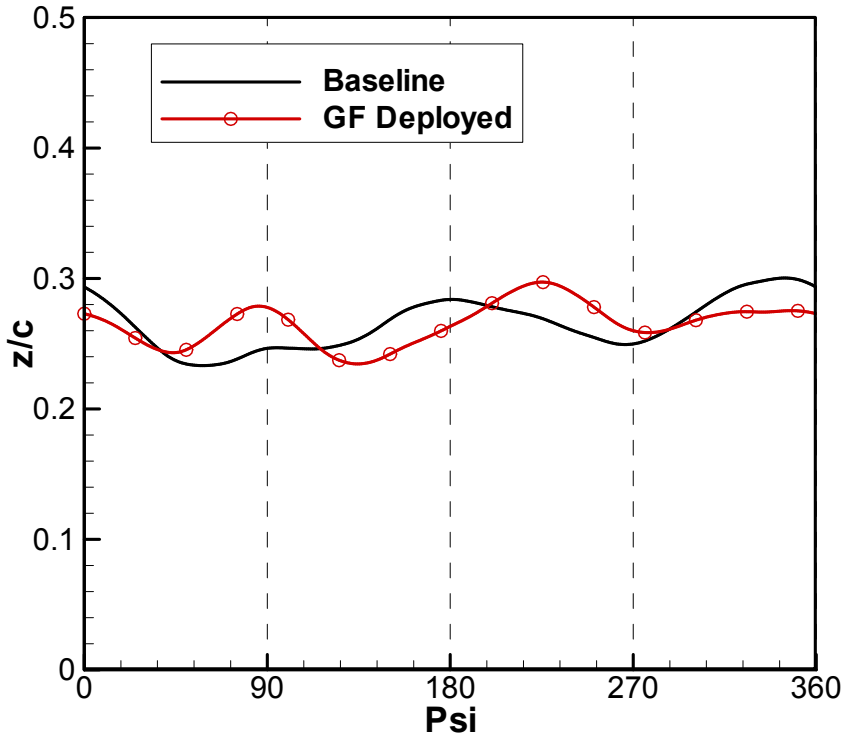

Figure 7.11 Vertical blade position at *r/R*=0.4

CHAPTER 8

CONCLUSIONS AND RECOMMENDATIONS

A physics based numerical investigation for Gurney flaps (or Micro flaps) has been carried out to explore its potential for improving rotorcraft flight characteristics. To this end, a hybrid Navier-Stokes/Free wake method has been used for efficient rotor analysis. The Navier-Stokes part is modeled with a newly developed solver, named GENCAS, which is able to simulate a deployable Gurney flap in an efficient manner. The Navier-Stokes solver has been coupled to a free wake model to take into account the wake that is not captured by the solver. The combined hybrid analysis has been coupled to a computational structural dynamics analysis. The hybrid method has been further enhanced to better capture BVI events. The numerical method has been validated for various standard benchmark cases prior to modeling Gurney flap.

The effect of a permanently deployed Gurney flap on the autorotation condition was studied in terms of descent rate and thrust benefits. The feasibility of the deployable Gurney flap on the rotor vibration reduction was thoroughly explored. Finally, a brief investigation has been carried out to investigate the possibility of using Gurney flaps for BVI avoidance. In these studies, HART-II blade was used as a representative rotor.

8.1 Conclusions

Based on the study, the following conclusions may be drawn:

1. A Navier-Stokes solver, named GENCAS, has been developed and validated for various benchmark cases. The adequacy of infinitely thin wall representation of

the Gurney flap has been verified. The deployable Gurney flap was successfully simulated using dynamic wall boundary condition.

2. Several attempts have been made to improve the hybrid method for its BVI prediction capability. It was found that the satisfaction of Geometric Conservation Law could remove non-physical mass and momentum accumulation at the far-field where the cell size and deformation is large. Improved procedures for computing the Jacobian and metrics were found necessary on highly skewed grids especially with high order special accuracy schemes. The temporal accuracy increase from first order to second order was not enough to influence the BVI predictions for the small time steps used in the present study.
3. It was identified that the inability of the baseline solver to accurately capture BVI phenomena is due to the high artificial viscosity due to coarse grid. It was shown that an embedded grid method could improve the BVI prediction efficiently.
4. The 7^{th} order WENO scheme in itself was not enough to improve BVI prediction with a coarse grid. However, the 7^{th} order scheme improved the solution quality when used in conjunction with embedded grids.
5. Although the hybrid method coupled with a CSD code shows reasonable prediction for the rotor air loads, prediction of the wake trajectory is still an issue.
6. When the rotor is operated in autorotation with a fixed control setting, it was found that the deployment of the Gurney flap at a moderate deflection angle simultaneously increased rotor thrust and decreased the descent rate needed to maintain autorotation. However, increasing the Gurney flap deflection above nominal values caused flow separation, and the attended drag rise reduced its

beneficial effect. The study indicates that an optimally deflected Gurney flap may be useful in flare maneuvers prior to touch-down by increasing thrust, especially for vehicles with high disk loading.

7. When the rotor was trimmed for identical thrust and for zero hub moments, the Gurney flap equipped rotor required a higher rate of descent rate compared the baseline rotor to maintain autorotation state. Although the flap installed blade section produced a higher propulsive force in the driving region, the profile and induced drag rise in the driven region was also higher, and the net effect increased the required shaft torque. This indicates that deploying the flap only over the driving region may benefit autorotation and decrease the descent rate. Similarly, the flap deployed in the driving region may enable the auto-gyro to operate at a low backward disk tilt angle, reducing vehicle drag and increasing lift.
8. Deployment of Gurney flaps over the lower side of blade trailing edge reduce rotor vibrations, but also had the adverse effect of high nose-down pitching moments.
9. A 4P harmonic deployment of Gurney flap over both lower and upper sides of the airfoil led to an 80% or greater reduction in vertical vibratory loads. The trim state is maintained without performance penalty and without significant local nose-down pitching moment issue.
10. It was found that the 4P and 8P harmonics of vibration could be successfully suppressed simultaneously through individual control of multi-segmented flaps.

8.2 Recommendations

Based on the study, the following recommendations are made for further research.

1. The wake model in the current hybrid method should be improved to increase its accuracy in load and wake trajectory predictions. The present work employed a single tip vortex trailer model. The present approach should be extended to include multiple trailers distributed along the span and shed wake vortex filaments. In the present work, the trailer vortex was assumed to leave the rotor at radial location where peak circulation occurs. Determining the tip vortex release point is another issue that should be further investigated.
2. Although the embedded grid is an efficient way of capturing vortices, a pre-defined embedded grid placed upstream of the rotor requires more computational time compared to typical coarse grid approach. An adaptive grid approach that places embedded grids only in the vicinity of the vortices using triggers such as vorticity or helicity may be beneficial.
3. Deployable Gurney flap was simulated by dynamic wall boundary condition with infinite thickness. For a more accurate analysis, Gurney flaps with finite thickness may be simulated with overset mesh.
4. Further study on the impact of Gurney flaps on vehicle autorotation characteristics is recommended.
5. The periodic load change due to the Gurney flap may be a source of high frequency noise. Its effect on the noise should be investigated using an acoustics analysis code.
6. In the present study, dynamics of the control system was not considered. In practical implementations, time lag between the control input and the flap deployment is an important factor and should be considered.

7. Using current methodology, the usage of a deployable Gurney flap may be explored in terms of performance improvement in high speed forward flight. Although its efficiency on the retreating side is low and it becomes ineffective in separated flow, a deployable Gurney flap may be used to alleviate dynamic stall issue in conjunction with other active control devices such as active leading edge droop.
8. The flap may be used as an active vortex attenuation device so that the BVI strength is reduced. For this, full Navier-Stokes simulations covering the entire rotor are required with a grid fine enough to capture the traveling vortices.
9. Rotor in high speed forward flight produces high pitch link load due to transonic flow. Study on the cancellation of the high pitch link load using deployable Gurney flap is recommended.
10. The current numerical methodology may be employed in the design process of a rotorcraft to provide high fidelity prediction of airloads. It is recommended that active control devices such as deployable micro flaps be explored using the current methodology in an early design stage to meet the increasingly stringent requirements on noise and vibration facing next generation vehicle designers.

APPENDIX A

GOVERNING EQUATIONS IN GENERALIZED COORDINATE SYSTEM

The three-dimensional non-dimensionalized compressible viscous flow Navier-Stokes equations in Cartesian coordinate system can be written as:

$$\frac{\partial Q}{\partial t}+\frac{\partial E}{\partial x}+\frac{\partial F}{\partial y}+\frac{\partial G}{\partial z}=\frac{M_\infty}{Re_\infty}\left(\frac{\partial E_v}{\partial x}+\frac{\partial F_v}{\partial y}+\frac{\partial G_v}{\partial z}\right) \tag{A.1}$$

The coordinate transformation from the physical domain, (x, y, z, t), to the generalized computational domain, (ξ, η, ζ, t), may be done in following manner.

Since

$$\begin{aligned}\xi &= \xi(x, y, z, t)\\ \eta &= \eta(x, y, z, t)\\ \zeta &= \zeta(x, y, z, t)\end{aligned} \tag{A.2}$$

Chain rule is applied to the differentials in equation (A.1)

$$\begin{aligned}\frac{\partial}{\partial x} &= \xi_x\frac{\partial}{\partial \xi}+\eta_x\frac{\partial}{\partial \eta}+\zeta_x\frac{\partial}{\partial \zeta}+t_x\frac{\partial}{\partial t}\\ \frac{\partial}{\partial y} &= \xi_y\frac{\partial}{\partial \xi}+\eta_y\frac{\partial}{\partial \eta}+\zeta_y\frac{\partial}{\partial \zeta}+t_y\frac{\partial}{\partial t}\\ \frac{\partial}{\partial z} &= \xi_z\frac{\partial}{\partial \xi}+\eta_z\frac{\partial}{\partial \eta}+\zeta_z\frac{\partial}{\partial \zeta}+t_z\frac{\partial}{\partial t}\\ \frac{\partial}{\partial t} &= \xi_t\frac{\partial}{\partial \xi}+\eta_t\frac{\partial}{\partial \eta}+\zeta_t\frac{\partial}{\partial \zeta}+t_t\frac{\partial}{\partial t}\end{aligned} \tag{A.3}$$

Where, the metrics are defined as:

$$\begin{aligned}\xi_t &= -x_t\xi_x - y_t\xi_y - z_t\xi_z\\ \eta_t &= -x_t\eta_x - y_t\eta_y - z_t\eta_z\\ \zeta_t &= -x_t\zeta_x - y_t\zeta_y - z_t\zeta_z\end{aligned} \tag{A.4}$$

$$
\begin{aligned}
\xi_x &= J\left(y_\eta z_\zeta - y_\zeta z_\eta\right) \\
\xi_y &= J\left(x_\zeta z_\eta - x_\eta z_\zeta\right) \\
\xi_z &= J\left(x_\eta y_\zeta - x_\zeta y_\eta\right) \\
\eta_x &= J\left(y_\zeta z_\xi - y_\xi z_\zeta\right) \\
\eta_y &= J\left(x_\xi z_\zeta - x_\zeta z_\xi\right) \\
\eta_z &= J\left(x_\zeta y_\xi - x_\xi y_\zeta\right) \\
\zeta_x &= J\left(y_\xi z_\eta - y_\eta z_\xi\right) \\
\zeta_y &= J\left(x_\eta z_\xi - x_\xi z_\eta\right) \\
\zeta_z &= J\left(x_\xi y_\eta - x_\eta y_\xi\right) \\
\xi_t &= -\left(y_\zeta z_\xi - y_\xi z_\zeta\right) \\
\eta_t &= J\left(y_\zeta z_\xi - y_\xi z_\zeta\right)
\end{aligned}
\tag{A.5}
$$

And the Jacobian of the coordinate transformation is defined as follows:

$$
\begin{aligned}
J = \frac{\partial(\xi,\eta,\zeta,t)}{\partial(x,y,z,t)} &= \frac{1}{x_\xi\left(y_\eta z_\zeta - y_\zeta z_\eta\right) - x_\eta\left(y_\xi z_\zeta - y_\zeta z_\xi\right) + x_\zeta\left(y_\xi z_\eta - y_\eta z_\xi\right)} \\
&= \frac{1}{Volume}
\end{aligned}
\tag{A.6}
$$

Equation (A.1) can be re-written in the following form after substituting equation (A.3) and divide by *J*:

$$
\begin{aligned}
&\xi_t \frac{1}{J}\frac{\partial Q}{\partial \xi} + \eta_t \frac{1}{J}\frac{\partial Q}{\partial \eta} + \zeta_t \frac{1}{J}\frac{\partial Q}{\partial \zeta} + t_t \frac{1}{J}\frac{\partial Q}{\partial t} + \\
&\xi_x \frac{1}{J}\frac{\partial \tilde{E}}{\partial \xi} + \eta_x \frac{1}{J}\frac{\partial \tilde{E}}{\partial \eta} + \zeta_x \frac{1}{J}\frac{\partial \tilde{E}}{\partial \zeta} + t_x \frac{1}{J}\frac{\partial \tilde{E}}{\partial t} + \\
&\xi_y \frac{1}{J}\frac{\partial \tilde{F}}{\partial \xi} + \eta_y \frac{1}{J}\frac{\partial \tilde{F}}{\partial \eta} + \zeta_y \frac{1}{J}\frac{\partial \tilde{F}}{\partial \zeta} + t_y \frac{1}{J}\frac{\partial \tilde{F}}{\partial t} + \\
&\xi_z \frac{1}{J}\frac{\partial \tilde{G}}{\partial \xi} + \eta_z \frac{1}{J}\frac{\partial \tilde{G}}{\partial \eta} + \zeta_z \frac{1}{J}\frac{\partial \tilde{G}}{\partial \zeta} + t_z \frac{1}{J}\frac{\partial \tilde{G}}{\partial t} + \\
&= 0
\end{aligned}
\tag{A.7}
$$

Where

$$
\begin{aligned}
\tilde{E} &= E - \frac{M_\infty}{Re_\infty} E_v \\
\tilde{F} &= F - \frac{M_\infty}{Re_\infty} F_v \\
\tilde{G} &= G - \frac{M_\infty}{Re_\infty} G_v
\end{aligned}
\tag{A.8}
$$

Since $t_t = 1, t_x = t_y = t_z = 0$ and $\frac{\xi_x}{J}\frac{\partial \tilde{E}}{\partial \xi} = \frac{\partial}{\partial \xi}\left(\tilde{E}\frac{\xi_x}{J}\right) - \tilde{E}\frac{\partial}{\partial \xi}\left(\frac{\xi_x}{J}\right)$, equation (A.7) may be reformed to:

$$\begin{aligned}
&\frac{1}{J}\frac{\partial Q}{\partial t} + \frac{\partial}{\partial \xi}\left[\frac{1}{J}\left(\tilde{E}\xi_x + \tilde{F}\xi_y + \tilde{G}\xi_z + Q\xi_t\right)\right] + \frac{\partial}{\partial \eta}\left[\frac{1}{J}\left(\tilde{E}\eta_x + \tilde{F}\eta_y + \tilde{G}\eta_z + Q\eta_t\right)\right] \\
&\quad + \frac{\partial}{\partial \zeta}\left[\frac{1}{J}\left(\tilde{E}\zeta_x + \tilde{F}\zeta_y + \tilde{G}\zeta_z + Q\zeta_t\right)\right] - \tilde{E}\left[\frac{\partial}{\partial \xi}\left(\frac{\xi_x}{J}\right) + \frac{\partial}{\partial \eta}\left(\frac{\eta_x}{J}\right) + \frac{\partial}{\partial \zeta}\left(\frac{\zeta_x}{J}\right)\right] \\
&\quad - \tilde{F}\left[\frac{\partial}{\partial \xi}\left(\frac{\xi_y}{J}\right) + \frac{\partial}{\partial \eta}\left(\frac{\eta_y}{J}\right) + \frac{\partial}{\partial \zeta}\left(\frac{\zeta_y}{J}\right)\right] - \tilde{G}\left[\frac{\partial}{\partial \xi}\left(\frac{\xi_z}{J}\right) + \frac{\partial}{\partial \eta}\left(\frac{\eta_z}{J}\right) + \frac{\partial}{\partial \zeta}\left(\frac{\zeta_z}{J}\right)\right] \\
&\quad - Q\left[\frac{\partial}{\partial \xi}\left(\frac{\xi_t}{J}\right) + \frac{\partial}{\partial \eta}\left(\frac{\eta_t}{J}\right) + \frac{\partial}{\partial \zeta}\left(\frac{\zeta_t}{J}\right)\right] = 0
\end{aligned} \tag{A.9}$$

By substituting the definition of metric, Eqn. (A.5), into the fifth, sixth, and seventh term in the above equation, those terms are summed up to be zero. An example is shown below:

$$\tilde{E}\left[\frac{\partial}{\partial \xi}\left(\frac{\xi_x}{J}\right) + \frac{\partial}{\partial \eta}\left(\frac{\eta_x}{J}\right) + \frac{\partial}{\partial \zeta}\left(\frac{\zeta_x}{J}\right)\right] = 0 \tag{A.10}$$

Where,

$$\begin{aligned}
\frac{\partial}{\partial \xi}\left(\frac{\xi_x}{J}\right) &= \frac{\partial}{\partial \xi}\left(y_\eta z_\zeta - y_\zeta z_\eta\right) = y_{\eta\xi} z_\zeta + y_\eta z_{\zeta\xi} - y_{\zeta\xi} z_\eta - y_\zeta z_{\eta\xi} \\
\frac{\partial}{\partial \eta}\left(\frac{\eta_x}{J}\right) &= \frac{\partial}{\partial \eta}\left(y_\zeta z_\xi - y_\xi z_\zeta\right) = y_{\zeta\eta} z_\xi + y_\zeta z_{\xi\eta} - y_{\xi\eta} z_\zeta - y_\xi z_{\zeta\eta} \\
\frac{\partial}{\partial \zeta}\left(\frac{\zeta_x}{J}\right) &= \frac{\partial}{\partial \zeta}\left(y_\xi z_\eta - y_\eta z_\xi\right) = y_{\xi\zeta} z_\eta + y_\xi z_{\eta\zeta} - y_{\eta\zeta} z_\xi - y_\eta z_{\xi\zeta}
\end{aligned} \tag{A.11}$$

The last term of the equation (A.9) is designated as GCL term.

$$RHS_{GCL} = Q\left[\frac{\partial}{\partial \xi}\left(\frac{\xi_t}{J}\right) + \frac{\partial}{\partial \eta}\left(\frac{\eta_t}{J}\right) + \frac{\partial}{\partial \zeta}\left(\frac{\zeta_t}{J}\right)\right] \tag{A.12}$$

The equation (A.9) is then re-written in the final form of the governing equation in generalized coordinate system.

$$\frac{1}{J}\frac{\partial Q}{\partial t} + \frac{\partial \bar{E}}{\partial \xi} + \frac{\partial \bar{F}}{\partial \eta} + \frac{\partial \bar{G}}{\partial \zeta} = \frac{\partial \bar{E}_v}{\partial \xi} + \frac{\partial \bar{F}_v}{\partial \eta} + \frac{\partial \bar{G}_v}{\partial \zeta} + RHS_{GCL} \tag{A.13}$$

Where,

$$\bar{E} = \frac{1}{J}\left(E\xi_x + F\xi_y + G\xi_z + Q\xi_t\right), \bar{E}_v = \frac{1}{J}\frac{M_\infty}{Re_\infty}\left(E_v\xi_x + F_v\xi_y + G_v\xi_z\right)$$

$$\bar{F} = \frac{1}{J}\left(E\eta_x + F\eta_y + G\eta_z + Q\eta_t\right), \bar{F}_v = \frac{1}{J}\frac{M_\infty}{Re_\infty}\left(E_v\eta_x + F_v\eta_y + G_v\eta_z\right) \tag{A.14}$$

$$\bar{G} = \frac{1}{J}\left(E\zeta_x + F\zeta_y + G\zeta_z + Q\zeta_t\right), \bar{G}_v = \frac{1}{J}\frac{M_\infty}{Re_\infty}\left(E_v\zeta_x + F_v\zeta_y + G_v\zeta_z\right)$$

A simpler form can be obtained using

$$\frac{1}{J}\frac{\partial Q}{\partial t} = \frac{\partial}{\partial t}\left(\frac{Q}{J}\right) - Q\frac{\partial}{\partial t}\left(\frac{1}{J}\right) \tag{A.15}$$

and

$$Q\frac{\partial}{\partial t}\left(\frac{1}{J}\right) + RHS_{GCL} = Q\left[\frac{\partial}{\partial t}\left(\frac{1}{J}\right) + \frac{\partial}{\partial \xi}\left(\frac{\xi_t}{J}\right) + \frac{\partial}{\partial \eta}\left(\frac{\eta_t}{J}\right) + \frac{\partial}{\partial \zeta}\left(\frac{\zeta_t}{J}\right)\right] = 0 \tag{A.16}$$

The above relation (A.16) can be verified by substituting the definition of the Jacobian and the metrics as follows:

$$\begin{aligned}
\frac{\partial}{\partial t}\left(\frac{1}{J}\right) &= \frac{\partial}{\partial t}\left[x_\xi\left(y_\eta z_\zeta - y_\zeta z_\eta\right) - x_\eta\left(y_\xi z_\zeta - y_\zeta z_\xi\right) + x_\zeta\left(y_\xi z_\eta - y_\eta z_\xi\right)\right] \\
&= \frac{\partial}{\partial t}\left[x_\xi\frac{\xi_x}{J} + x_\eta\frac{\eta_x}{J} + x_\zeta\frac{\zeta_x}{J}\right] \\
&= \frac{\xi_x}{J}\frac{\partial x_\xi}{\partial t} + x_\xi\frac{\partial}{\partial t}\left(\frac{\xi_x}{J}\right) + \frac{\eta_x}{J}\frac{\partial x_\eta}{\partial t} + x_\eta\frac{\partial}{\partial t}\left(\frac{\eta_x}{J}\right) + \frac{\zeta_x}{J}\frac{\partial x_\zeta}{\partial t} + x_\zeta\frac{\partial}{\partial t}\left(\frac{\zeta_x}{J}\right) \\
&= \frac{\xi_x}{J}\frac{\partial x_t}{\partial \xi} + \frac{\eta_x}{J}\frac{\partial x_t}{\partial \eta} + \frac{\zeta_x}{J}\frac{\partial x_t}{\partial \zeta} + x_\xi\frac{\partial}{\partial t}\left(y_\eta z_\zeta - y_\zeta z_\eta\right) + \\
&\quad x_\eta\frac{\partial}{\partial t}\left(y_\zeta z_\xi - y_\xi z_\zeta\right) + x_\zeta\frac{\partial}{\partial t}\left(y_\xi z_\eta - y_\eta z_\xi\right)
\end{aligned} \tag{A.17}$$

The last three terms may be expanded as:

$$
\begin{aligned}
x_\xi \frac{\partial}{\partial t}\left(y_\eta z_\zeta - y_\zeta z_\eta\right) &= x_\xi\left[y_{t\eta} z_\zeta + y_\eta z_{t\zeta} - y_{t\zeta} z_\eta - y_\zeta z_{t\eta}\right] \\
x_\eta \frac{\partial}{\partial t}\left(y_\zeta z_\xi - y_\xi z_\zeta\right) &= x_\eta\left[y_{t\zeta} z_\xi + y_\zeta z_{t\xi} - y_{t\xi} z_\zeta - y_\xi z_{t\zeta}\right] \\
x_\zeta \frac{\partial}{\partial t}\left(y_\xi z_\eta - y_\eta z_\xi\right) &= x_\zeta\left[y_{t\xi} z_\eta + y_\xi z_{t\eta} - y_{t\eta} z_\xi - y_\eta z_{t\xi}\right]
\end{aligned}
\tag{A.18}
$$

The terms in the RHS_{GCL} are:

$$
\begin{aligned}
\frac{\partial}{\partial \xi}\left(\frac{\xi_t}{J}\right) &= -\left[x_t \frac{\partial}{\partial \xi}\left(\frac{\xi_x}{J}\right) + y_t \frac{\partial}{\partial \xi}\left(\frac{\xi_y}{J}\right) + z_t \frac{\partial}{\partial \xi}\left(\frac{\xi_z}{J}\right) + \frac{\xi_x}{J}\frac{\partial x_t}{\partial \xi} + \frac{\xi_y}{J}\frac{\partial y_t}{\partial \xi} + \frac{\xi_z}{J}\frac{\partial z_t}{\partial \xi}\right] \\
\frac{\partial}{\partial \eta}\left(\frac{\eta_t}{J}\right) &= -\left[x_t \frac{\partial}{\partial \eta}\left(\frac{\eta_x}{J}\right) + y_t \frac{\partial}{\partial \eta}\left(\frac{\eta_y}{J}\right) + z_t \frac{\partial}{\partial \eta}\left(\frac{\eta_z}{J}\right) + \frac{\eta_x}{J}\frac{\partial x_t}{\partial \eta} + \frac{\eta_y}{J}\frac{\partial y_t}{\partial \eta} + \frac{\eta_z}{J}\frac{\partial z_t}{\partial \eta}\right] \\
\frac{\partial}{\partial \zeta}\left(\frac{\zeta_t}{J}\right) &= -\left[x_t \frac{\partial}{\partial \zeta}\left(\frac{\zeta_x}{J}\right) + y_t \frac{\partial}{\partial \zeta}\left(\frac{\zeta_y}{J}\right) + z_t \frac{\partial}{\partial \zeta}\left(\frac{\zeta_z}{J}\right) + \frac{\zeta_x}{J}\frac{\partial x_t}{\partial \zeta} + \frac{\zeta_y}{J}\frac{\partial y_t}{\partial \zeta} + \frac{\zeta_z}{J}\frac{\partial z_t}{\partial \zeta}\right]
\end{aligned}
\tag{A.19}
$$

Summing up the three terms in the equation (A.19) and using the relation in (A.10), the RHS_{GCL} term may be written as:

$$
\begin{aligned}
RHS_{GCL} &= Q\left[\frac{\partial}{\partial \xi}\left(\frac{\xi_t}{J}\right) + \frac{\partial}{\partial \eta}\left(\frac{\eta_t}{J}\right) + \frac{\partial}{\partial \zeta}\left(\frac{\zeta_t}{J}\right)\right] \\
= -Q\Bigg\{&\left[\frac{\xi_x}{J}\frac{\partial x_t}{\partial \xi} + \frac{\eta_x}{J}\frac{\partial x_t}{\partial \eta} + \frac{\zeta_x}{J}\frac{\partial x_t}{\partial \zeta}\right] + x_\xi\left[y_{t\eta} z_\zeta + y_\eta z_{t\zeta} - y_{t\zeta} z_\eta - y_\zeta z_{t\eta}\right] \\
&+ x_\eta\left[y_{t\zeta} z_\xi + y_\zeta z_{t\xi} - y_{t\xi} z_\zeta - y_\xi z_{t\zeta}\right] \\
&+ x_\zeta\left[y_{t\xi} z_\eta + y_\xi z_{t\eta} - y_{t\eta} z_\xi - y_\eta z_{t\xi}\right]\Bigg\}
\end{aligned}
\tag{A.20}
$$

Thus, from the expression (A.17) and (A.20),

$$
Q\frac{\partial}{\partial t}\left(\frac{1}{J}\right) + RHS_{GCL} = 0 \tag{A.21}
$$

Then, the governing equation becomes:

$$
\frac{\partial \bar{Q}}{\partial t} + \frac{\partial \bar{E}}{\partial \xi} + \frac{\partial \bar{F}}{\partial \eta} + \frac{\partial \bar{G}}{\partial \zeta} = \frac{\partial \bar{E}_v}{\partial \xi} + \frac{\partial \bar{F}_v}{\partial \eta} + \frac{\partial \bar{G}_v}{\partial \zeta} \tag{A.22}
$$

Where, $\bar{Q} = Q/J$.

REFERENCES

[1] Bousman, W. G., "Putting the Aero Back Into Aeroelasticity," *NASA TM-2000-209589*, March 2000.

[2] Kretz, M., "Research in Multicyclic and Active Control of Rotary Wings," *Vertica*, Vol. 1, No. 1/2, 1976, pp. 95-105.

[3] Wasikowski, M. E., "An Investigation of Helicopter Individual Blade Control using Optimal Output Feedback," Ph. D. Dissertation, School of Aerospace Engineering, Georgia Institute of Technology, Atlanta, GA, 1989.

[4] Nygren, K. P., "An Investigation of Helicopter Higher Harmonic Control using a Dynamic System Coupler Simulation," Ph. D. Dissertation, School of Aerospace Engineering, Georgia Institute of Technology, Atlanta, GA, 1986.

[5] Patt, D., Liu, L., Chandrasekar, J., Bernstein, D. S., and Fridemann, P. P., "The HHC Algorithm for Helicopter Vibration Reduction Revisited," AIAA 2004-1948, 45th AIAA/ASME/ASCE/AHS/ASC Structural Dynamics & Materials Conference, Palm Springs, CA, 19-22 April, 2004.

[6] Reichert, G., "Helicopter Vibration Control-A Survey," *Vertica*, Vol. 5, No. 1, 1981, pp. 1-20.

[7] Loewy, R. G., "Helicopter Vibrations: A Technological Perspective," *AHS Journal*, Vol. 29, Oct. 1984, pp. 4-30.

[8] Friedmann, P. P., "Helicopter Vibration Reduction Using Structural Optimization with Aeroelastic/Multidisciplinary Constraints-A Survey," *Journal of Aircraft*, Vol. 28, No. 1, 1991, pp. 8-21.

[9] Fridemann, P. P., and Millott, T. A., "Vibration Reduction in Rotorcraft Using Active Control: A Comparison of Various Approaches," *Journal of Guidance, Control and Dynamics*, Vol. 18, No. 4, July-August 1995, pp. 664-673.

[10] Depailler, G., and Friedmann, P. P., "Reduction of Vibration Due to Dynamic Stall in Helicopters Using an Actively Controlled Flap," AIAA 2002-1431, 43rd AIAA/ASME/ASCE/AHS/ASC Structural Dynamics & Materials Conference, Denver, Colorado, 22-25 April, 2002.

[11] Glaz, B., Friedmann, P. P., and Liu, L., "Vibration Reduction and Performance Enhancement of Helicopter Rotors Using an Active/Passive Approach," AIAA 2008-2178, 49th AIAA/ASME/ASCE/AHS/ASC Structural Dynamics & Materials Conference, Schaumburg, IL, 7-10 April, 2008.

[12] Shin, S., and Cesnik, C. E. S., "Helicopter Vibration Reduction in Forward Flight Using Blade Integral Twist Control," *AMSL-01-07*, Aug. 2001.

[13] Shin, S., and Cesnik, C. E. S., "Helicopter Vibration Reduction in Forward Flight Using Blade Integral Twist Control," AIAA 2002-1447, 43th AIAA/ASME/ASCE/AHS/ASC Structural Dynamics & Materials Conference, Denver, Colorado, 22-25 April, 2002.

[14] Kinzel, M. P., Maughmer, M. D., and Lesieutre, G. A., "Miniature Trailing-Edge Effectors for Rotorcraft Performance Enhancement," *Journal of AHS*, Vol. 52, No. 2, April 2007, pp.146-158.

[15] Thiel, M. R., Lesieutre, G. A., Maughmer, M. D., and Koopmann, G. H., "Actuation of an Active Gurney Flap for Rotorcraft Applications," AIAA 2006-2181, 47th AIAA/ASME/ASCE/AHS/ASC Structures, Structural Dynamics, and Materials Conference, Newport, Rhode Island , 1-4 May 2006.

[16] Min, B. Y., Sankar, L. N., and Yu, Y. H., "Computational Studies of the Effects of Gurney Flaps on the Autorotative Performance of Rotors in Descent Flight," Proceedings of the AHS Aeromechanics Specialists Meeting, San Francisco, CA, January 2008.

[17] Troolin, D. R., Longmire, E., and Lai, W. T., "Time Resolved PIV Analysis of a Gurney flap on a NACA 0015 Airfoil," 6th International Symposium on Particle Image Velocimetry, Pasadena, California, 21-23 September, 2005.

[18] Prouty, R.W., "Aerodynamics: The Gurney Flap, Part 2," Rotor & Wing, 1 March 2000.

[19] Matalanis, C. G., and Eaton, J. K., "Wake Vortex Control Using Static Segmented Gurney Flaps," *AIAA Journal*, Vol. 45, No. 2, February 2007, pp. 321-328.

[20] Lee, H., Kroo, I. M., and Bieniawski, S., "Flutter Suppression for High Aspect Ratio Flexible Wings Using Microflaps," AIAA Paper 2002-1717, 2002.

[21] Vey, S., Paschereit, O. C., Greenblatt, D., and Meyer, R., "Flap Vortex Management by Active Gurney Flaps," AIAA Paper 2008-286, 2008.

[22] Duquette, S. M., and Wei, F., "Development of Piezoelectric Servo Flap Actuator," AIAA Paper 2007-1257, 2007.

[23] Neuhart, D. H. and Pendergraft, O. C., Jr., "A Water Tunnel Study of Gurney Flaps," *NASA TM 4071*, November 1988.

[24] Jang, C. S., Ross, J. C. and Cummings, R. M., "Computational Evaluation of an Airfoil with a Gurney Flap," AIAA Paper 92-2708, June 1992.

[25] Giguere, P., Lemay, J. and Dumas, G., "Gurney Flap Effects and Scaling for Low-Speed Airfoils," AIAA Paper 95-1881, 1995.

[26] Myose, R., Papadakis, M. and Heron, I., "Gurney Flap Experiments on Airfoils, Wings, and Reflection Plane Model," *Journal of Aircraft*, Vol. 35, March-April 1998, pp. 206-211.

[27] Jeffrey, D., Zhang, X. and Hurst, D. W., "Aerodynamics of Gurney Flaps on a Single- Element High-Lift Wing," *Journal of Aircraft*, Vol. 37, March-April 2000, pp. 295-301.

[28] Price, J. L., Chokani, N., and Mangalam, S., "Unsteady Aerodynamic Simulations of an Oscillating Airfoil with Miniflaps," AIAA 2002-0118, 40th AIAA Aerospace Sciences and Exhibit, Reno, Nevada, 14-17 Jan. 2002.

[29] Chandrasekhara, M. S., Martin, P. B., and Tung, C., "Compressible Dynamic Stall Performance of a Variable Droop Leading Edge Airfoil with a Gurney Flap," AIAA 2004-0041, 42nd AIAA Aerospace Science Meeting, Reno, Nevada, 2004.

[30] Lee, B., Yee, K., Joo, W., and Lee, D., "Passive Control of Dynamic Stall via Nose Droop with Gurney Flap," AIAA Paper 2005-1364.

[31] Guzel, G., Sankar, L. N., and Rhee, M., "Computational Investigation of the Effects of Gurney Flap on the Aerodynamic Performance of VR-12 Airfoil," AIAA 2005-4960, 23rd AIAA Applied Aerodynamics Conference, Toronto, Ontario Canada, 6-9 June 2005.

[32] Nelson, J., and Koratkar, N., "Effect of Miniaturized Gurney Flaps on Aerodynamic Performance of Microscale Rotors," *Journal of Aircraft*, Vol. 42, No. 2, March-April 2005, pp. 557-560.

[33] Liu, L., Padthe, A. K., and Friedmann, P. P. "A Computational Study of Microflaps with Application to Vibration Reduction in Helicopter Rotors," AIAA Paper 2009-2604, 2009.

[34] Min, B. Y., Sankar, L. N., Rajmohan, N., and Prasad, J.V.R., "Computational Investigation of the Effects of Gurney Flaps on Rotors in Forward Flight," *Journal of Aircraft*, Vol. 46, No. 6, Nov.-Dec. 2009.

[35] Bae, E. S., Gandhi, F., and Maughmer, M., "Optimally Scheduled Deployments of Miniature Trailing-Edge Effectors for Rotorcraft Power Reduction," American Helicopter Society 65th Annual Forum, Grapevine, TX, May 27-29, 2009.

[36] Roget, B., and Chopra, I., "Closed-Loop Test of a Rotor with Individually Controlled Trailing-Edge Flaps for Vibration Reduction," *Journal of the American Helicopter Society*, Vol. 55, No. 1, 2010, pp. 012009-1 - 012009-12.

[37] Mayda, E., and van Dam, C. P., "Computational Investigation of Finite Width Microtabs for Aerodynamic Load Control," AIAA Paper 2005-1185.

[38] Chow, R., and van Dam, C. P., "Unsteady Computational Investigations of Deploying Load Control Microtabs," *Journal of Aircraft*, Vol. 43, No. 5, 2006, pp. 1458-1469.

[39] Baker, J. P., Standish, K. J., and van Dam, C. P., "Two-Dimensional Wind Tunnel and Computational Investigation of a Microtab Modified Airfoil," *Journal of Aircraft*, Vol. 44, No. 2, 2007, pp. 563-572.

[40] Tongchitpakdee, C., "Computational Studies of the Effects of Active and Passive Circulation Enhancement Concepts on Wind Turbine Performance," Ph. D. Dissertation, School of Aerospace Engineering, Georgia Institute of Technology, Atlanta, GA, 2007.

[41] Yeo, H., "Assessment of Active Controls for Rotor Performance Enhancement," *AHS Journal*, Vol. 53, No. 2, 2008, pp.152-163.

[42] Yee, K., Joo, W., and Lee, D., "Aerodynamic Performance Analysis of a Gurney Flap for rotorcraft Application," *Journal of Aircraft*, Vol. 44, No. 3, May-June 2007, pp.1003-1014.

[43] Nicolic, V. R., "Effect of Full-Span Gurney Flap Height on Wing Wake Vortex Alleviation," *Journal of Aircraft*, Vol. 43, No. 5, September-October 2006, pp. 1555-1557.

[44] Lee, L. and Lee, T., "Effect of Gurney Flap on Unsteady Wake Vortex," *Journal of Aircraft*, Vol. 44, No. 4, July-August 2007, pp. 1398-1401.

[45] Sankar, L. N., Bharadvaj, B. K., and Tsung, F. L., "A three-dimensional Navier-Stokes/full-potential coupled analysis for viscous transonic flow," AIAA-1991-1595, AIAA 10th Computational Fluid Dynamics Conference, Honolulu, HI, June 24-27, 1991.

[46] Berezin, C. R., and Sankar, L. N., "An Improved Navier-Stokes/Full-Potential Coupled Analysis for Rotors," *Mathematical Computational Modeling*, Vol. 19, No. 3/4, 1994, pp. 125-133.

[47] Sopher, R., and Hallock, D. W., "Time-history analysis for rotorcraft dynamics based on a component approach," *Journal of the American Helicopter Society*, Vol. 31, No. 1, 1986, pp.43-51.

[48] Berkman, M. E., Sankar, L. N., Berezin, C. R., and Torok, M. S., "Navier-Stokes/Full Potential/Free-Wake Method for Rotor Flows," *Journal of Aircraft*, Vol. 34, No. 5, 1997, pp. 635-640.

[49] Caradonna, F. X., and Tung, C., "Experimental and Analytical Studies of a Model Helicopter Rotor in Hover," NASA TM-81232, Sept. 1981.

[50] Yang, Z., Sankar, L. N., Smith, M. J., and Bauchau, O., "Recent Improvements to a Hybrid Method for Rotors in Forward Flight," *Journal of Aircraft*, Vol. 39, No. 5, 2002, pp. 804-812.

[51] Phanse, S, Sankar, L. N., Charles, B. D., "Efficient Coupled Fluid Structure Interaction Approach for Analysis of Rotors in Forward Flight," American Helicopter Vertical Lift Aircraft Design Conference, San Francisco, CA, January 18-29, 2006.

[52] Rajmohan, N., Sankar, L.N., Bauchau, O., Makinen, S.M., T.A. Egolf and Charles, B.D., "Application of Hybrid Methodology to Rotors in Steady and Maneuvering Flight," *American Helicopter Society 64th Annual Forum*, Montreal, Canada, April 29 − May 1, 2008.

[53] Egolf, T. A., Rajmohan, N., Reed, E., and Sankar, L. N., "A Hybrid CFD Methodfor Coaxial Rotor Performance Prediction in Forward Flight," AHS Aeromechanics Specialists Meeting, San Francisco, CA, January 2010.

[54] Min, B. Y., Collins, K., and Sankar, L. N., "HART-II Correlation Using a Hybrid Method," 5th International HART-II Workshop, Montreal, Canada, April, 2008.

[55] Min, B. Y., Lee, W., Englar, R., and Sankar, L. N., "Numerical Investigation of Circulation Control Airfoils," *Journal of Aircraft*, Vol. 46, No. 4, July-August 2009, pp. 1403-1410.

[56] Min, B. Y., and Sankar, L. N., "Enhancements to a Hybrid Navier-Stokes/Free Wake Method for Modeling of Blade Vortex Interactions," *Journal of Aircraft* (accepted).

[57] Min, B. Y., Sankar, L. N., and Yu, Y. H., "Combined Lagrangean-Eulerian Approaches for Improved Prediction of Blade-Vortex-Interaction Phenomena," 2nd International Forum on Rotorcraft Multidisciplinary Technology, Seoul, Korea, Oct. 19-20, 2009.

[58] Roe, P. L., "Approximate Riemann Solvers, Parameter Vectors, and Difference Schemes," *Journal of Computational Physics*, Vol. 43, 1981, pp. 357-372.

[59] Van Leer, B. "Upwind Difference Methods for Aerodynamic Problems Governed by the Euler Equations," *Lectures in Applied Mathematics*, Vol. 22, 1985.

[60] Van Albada, G. D., van Leer, B., and Roberts, W. W. Jr., "Comparative Study of Computational Methods in Cosmic Gas Dynamics," *Astronomy and Astrophysics*, Vol. 108, 1982, pp. 76-84.

[61] Vinokur, M. and Liu, Y., "Equilibrium Gas Flow Computations. II. An Analysis of Numerical Formulations of Conservation Laws," AIAA Paper 88-0127,1988.

[62] Pulliam, T. H. and Steger, J. L., "Implicit Finite Difference Simulations of Three Dimensional Compressible Flow," *AIAA Journal*, Vol. 18, No. 2, 1980, pp. 159-167.

[63] Yoon, S. and Jameson, A., "Lower-Upper Symmetric-Gauss-Seidel Method for the Euler and Navier-Stokes Equations," *AIAA Journal*, Vol. 26, No.9, 1988, pp. 1025-1026.

[64] Spalart, P. R. and Allmaras, S. R., "A One-Equation Turbulence Model for Aerodynamic Flows," *La Recherche Aerospatiale*, 1994.

[65] Spalart, P. R., Jou, W-H., Strelets, M., and Allmaras, S. "Comments on the Feasibility of LES for Wings and on a Hybrid RAN/LES Approach," Proceeding 1st AFOSR Int. Conf. on DNS/LES, Ruston, LA. 1997.

[66] Menter, F. R., "Two-Equation Eddy-Viscosity Turbulence Models for Engineering Applications," *AIAA Journal*, Vol. 32, No. 8, August 1994, pp. 1598-1605.

[67] Strelets, M., "Detached Eddy Simulation of Massively Separated Flows," AIAA-2001-0879, 39th AIAA Aerospace Sciences Meeting and Exhibit, Reno, Nevada, January 2001.

[68] Fang, Y., and Menon, S., "A Two-Equation Subgrid Model for Large-Eddy Simulation of High Reynolds Number Flows," AIAA paper 2006-116, 44th AIAA Aerospace Sciences Meeting and Exhibit, Reno, Nevada, 9-12 January, 2006.

[69] Fang, Y., and Menon, S., " Kinetic Eddy Simulation of Static and Dynamic Stall," AIAA 2006-3847, 24th Applied Aerodynamics Conference, San Francisco, California, 5-8 June, 2006.

[70] Zaki, M., Menon, S., and Sankar, L. N., "A Hybrid RANS/KES Model for External and Internal Flow Applications," AIAA 2008-5216, *44th AIAA/ASME/SAE/ASEE Joint Propulsion Conference and Exhibit*, Hartford, CT, 21-23 July, 2008.

[71] Zaki, M., "Physics Based Modeling of Axial Compressor," Ph. D. Dissertation, School of Aerospace Engineering, Georgia Institute of Technology, Atlanta, GA, 2009.

[72] Benjanirat, S., "Computational Studies of Horizontal Axis Wind Turbines in High Wind Speed Condition Using Advanced Turbulence Models," Ph. D. Dissertation, School of Aerospace Engineering, Georgia Institute of Technology, Atlanta, GA, 2006.

[73] Message Passing Interface Forum, "MPI: A message-passing interface standard," *International Journal of Supercomputer Applications*, Vol. 8, No. 3/4, 1994, pp. 159-416.

[74] Hoffmann, K. A. and Chiang, S. T., *Computational Fluid dynamics Volume II, Fourth Edition*, Engineering Education System, Wichita, Kansas, 2000.

[75] Nygaard, T. A., Saberi, H., Ormiston, R. A., Strawn, R. C., Potsdam, M., and Johnson, W., "Fluid Structure Interface for Rotorcraft Aeromechanic Computations," ELORET Corp., Advanced Rotorcraft Technology, AMRDEC, NASA-Ames Research Center, May 3, 2005. (Unpublished report)

[76] Sitaraman, J., "CFD Based Unsteady Aerodynamic Modeling for Rotor Aeroelastic Analysis," Ph. D. Dissertation, Department of Aerospace Engineering, University of Maryland, College Park, MD, 2003.

[77] Potsdam, M., Yeo, H., and Johnson, W., "Rotor Aerodynamic Prediction using Loose Aerodynamic/Structural Coupling," *American Helicopter Society 60th Annual Forum*, Baltimore, MD, June 2004.

[78] Datta, A., and Chopra, I., "Prediction of UH-60A Dynamic Stall Loads in High Altitude Level Flight using CFD/CSD Coupling," *American Helicopter Society 61st Annual Forum*, Grapevine, TX, June 2005.

[79] Datta, A., Sitaraman, J., Chopra, I., and Baeder, J. D., "CFD/CSD Prediction of Rotor Vibratory Loads in High-Speed Flight," *Journal of Aircraft*, Vol.43, No.6, Nov.-Dec. 2006, pp. 1698-1709.

[80] Vinokur, M., "An Analysis of Finite-Difference and Finite-Volume Formulations of Conservation Laws", *Journal of Computational Physics*, Vol. 81, 1989, pp. 1-52.

[81] Nichols, R. H., and Heikkinen B. D., "Validation of Implicit Algorithms for Unsteady Flows Including Moving and Deforming Grids," AIAA paper 2005-683, Jan. 2005.

[82] Shu, C. W., "Essentially non-oscillatory and weighted essentially non-oscillatory schemes for hyperbolic conservation laws," in *Advanced Numerical Approximation of Nonlinear Hyperbolic Equations*, Lecture Notes in Mathematics, volume 1697, Springer, 1998, pp. 325-432.

[83] Shu, C. W., "High order ENO and WENO schemes for Computational Fluid Dynamics," in *High-Order Methods for Computational Physics,* Lecture Notes in Computational Science and Engineering, volume 9, Springer, 1999, pp. 439-582.

[84] Yeshala, N., Egolf, T. A., Vasilescu, R., and Sankar, L. N., "Application of Higher Order Spatially Accurate Schemes to Rotors in Hover," AIAA 2006-2818, 24th Applied Aerodynamics Conference, San Frnacisco, CA, 5-8 June 2006.

[85] Cook, P.H., McDonald, M. A., and Firmin, M. C. P., "Aerofoil RAE 2822 - Pressure Distributions, and Boundary Layer and Wake Measurements," *Experimental Data Base for Computer Program Assessment*, AGARD Report AR 138, 1979.

[86] Piziali, R. A., "2-D and 3-D Oscillating Wing Aerodynamics for a Range of Angles of Attack Including Stall," NASA TM 4632, Sep. 1994.

[87] McAlister, K. W., Pucci, S. L., McCroskey, W. J., and Carr, L. W., "An Experimental Study of Dynamic Stall on Advanced Airfoil Sections, Volume2. Pressure and Force Data," NASA TM 84245, Sep. 1982.

[88] Greenblatt, D., Paschal, K. B., Yao, C.-S., Harris, J., Schaeffler, N. W., and Washburn, A. E., "A Separation Control CFD Validation Test Case, Part 1: Baseline and Steady Suction," *AIAA Journal*, Vol. 44, No. 12, 2006, pp. 2820-2830.

[89] http://cfdval2004.larc.nasa.gov/case3.html

[90] Goldman, L. J., and McLallin, K. L., "Cold Air Annular Cascade Investigations of Aerodynamic Performance of Core- Engine- Cooled Turbine Vanes. 1: Solid Vane Performance and Facility Description," *NASA TM X-3224*.

[91] Schmitt, V. and Charpin, F., "Pressure Distributions on the ONERA-M6-Wing at Transonic Mach Numbers," *Experimental Data Base for Computer Program Assessment.* Report of the Fluid Dynamics Panel Working Group 04, AGARD AR 138, May 1979.

[92] Yu, Y. H., Tung, C., van der Wall, B. G., Pausder, H., Burley, C., Brooks, T., Beaumier, P., Delrieux, Y., Mercker, E., and Pengel, K., "The HART-II Test: Rotor Wakes and Aeroacoustics with Higher-Harmonic Pitch Control (HHC) Inputs – The Joint German/French/Dutch/US Project," American Helicopter Society 58th Annual Forum, Montreal, Canada, June 11-13, 2002.

[93] van der Wall, and B.G., and Burley, C.L., "2nd HHC Aeroacoustic Rotor Test (HART II) - Part II: Representative Results -," DLR-IB 111-2005/03, 2005.

[94] Lim, J. W., Nygaard, T. A., Strawn, R., Potsdam, M., "BVI Airload Prediction Using CFD/CSD Loose Coupling," AHS 4th Vertical Lift Aircraft Design Conference, San Francisco, CA, Jan. 18-20, 2006.

[95] Jeong, J., and Hussain, F., "On the identification of a vortex," *Journal of Fluid Mechanics*, Vol. 285, 1995, pp. 69-94.

[96] van der Wall, B. G., "Mode identification and data synthesis of HART-II blade deflection data," DLR-IB-111-2007/28, June. 2007.

[97] Yang, C., and Aoyama, T. "Effect of Computation Parameters on BVI Noise Prediction Using HART II Motion Data," *34th European Rotorcraft Forum*, Liverpool, England, Sep. 2008.

VITA

BYUNG-YOUNG MIN

Byung-Young Min was born in Jeongseon, Korea on January 1st, 1976. He graduated from Konkuk University, Seoul, Korea. He received a Bachelor degree in Aerospace engineering from Konkuk University in February 2001 and Master's degree in Aerospace engineering from Konkuk University, Seoul, Korea in February 2003. He worked as an intern researcher at Thermvac Eng. Co. for one year and joined Georgia Institute of Technology in fall semester of 2004 to pursue a doctorate in school of aerospace engineering. He is a student member of the American Institute of Aeronautics and Astronautics, and the American Helicopter Society.